SKIN-FRICTION DRAG REDUCTION WITHIN TURBULENT FLOWS

by

Brian R. Elbing

A dissertation submitted in partial fulfillment
of the requirements for the degree of
Doctor of Philosophy
(Mechanical Engineering)
in The University of Michigan
2009

Doctoral Committee:

Professor Steven L. Ceccio, Co-Chair
Professor Marc Perlin, Co-Chair
Professor David R. Dowling
Associate Professor Michael J. Solomon

DEDICATION

To my parents, Ron and Ann, for their unfailing love and support throughout my life and trust in my decision making. To my sisters, Renee' and Teresa, who have helped me throughout my life, I could not ask for better sisters. To my fiancé Demoree whose support and understanding during my research and writing has made this possible. And finally to God who has always been my source of strength and direction in my life.

ACKNOWLEDGEMENTS

With such a large scale research effort there are numerous individuals that deserve recognition for their contributions to this work. First I have to thank my doctoral committee for their help and guidance. I appreciate Prof. Steven Ceccio who probably had more confidence in my ability when I started than I did and has provided continual guidance throughout my graduate studies. Prof. Marc Perlin whose willingness to fly to Memphis numerous times to do backbreaking manual labor and instruction in publication writing has been invaluable. Prof. David Dowling has significantly improved my ability to write publications and analyze data, and he has been the most influential classroom instructor I've had during my graduate studies. Prof. Michael Solomon's explanation of the rheology of polymer solutions has been a great help.

Nearly as important has been the sponsorship from the Defense Advanced Research Projects Agency (DARPA) and the Office of Naval Research (ONR) that has financially supported my research and education. Conversations with Dr. Thomas Beutner, Dr. Ki-Han Kim and Dr. L. Patrick Purtell has helped guide and direct my research. The polymer degradation in the large pipe flows was supported by DARPA under contract HR0011-04-1-0001 (Dr. Lisa Porter, Program Manager). The HIPLATE experiments were supported by DARPA under contracts HR0011-04-1-0001 and HR0011-06-1-0057 (Dr. Thomas Beutner, Program Manager) and contract N00014-06-1-0244 (Dr. L. Patrick Purtell, program manager). The content of this document does not

necessarily reflect the position or the policy of the United States Government, and no official endorsement should be inferred.

A special thanks is extended to Dr. Eric Winkel who has had a significant impact on nearly all aspects of my research work at the University of Michigan. He has helped me from the start of my research career at the University of Michigan, which has included guidance during HIPLATE Phase 3 when I received my first responsibilities, taught me drag reduction fundamentals during my first experiments with the pipe flow experiment, taught me how to manage a HIPLATE experiment during Phase 4 and assisted me with preparation and sampling on HIPLATE Phase 5.

Another colleague who has had a significant impact on my time at the University of Michigan is Dr. Shiyao Bian. Besides her great effort during HIPLATE Phase 5 for me and other collaborative research efforts, she has been a great friend from the moment I joined this research group. She encouraged me from the start when I doubted my ability.

Additionally, I have to thank the efforts of Mr. Kent Pruss with his many, many hours machining parts for us, Mr. William Kirkpatrick for his efforts modifying the HIPLATE model, the staff at the Large Cavitation Channel (Dr. J. Michael Cutbirth, Mr. Robert Etter and the technical crew) whose hard work made HIPLATE testing possible, Dr. Wendy Sanders & Dr. Ghanem Oweis whose past work on HIPLATE simplified the work I needed to do, Mrs. Doris Swanson who has helped throughout testing with travel and finances on our projects, the Prof. Michael Solomon's chemical engineering group

(Dr. Siva Vanapalli, Mr. Robert Glied and Mr. Abhi Shetty) that we have worked closely with for polymer drag reduction work, all my fellow students who have sacrificed time in Memphis (Dr. Xiaochun Shen, Dr. Chinar Aphale, Dr. Keary Lay, Dr. Natasha Chang, Dr. Jaeyhug Choi, Mr. Ryo Yakushiji and Mr. Simo Makiharju), others that have added an extra hand (Ms. Ciara Stella, Ms. Laetitia Decoster, Ms. Valentine Jaillant, Mr. Steve Patterson and Mr. Jishnu Bhattacharya) and the intellectual guidance from Dr. Duncan Brown (John Hopkins University), Dr. Howard Petrie (Pennsylvania State University) & Mr. Gordon Garwood.

The material presented in Part II was submitted in a similar form for publication in *Experiments in Fluids* in May of 2008 with co-authors Eric S. Winkel, Michael J. Solomon & Steven L. Ceccio and is currently under review. With the exception of the scaling of ALDR the work presented in Part III has been published in 2008 as part of "Bubble-induced skin-friction drag reduction and the abrupt transition to air-layer drag reduction" in the *Journal of Fluid Mechanics* with co-authors Eric S. Winkel, Keary A. Lay, Steven L. Ceccio, David R. Dowling & Marc Perlin. Portions of Parts IV and V have been presented in the 2008 conference paper "Polymer degradation within a high-Reynolds-number, flat-plate turbulent boundary layer that is fully rough," in the *Proceedings of the 27th Symposium on Naval Hydrodynamics* in Seoul, Korea. This conference paper was co-authored with David R. Dowling, Michael J. Solomon, Marc Perlin & Steven L. Ceccio.

Finally a special thanks to all my family and friends that have supported me during my graduate studies. Without them I could not have been able to get through this period of my life. Thank you.

TABLE OF CONTENTS

LIST OF FIGURES

LIST OF TABLES

PART I. INTRODUCTION (GLOBAL)

According to a recent report distributed by UN-Energy (*The Energy Challenge for Achieving the Millennium Goals*) the supply and use of energy is fundamental to achieving the Millennium Development Goals established by the United Nations (UN). UN-Energy's report argues that the limited supply of energy "entrenches poverty, constrains the delivery of social services, limits opportunities for women and erodes the environmental sustainability at local, national and global levels." This statement emphasizes the need to develop reliable energy sources that are renewable and develop new technologies that can increase the efficiency of current energy supplies.

The majority of the energy currently consumed in the world is supplied by oil, coal, natural gas, hydroelectricity and nuclear. According to the June 2008 *BP Statistical Review of World Energy* oil was the world's largest source for energy consumed in 2007 (~36%) with coal (~27%) and natural gas (~23%) being the second and third largest sources, respectively. While these energy sources are convenient due to their ability to be relatively easily stored, transported and used (since the infrastructure is already available), they have the disadvantage of being limited in quantity (extremely long renewal time period) and having a negative impact on the environment (e.g. particulate and greenhouse gas emissions). For these reasons numerous research efforts around the world have searched for alternative energy sources that are renewable and

environmentally friendly such as wind, solar and geothermal. Additionally, much effort has been focused on the efficient use of the oil, coal and natural gas sources, which would result in a reduction in wasted energy and a decrease in air pollution (i.e. lower particulate levels and reduced greenhouse gas emissions). For example, in the automotive industry the development of "hybrid cars" can increase the average miles per gallon of gasoline from ~25 to ~50. According to the 2007 *Motor Fuel Report* from the United States Department of Transportation – Federal Highway Administration approximately 9 million barrels of oil per day were consumed for automotive transportation in the United States of America (USA). Since hybrid sales account for only about 2% of the total USA car sales, if all current automobiles could be replaced with hybrids (obvious practical limitations exist for this possibility) approximately 4.5 million barrels of oil could be saved each day in the USA alone.

When discussing world energy consumption the USA is the primary focus of most discussions since it is the world's largest consumer of energy. According to the June 2008 *BP Statistical Review of World Energy* the USA used over 20% of the total energy consumed in the world (these results excluded use of wind, geothermal, solar, wood and animal waste as energy sources). As a result the USA is the world's largest consumer of oil (~25% world consumption in 2007), gas (~22% world consumption in 2007) and nuclear (~30% world consumption in 2007) energy, and is the second largest consumer of coal (~18% world consumption in 2007) behind China. The use of energy in the USA is typically divided into four categories; (1) transportation, (2) industrial, (3) residential & commercial and (4) electric power. Nearly 30% of the total energy consumption in the

USA is for transportation, which is primarily (96%) provided from oil (according to 2007 statistics provided by the United States Energy Information Administration). The objective for the current work is to develop methods for reducing the transportation fuel consumption for the USA. Specifically, the technologies developed are for the reduction of the skin-friction drag component of the total resistance on US Navy surface ships. However, application of such technologies could easily be adapted for non-military ships around the world.

As part of the UNFCCC Subsidiary Body for Scientific and Technological Advice's report on greenhouse gas emissions from ships in 2008 several estimates were compiled for the consumption of fuel by the world's non-military fleet in 2007, which was approximately 1.9 billion barrels of oil. Methods discussed in the current study have been shown to have the potential of reducing the total resistance on a surface ship by more than 60% at some speeds. This percentage varies with speed and a more detailed analysis is required to assess the overall fuel savings created with the reduced resistance. However, potentially over one billion barrels of fuel could be saved each year from the world's non-military fleet (this estimate assumes no energy cost to reduce the drag, 60% reduction could be achieved at all speeds and no new ship design is employed to convert a larger percentage of the total ship resistance to skin-friction drag).

The two drag reduction methods discussed within this paper are both active methods, which require continuous injection of an additive to the water flow around the ship surface to achieve drag reduction. The result is in an added energy cost associated

with the delivery of the additive to the flow and the carrying of additional materials (injection equipment and/or additives). The additives tested are dilute high molecular weight polymers and gas (air). Both methods have been heavily studied with varying degrees of successful application.

Polymer drag reduction (PDR) has become widely used in applications involving internal flows (e.g. pipes and ducts) such as oil pipelines, sewage systems and fire hoses. However, application to external flows (e.g. surface ships) has not been possible due to the continual dilution of the polymer solution away from the surface (PDR needs a sufficient quantity or concentration near the surface to reduce the drag). It has long been suspected that with improved injection schemes and/or improved polymers (i.e. polymers that can reduce the drag with lower concentrations) PDR could be implemented on external flow applications. The current work addresses two pressing issues for this possibility: (1) proper scaling of the diffusion process to assess possible improvements with ideal injection schemes and (2) under what conditions do the polymer chains break (i.e. polymer chain scission). The second issue is very critical since the efficiency of a given polymer solution is most sensitive to the length of the polymer chain (i.e. the molecular weight for a given polymer type). To date experiments studying PDR for external flow applications have assumed that the breaking of the polymer chains is not important in the analysis. However, in the current study the first measurements of the length of the polymer chains within a turbulent boundary layer (TBL) are acquired and it is shown that the length of the polymer chain decreases within the flow (i.e. the flow conditions reduce the ability of the polymer solution to reduce the skin-friction drag).

Furthermore, the reduction in polymer chain length was directly correlated to flow conditions and show that the breaking of the polymer chains will occur if used on a surface ship. Both the diffusion and polymer chain scission findings indicate that PDR in its current state is not practical for application on a surface ship (for the purpose of reduced fuel usage and cost). However, if a stronger polymer (i.e. a polymer less susceptible to the breaking of the chain) that could achieved significant drag reduction at lower concentrations could be developed then PDR should be reconsidered as a possible fuel saving option for surface ship applications.

The second method studied in the current work is the reduction of skin-friction drag with the injection of gas (air) into the water TBL. This method has been studied since the early 70's with minimal success. High levels of drag reduction could be achieved near the point where the air was injected into the water, but drag reduction would only persist downstream for a relatively short distance (on the order of one meter). The possibility of implementing air injection drag reduction appeared unlikely until recently when Winkel (2007) and Elbing *et al*. (2008) reported that with sufficient volume fluxes of air a thin, stable layer of air would form on the surface achieving nearly 100% skin-friction drag reduction over the entire model length (12.9 m long). This type of air injection drag reduction has been termed air-layer drag reduction (ALDR) and recently become the focus of several research efforts (experimental and computational). In the current work a brief discussion is provided about the types of drag reduction associated with the injection of air (bubble, transitional and air-layer drag reduction) and the scaling of the minimum volume flux of air required to achieve ALDR is proposed.

Currently ALDR appears the most promising technology for reduction of the skin-friction component of a surface ship's total resistance.

The remainder of this dissertation is divided into five parts. Parts II through V represent individual studies that have been separated based on how they are/will be submitted for publication. Part II is a study of PDR with a pipe flow experiment, which was used to validate a scaling law proposed by Vanapalli *et al*. (2006) that is then adapted for boundary layer flow in non-homogeneous polymer solution in Part IV. Part III presents the results obtained from large laboratory scale boundary layer testing of drag reduction with air injection. Parts IV and V study PDR with boundary layer flow in a large (~ 10 m) and a typical (~ 1 m) laboratory scale experiment, respectively. The final two studies investigate the diffusion process of polymer solutions within a TBL and how the polymer chains break within the flow. As previously stated the polymer chain length measurements are the first made within a TBL flow and are then scaled based on flow parameters. The dissertation then concludes with Part VI that provides a brief summary of the conclusions drawn from the entire work.

References

Elbing, B.R., Winkel, E.S., Lay, K.A., Ceccio, S.L., Dowling, D.R. & Perlin, M., 2008, "Bubble-induced skin-friction drag reduction and the abrupt transition to air-layer drag reduction," *Journal of Fluid Mechanics*, **612**, 201-236.

Winkel, E. S., 2007, "High Reynolds Number Flat Plate Turbulent Boundary Layer Measurements and Skin Friction Drag Reduction with Gas or Polymer Injection," *Doctoral thesis*, University of Michigan.

Vanapalli, S.A., Ceccio, S.L. & Solomon, M.J., 2006, "Universal scaling for polymer chain scission in turbulence," *Proceedings of the National Academy of Sciences of the United States of America*, **103**(45), 16660-16665.

PART II. DEGRADATION OF POLYMER SOLUTIONS IN LARGE DIAMETER, HIGH SHEAR TURBULENT PIPE FLOW

Chapter 1. Introduction

1.1 Abstract

This study quantifies degradation of polyethylene oxide (PEO) and polyacrylamide (PAM) polymer solutions in a relatively large diameter (2.72 cm) turbulent pipe flow at Reynolds numbers to 3×10^5 and shear rates greater than 10^5 s^{-1}. The present results support the scaling law for polymer chain scission reported by Vanapalli *et al.* (2006) that predicts the maximum chain drag force is proportional to $Re_D^{3/2}$, validating this scaling law at higher Reynolds numbers than prior studies. This scaling estimates that the bond strengths for PEO and PAM are 4.32 and 10.3 nN, respectively. Additionally, with the use of synthetic seawater as a solvent the onset of drag reduction occurred at higher shear rates relative to the tap-water solvent solutions. However solvents had minimal impact on the degradation measured at higher shear rates. These results are significant for large diameter pipe flow applications that use polymers to reduce skin-friction and pumping costs.

1.2 Background and Motivation

Since Toms (1948) first published results indicating that skin-friction drag could be reduced with the addition of dilute polymer solutions numerous research efforts have been conducted in attempts to make practical use of this finding. To date there have been many successful applications of polymer drag reduction (PDR), primarily in pipes and conduits (Sellin *et al*., 1982b), and work continues on external flows such as for surface ships and submarines. In spite of great interest and much technological advancement, a comprehensive theory of PDR remains elusive. Over the years there have been numerous useful review articles on PDR (Lumley, 1969; Liaw *et al*., 1971; Hoyt, 1972; Virk, 1975; Berman, 1978; Sellin *et al*., 1982a; McComb, 1990; Nieuwstadt & Den Toonder, 2001). Most recently, White & Mungal (2008) provided a brief review of PDR advancements and a summary of remaining questions. Since the literature on PDR is voluminous, only the work most relevant to the current study is reviewed.

For a given polymer and solvent, Virk (1975) showed that the quantity of polymer and its molecular weight, $M_{w,}$ were the factors with the largest effect on drag reduction. Typically larger quantities of polymer and higher M_w produce higher drag reduction. This trend holds until maximum drag reduction (MDR), as defined by Virk *et al*. (1967), is achieved. Furthermore, the quantity of polymer necessary for MDR decreases with increasing M_w. Thus to limit the cost of PDR, small quantities of high M_w polymers are desirable and have become the focus of most current PDR research efforts. However, high molecular weight polymers are highly susceptible to degradation by chain scission (Patterson & Abernathy, 1970; Culter *et al*., 1975; Merrill & Horn, 1984), which

effectively reduces the M_w and the polymers ability to reduce drag. Horn & Merrill (1984) showed polymer chains tend to undergo scission at the midpoint where stresses are the highest, which halves the molecular weight for each chain scission event that occurs. These observations have inspired numerous research efforts focused on determining the conditions under which polymer degradation occurs. Additionally, other research efforts have attempted to strengthen the backbone of the polymers to make them less susceptible to chain scission (e.g. co-polymers).

Since the first treatise of polymer chain scission (Frenkel, 1944) there has been ongoing investigation into chain scission mechanics. Most early work on polymer degradation was performed with pipe flow apparatuses (Patterson & Abernathy, 1970; Culter *et al*., 1975; Sedov *et al*., 1979; Hunston & Zalkin, 1980; Merrill & Horn, 1984; Moussa & Tiu, 1994) similar to the style used in the current work, but more recent degradation work has been performed in rotational Taylor-Couette flow devices (Kim *et al*., 2000; Nakken *et al*., 2001; Choi *et al*., 2002; Kalashnikov, 2002). From these studies it has been shown that polymer degradation is influenced by molecular weight, polymer concentration, solvent, turbulent intensity and flow geometry. To date the majority of studies have assessed the influence of these parameters on polymer degradation from changes in either the friction factor or intrinsic viscosity. Only recently have studies directly quantified polymer degradation within turbulent flows with measurements of the molar mass distributions via light scattering techniques (Vanapalli *et al*., 2005).

These prior studies were all analyzed within the context of laminar flow scission theory, but Vanapalli *et al*. (2006) showed that polymer degradation by chain scission occurs primarily on the Kolmogorov length scale (i.e. turbulence dominated). Furthermore, that work has predicted a universal scaling of polymer chain scission in turbulent flows. This implies that the proper scaling of chain scission should be insensitive to flow geometry as the Kolmogorov cascade theory predicts that the turbulence at scales approaching the Kolmogorov scale are universal and independent of the mean flow. While Vanapalli *et al*. (2006) showed good collapse over nearly four decades of Reynolds number the scission data within the literature, excluding their own data set, are limited both to Reynolds numbers below 3×10^3 as well as small diameter pipes. Further review of the extensive polymer degradation literature is available in Moussa & Tiu (1994) and Vanapalli *et al*. (2005), and the interested reader is referred to these studies for additional discussion.

The current study intends to extend the PDR data set with a large diameter (D = 2.72 cm) turbulent pipe flow experiment at Reynolds numbers, Re_D, (= $U_{avg}D/\nu$, where U_{avg} is the mean velocity, D is the pipe inner diameter and ν is the solvent kinematic viscosity) to 3×10^5 and wall shear rates, γ_w, greater than 10^5 s^{-1}. The high shear-rates and Re_D of the present study should promote polymer degradation, and thus can be used to assess and extend the scaling law of Vanapalli *et al*. (2006). In addition, this scaling of polymer chain scission can be used to estimate the bond strength of the polymer chains. The current study is significant because it bridges the small diameter, moderate Reynolds number studies typical of the literature (in which experimental conditions can be

carefully controlled) and the large diameters and high Reynolds numbers of many practical applications (in which control of experimental conditions is more difficult). By providing a careful study at high Reynolds numbers and large pipe diameters, this work increases the confidence with which correlations and theories developed for low Re_D flows (Vanapalli *et al*., 2005 and 2006) can be applied to large scale applications in pipeline flow and ocean transport. The results of this study do support the application of these small scale correlations to larger scale flows such as those studied here. Furthermore, agreement with the work of Vanapalli *et al*. (2006) indicates the reduced performance of the polymer solutions used was caused by chain scission. Thus throughout the manuscript polymer degradation refers specifically to degradation by polymer chain scission.

The possibility of implementing PDR for ocean transport (i.e. surface ships and submarines) inspired a subset of experiments investigating the effect of using saltwater as the solvent instead of tap-water. Moussa *et al*. (1993) reviews the effects various solvents have on polymer degradation, but saltwater was not considered in that study. Little (1971) used salt (magnesium sulfate) in the solvent and monitored how the salt concentration affected PDR. It was found that the presence of salt delays the onset of drag reduction, a result which is supported by the present study at much higher Re_D. However, the experiments in Little (1971) used a small capillary tube (1.6 mm) at relatively low Re_D ($< 8\times10^3$), where significant degradation is not expected and as a result has limited applicability to high speed ocean transport. In the current study the higher Re_D

and shear rates serve provide a unique opportunity to assess any potential impact of saltwater on degradation and drag reduction.

1.3 Polymer Drag Reduction Fundamentals

To assist the reader a brief review of turbulent pipe flow (Newtonian and polymeric) friction factor relationships is provided. The current findings are plotted in the traditional Prandlt-von Kármán (PK) coordinates, $f^{-1/2}$ versus $Re_D f^{1/2}$, where f is the Fanning friction factor defined in equation (1.1). Here τ is the wall shear stress and ρ is the fluid mass density. In the current study the wall shear stress was not directly measured, but f can be determined from the pressure drop along a section of the pipe with the relationship given in equation (1.2).

$$f = \frac{2\tau}{\rho U_{avg}^2} \qquad (1.1)$$

$$f = \frac{D}{2\rho U_{avg}^2}\frac{\Delta p}{\Delta z} \qquad (1.2)$$

Here Δp is the measured pressure drop and Δz is the length of pipe over which the Δp was measured (2.69 m). PK coordinates are a natural way of presenting drag reduction in pipe flow as the ordinate represents the ratio of bulk fluid velocity to the turbulent friction velocity, and the abscissa is a ratio of pipe to turbulent length scales. In PK coordinates the friction-law for fully turbulent flow of a Newtonian fluid in a smooth, round pipe is given by equation (1.3), and is traditionally referred to as the PK law.

$$\frac{1}{\sqrt{f}} = 4.0 \log_{10}\left(Re_D \sqrt{f}\right) - 0.4 \qquad (1.3)$$

Equation (1.3) is labeled "turbulent" in figure 1 and tap-water (Newtonian) results from the current study are also included. The water results and equation (1.3) are in good agreement and provide an estimate of the uncertainty in the drag reduction measurements. Figure 1 also includes the curve predicted by Virk *et al*. (1967) for the maximum drag reduction (MDR) asymptote, given in equation (1.4). Numerous studies over the years (Toms, 1948; Virk *et al*., 1970; Moussa & Tiu, 1994; Ptasinski *et al*., 2001) have shown excellent agreement with the MDR asymptote independent of polymer tested.

$$\frac{1}{\sqrt{f}} = 19.0 \log_{10}\left(Re_D \sqrt{f}\right) - 32.4 \qquad (1.4)$$

Figure 1 also illustrates the predicted friction relationship for a non-degraded, drag reducing polymer solution in turbulent pipe flow. These "predicted results" show three regimes typical of such turbulent flows: (1) Newtonian (if solvent is Newtonian), (2) polymeric and (3) asymptotic. In the Newtonian regime the shear-stress is less than that required for the onset of drag reduction, the turbulent flow is unmodified and the friction factor relationship is equivalent to the solvent (equation 1.3 for the current study). In the polymeric regime the friction factor relationship is dependent on the properties of the polymer solution. Virk (1975) used equation (1.5) as an approximate relationship for the polymer solution behavior in the polymeric regime. The two polymer solution

dependent properties Virk (1975) termed the slope increment (δ) and onset wave number (W^*). Equation (1.5) accurately describes the behavior of non-degraded polymer solutions. In figure 1 drag reduction data for polyacrylamide (PAM) at 1000 weight-parts-per-million (wppm) are included to illustrate the PDR behavior in the polymeric regime. A best fit curve to the two lowest shear rate data points was used to determine δ and W^* for equation (1.5), which were approximately 45.7 and 3.67×10^4 m^{-1}, respectively. This best fit curve extends from onset of drag reduction on the Newtonian, turbulent curve until the asymptotic regime is reached. In the asymptotic regime the friction factor relationship follows the MDR asymptote, given by equation (1.4). These three segments form the predicted PDR friction relationship if the polymer solution were not degraded.

$$\frac{1}{\sqrt{f}} = (4.0+\delta)\log_{10}\left(Re_D\sqrt{f}\right) - 0.4 - \delta\log_{10}\left(\sqrt{2}\,DW^*\right) \qquad (1.5)$$

If polymer degradation was negligible then the results obtained from the current study would be consistent with the predicted curve shown in figure 1. However, it is apparent that at higher shear rates the drag reduction results are not well explained by equation (1.5). This indicates that at these higher shear rates the strain rates in the flow were sufficient to cause the carbon bonds (C-C or C-O) of the polymer chain to be broken (i.e. chain scission), thus reducing the molecular weight of the polymer solution and consequently causing the polymer solution to perform below the predicted curve. Therefore the behavior of a given polymer-solvent combination in the polymeric regime is determined by the slope increment, onset wave number and an onset condition for polymer degradation (following the onset of degradation δ and W^* are altered). In the

current study the onset of degradation is difficult to define due to limited data collected at low shear rates resulting in poor estimates of δ and W^*. Consequently in the current work, data are considered degraded once the drag reduction results are at least 10% below the best-fit curve of equation (1.5) relative to the data collected at lower shear rates.

Chapter 2. Experimentation

2.1 Test Matrix

Two polymers types were tested; polyethylene oxide (PEO) and PAM. The structural unit for PEO is (-O-CH_2-CH_2-), which results in the polymer backbone consisting of carbon-carbon (C-C) and carbon-oxygen (C-O) bonds. PAM lacks the oxygen in the backbone and replaces a hydrogen atom with $CONH_2$. The (C-C) and (C-O) bond strengths and lengths are quite similar and thus the breaking (chain scission) of the backbones are expected to occur at approximately the same shear rates. However, Vlassopoulos & Schowalter (1993) used the same PAM and similar PEO samples and found that PAM solutions are less susceptible to degradation than PEO solutions, which was also observed in the current study. Three PEO polymers were tested having manufacturer (Dow Chemical) specified M_w of 2, 4 and 8 million, herein termed N60K, WSR301 and WSR308, respectively. Only a single M_w, nominally 5.5 million, was tested for PAM (Polyscience Inc.). For each polymer and M_w combination a minimum of three concentrations were tested ranging from 1 to 1000 wppm. A subset of experiments was conducted to compare the drag reduction behavior with synthetic seawater (i.e. saltwater) as the polymer solvent relative to tap-water. Saltwater experiments were performed only with WSR301 at two polymer concentrations (20 and 200 wppm). Each polymer solution and concentration was tested over a range of Reynolds numbers ($3\times10^4 < Re_D < 3\times10^5$)

and wall shear rates ($1.3\times10^4 < \gamma_w < 1.2\times10^5$ s^{-1}) to determine the drag reduction performance in the polymeric regime and assess polymer degradation, if any. Here γ_w is defined as the wall shear stress divided by the product of the mass density and kinematic viscosity of water.

2.2 Experimental Setup

The experimental setup, shown in figure 2, consisted of a 1.1 m^3 feed tank, a progressive-cavity, positive displacement pump (1H115G1, Moyno), 12 m long straight pipe and a collection tank. Solutions were gravity fed from the feed tank to the pump that had a conical contraction at the outlet. The contraction reduced the diameter from 20.3 cm at the pump outlet to the test pipe inner diameter of 2.72 cm. The reduction in diameter was gradual with a 10.5° included angle, yet results indicate that the contraction still caused degradation of the polymer solutions. The experimental setup had two pressure taps and five sampling ports. The first port was located immediately upstream of the contraction to detect degradation of the polymer solution from the pump. The other four sampling ports were positioned at z/D = 1, 207, 337 and 467, where z is measured downstream from the conical contraction along the pipe centerline. The pressure taps were positioned at z/D = 311 and 417. The first pressure tap position was selected to ensure fully developed pipe flow at the measurement section. In general z/D = 60-80 is a sufficient entrance length for the flow to be fully developed with Newtonian fluids, but Draad *et al*. (1998) have shown that the development region is extended with polymeric solutions when the Weissenberg number, *We*, as defined in equation (2.1) exceeds unity.

$$We = \frac{U_{avg}\lambda}{D} \qquad (2.1)$$

Here λ is the polymer relaxation time. An estimate of the *We* for the lowest M_w PEO polymer (N60K) used ($\lambda \sim 5$ ms, $U \sim 10$ m s^{-1}, $We \approx 2$) indicates that the development length was increased from Newtonian flow for all test conditions. Unfortunately, Draad *et al*. (1998) did not provide a method to quantify the increase in development length for polymeric flow so the first tap was positioned as far downstream as space allowed.

2.3 Instrumentation

The results presented here are based on pressure drop measurements along the pipe, solution flow rate measurements and rheological analysis of drawn samples. Static pressure measurements were made at two locations, through 1.6 mm diameter holes in the pipe wall *via* diaphragm-type pressure transducers (PX303, Omega). Flow rate was inferred by recording the rate of change in hydrostatic head with a high-resolution pressure transducer (PX437, Omega) mounted on the inside bottom of the feed tank. The transducer output was calibrated to the tank volume using a factory calibrated liquid turbine flowmeter (FTB-903, Omega). The pressure drop and flow rate data were recorded simultaneously at 250 Hz *via* a data acquisition card (NI-DAQ, National Instruments) and a LabView virtual instrument.

Rheological analysis of the polymer solution collected at the highest flow rates from the five sampling ports was conducted using a cone and plate rheometer (AR1000,

TA Instruments). The samples were drawn through 5.9 mm inner diameter tubes at approximately 5 mL s^{-1} (from each port), which altered the mean velocity by less than 1%. This produced a mean velocity in the sampling tube of approximately 0.2 m s^{-1}. At this flow rate the wall shear stress in the sampling tube was less than 5% of that experienced in the pipe, which ensured that the primary contribution to degradation of the polymer solutions, if any, would occur prior to sampling. While the low sampling rate minimized the potential for degradation within the sampling system, it also significantly increased the required sampling period and consequently the rheological analysis was only conducted at a single flow-rate. The samples were steadily drawn (L3 Series, DuraPlus) into five individual cylindrical containers with pistons operated by a linear actuator (L3 Series, DuraPlus). The viscosities of the samples were measured using a cone and plate (6 cm diameter, 2° angle) rheometer at shear rates to 1000 s^{-1}. The low shear rates are ideal for characterizing polymer solutions and preventing inadvertent polymer degradation by the characterization technique, as the shear rates experienced in the rheometer were two orders of magnitude less than those experienced in the test section. The rheology test was performed at constant temperature (25°C) and the torque was recorded once the angular velocity had reached steady-state. Typically, ten measurements were made for each decade of shear rate. The measurements revealed the shear-rate dependent viscosity of the specimen, which was used to quantify the extent of polymer degradation.

2.4 Polymer Preparation

The polymer solutions were prepared by sprinkling dry powder into a dechlorinated water jet, which allowed the polymer to be wetted prior to making contact

with the mixing/feed tank free surface. The powder pre-wetting minimized the formation of polymer aggregates in the stock solution. The use of dechlorinated water as the solvent was required as the presence of chlorine is known to promote polymer degradation (Petrie *et al*., 2003). The dechlorination was performed with an inline activated carbon filter (RT-2260-4, Aquapure). The polymer powder was weighed with a precision digital balance (FX400, A&D), and the water volume was measured with a flowmeter (FTB-903, Omega). During mixing the polymer concentration was maintained at approximately 1000 wppm until the required quantity of powder had been added to the feed tank. Then the solution was diluted with additional dechlorinated water to the desired test concentration. Each batch produced approximately 1.0 m^3 of polymer solution. The stock solution was periodically stirred for at least 24 hours prior to use and was only tested once the entire batch appeared homogenous. All testing was performed within 48 hours of mixing.

The polymer preparation procedure for the subset of tests with saltwater as the solvent was identical to the above method with a single variation during the dilution stage. The saltwater mix (Instant Ocean synthetic sea salt, Aquarium Systems) was pre-dissolved in buckets prior to being added to the feed tank following the addition of the polymer powder. The quantity of salt dissolved was selected to produce a final salt concentration of 3.5% by weight (similar to salt concentrations in the ocean).

The repeatability of the mixing process was confirmed with measurements of the stock solution viscosity with the cone and plate rheometer. Figure 3 shows the results

obtained from three batches of WSR301 at 1000 wppm. The sudden rise following the steady decline (shear thinning) in viscosity corresponds to an inertioelastic instability associated with the polymer solution. The good collapse of the data prior to the instability onset (~200 s^{-1}) confirms the repeatability of the mixing procedure.

The stability of the polymer solutions was investigated separately to determine whether the time between preparation and testing was a source of variation. These tests were performed with a separate, smaller (4.57 mm diameter) pressure drop apparatus. An example of one of the stability tests with N60K at 10 wppm is shown in figure 4. All polymer solutions were tested at either 10 or 20 wppm over a period of time ranging from 18 to 90 hours. Results show that there was minimal change in the polymer properties over this period, which indicates that time dependent properties of the polymer solutions are negligible for the current study, and that the 24 hour hydration time was sufficient.

Chapter 3. Results and Analysis

3.1 PEO Results

The drag reduction results obtained with the PEO solutions (N60K, WSR301 and WSR308) are presented in figure 5 in traditional PK coordinates. These results illustrate three experimental observations: (1) all data collected were within the polymeric regime, (2) the drag reduction is dependent on polymer concentration and (3) polymer degradation limits the amount of drag reduction for a given solution and the MDR asymptote was never achieved.

The first observation is apparent since all results fall between the Newtonian (equation 1.3) and the MDR asymptote (equation 1.4) friction relationships. This range was selected since in the polymeric regime the drag reduction is dependent on the polymer solution properties and thus degradation is more readily detected. The original design of the experiment involved relating equation (1.5) to molecular weight and thus polymer degradation, but due to the presence of degradation throughout the experimental setup the molecular weight at the pipe inlet was unknown for most test conditions (time limits required that only a select few shear rates be sampled). This coupled with an inability to precisely measure the onset of drag reduction prevented the possibility of relating equation (1.5) to molecular weight.

The second observation has two main points: First, for a fixed test condition (i.e. Reynolds number) higher polymer concentration results in greater reduction in shear stress (i.e. lower friction factor) within the polymeric regime, a phenomenon well established in prior studies (Virk, 1975; Moussa & Tiu, 1994). Second, at lower Re_D and higher concentrations the data for each M_w appear to be less sensitive to the polymer concentration. Estimates of the slope increment are not ideal for the current experimental setup, but slope increments at lower concentrations were found to be consistent with the findings of Virk (1975) that $\delta \propto C^{1/2}$, where C is the polymer concentration (data not shown).

At high shear rates the third observation is evidenced by the deviation from the logarithmic profile predicted for the polymeric regime (equation 1.5). In the cases of the two higher M_w polymers, the PK data appears to plateau and curve back toward the Newtonian line with increasing shear-rate. Since the observed drag reduction is lower (in some cases, drastically lower) than predicted from low shear-rate data and equation (1.5), substantial degradation is suspected. This observation will be further discussed subsequently.

The results of the experiments using saltwater as the solvent with WSR301 are shown in figure 6 compared with equivalent tests conducted with tap-water solvent. Estimates of the slope increment, though crude, indicate that both the water and saltwater solvent solutions produced approximately the same slope increment. Since the peak drag

reduction in the polymeric regime occurs earlier with the tap-water solvent, it appears that using a saltwater solvent delays the onset of drag reduction, which is in agreement with Little (1971). However, at higher Re_D and consequently higher shear rates the two solutions appear to behave similarly. This indicates that the use of saltwater as the solvent impacts only the onset of drag reduction and not the slope increment or the onset of degradation. The minimal impact on the degradation onset is expected since the polymer degradation is assumed (based on subsequent analysis) to be caused by the breaking of carbon bonds (i.e. chain scission), which would be approximately identical when using the same polymer type.

The presence of polymer degradation was apparent in figures 5 and 6, and thus samples were collected for rheological analysis to better understand the degradation process. Samples were collected only at the highest attainable flow-rate for each polymer and M_w (N60K, WSR301, WSR308 and PAM) with a single polymer concentration of 1000 wppm. The shear-dependent viscosities of the samples collected using WSR308 are presented in figure 7, which indicates that degradation occurred within the pump, the contraction and along the pipe length. This finding is consistent with the results of Moussa & Tiu (1994) and Vanapalli *et al.* (2005). N60K, WSR301 and PAM produced similar results, but the viscosities of the drawn samples were significantly below that of WSR308 making the changes less pronounced. At the time the data were collected this prevented further analysis of the polymer degradation mechanism since the condition of the polymer solution entering the test section was unknown.

As it is not possible to directly assess the resultant polymer M_w from the drag reduction phenomena presented in figures 5 and 6, a unique approach was taken to relate polymer degradation (i.e. resultant M_w) to Re_D. We thus proceed in the following way: As previously described, Vanapalli *et al*. (2006) developed a universal scaling law for polymer chain scission in turbulence that was found to be insensitive to flow geometry, effectively collapsing degradation data from contraction-expansion, cross-slot and rotational turbulent experiments. Given their finding, if this scaling relationship is truly universal it should be expected to collapse the data from the current data set at higher Re_D and shear-rates.

The scaling law of Vanapalli *et al*. (2006) suggests that chain scission occurs on the Kolmogorov scale and consequently produces a relationship for the maximum drag force on a polymer chain, F_{max}, given in equation (3.1).

$$F_{\max} = A^{3/2} \frac{\pi \rho v^2 Re_D^{3/2} L^2}{4D^2 \ln(L/a)} \qquad (3.1)$$

Here F_{max} is the maximum drag force on the polymer chain, A is a proportionality constant related to flow geometry (found to be nearly constant with geometries tested in Vanapalli *et al*., 2006), L is the contour length of the chain (i.e. maximum extension length of the polymer chain) and a is the polymer chain diameter. The chain diameter was estimated to be ~ 1 nm for both PEO and PAM (Boyer & Miller, 1977). An estimate of the contour lengths (i.e. the maximum extension of the polymer chain) for the polymers studied here was obtained by applying the relationship provided by Larson (1999),

$L = 0.82\, n\, l_o$. Here n is the number of backbone bonds ($n = n_o M_{ws} / M_o$, where n_o is the number of backbone bonds per monomer, M_{ws} is the critical molar mass for scission at a steady-state wall shear rate and M_o is the monomer molar mass) and l_o is the C-C bond length (0.154 nm). Note that the C-O bond length (0.143 nm) is very close to the C-C bond length.

With the above mentioned relationships a method of independently evaluating equation (3.1), given the data from figures 5 and 6, was needed. Equation (3.1) establishes a relationship between the Reynolds number of the turbulent pipe flow and the contour length, L, of the chain. Given measurements of these two quantities, the scission tension, F_{max}, for PEO and PAM can be extracted from the data and compared to literature estimates. Of course, Re_D is available directly from the friction drag measurements. To assess the contour length of the polymers in the flow at a particular Re_D, we use the following procedure that employs the known physics that the contour length of the polymer scales with the measured friction factor of the flow. That is, L is proportional to M_{ws} per the relationships discussed above. The scaling of M_{ws} for PEO and PAM with the wall shear rate is readily available from Vanapalli *et al*. (2005). The wall shear rate is proportional to the wall shear stress, itself a function of the measured friction factor. The γ_w used in the analysis was determined from the measured Fanning friction factor from the pipe data results as presented in equation (3.2).

$$\gamma_w = \frac{\tau}{\rho \nu} = \frac{U_{avg}^2}{2\nu} f \qquad (3.2)$$

Scaling of the PEO measurements with steady-state molar mass were readily available from Vanapalli *et al*. (2005) and given in equation (3.3).

$$\gamma_w = 3.4 \times 10^{18} M_{ws}^{-2.20} \qquad (3.3)$$

Figure 8A shows the Re_D dependence of F_{max} determined from the current study. While there is significant scatter in the results, the results do exhibit a clear trend. To ensure that only data affected by chain scission were analyzed, only data that deviated by at least 10% from the best-fit curve of equation (1.5) to data at lower shear rates were correlated. Using these degraded results and applying $F_{max} \propto Re_D^{\alpha}$, α was found to be 1.45, 1.52 and 1.47 from the least-squares power-law best fit curves of N60K, WSR301 and WSR308 data, respectively. Plotted separately in figure 8B are the results obtained for WSR301 with saltwater as the solvent and the best fit curve, which sets α = 1.45. Thus for all PEO samples in the current study α = 1.47 ± 0.06, which is in excellent agreement with the theoretical prediction of 1.5 by Vanapalli *et al*. (2006). These results are significantly different from those predicted with near wall scales, which estimate α between 1.75 and 1.87, depending on flow geometry (Vanapalli *et al*., 2006).

The above agreement with the findings of Vanapalli *et al*. (2006) support the use of the universal scaling law for polymer scission in the current study. This permits an estimate of the bond strength with PEO by assuming that the maximum drag force on the chain corresponds to the bond strength. The only unknown from equation (3.1) is the proportionality constant A that is dependent on flow geometry. Fortunately, as predicted

by the scaling law the proportionality constant was found to be nearly constant and $A \sim O(1)$. This ensures that the use of an approximate value will have minimal impact on the results. Vanapalli *et al*. (2006) estimated A to be 2.09 ± 1.15. Thus, two was selected for A to estimate of the bond strength. The bond strength obtained from the current study, 4.32 ± 1.02 nN, agrees with the theoretically derived bond strengths for C-C and C-O bonds of 4.1 and 4.3 nN, respectively (Grandbois *et al*., 1999).

3.2 PAM Results

PAM pipe flow results are shown in figure 9. It is apparent from the figure that all the data were collected in the polymeric regime, the drag reduction potential of PAM in the polymeric regime is dependent on the concentration and at high shear rates significant polymer degradation was observed. Additionally, data were collected at Re_D approaching that of the onset of drag reduction allowing for additional analysis. Data in this region support previous findings summarized in Virk (1975) that the slope increment is approximately proportional to $C^{1/2}$. Virk (1975) also predicted that the onset wall shear stress was affected negligibly by polymer concentration, but this appears less obvious in the current results. From the three concentrations the onset wall shear stress, τ^*, is 1.68 ± 0.60 Pa, which has a significant variation. However, for the accuracy of the current study at the lower Re_D the deviation is in no way conclusive and can only indicate a possible weak dependence on polymer concentration. Also of note is that while the solutions appear to be curving back towards the Newtonian curve, they do not collapse on each other as rapidly as observed with PEO, which indicates that PAM is less susceptible to degradation than PEO as observed by Vlassopoulos & Schowalter (1993).

As before data from significantly degraded polymer solutions were used to validate the universal scaling law for polymer chain scission in turbulence and estimate the bond strength. Estimates for the parameters in equation (3.1) were made using the same approach as with PEO. The only variation was the relationship between M_{ws} and γ_w, which was obtained from Vanapalli *et al*. (2005) in a contraction-expansion geometry for PAM and given by equation (3.4).

$$\gamma_w = 1.16 \times 10^{23} M_{ws}^{-2.73} \qquad (3.4)$$

The results from this scaling, shown in figure 10, provide further support for $F_{max} \propto Re_D^{3/2}$. The least-squares best-fit power-law curves set α = 1.30, 1.38 and 1.30 for 20, 200 and 1000 wppm, respectively. The concentration dependence of the curves is unexpected since it is not predicted from the scaling law. There are a number of causes that could lead to a concentration dependent bias error in the maximum drag force. Possible problems include error in equation (3.4) used to predict M_{ws}, insufficient degradation for the solution to be considered at the steady state molar mass and/or the polymer solutions could not be considered dilute due to the high concentrations tested. Unfortunately, due to the small set of conditions tested with PAM the exact cause for the concentration dependence could not be determined. However, these results still support the universal scaling since the slopes of each sample are much closer to those predicted with turbulent scaling (1.5) than with laminar scaling (1.75 to 1.87).

While the concentration dependence of the PAM results was unexpected, the data still permits an estimate of the bond strength of PAM. As before the proportionality constant, A, in equation (3.1) was estimated to be two. The bond strength for PAM was determined to be 10.3 ± 1.9 *nN*, which is consistent with the observation that PAM solutions are less susceptible to degradation than PEO. These findings are still within an order of magnitude of the bond strength of C-C (4.1 *nN*). The discrepancy is most likely the product of the error that produced the concentration dependence shown in figure 10. However, it should be noted that Vanapalli *et al*. (2006) similarly found that the bond strength for PAM was approximately twice that of PEO.

One additional possibility for the observed discrepancy in the PAM findings is that the pipe flow was not responsible for the final molecular weight of the polymer solution. The assumption that the pipe flow sets the final molecular weight is implicitly made when the scaling was performed using the Reynolds number and friction factor relationships from the pipe flow only. If the final molar mass of the sample was determined at the contraction and not in the pipe flow this assumption would be faulty causing a bias error in the results. This was not a problem in the PEO solutions as illustrated in figure 7. While it is obvious from figure 7 that degradation occurs upstream of the pipe flow, it is also apparent that the pipe flow determines the final molecular weight (i.e. the steady-state molar mass is determined by the pipe shear rates). That is, the upstream degradation only serves to aid in degrading the polymer solution more rapidly to the steady-state condition determined by the pipe flow. However, with the PAM rheological analysis (not shown) this observation was less apparent primarily due to the

low viscosity of the PAM solution and the limited sensitivity of the rheometer. Thus it is possible that the above concentration dependence and large bond strengths with the PAM solutions are in part due to a bias error caused by the molar mass being set at the pump contraction and not the pipe flow. The concentration dependence would be the result of inappropriately scaling the data based on the pipe shear rates, and the bond strengths would have error due to the scaling as well as the geometry proportionality constant, A, being altered.

Chapter 4. Conclusions

From the high Re_D, high shear rate homogeneous polymer solution experiment in a relatively large diameter pipe several conclusions can be made: (1) The use of saltwater as the solvent increases the onset wall shear stress compared to a tap-water solvent, (2) saltwater has minimal impact on the degradation process compared to solutions prepared with a tap-water solvent, (3) results obtained with PEO and PAM polymer solutions support the prediction made by the universal scaling law for polymer chain scission by Vanapalli *et al*. (2006) that the maximum drag force on the chain is proportional to $Re_D^{3/2}$, (4) the bond strength for PEO is approximately 4.32 nN and (5) the bond strength for PAM is approximately 2.5 times stronger though PAM results are uncertain due to a lack of information on the degradation process within the experimental setup.

Figures

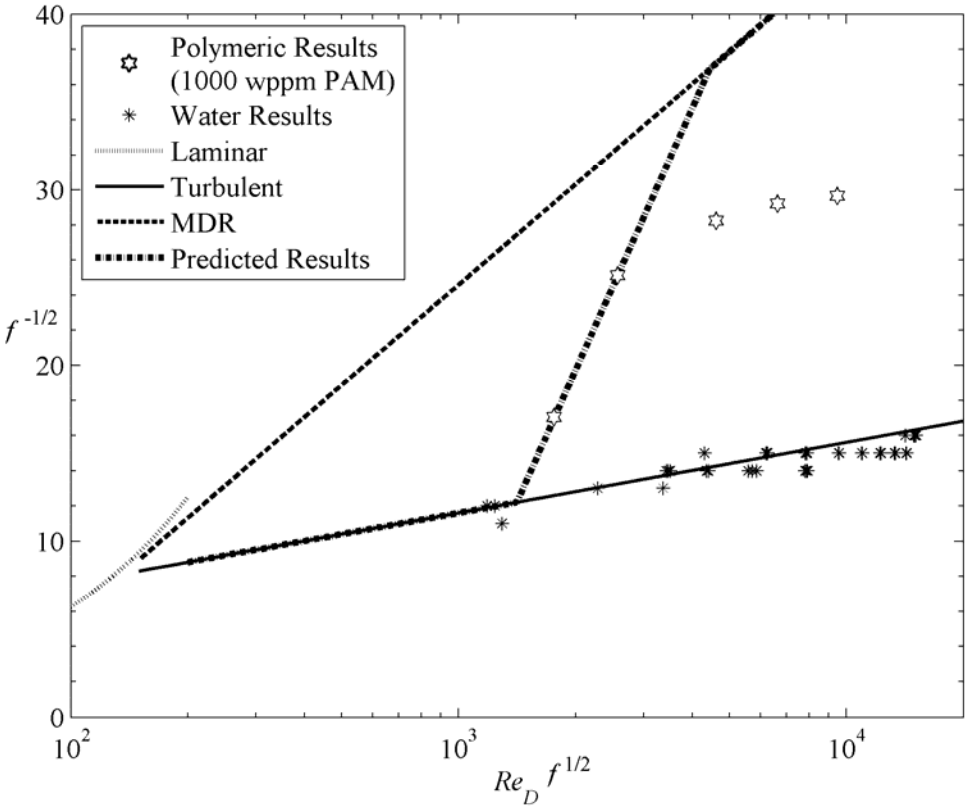

Figure 1. Example PK plot that includes the laminar curve, Newtonian turbulent curve (PK law given by equation 1.3), MDR asymptote given by equation (1.4), current results with tap-water and current results with 1000 wppm PAM solution. The water results are in good agreement with the turbulent Newtonian curve. Also included are the predicted results for the PAM solution tested if no polymer degradation occurred.

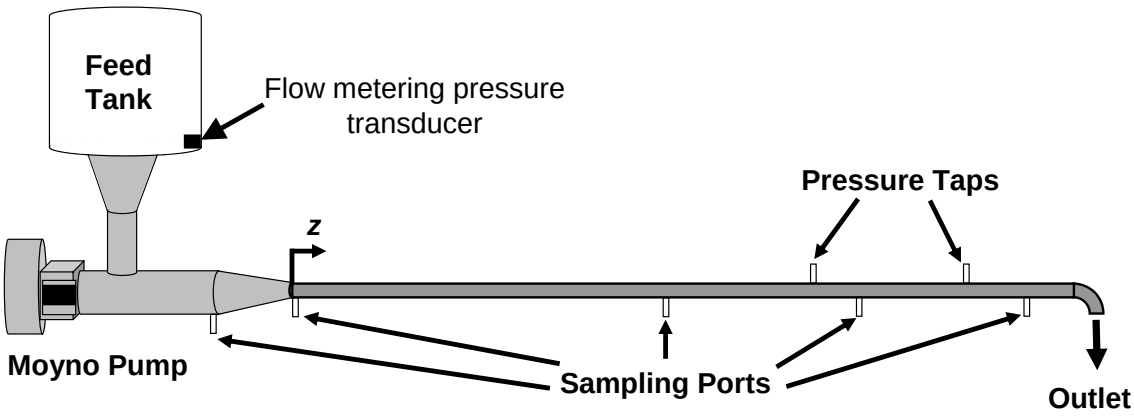

Figure 2. The experimental setup with the feed tank, pump with contraction and a 12 m long, 2.72 cm diameter test section (pipe). Also shown are the approximate locations of the two pressure taps and five sampling ports.

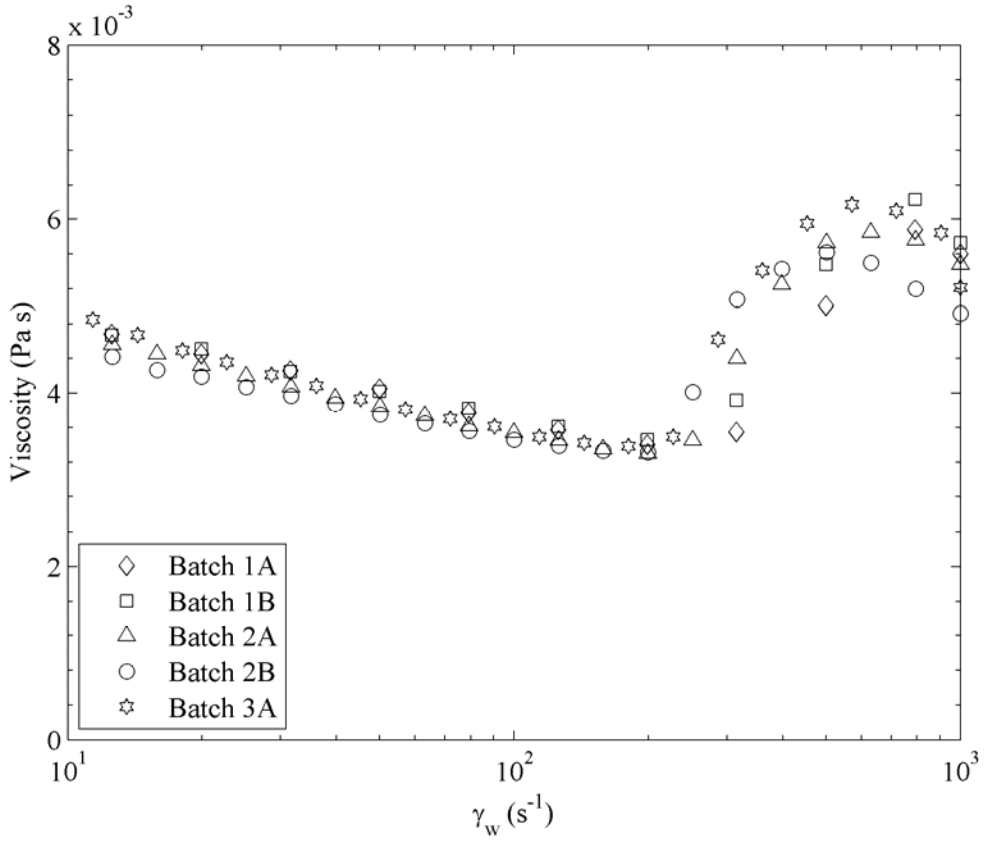

Figure 3. Rheological analysis of three separate stock batches of WSR301 at 1000 wppm. The good collapse of the data prior to the onset of inertioelastic instability (~200 s^{-1}) confirms the repeatability of the mixing process.

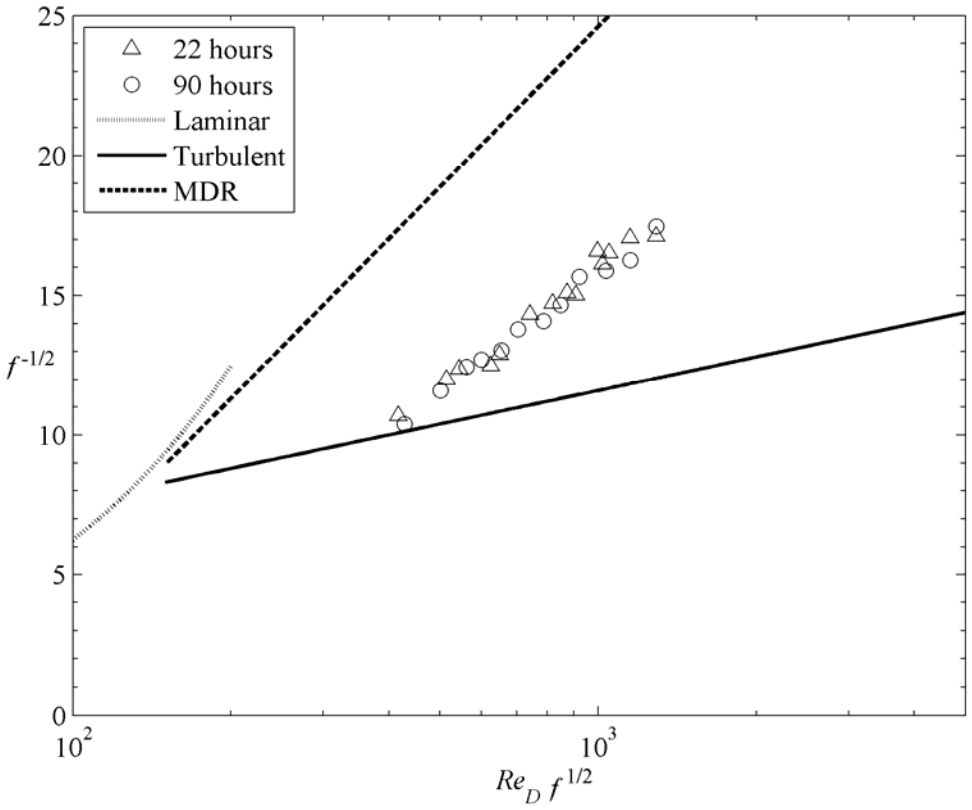

Figure 4. Stability test for 10 wppm N60K with the small diameter pressure drop apparatus. Data confirms that 24 hours was a sufficient hydration time and no polymer degradation occurred prior to testing the sample.

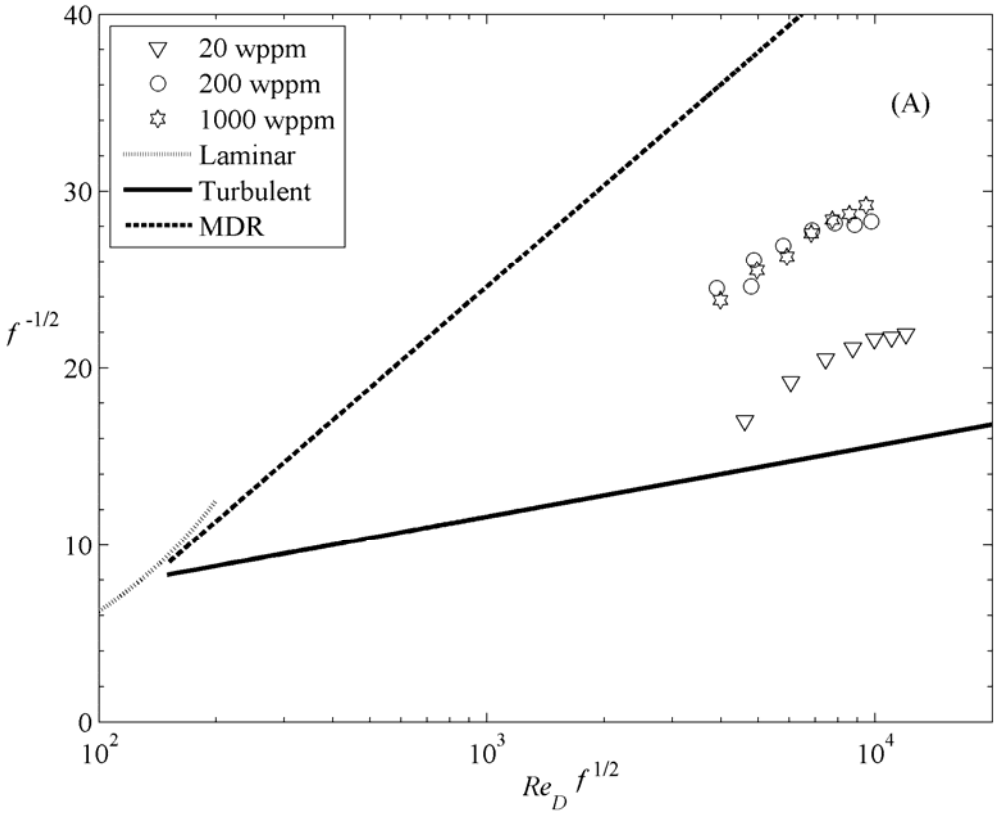
20 wppm
200 wppm
1000 wppm
Laminar
Turbulent
MDR
(A)
$f^{-1/2}$
$Re_D f^{1/2}$
0
10
20
30
40
10^2
10^3
10^4

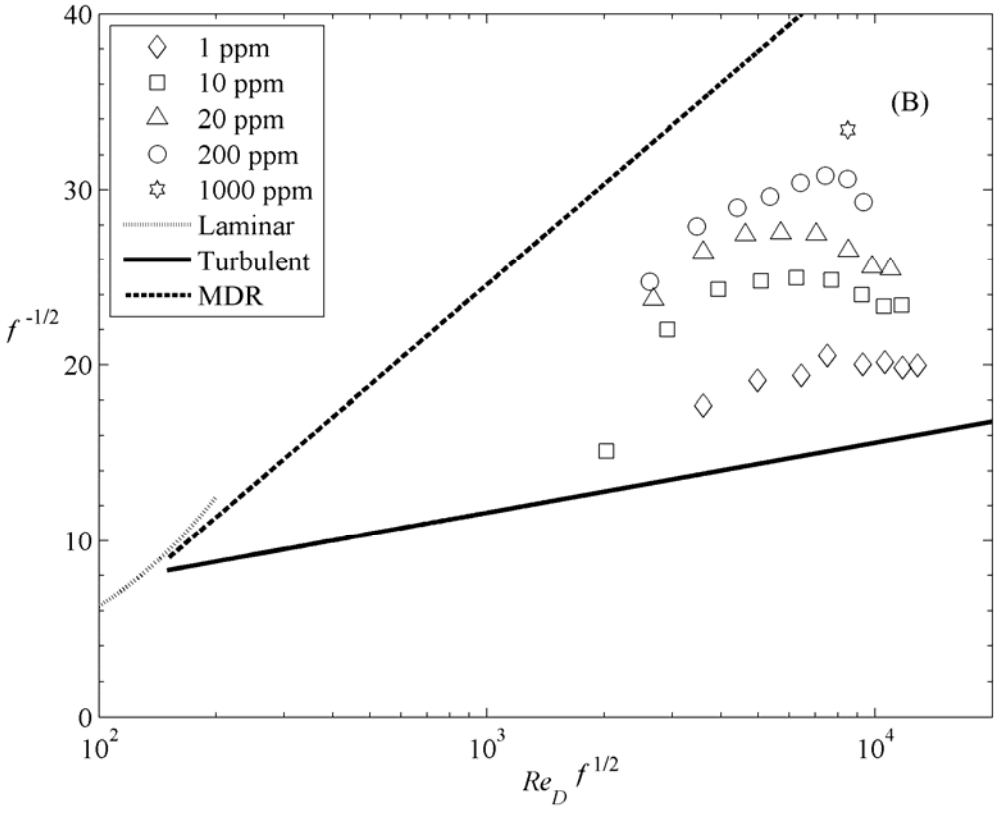
1 ppm
10 ppm
20 ppm
200 ppm
1000 ppm
Laminar
Turbulent
MDR
(B)
$f^{-1/2}$
$Re_D f^{1/2}$
0
10
20
30
40
10^2
10^3
10^4

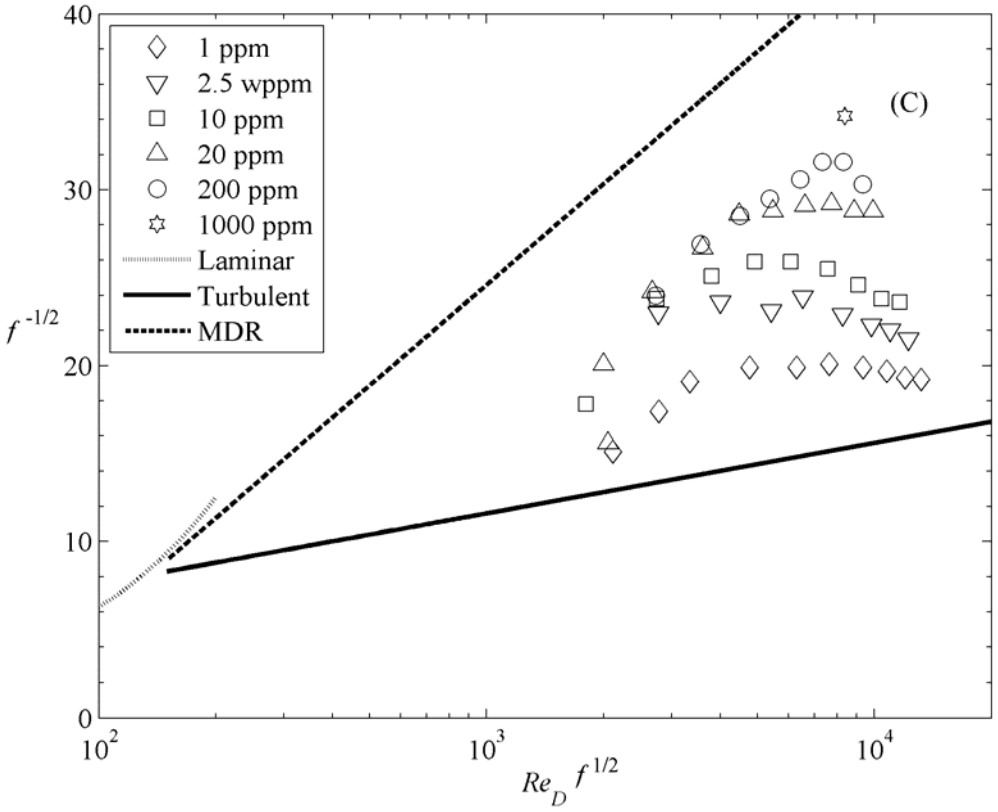

Figure 5. Pressure drop results for PEO samples: (A) N60K, (B) WSR301 and (C) WSR308 with corresponding nominal M_w of 2, 4 and 8 million, respectively.

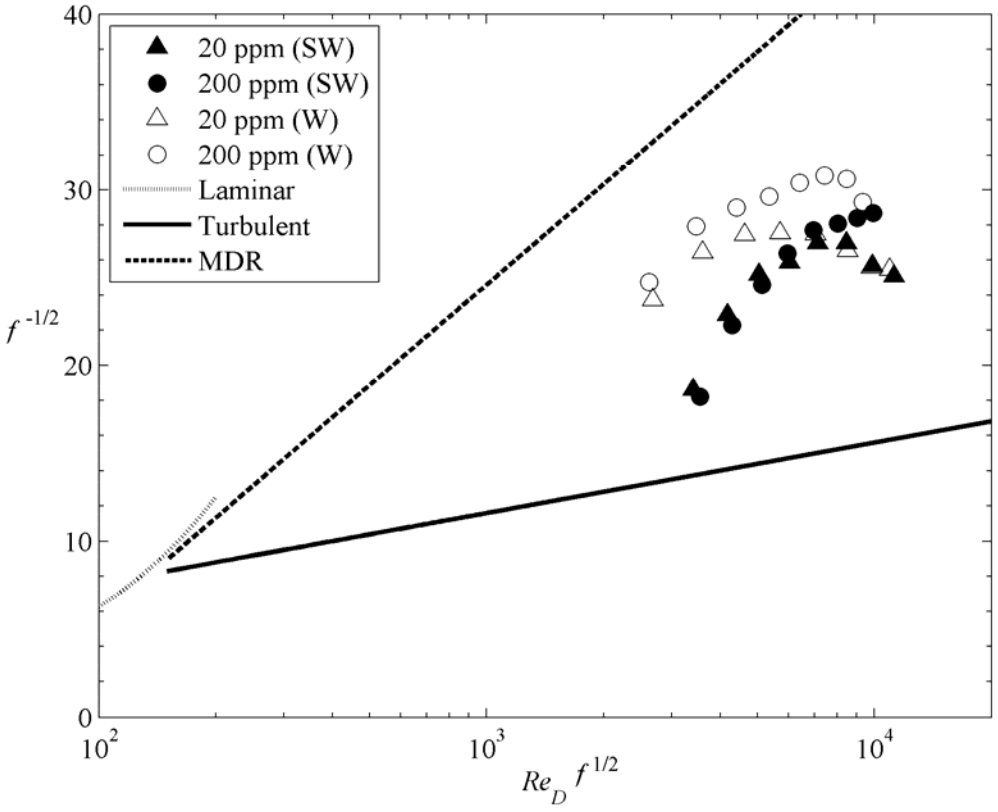

Figure 6. Friction factor relationship for WSR301 using saltwater (SW) or tap-water (W) as the solvent. Results indicate that the onset of drag reduction is delayed with a saltwater solvent, but minimal impact on polymer degradation.

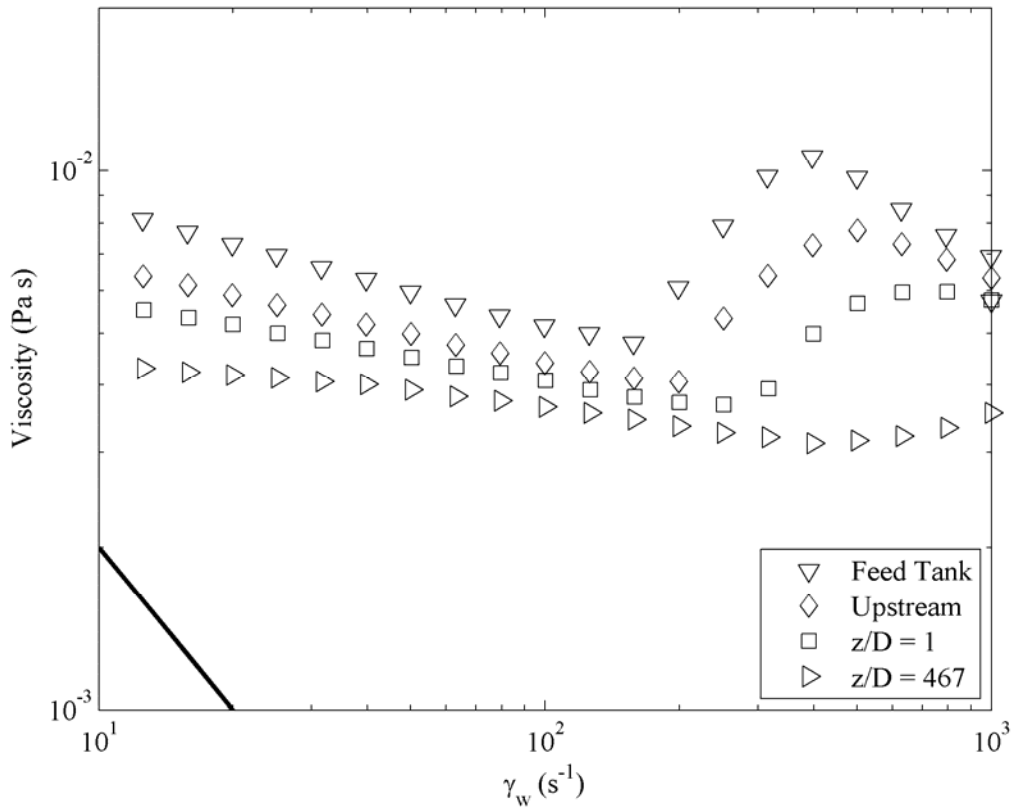

Figure 7. Shear-rate dependent viscosity for PEO (WSR308). The samples were collected at C = 1000 wppm and tested in the pipe at a shear rate of 5×10^4 and $Re_D = 2.9\times10^5$. The solid line is the minimum shear rate for the rheometer.

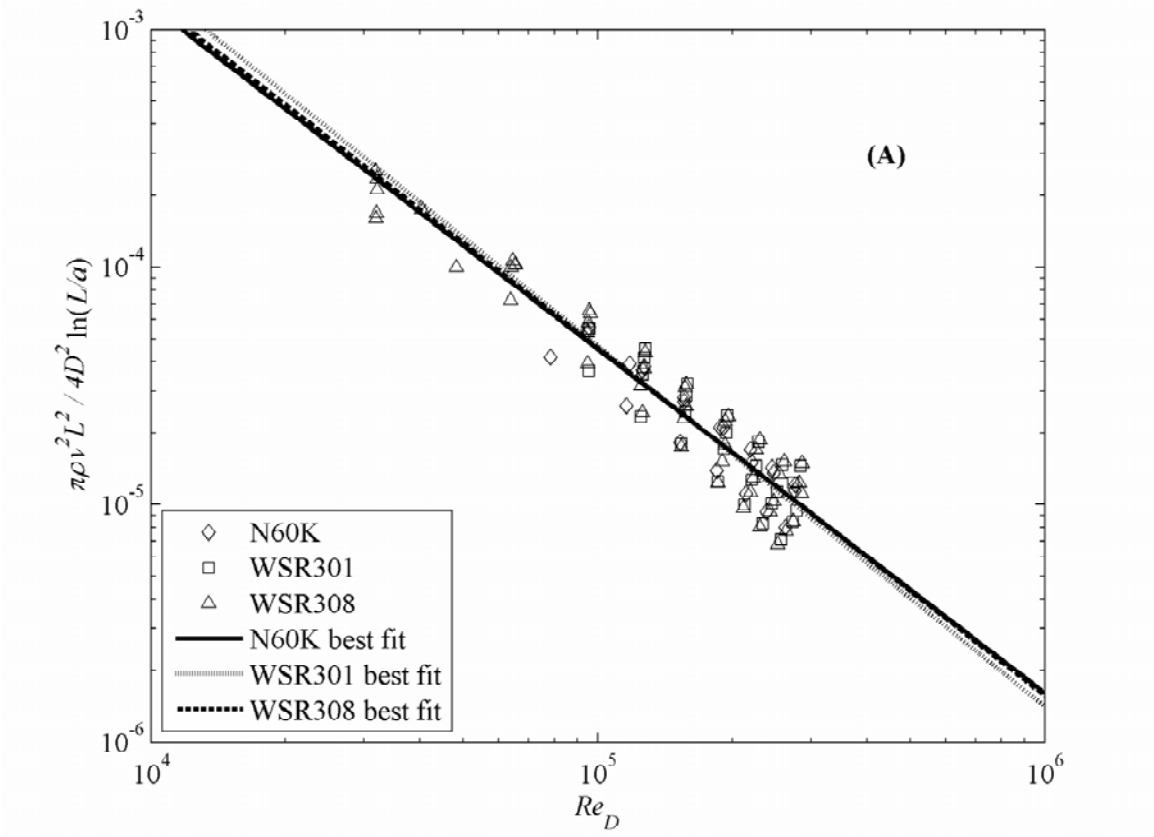
(A)
N60K
WSR301
WSR308
N60K best fit
WSR301 best fit
WSR308 best fit
$\pi\rho v^2 L^2 / 4D^2 \ln(L/a)$
Re_D
10^{-3}
10^{-4}
10^{-5}
10^{-6}
10^4
10^5
10^6

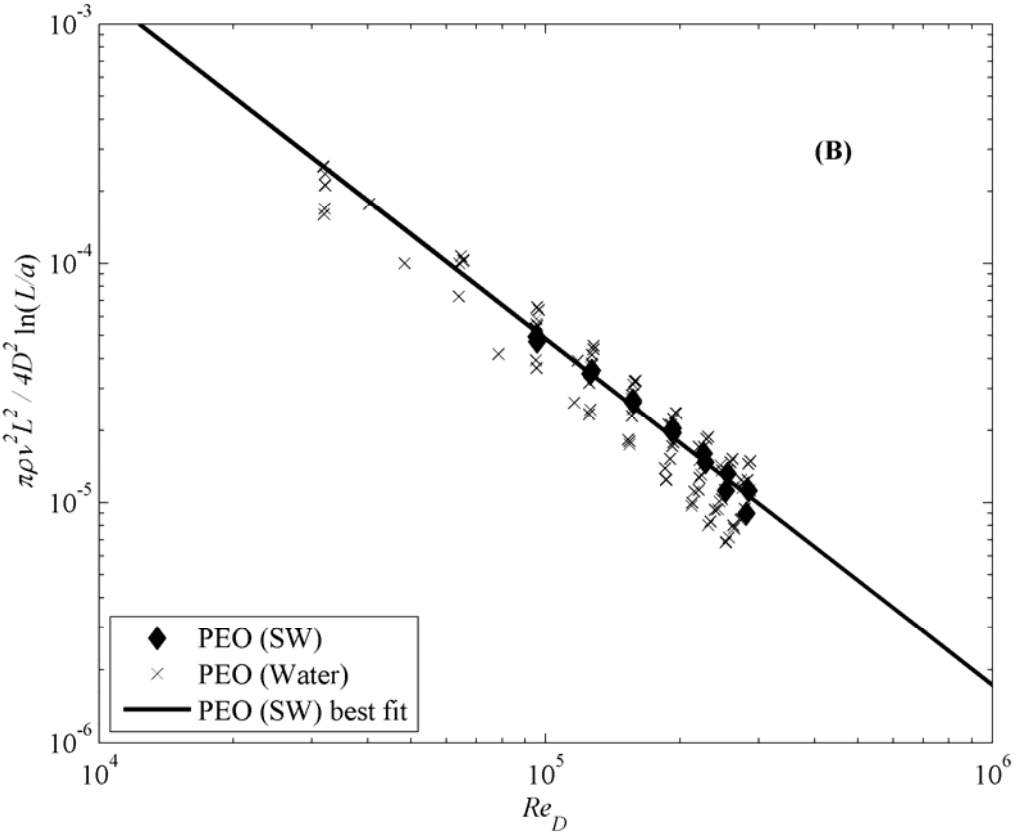

Figure 8. F_{max} dependence on Re_D: (A) Plotted with all results for PEO solutions having a tap-water (W) solvent and (B) PEO solutions with a saltwater (SW) solvent plotted with tap-water results. Both graphs include least-squares power-law best fit curves, which were used to estimate the Reynolds number dependence.

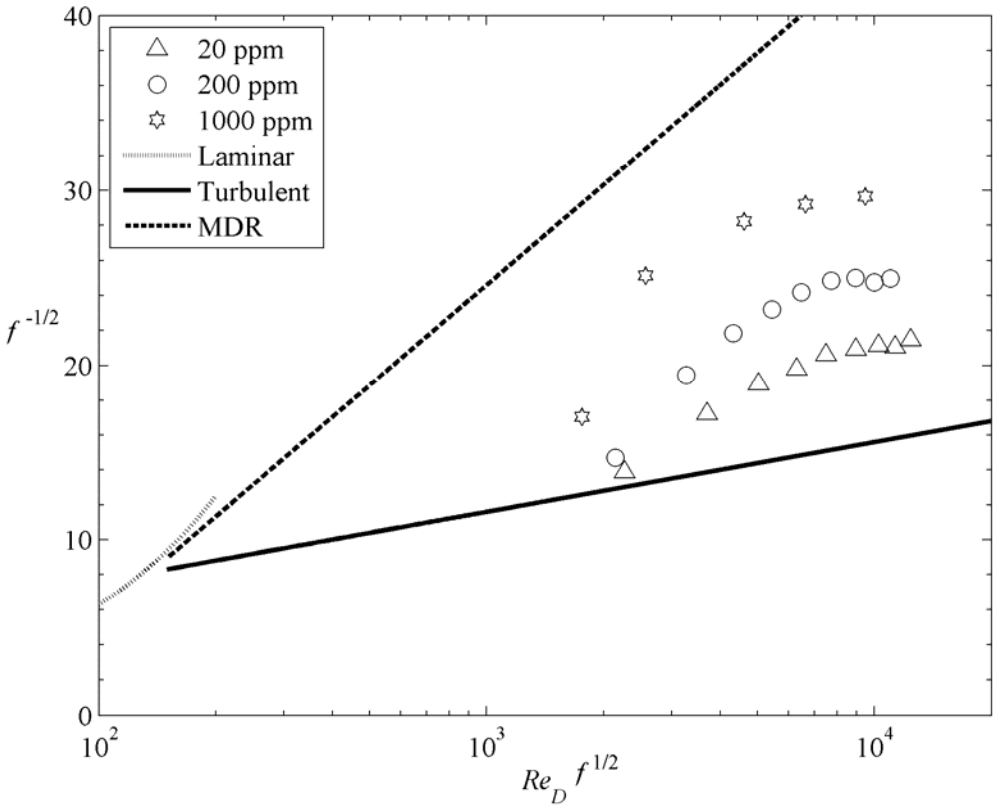

Figure 9. Pressure drop results for PAM samples with a nominal initial $M_w = 5.5\times10^6$.

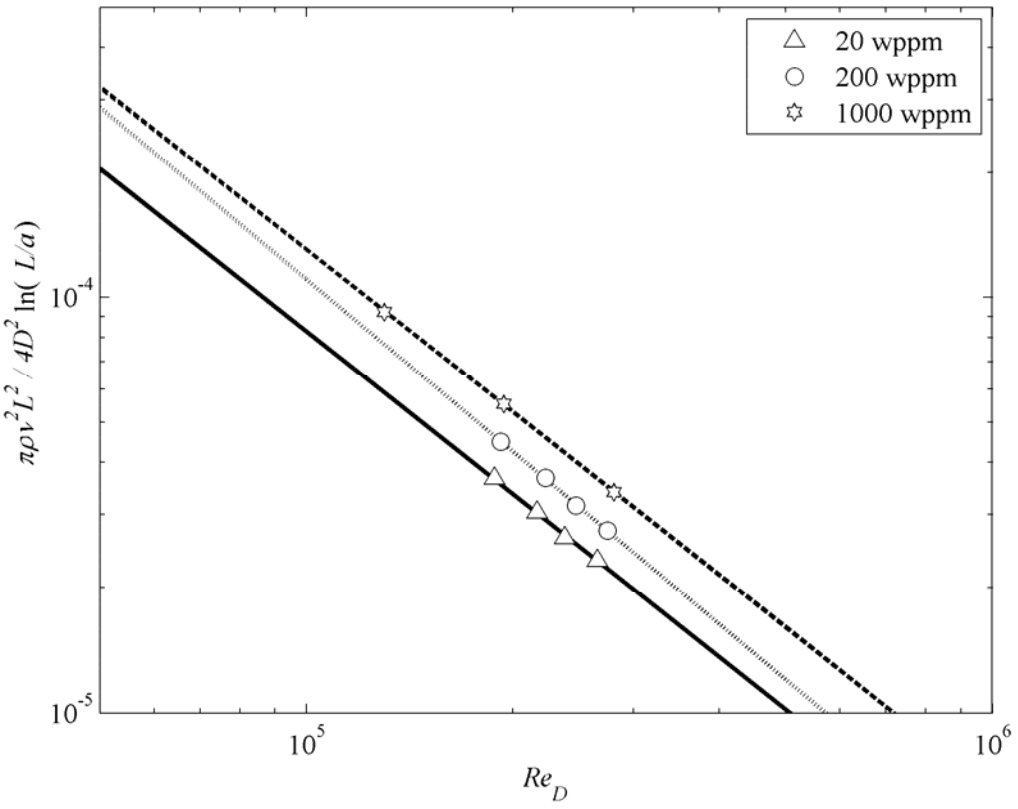

Figure 10. F_{max} dependence on Re_D for PAM solutions at C = 20, 200 and 1000 wppm. Least-squares power best fit curves for 20, 200 and 1000 wppm are the solid, short dash and long dash lines, respectively.

References

Berman, N.S. (1978) "Drag reduction by polymers," *Annual Review of Fluid Mechanics*, **10**, 47-64.

Boyer, R.F. & Miller, R.L. (1977) "Polymer-chain stiffness parameter, sigma, and cross-sectional area per chain," *Marcomolecules*, **10**(5), 1167-1169.

Choi, H.J., Lim, S.T., Lai, P.Y. & Chan, C.K. (2002) "Turbulent drag reduction and degradation of DNA," *Physical Review Letters*, **89**(8), 088302.

Culter, J.D., Zakin, J.L. & Patterson, G.K. (1975) "Mechanical degradation of dilute solutions of high polymers in capillary tube flow," *Journal of Applied Polymer Science*, **19**, 3235-3240.

Draad A., Kuiken G.D.C. & Nieuwstadt, F.T.M. (1998) "Laminar-turbulent transition in pipe flow for Newtonian and non-Newtonian fluids," *Journal of Fluid Mechanics*, **377**, 267-312.

Frenkel, J. (1944) "Orientation and rupture of linear macromolecules in dilute solutions under the influence of viscous flow," *Acta Physicochimica URSS*, **19**(1), 51-76.

Grandbois, M., Beyer, M., Rief, M. Clausen-Schaumann, H. & Gaub, H.E. (1999) "How strong is a covalent bond," *Science*, **283**(5408), 1727-1730.

Horn, A.F. & Merrill, E.W. (1984) "Midpoint scission of macromolecules in dilute solution in turbulent flow," *Nature*, **312**, 140-141.

Hoyt, J.W. (1972) "Effect of additives on fluid friction," *Journal of Basic Engineering*, **94**(2), 258-285.

Hunston, D.L. & Zakin, J.L. (1980) "Flow-assisted degradation in dilute polystyrene solutions," *Polymer Engineering and Science*, **20**(7), 517-523.

Kalashnikov, V.N. (2002) "Degradation accompanying turbulent drag reduction by polymer additives," *Journal of Non-Newtonian Fluid Mechanics*, **103**, 105-121.

Kim, C.A., Kim, J.T., Lee, K., Choi, H.J. & Jhon, M.S. (2000) "Mechanical degradation of dilute polymer solutions under turbulent flow," *Polymer*, **41**(21), 7611-7615.

Larson, R.G. (1999) *The Structure and Rheology of Complex Fluids*, Oxford Univ. Press, New York.

Liaw, G.C., Zakin, J.L. & Patterson, G.K. (1971) "Effects of molecular characteristics of polymers on drag reduction," *AICHE Journal*, **17**(2), 391-397.

Little, R.C. (1971) "The effect of added salt on the flow of highly dilute solutions of poly(ethylene oxide) polymers," *Journal of Applied Polymer Science*, **15**, 3117-3125.

Lumley, J.L. (1969) "Drag reduction by additives," *Annual Review of Fluid Mechanics*, **1**, 367-387.

McComb, W. (1990) *The Physics of Fluid Turbulence*, Oxford Univ. Press, Oxford, UK.

Merrill, E.W. & Horn, A.F. (1984) "Scission of macromolecules in dilute solution: Extensional and turbulent flows," *Polymer Communications*, **25**(5), 144-146.

Moussa T., Tiu C. & Sridhar T. (1993) "Effect of solvent on polymer degradation in turbulent flow," *Journal of Non-Newtonian Fluid Mechanics*, **48,** 261-284.

Moussa T. & Tiu C. (1994) "Factors affecting polymer degradation in turbulent pipe flow," *Chemical Engineering Science*, **49**(10), 1681-1692.

Nakken, T., Tande, M. & Elgsaeter, A. (2001) "Measurements of polymer induced drag reduction and polymer scission in Taylor flow using standard double-gap sample

holders with axial symmetry," *Journal of Non-Newtonian Fluid Mechanics*, **97**(1), 1-12.

Nieuwstadt, F. & Den Toonder, J. (2001) "Drag reduction by additives: A review," *Turbulence Structure and Motion*, ed. A. Soldati, R. Monti, Springer, New York, 269-316.

Patterson, R.W. & Abernathy, F.H. (1970) "Turbulent flow drag reduction and degradation with dilute polymer solutions," *Journal of Fluid Mechanics*, **43**(4), 689-710.

Petrie, H.L., Deutsch, S., Brungart, T.A. & Fontaine, A.A. (2003) "Polymer drag reduction with surface roughness in flat-plate turbulent boundary layer flow," *Experiments in Fluids*, **35** (1), 8-23.

Ptasinski, P.K., Nieuwstadt, F.T.M., van den Brule, B.H.A.A. & Hulsen, M.A. (2001) "Experiments in turbulent pipe flow with polymer additives at maximum drag reduction," *Flow Turbulence and Combustion*, **66**(2), 159-182.

Sedov, L.I., Ioselevich, V.A., Pilipenko, V.N. & Vasetskaya, N.G. (1979) "Turbulent diffusion and degradation of polymer molecules in a pipe and boundary layer," *Journal of Fluid Mechanics*, **94**(3), 561-576.

Sellin R.H.J., Hoyt J.W. & Scrivener O. (1982a) "The effect of drag reducing additives on fluid flows and their industrial applications: Part I. Basic aspects," *Journal of Hydraulic Research*, **20**(1), 29-68.

Sellin R.H.J., Hoyt J.W., Pollert, J. & Scrivener O. (1982b) "The effect of drag reducing additives on fluid flows and their industrial applications: Part II. Basic

applications and future proposals," *Journal of Hydraulic Research*, **20**(3), 235-292.

Toms, B.A. (1948) "Some observations on the flow of linear polymer solutions through straight tubes at large Reynolds numbers," *Proceedings of the First International Congress on Rheology*, **2**, 135-141.

Vanapalli, S.A., Islam, M.T. & Solomon, M.J. (2005) "Scission-induced bounds on maximum polymer drag reduction in turbulent flow," *Physics of Fluids*, **17**(9), 095108.

Vanapalli, S.A., Ceccio, S.L. & Solomon, M.J. (2006) "Universal scaling for polymer chain scission in turbulence," *Proceedings of the National Academy of Sciences of the United States of America*, **103**(45), 16660-16665.

Virk P.S. (1975) "Drag reduction fundamentals," *AIChe Journal*, **21** (4), 625-656.

Virk, P.S., Merrill, E.W., Mickley, H.S., Smith, K.A. & Mollo-Christensen, E.L. (1967) "The Toms phenomenon: turbulent pipe flow of dilute polymer solutions," *Journal of Fluid Mechanics*, **20**(2), 305-328.

Vlassopoulos, D. & Schowalter, W.R. (1993) "Characterization of the non-Newtonian flow behavior of drag-reducing fluids," *Journal of Non-Newtonian Fluid Mechanics*, **49**, 205-250.

White, C.M. & Mungal, M.G. (2008) "Mechanics and prediction of turbulent drag reduction with polymer additives," *Annual Review of Fluid Mechanics*, **40**, 235-256.

PART III. SKIN-FRICTION DRAG REDUCTION BY INJECTION OF GAS WITHIN A HIGH-REYONDS-NUMBER TURBULENT BOUNDARY LAYER

Chapter 5. Introduction

5.1 Abstract

This paper expands upon results presented in Elbing *et al*. (2008) as well as extends the analysis of those results with an investigation into a possible ALDR scaling method. The results used are from two experiments conducted at the US Navy's Large Cavitation Channel on a 12.9 m long flat plate model. Separate experiments were performed to study either bubble drag reduction (BDR) or air layer drag reduction (ALDR). The BDR program acquired local skin-friction and near-wall void fraction measurements at a fixed injection condition, while the ALDR experiments used only local skin-friction measurements as the injection rate was increased from zero to levels sufficient for ALDR. The skin-friction measurements were obtained directly with floating-plate drag balances; the void fraction was estimated from near-wall electrical impedance probes. For BDR and ALDR testing the mass flux of air, tunnel static pressure and tunnel water temperature were acquired simultaneously with the skin-friction data to determine local volumetric fluxes of air along the model surface. The BDR program investigated the influence of injector design, surface tension, injection boundary layer

thickness, injection rates and flow conditions on drag reduction and near-wall void fraction to speeds of 20 ms^{-1} and Reynolds numbers to 220 million. The maximum air injection rate was sufficient for ALDR to be achieved at downstream distance based Reynolds numbers of 160 million at a maximum speed of 15.3 ms^{-1}. ALDR's dependence on injector design and surface condition (hydraulically smooth and fully rough surfaces were tested) was quantified.

ALDR experimental procedure exhibited three drag reduction regions with the injection of air into a turbulent boundary layer: Region I – BDR region where percent drag reduction appears linearly proportional to the injection rate; Region II – a transitional region where percent drag reduction remains linearly proportional to injection rate, but with a much steeper slope; Region III – ALDR where percent drag reduction becomes independent of injection rate and drag reduction in excess of 80% is observed over the entire model. The void fraction measurements supported previous work that showed: (i) the peak void fraction occurs some distance from the model surface; (ii) injector design has a weak influence on BDR (the porous plate injector consistently showed slightly higher void fractions compared to the slot injector); and (iii) surface tension has a negligible impact on BDR. In addition it was demonstrated that *%DR* approximately was linearly proportional to the near-wall void fraction, which supports the notion that a reduction in bulk density is one of the physical mechanisms responsible for BDR. Finally a scaling argument indicates that the critical flux of air required to transition to ALDR should be proportional to $u_\tau/(\nu g)^{1/3}$. Scaling results from two injector designs (porous plate and slot injectors), over two surface conditions (hydraulically

smooth and fully rough) and at two background surface tension levels (tap-water and 15 wppm surfactant) support this proposed scaling.

5.2 Background and Motivation

In nearly all transportation systems moving in a fluid, skin-friction drag is a major contributor to the total resistance and can constitute in excess of 60% of a ship's total resistance when the Froude number is on the order of 10^{-1}. As a result skin-friction reduction techniques have been investigated for several decades with both active (e.g. gas or polymer injection) and passive (e.g. hydrophobic coatings) methods. The current study focuses on active drag reduction through the injection of gas (air) into the near-wall region of a liquid (water) turbulent boundary layer (TBL). Drag reduction by injection of air has attracted the interest of numerous investigators over the years since it has been shown to produce local drag reduction in excess of 80% in laboratory scale experiments. However, most of these studies have focused on bubble drag reduction (BDR) at low Reynolds numbers (to the order of 10^7, based on downstream distance) and small scales (typically on the order of one meter). This has precluded a full understanding of the proper scaling of BDR, which for practical application on a full-scale ship are two orders of magnitude larger in scale than most studies. Furthermore, BDR is the low injection regime of air injection drag reduction, and early studies of the high injection regime of air injection drag reduction have shown significantly improved downstream persistence compared with BDR. This high injection drag reduction regime has been termed air layer drag reduction (ALDR) due to evidence that a thin layer of air forms over the surface. The current work is a continuation of the first studies specifically focused on ALDR

(Elbing *et al*., 2008) and aimed at further understanding the physical mechanisms governing BDR and ALDR.

A brief review of BDR is provided since this has been the primary focus of past air injection studies. The earliest report of BDR (McCormick & Battacharyya, 1973) showed net drag reduction approaching 40% at flow speeds to 2.6 ms^{-1} with bubbles produced by electrolysis near the leading edge of an axisymmetric body. A few years later Bogdevich & Evseev (1976) showed that the observed drag reduction decreases with increased distance from the injection location until the original drag levels are achieved. Additional research on BDR has revealed that in addition to downstream distance from the injector, BDR is also sensitive to gas flow rates, free-stream speed, plate orientation (buoyancy), injector geometry, surface tension and surface roughness. See Merkle & Deutsch (1992) for a review of BDR.

Significant contributions to BDR technology have been produced also by researchers at the Pennsylvania State University (PSU) in laboratory scale testing. These studies (Madavan *et al*., 1984a,b; Madavan *et al*., 1985; Clark & Deutsch, 1991; Fontaine & Deutsch, 1992; Merkle & Deutsch, 1992; Deutsch *et al*., 2003) measured drag reduction on a small (on the order of one meter) flat plate TBL under many flow and injection conditions. Included in their findings is that the type of gas has minimal impact on BDR, injector pore size does not effect drag reduction (pore sizes from 0.5 to 100 μm), bubble size is most sensitive to free-stream velocity and gas injection rates, gravitational forces affect the performance of BDR (plate on top better then plate on bottom

orientation) and favorable pressure gradients can reduce BDR efficiency (similar results have been reported recently by Kawakita & Takano, 2000).

A major issue that has persisted in the study of BDR is the influence of bubble size. This is an important issue because most BDR experiments are conducted in fresh water, and saltwater has been shown to be capable of reducing bubble diameters by approximately a factor of four (Winkel *et al*., 2004). Most studies have shown either that smaller bubbles are better (e.g. Kawamura *et al*., 2003) or that results are independent of bubble size (e.g. Takahashi *et al*., 2001). Recent work by Shen *et al*. (2006) made direct measurements of the skin-friction with gas injection into fresh and saltwater and observed no significant change in the drag reduction. Shen *et al*. also injected lipid-stabilized bubbles that were on the order of 10 viscous wall units in diameter into the boundary layer and still observed no measureable improvement in drag reduction compared to equivalent void fractions with larger bubbles. These results indicate that saltwater effects will either improve or not affect BDR.

A series of experiments have been conducted by a group of Japanese researchers on towed large scale ship models (12 to 50 m in length). They have done investigations on long, slender (0.6 or 1.0 m wide) flat-bottom ship models at speeds to 7 ms^{-1} (Watanabe *et al*., 1998; Kodama *et al*., 1999; Kodama *et al*., 2002). Span-wise uniformity of the injected gas has been problematic with these studies due to air being injected over only the center 50% of the model span and no “skegs” or “strakes” used to contain the gas underneath the model likely resulting in air escaping from beneath. In spite of these

problems overall skin-friction reduction approaching 20% has been reported on the 50 m long model, though drag reduction decreased along the model until only a few percent was observed at its end. Recently this same group conducted some BDR experiments on a full scale vessel (over 100 m in length). From the first at-sea trial (Kodama *et al*., 2000) there was no net power savings observed. However, it was stated that the lack of net power savings was suspected to be the result of gas entrainment into the propeller intake, which offset any reduction in skin-friction drag. Since the first sea-trial, additional work has been conducted (Nagamatsu *et al*., 2002; Kodama *et al*., 2006) that has shown net friction and power savings on the order of a few percent with gas injection. Unfortunately, the complexity (i.e. scale, repeatability of sea conditions, surface curvature and roughness and difficulty in producing high fidelity measurements of fluid parameters) of an at-sea trial has prevented much quantitative information about either the gas distribution (stream-wise or span-wise) or the corresponding drag reduction. Thus while these experiments are a significant step towards applying air injection drag reduction on a ship, they offer little information on the physical mechanisms governing BDR. These problems stress the need for high-Reynolds number testing that can bridge the gap between the small scale laboratory experiments and the full scale ship studies.

The first experiments aimed at bridging this gap were the high-Reynolds number BDR experiments reported by Sanders *et al*. (2006), which were conducted on the same 12.9 m test model used in the current study. Drag reduction was measured directly on this near-zero pressure-gradient TBL at Reynolds numbers over 10^8 based on downstream distance. This study showed that significant levels of drag reduction were only present

within the first couple meters of injection (with the exception of a few conditions at low speed and high injection rates) and that negligible drag reduction persisted downstream. The poor downstream persistence makes BDR quite impractical for most real world applications. Further investigation by Winkel (2007) and Elbing *et al*. (2008) on the same model has produced additional insights into BDR, but significant improvements to downstream persistence have not been realized. However, it has long been suspected that further insights into the physical mechanisms governing BDR would allow for more efficient injection schemes that could result in improved downstream persistence.

In spite of a plethora of BDR experiments spanning a wide range of scales and flow conditions, the governing physical mechanisms remain unclear. However, it is generally agreed that the bubbles in some way reduce the exchange of turbulent momentum within the buffer region of the boundary layer, which ultimately results in a reduction in drag. Experimental results indicate that multiple mechanisms are at work simultaneously. Meng & Uhlman (1998) proposed that "bubble-splitting" could be responsible for the observed reduction in drag by arguing that energy is extracted as larger bubbles split into two or more smaller bubbles (i.e. more small bubbles result in a larger surface area and thus higher surface energy). A reduction in bulk density is also thought to be a possible cause for the drag reduction. The reduction in bulk density would result in decreased Reynolds shear stresses in the near-wall region. If the drag reduction is the product of a reduction in bulk density then the drag reduction should scale with the near-wall void fraction (current results support this theory). Lumley (1973, 1977) hypothesized that bubbles locally increased viscosity and thus reduced turbulent

fluctuation levels and increased the thickness of the sub-layer and buffer region. This theory has been supported by the work of Pal *et al*. (1989), which observed decreased fluctuations in skin-friction in addition to reduction in mean skin-friction. However, Nagaya *et al*. (2001) observed an increase in turbulent fluctuations with gas injection (u' and v' were increased but decoupled resulting in decreased Reynolds shear stresses), which contradicts this theory.

ALDR, as opposed to BDR, occurs when a continuous or nearly-continuous layer of air is formed between a solid surface and the outer liquid flow. Although only the recent work of Elbing *et al*. (2008) has tailored experiments specifically for ALDR, past BDR researchers have inadvertently created and reported some of the characteristics of ALDR. For example, Madavan *et al*. (1985) has reported drag reduction levels in excess of 80% with little improvement with increased air fluxes, and Kodama *et al.* (2002) described an attempt to establish an air-layer along a flat-plate test model at a free-stream speed of 10 ms^{-1}. Although the exact gas injection rates were not described, no stable persistent air-layer was established. They described an air-film which only "lived" about 20 cm downstream of injection, and subsequently separated into slugs of air and eventually bubbles further downstream. (Similar observations have been made with the current study at injection rates near but slightly below fluxes sufficient for ALDR). Sufficient injection fluxes for ALDR have been reported in Watanabe *et al*. (1998) and Kodama *et al*. (1999), but a persistent air layer with dramatic drag-reduction was not observed over the length of their model. Drag reduction levels never exceeded 40% beyond the first few meters of the 50 m test model. This discrepancy is suspected to be

from the lack of span-wise uniformity and gas leakage from beneath the model as previously mentioned.

Sanders *et al*. (2006) observed at low flow speeds and high injection rates drag reduction in excess of 80% over the entire model length. This improved performance was attributed to the formation of an air layer on the model surface, but the air layer could only be achieved for a limited number of conditions and further investigation was not possible since it was not the focus of that study. In contrast, Winkel (2007) and Elbing *et al*. (2008) conducted specific experiments aimed at studying ALDR. They reported ALDR at speeds to 15.3 ms^{-1} on a 12.9 m long test model with injection over nearly 90% of the model width, and air trapped below the model by the tunnel walls. Much of the results presented in the current paper are presented also in Elbing *et al*. (2008), but the current discussion expands void fraction measurements obtained during BDR studies and proposes a scaling for the critical flux of air required to transition to ALDR.

The remainder of this paper is as follows: The experimental methods used in the collection of the data and the experimental program are presented in § 6. The results and analysis of both BDR and ALDR as well as a brief summary of the drag reduction regions with injection of air are provided in § 7. While much of the work has been already presented in Elbing *et al*. (2008) further analysis of the experimental results has provided insight into the physical mechanism for transition from BDR to ALDR. Finally in § 8 the paper is summarized and conclusions are drawn.

Chapter 6. Experimentation

This paper includes results from two separate experiments conducted at the US Navy's William B. Morgan Large Cavitation Channel (LCC) on a single test model. The first test (Test 1) investigated both BDR and ALDR with the test model hydraulically smooth, and the second test (Test 2) studied ALDR with two surface conditions (hydraulically smooth and fully rough). Additional details for these tests as well as a third test focused on ALDR inlet sensitivity can be found in Winkel (2007) and Elbing *et al*. (2008).

6.1 Test Facility

All experimentation was conducted at the LCC, the world's largest low-turbulence (free-stream turbulence < 0.5%) re-circulating water tunnel. The tunnel has a total capacity of 5300 m^3 and a test section that measures 13 m long with a 3.05 × 3.05 m cross-section. Without a model in the test section flow speeds to 18 ms^{-1} can be achieved at absolute pressures between 3.4 and 414 kPa. Additional LCC facility details can be found in Etter *et al*. (2005).

Two 10.2 cm diameter, manually operated vents were added to the top of the LCC test section to help regulate pressure rise caused by the injection of gas during testing. As

gas was injected the vents were manually adjusted to allow air and water to be purged from the tunnel, and as a result, maintain near constant pressure within the test section. While the vents significantly improved pressure control, variations remained and pressure rise was still observed during tests involving injection of high volumes of gas.

At the start of each day of testing the test section was filled and air scavenged from the tunnel for as long as an hour prior to the start of injection testing. If air remained in the free-stream following the air scavenge, deaeration of the tunnel water was performed. Air scavenging and deaeration (if needed) was performed regularly to minimize the air content in the LCC background water.

6.2 Test Model

The test model was a rigid, flat-plate that measured 12.9 m long, 3.05 m wide and 18 cm thick. This test model has been used in several studies investigating drag reduction and turbulent pressure fluctuations at high-Reynolds-numbers (Sanders *et al*., 2006; Sabra *et al*., 2007; Elbing *et al*., 2008; Winkel *et al*., 2008a; Winkel *et al*., 2008b). The test model produced a 6% blockage in the test section, which coupled with boundary layer growth on the model and LCC walls generated free-stream speeds over 20 ms^{-1}. The leading edge was a 4:1 ellipse with a distributed roughness boundary layer trip for the smooth model starting 2.5 cm from the leading edge and extending 25 cm downstream. The roughness trip was made from 120 μm diameter sand grains (100 grit) loosely packed in an epoxy film. The model trailing edge was a 15° full angle truncated wedge. To minimize cavitation and stream-wise junction vortices at the model-sidewall

intersections, 45° triangular-wedge edge-fairings were installed around the entire model. An inflatable seal was installed between the upper and lower surfaces to prevent bypass flow across the top and bottom of the model. Figure 11 shows a schematic of the test model with the instrumental suite used during Test 1 (Test 2 had the same layout minus the electrical impedance probes). The model was mounted slightly below the LCC test section centerline, spanned the entire test section width and had the working surface facing downward (schematically shown in figure 12). The coordinate system used throughout the paper has the X coordinate starting at the leading edge of the model and extending downstream in the flow direction, Y is zero at the model surface and increases perpendicularly into the flow and Z extends in the span-wise direction and completes a right-handed coordinate system (see figure 11).

Gas was injected through the lower surface of the test model at two locations (X_{inj} = 1.38 and 3.73 m) during Test 1 and from a single location during Test 2 (X_{inj} = 1.40). Here X_{inj} is the downstream distance from the model leading edge to the injection location. Test 1 used two types of injectors (slot and porous-plate) while Test 2 used only a slot injector. The injectors spanned the center 2.65 m of the test model (~ 87% of the model span). Cross-sectional schematics of the slot injectors used during Test 1 (Slot A) and Test 2 (Slot B) are shown in figure 13, and the schematic of the porous-plate injector can be found in Sanders *et al*. (2006). The porous-plate injector consisted of a slot inclined at a mean angle of 25° from the model surface and contracting at a full angle of 10°. The slot was capped by a layer of porous (40 μm mean pore diameter) sintered stainless steel (Mott Corporation), ~6 mm thick extending 25 mm in the stream-wise

direction. The layer of sintered metal was flush with the model working surface and fastened to the injector to ensure that all injected air passed through the porous material (Sanders *et al*., 2006). Slot A was inclined 12° from the working surface with a constant throat gap of 5.75 mm that produced an opening in the stream-wise direction of 28 mm. Slot B had the slot inclined at a shallow 5.7° from the model surface and contracting at a full angle of 6.1°. The downstream edge was broken giving it a convex surface that produced a 15 mm opening on the test model surface. A porous material was inserted in the contracting slot to produce additional pressure drop near the surface opening (required for a separate experiment not reported here). Each injector had the gas delivered *via* 40 evenly spaced 12.8 mm diameter ports along a manifold that spanned each injector inlet. Inside the manifold, three layers of screens and baffles (specifics can be found in Sanders *et al*., 2006) were employed to generate a pressure drop that promoted an even distribution of gas flux along the injector span.

6.3 Instrumentation

6.3.1 Air Flow Metering

The gas injection rate was monitored during both Test 1 and 2 with two insertion thermal mass-flow meters (640S Steel-Mass, Sierra Instruments) mounted at the center of straight steel pipes with an inner diameter of 6.3 cm. To ensure that the flow was fully developed at the measurement locations, the flow meters were located 30 inner diameters (1.90 m) downstream and 10 inner diameters (0.63 m) upstream of any line junctions. The flow meters were factory calibrated for the range of 0 to 0.5 $kg\,s^{-1}$ over an operating range of 0-345 kPa and 10-54 °C. An analog voltage signal from each flow meter was

digitized and recorded simultaneously with the skin-friction data. The air entering the flow meters was first passed through a series of filters. A cyclone filter (AGZ1650, Donaldson) was used to remove large particles, then the second filter removed particles larger then 5 μm (PE20/30, Donaldson) and the final filter removed particles larger then 0.01 μm (SMF20/30 and AK20/30, Donaldson) prior to reaching the meters.

Since BDR and ALDR scale with the volumetric rate of gas injected into the boundary layer (Shen *et al*., 2006; Elbing *et al*., 2008), the mass-flow rate (recorded as standard volumetric flow-rate) was converted to a true volumetric flow-rate per unit span (q) at the test model surface using the ideal gas law and measurements of the test section static pressure and water temperature. The injection of air within the enclosed space of the LCC caused a rise in static pressure within the test section that resulted in a decrease in volumetric flow-rate. Thus the injection rates and skin-friction data were acquired simultaneously to correlate skin-friction with volumetric air fluxes, which will be further discussed subsequently.

6.3.2 Skin Friction Balances

During Tests 1 and 2 local skin-friction measurements were made at six stream-wise locations (shown in figure 11) using floating-plate-type drag balances, schematically shown in figure 14. The sensors are a modified design of those used by the PSU group, but were fabricated in-house. The floating plates were 15.2 cm in diameter, 0.79 cm thick and made of 17-4PH stainless steel. Each plate was fixed rigidly to a beryllium copper flexure that was instrumented with a full Wheatstone bridge of semiconductor strain

gages. The drag balance and its housing were flush mounted using an eight point leveling system. The annular gap between the housing and the floating plate was 60 ± 20 μm. These are the same type of sensors used in previous studies on this model (Sanders *et al*., 2006, with a slight modification to prevent through flow; Elbing *et al*., 2008; Winkel *et al*. 2008b). The semi-conductor strain gages were excited using a Vishay signal-conditioning amplifier (Model 2310, Vishay Measurement Group). The sensor outputs were amplified and low-pass filtered at 10 Hz with the same Vishay unit. The output signal was recorded at 50 Hz with a data acquisition board (NI-DAQ, National Instruments) and a LabView virtual instrument.

The skin-friction balances were calibrated *in situ* between zero and 9 or 15 N for the smooth and rough models, respectively. The loads were applied to the plates *via* a cable and suction cup or eyelet attached to the center of the floating plate for the smooth and rough models, respectively. The rough model floating plates had a screw hole at the center of the plate where an eyelet could be inserted for calibration (during testing the hole was filled). The opposite end of the cable was affixed to a precision load cell (Model LCEB-5, Omega Engineering) on a linear traverse, which was capable of applying the necessary range of tensions to the cable. The precision load cell was calibrated in the vertical position by hanging laboratory weights from it prior to its use. This calibration setup has been shown to eliminate bias error caused by using pulleys and weights for the calibration (Elbing *et al*., 2008). Multiple calibrations were performed on the skin-friction sensors to confirm their repeatability and to assess their uncertainty. The measurement uncertainty was typically ±5%.

The percent drag reduction (*%DR*), defined in equation (6.1), was computed directly from the skin-friction measurements with and without injection of air. Here τ_w and τ_{wo} are the skin-friction measurements from the skin-friction drag balances with and without air injection, respectively.

$$\%DR = \left(1 - \frac{\tau_w}{\tau_{wo}}\right) \times 100 \qquad (6.1)$$

As previously stated when gas was injected into the confined volume of the LCC, the static pressure in the test section increased and caused decreased volumetric air injection fluxes as well as baseline drift in the shear stress measurement. The skin-friction baseline drift and volumetric injection rates were corrected with the time-record of the static pressure on the upper wall of the LCC test-section previously mentioned, which was recorded simultaneously with the skin-friction and gas injection rate measurements. The pressure rise during an injection test (typically 30-60 seconds) resulted in decreased volumetric injection rate by as much as 30% (dependent on the free-stream velocity and gas injection rate), which can have a significant effect on the level of drag reduction achieved. To account for this, the time traces of shear stress and volumetric gas injection rate were segmented into half second intervals. The drag reduction observed during each interval was divided into 0.3 $m^3 min^{-1}$ bins.

6.3.3 Void Fraction Probes

Electrical impedance probes were mounted on the model surface during Test 1 to measure the bulk void fraction in the near-wall region of the flow. Each probe consisted of two brass electrodes soldered to signal conductors. The brass electrodes that were to be in contact with the flow were machined flush and mounted in an 11.4 cm diameter non-conducting, flat PVC disk. Each disk had a large (3.2 mm diameter electrodes with 6.4 mm cross-stream separation) and a small (1.6 mm diameter electrodes with 3.2 mm cross-stream separation) electrode pair embedded and was flush mounted with the test model surface. The purpose of the two sizes was to detect qualitatively void fraction gradients normal to the surface as illustrated in Cho *et al.* (2005). The probes were positioned 1.91 cm upstream and 1.91 cm downstream of the disk center for the small and large probes, respectively. The disks were positioned slightly off the model's span-wise centerline and were centered at 12 stream-wise locations (X = 1.07, 1.96, 2.59, 3.41, 5.09, 5.94, 6.61, 7.43, 9.23, 10.05, 10.68, 11.50 m). Each probe's interior surface was encased in an epoxy, which electrically isolated each electrode prior to contact with the flow at the model surface.

The basic circuit for the electrical impedance probes is shown in figure 15 and consists of an AC excitation voltage (V_s), reference resistor (R_{ref}), probe electrical impedance associated with the flow (Z_{el}), stray capacitance from the input and output wires (Z_{c1} and Z_{c2}, respectively), and stray capacitance between the input and output wires (Z_{c3}). The stray capacitance between the input and output leads was minimized by shielding each separately, but it is included due to its significant influence during high

void fraction measurements. The input and output stray capacitance can not be neglected due to the length of the wires required for the experimental setup. This stray capacitance was measured *in situ* by short circuiting the probe with a known resistor and measuring the voltage (V_{ref}) across R_{ref}. The stray capacitance was measured repeatedly throughout testing and showed negligible variation. The AC excitation voltage was produced with a signal generator (8904A multifunction synthesizer, HP). The reference resistor had a nominal resistance of 75 kΩ, which maximized the output signal and sensitivity. Applying Kirchhoff's current law to the circuit provides the relationship between the electrode impedance and the known parameters, which is provided in equation (6.2).

$$Z_{el} = \frac{\left(V_s - V_{ref}\right) R_{ref}\, Z_{c2}\, Z_{c3}}{V_{ref}\left[Z_{c2}\left(R_{ref} + Z_{c3}\right) + R_{ref} Z_{c3}\right] - R_{ref} Z_{c2} V_s} \tag{6.2}$$

Four impedance measurement systems were fabricated to facilitate simultaneous measurements, which reduced the required injection time. During each injection condition, measurements were acquired from each electrode pair, necessitating the use of a (128-channel) multiplexer (PXI-2530, National Instrument) that was capable of switching between each set of four probes at more than 200 Hz. The sampling time for each probe was approximately three seconds; the data were acquired at 1000 Hz. Once the skin-friction sensors reached steady state following the start of injection, impedance-probe data acquisition was initiated.

Increased probe sensitivity was achieved by recording the deviation of the measured impedance from the baseline (zero void fraction) impedance. A lock-in amplifier (LIA) (SR830 DSP LIA, Stanford Research Systems) and a signal generator (8904A multifunction synthesizer, HP) were used to excite and balance the bridge as well as to demodulate the resulting signal. The typical recorded output from the LIA was the amplitude and phase of V_{ref} - V_w with a gain of 20, averaged over three milliseconds and band-pass filtered (0.01 Hz about the center frequency). Here V_w is the voltage across the reference resistor in tunnel water (i.e. zero void fraction). Each circuit had a separate excitation frequency (5, 7, 9, and 11 kHz) to prevent cross-talk between systems. A single computer controlled all the probe multiplexing, V_w amplitude and phase variation and data acquisition *via* a LabView virtual instrument and data acquisition card (PCI-6040E, National Instruments).

The measured impedance given in equation (6.2) can be related to the volume averaged void fraction, α, using Maxwell's mixture model given in equation (6.3) (Ceccio and George, 1996). This model provides an estimate only since the analysis of Hewitt (1978) following Maxwell (1881) assumed a uniformly disperse bubbly mixture, which is not expected in the present experiments.

$$\alpha = \frac{(Z_m - Z_w)(2 + \sigma_g/\sigma_w)}{(2Z_m + Z_w)(1 - \sigma_g/\sigma_w)} \qquad (6.3)$$

Here, Z_m and Z_w are the impedance of the mixture and water, respectively. σ_g (~ 0) and σ_w (~3.5 μS cm^{-1}) are the electrical conductivity of the gas and water, respectively. For the

present study the complex part of the mixture impedance is assumed to be negligible since $\sigma_w >> 2\pi f \widetilde{\varepsilon}_L \varepsilon_o$, where f is the input frequency (~10 kHz), $\widetilde{\varepsilon}_L$ is the non-dimensionalized permittivity of the water (~80), and ε_o is the permittivity of a vacuum (8.85×10^{-12} F m^{-1}) (George *et al*., 2000). Thus the real part of the mixture impedance (i.e. the conductivity) dominates when σ_w is greater than 0.44 μS cm^{-1}, which is accurate in the current study. The system was designed to measure the void fraction in bubbly flows, and as a result the void fraction measurements above ~50% (i.e. with an air layer) are only qualitative. Thus, void fraction measurements are not reported when an air-layer is present. However the impedance measured between the electrode pairs was large compared with bubbly flow measurements indicating that the near-wall region was primarily air.

6.4 Test Matrix

The free-stream velocity, gas injection rate, injection location, background surface tension and injector type were varied during Test 1, which studied both BDR and ALDR. Free-stream speeds (U_∞) from 6.7 to 20.0 ms^{-1} and gas mass flow-rates of 0.06 to 0.45 kg s^{-1} with a maximum volumetric flux of 0.11 m^{2}s^{-1} per unit injector span were tested. Downstream distance based Reynolds numbers ($Re_X = U_\infty X / \nu$, where ν is the kinematic viscosity of water) to 220 million were investigated. A subset of experiments during Test 1 investigated the influence of surface tension on BDR and ALDR by reducing the LCC background water surface tension from about 70 to 50 dyne cm^{-1} (measured following the procedure of Lapham *et al*., 1999) with the addition of 15 wppm of a common soluble surfactant (Triton-X-100). Winkel *et al*. (2004) showed that the addition of surfactant to

the tunnel volume can reduce mean bubble diameters by more than a factor of two immediately downstream of injection, but Elbing *et al*. (2008) showed that this effect is limited to the region near the injector.

Only ALDR was investigated during Test 2 with the model surface either hydraulically smooth or fully rough. The smooth model testing was to repeat the results from Test 1 as well as investigate ALDR's sensitivity to injector design (Test 1 ALDR program used a porous plate injector and Test 2 used the Slot B injector). The rough model testing was performed by roughening the entire model surface *via* tightly packed glass bead grit embedded within epoxy paint (High Build Semi-Gloss 97-130, Aquapon). The tightly packed particles produced a sand grain type roughness. Based on the skin-friction measurements and the assumption that the model was fully rough (which is supported by the lack of Reynolds number dependence in the baseline skin-friction, see figure 17), the leading 75% of the model was very uniform yielding an average roughness height, k, between 350 and 580 μm. The remaining 25% of the model was less uniform with a range of k from 830 to 1100 μm. Free-stream speeds from 6.7 to 15.8 ms^{-1} and volumetric air fluxes from 0.03 to 0.14 $m^2 s^{-1}$ per unit injector span were tested.

For all drag reduction experiments, prior to each injection a baseline (non-injection) skin-friction measurement was recorded for a period of about 15 seconds. For an injection run, shear stress data acquisition was initiated five seconds prior to gas injection and concluded five seconds post injection. In addition to the shear stress measurements, the gas mass flow-rate, water temperature and static pressure of the LCC

test section were recorded simultaneously to determine a more accurate volumetric flux of air using the ideal gas law. A control valve was preset to provide a desired gas injection rate according to the pre-determined test matrix for BDR experiments. The ALDR experiments were conducted by slowly varying the control valve (i.e. the volumetric flux of air) to produce relationships between air volumetric fluxes and *%DR* over a wide range of injection conditions. Two manually operated 10.2 cm diameter vents were added to the top of the LCC test section to help regulate pressure in the test section during gas injection. While the vents improved the pressure control, variations remained and some pressure rise was recorded during gas injection.

Chapter 7. Results and Analysis

The presentation of results is divided into four subsections: (1) baseline (non-injection) results for both the smooth and rough models, (2) review of drag reduction regimes with the injection of air into a TBL, (3) presentation and discussion of BDR results and (3) presentation and scaling of ALDR results. The BDR and ALDR results are separated because they are fundamentally different flow morphologies, though air layers can arise as a consequence of bubble injection.

7.1 Baseline Results

Figure 16 provides the non-injection skin-friction coefficient results from Tests 1 and 2 on the smooth test model, where $C_{fo} = 2\,\tau_{wo} / \rho\, U_{\infty}^{2}$ and ρ is the mass density of water. Also plotted with the current baseline results are the Schultz-Grunow (1941) friction curve that is given by equation (7.1) and the best-fit power-law curve from Test 1 and 2 data, which is provided by equation (7.2).

$$C_{fo} = 0.370 \log^{-2.584}\left(\mathrm{Re}_{X}\right) \qquad (7.1)$$

$$C_{fo} = 0.0168\, \mathrm{Re}_{X}^{-0.123} \qquad (7.2)$$

The current results are in good agreement with the Schultz-Grunow (1941) friction curve. The slight deviation from the Schultz-Grunow (1941) friction curve is mostly likely the result of a very mild pressure gradient present in addition to residual effects from the boundary layer trip at lower Reynolds-numbers.

The non-injection (baseline) skin-friction results on the rough model are shown in figure 17. These results show that on the rough model at a fixed downstream location the friction coefficient is independent of Reynolds number. This indicates that the test model was fully rough since both White's and Schlichting's friction curves (provided by equations 7.3 and 7.4, respectively) for a fully rough flat plate (White, 2006) depend only on the average roughness height and the downstream distance. By assuming that the roughness is sand grain type and that the model was fully rough, equations (7.3) and (7.4) can be used to estimate the average roughness of the model. Table 1 gives the average coefficient of friction for each measurement location and the corresponding average roughness height, k, determined from the average obtained from equations (7.3) and (7.4).

$$C_{fo} \approx \left[1.4 + 3.7 \log\left(\frac{X}{k}\right)\right]^{-2} \qquad (7.3)$$

$$C_{fo} \approx \left[2.87 + 1.58 \log\left(\frac{X}{k}\right)\right]^{-2.5} \qquad (7.4)$$

From table 1 it is apparent that the average roughness height was quite uniform over the first nine meters of the model and produced $k \sim 470 \pm 200$ μm. This estimate is in excellent agreement with direct measurement of the diameter of individual grit particles

used to produce the roughness (average particle diameter = 450 ± 250 μm). However, further downstream the roughness level appears to be approximately double that of the upstream section of the model, which indicates that the downstream roughness was not applied as uniformly as the upstream section. From the skin-friction measurements this observation is consistent with a visual examination of the surface-embedded particles upstream and downstream of approximately X = 9 m. Table 2 provides estimated friction velocities ($u_\tau = \sqrt{\tau_{wo}/\rho}$) and viscous wall units ($l_v = v/ u_\tau$) for the rough model over the range of speeds tested with the roughened surface, which was determined from the mean coefficient of friction along the model length. The values presented in table 2 were used to scale the rough model ALDR results presented later.

7.2 Air-Injection Drag Reduction Regions

Elbing *et al*. (2008) established that with the injection of air into a turbulent boundary layer there are three drag reduction regions: Region I – BDR zone where *%DR* is approximately linearly related to the gas injection rate; Region II - A transition zone between BDR and ALDR where the *%DR* still appears well approximated as linearly related to q but with a much steeper slope compared to region I; and Region III – ALDR zone where the level of drag reduction has reached a maximum (*%DR* ~ 80-100) and increased air injection causes little or no change in drag reduction due to the near complete elimination of friction drag. Figure 18 shows an example from a single downstream location (X = 9.23 m) on the smooth model at U_∞ = 8.8 ms^{-1} over a range of q spanning all three regions of air injection drag reduction. It is important to note that these curves are not sensitive to the downstream distance once X/δ is greater then about

ten, where δ is the boundary layer thickness. Only the first measurement station was positioned within that region of the flow, and it produced a similar curve though significantly shifted to lower *q*.

Due to the steep slope within the transition region it is quite difficult to investigate that region, but both BDR and ALDR can be studied in detail. Further discussion of the two regions is separated since they involve separate flow morphologies and the governing physics are disparate. Video imaging of the flow from Elbing *et al*. (2008) and shown in figure 19, illustrates this morphological difference with surface images of the rough model at 6.8 ms^{-1} with non-injection (left), air injection within the BDR region (center) and air injection with the ALDR region (right). The imager was mounted outside the tunnel with a fixed view of the stream-wise and span-wise directions of the test surface about five meters downstream of the leading edge. In the non-injection image (left) the roughened model surface is clearly visible along with an instrumentation hatch (large outlined rectangle in the lower right corner) and a sampling port (dark, small rectangle in the upper right used for a separate experiment). In the middle image, during BDR, the region above the surface becomes opaque (typical of bubbly flow, even with low void fractions) causing the hatch and sampling port to no longer be visible. Finally once sufficient air flux is achieved to transition from BDR to ALDR the image immediately transforms from the opaque bubbly cloud (center) to a semi-transparent layer (right). This transition is evidenced in the right image by the reappearance of the sampling port and the appearance of specular reflections from the air-water interface. These differences indicate that during BDR the flow morphology is well represented by discrete bubbles

spread through the boundary layer, and that during ALDR there is stratification with the water boundary layer below the layer of air at the model surface. The presence of an air layer during ALDR is further supported by large impedance measurements with the electrical impedance probes (void fractions not included since the system was not designed to measure large void fractions) and near-wall images presented in Elbing *et al*. (2008) indicating that the near-wall region is nearly void of air-water interfaces.

7.3 BDR Results

BDR was investigated only during Test 1 with measurements of both the local skin-friction and the near-wall void fraction. The following analysis expands on the electrical impedance measurements since the skin-friction results were discussed in detail in both Winkel (2007) and Elbing *et al*. (2008), while only a subset of conditions were shown from the impedance measurements with minimal discussion. The use of these measurements should be approached cautiously due to their large degree of uncertainty. Thus in the work of Elbing *et al*. (2008) two independent methods for measuring void fractions (impedance probes and near-wall imaging) were deemed necessary and not just advantageous. The uncertainty in the void fraction measurements is approximately ±10% at low void fraction and increases with increasing void fraction due to the breakdown of the mixture model used. Conditions sufficient for ALDR were excluded from the following BDR results and analysis. Thus from the predetermined test matrix there were seven conditions that were available for the BDR analysis. Included from $U_\infty = 20.0$ m s^{-1} were four nominal injection rates (1.6, 3.0, 5.7, and 9.6×10^{-2} m^{2}s^{-1}) and for $U_\infty = 13.3$ m s^{-1} the three lower injection rates were used. For each of these seven test conditions

four injection conditions were studied (porous plate injection into tunnel water and 15 wppm surfactant, Slot A injection from $X = 1.38$ m and Slot A injection from $X = 3.73$ m). The addition of surfactant caused a decrease in the tunnel surface tension from 70 to 50 dyne cm^{-1}, which prior to testing was thought to cause a decrease in bubble size (Winkel *et al*., 2004). However, measurements of the bubble diameters with and without surfactant, provided in Elbing *et al*. (2008), revealed that the decreased surface tension had a negligible effect on bubble size. The change of the injection location from $X = 1.38$ m to $X = 3.73$ m with the slot injector was implemented to investigate the influence of the injection boundary layer thickness on BDR (the boundary layer was increased by a factor of 2.5 with a minimal change in friction velocity). However, due to the position of the measurement locations relative to the farther downstream injection location, only low void fraction measurements were acquired with the downstream injector. This makes it difficult to compare the upstream and downstream injections, but the drag reduction results presented in Elbing *et al*. (2008) from the different injection locations indicate that the injection boundary layer thickness has minimal influence on BDR.

Prior research (Merkle & Deutsch, 1990) has shown that the peak void fraction occurs a few hundred wall units above the surface. There is also evidence (Pal *et al*., 1989; Elbing *et al*., 2008) that bubbles do not reside in the viscous sub-layer, which creates a "liquid sub-layer" in the near-wall region during BDR. The near-wall void fraction measurements from the current study provide corroborative evidence for these findings. Figure 20 shows the void fraction results with injection from the porous plate injector at 20.0 m s^{-1} versus downstream distance from the injection location for the large

and small electrode spacing. The void fraction measurements from the larger spacing consistently show higher void fraction. The larger electrode spacing results in a larger "influence volume" and therefore is more sensitive to the flow farther from the surface then the small spacing. Similar results were acquired at the lower speeds and various injection conditions. From these results it can be qualitatively inferred that the void fraction increased with distance from the wall, as discussed by Cho *et al*. (2005). These results are in agreement with the findings reported by Nagaya *et al*. (2001).

Comparison between the various injection conditions from X_{inj} = 1.38 (porous plate injection into tunnel water or surfactant and Slot A injection) is provided in figure 21. Shown are the void fraction measurements from the large spacing for the four nominal injection rates at 20.0 $\mathrm{m\,s^{-1}}$ versus downstream distance from the injector. The general trends are quite similar between the slot and porous plate injectors, and between the porous plate injection into tunnel water and 15 wppm surfactant laden water. However, the slot injector void fractions are consistently lower than with the porous plate and the injection into the 15 wppm surfactant is consistently slightly below injection into tunnel water. These results are consistent with the drag reduction measurements provided in Elbing *et al*. (2008). Thus both surface tension and injector design influence the behavior of BDR, but there is only a weak dependence on both.

Combining the skin-friction results and the void fraction measurements provides information on the relationship between the *%DR* and the near-wall void fraction. Figure 22 shows the results from the large electrode spacing and injection from the porous plate

injector with and without surfactant in the background water. Also provided in the graph is the best fit curve to the entire data set ($\%DR = 200\,\alpha$). The results from the slot injection testing were quite similar to those shown in figure 22. Due to the large degree of uncertainty in the void fraction measurements it is difficult to conclusively state that *%DR* is linearly related to the near-wall void fraction. However, a crude trend is apparent which indicates that the *%DR* is proportional to the near-wall void fraction. This supports the bulk density reduction theory for BDR.

An attempt to scale the void fraction measurements with a method similar to the Madavan *et al*. (1984a) scaling was made with some success. The results from the various injection conditions collapsed on a single curve, but with large scatter. Due to the large uncertainty in the measurements it was impossible to determine with any degree of precision the appropriate scaling that could collapse the near-wall void fraction measurements in the current test.

7.4 ALDR Results

Elbing *et al*. (2008) showed that the critical flux of air required to achieve ALDR, q_{crit}, is strongly influenced by the free-stream speed and surface roughness (increased roughness requires larger fluxes of air to achieve ALDR). There is minimal discussion in that paper as to the cause of the higher fluxes with increased roughness. Therefore a simple scaling argument is provided to attempt to explain the required increase in air flux. First it is assumed that the required volumetric flux of air required for ALDR is dependent on the ratio of shear to gravitational (buoyancy) forces. This ratio can be

determined by investigating the forces on a single bubble of radius R in the near wall region. The shear force on the bubble, F_S, scales with $A_B \rho \nu u_\tau / R$, where A_B ($=\pi R^2$) is the projected area of the bubble. The buoyancy force, F_B, on the bubble scales with $\rho g V_B$, where V_B ($=4\pi R^3/3$) is the bubble volume and g (= 9.81 $\mathrm{m\,s^{-2}}$) is gravitational acceleration. Thus $F_S/F_B \propto \nu u_\tau / R^2 g$. Furthermore, within Elbing *et al*. (2008) the bubble diameter was shown to be independent of injection method and even surface tension, which indicates that the size of the bubble is determined primarily from the turbulent motions within the flow for a fixed injection rate. This implies that the bubble radius should be proportional to the turbulent length scale (i.e. $R \propto \nu / u_\tau$). Thus the critical volumetric flux, q_{crit}, should scale with $u_\tau / (\nu g)^{1/3}$. Results using this scaling from Tests 1 with injection over the smooth model into tunnel water and surfactant laden water, and Test 2 with injection over the smooth and rough surfaces are shown in figure 23. The critical injection flux is scaled with the flux of fluid in the near-wall region, q_S, where the near-wall region is defined as $0 \leq Y/l_\nu \leq 11.6$. Wu & Tulin (1972) assumed a linear velocity profile in this region and integrated to find that $q_S = 67.3\nu$. The friction velocities at the injection location were used for the smooth model while the rough model friction velocity was determined from the average coefficient of friction along the model length (friction velocities used are provided in table 2). These results collapse quite well for both smooth model tests with different injectors (porous plate and slot type injectors) as well as with the rough surface model. The best-fit curve to the entire data set is included in the figure and provided by equation (7.5).

$$\frac{q_{crit}}{q_s} = 6.1354\left[\frac{u_\tau}{(\nu g)^{1/3}}\right]^{1.81} \qquad (7.5)$$

The success of this scaling approach indicates that the critical volumetric flux of air required for transition to ALDR is primarily dependent on the balance between the shear forces and buoyancy forces.

Chapter 8. Summary and Conclusions

Several conclusions can be drawn from the analysis of results presented in Elbing *et al*. (2008) from an experiment on a 12.9 m long flat plate model at Reynolds numbers to 2×10^8. A summary was provided of the three regions typical of drag reduction with injection of air: Region I – BDR; Region II – transition; Region III – ALDR. Both the BDR and transition regions appeared to be linearly proportional to the injection flux with the transition region having a much steeper slope. Once ALDR was reached the percent drag reduction became independent of injection rate due to the near complete elimination of the skin-friction drag (%DR ~ 80-100 observed over the entire friction measured length of ~10 m).

Near-wall void fraction measurements support the findings of Merkle & Deutsch (1990) that the peak void fraction occurs off the surface by showing that the void fraction increases with increasing measurement volume. Void fraction measurements also support drag reduction measurements provided in Elbing *et al*. (2008) that both the injector design and surface tension have a weak dependence on BDR. The largest void fractions were observed with a tunnel water background and the porous plate injector. If the surface tension was reduced with surfactant, a marginal decrease in void fraction was observed, and if the slot injector was used a slightly larger drop in void fraction was experienced. Investigation of all the BDR near-wall void fraction measurements revealed

that over the range of conditions tested ($13.3 < U_\infty < 20.0$ ms^{-1}, $1.6\times10^{-2} < q < 9.6\times10^{-2}$ m^{2}s^{-1} and $0.58 < X\text{-}X_{inj} < 9.3$) the *%DR* appeared to be linearly related to the near-wall void fraction. This supports the theory that a reduction in bulk density is the physical mechanism responsible for BDR.

The ALDR results from Elbing *et al*. (2008) showed that the critical flux of air required to achieve ALDR was sensitive to both surface roughness and free-stream speed. These findings were analyzed using a scaling argument that the critical injection flux required to form an air-layer should depend on a balance between shear and gravitational (buoyancy) forces. The new scaling parameter, $u_\tau/(\nu g)^{1/3}$, was used successfully to collapse both the smooth and rough ALDR results from Elbing *et al*. (2008).

TABLES AND FIGURES

X (m)	1.96	3.41	5.94	7.43	9.23	10.68
$C_{fo} \times 10^3$	4.5	3.9	3.8	3.7	4.0	3.7
k (μm)	400	350	550	580	1100	830

Table 1. Average roughness height on the rough model determined from the average C_{fo} at each downstream location.

U_∞ (ms^{-1})	6.8	7.9	9.1	10.1	11.3	12.4
u_τ (ms^{-1})	0.30	0.35	0.40	0.45	0.50	0.55
l_v (μm)	3.3	2.8	2.5	2.2	2.0	1.8

Table 2. Friction velocity and viscous wall units determined from the skin-friction measurements near the injection location. These values are used subsequently to scale the ALDR results.

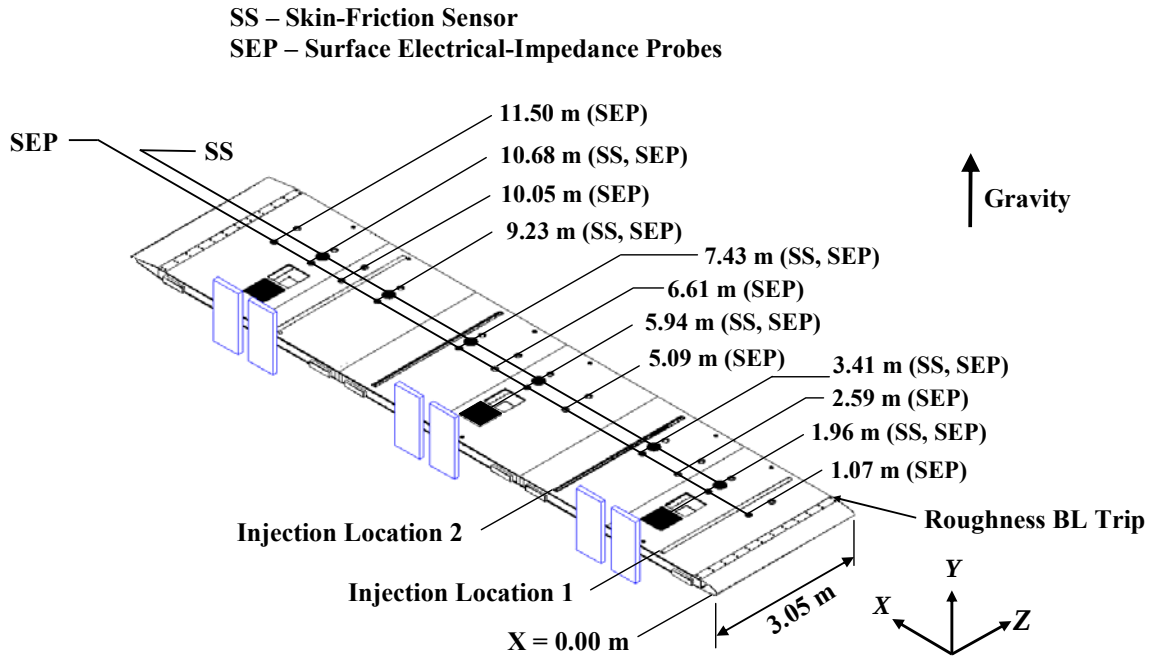

Figure 11. Schematic view of the test model with the instrument suite used during Test 1. Test 2 had the same layout, but without the electrical impedance probes. Injection location 1, X_{inj}, was 1.38 m and 1.40 m for Test 1 and Test 2, respectively. Injection location 2 was only used during Test 2 and was X_{inj} = 3.73 m.

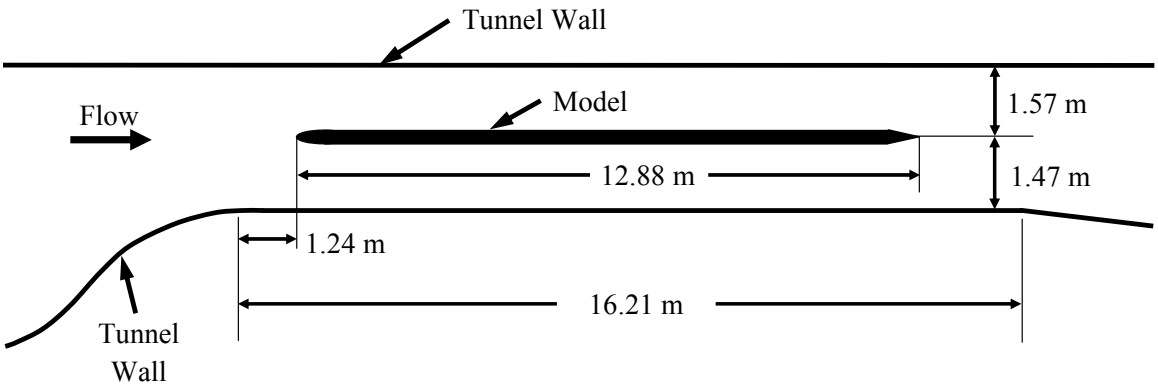

Figure 12. Schematic of the test model mounted in the LCC test section with gravity and the model working surface downward.

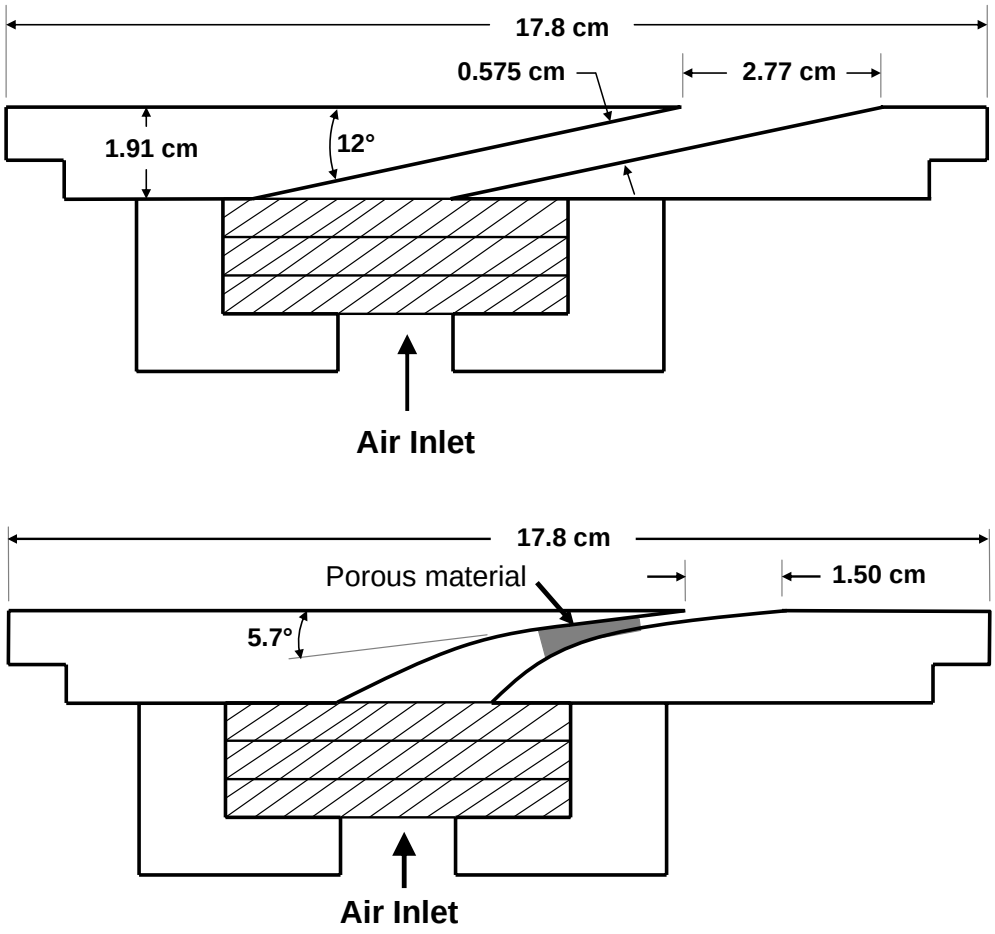

Figure 13. Cross-sectional schematic of Slot A (upper) used during Test 1 and Slot B (lower) used during Test 2. The air inlet consisted of 40 evenly spaced ports that fed the manifold, which spanned the rear of the injector. Three layers of baffles and screens served to create a pressure drop within the manifold that produced span-wise uniform injection. See Sanders *et al*. (2006) for the screen and baffle specifications and the porous-plate injector schematic.

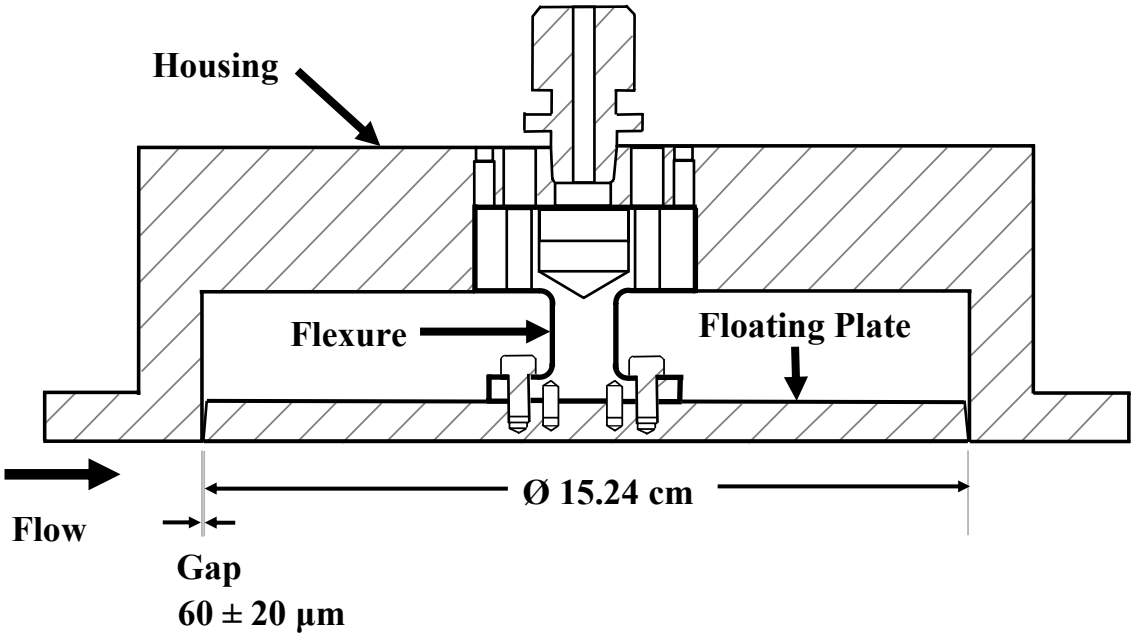

Figure 14. Cross sectional schematic view of the skin-friction balance with floating plate, flexure and housing.

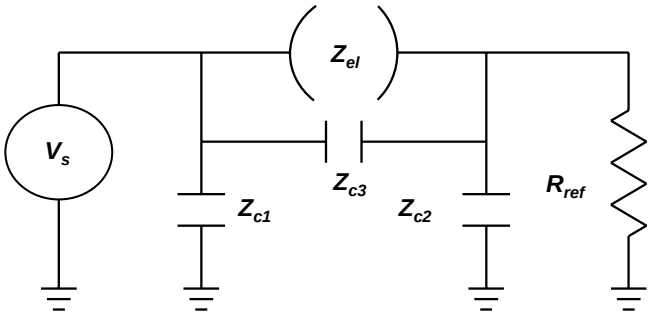

Figure 15. Circuit diagram of the electrical impedance probes used in Test 1. Shown is the voltage source (V_s), the impedance of the bubbly flow (Z_{el}), reference resistor, (R_{ref}) and the stray capacitance from the lead wires (Z_{c1}, Z_{c2} and Z_{c3}).

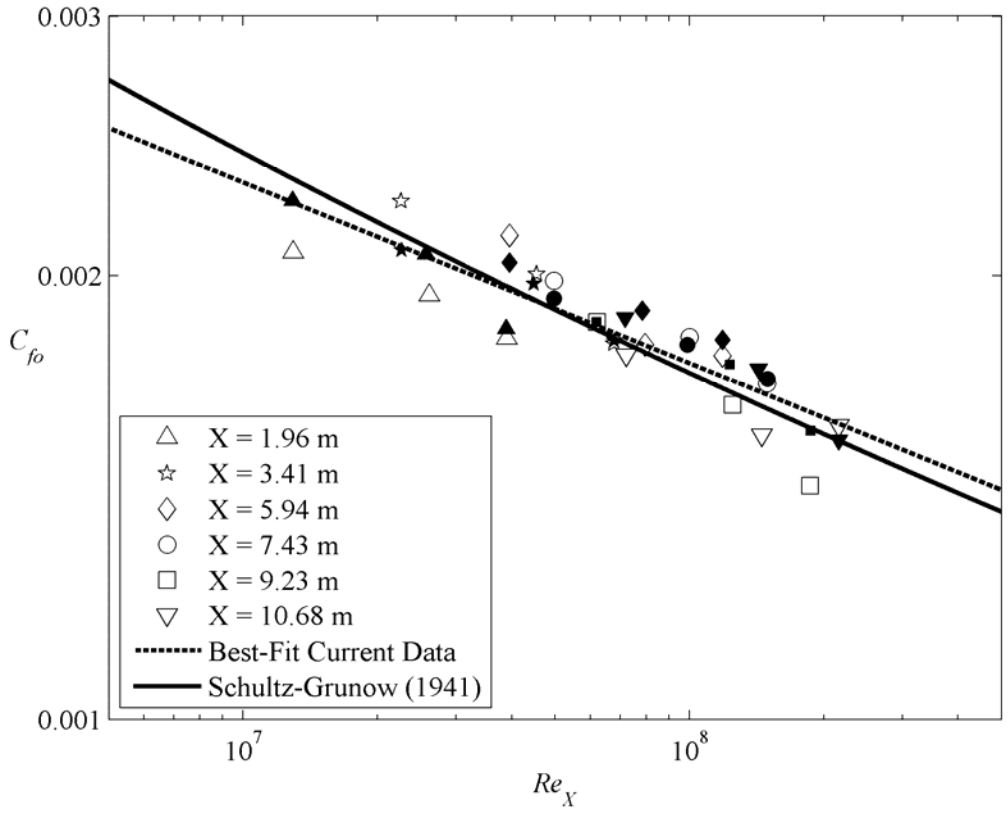

Figure 16. Baseline skin-friction results obtained from Test 1 (solid symbols) and Test 2 (outlined symbols) on the smooth model at each stream-wise measurement location at speeds from 6.7 to 20 m s^{-1}. Also shown are the best fit curves to the current data and the Schultz-Grunow (1941) flat plate skin-friction curve.

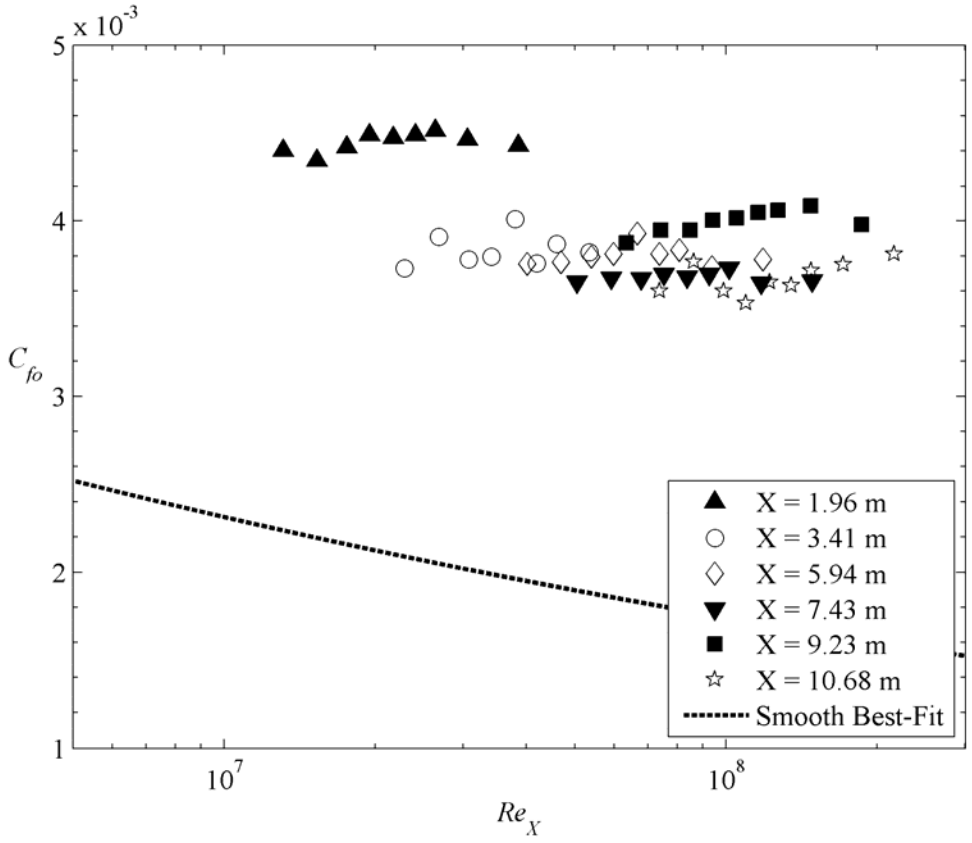

Figure 17. Baseline skin-friction results from Test 2 on the rough model at each stream-wise measurement location at speeds from 6.7 to 20.3 m s^{-1}. The Reynolds independence at each downstream location indicates that the model was fully rough. Also included for comparison is the best fit curve from the smooth data.

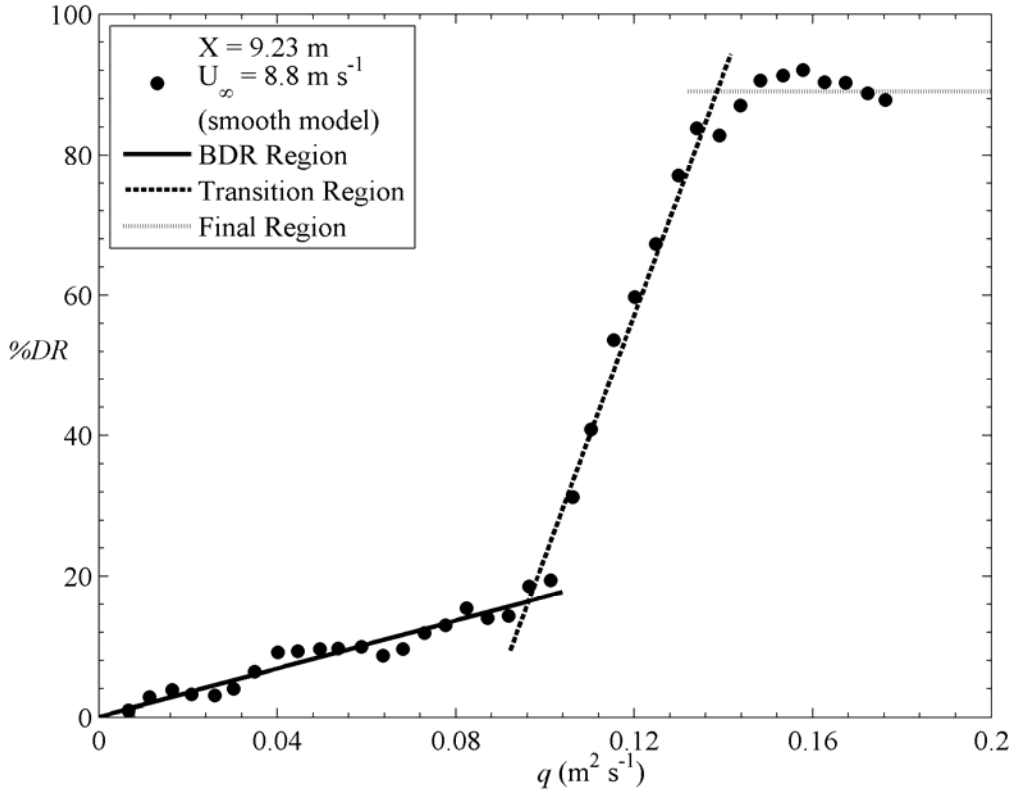

Figure 18. The three air injection drag reduction regions (BDR, transition and ALDR) illustrated with a typical graph of *%DR* versus the injection flux per unit span, q, at X = 9.23 m and $U_\infty = 8.8\ m\,s^{-1}$ on the smooth model.

Figure 19. Images recorded during Test 2 on the rough surface model at 6.8 $m s^{-1}$: (left) non-injection – surface clearly visible; (center) BDR – opaque cloud above surface; and (right) ALDR – semitransparent layer above surface. The stream-wise (right to left in images) and span-wise (top to bottom in images) directions of the model were observed by the video imaging system. (The same figure is included in Elbing *et al*., 2008).

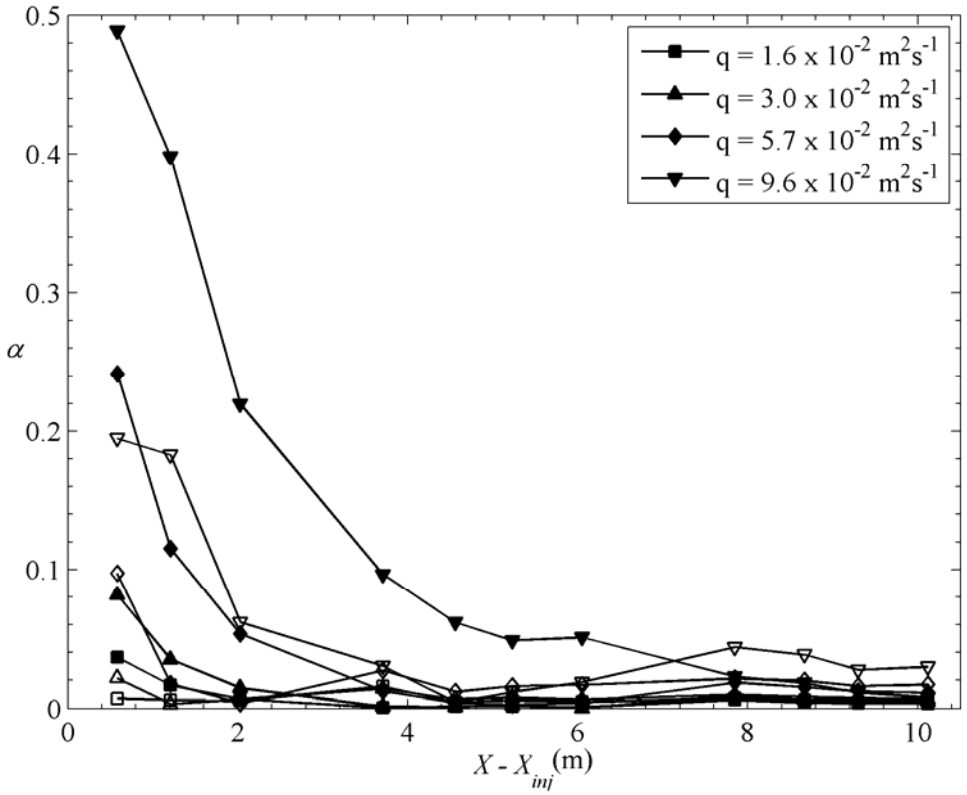

Figure 20. Near-wall void fraction versus downstream distance from the point of injection for 20.0 $m\,s^{-1}$. Solid symbols correspond to the large electrode spacing while the open symbols are for the small electrode spacing. The large spacing consistently shows higher void fractions indicating that void fraction is increasing with increasing distance from the surface.

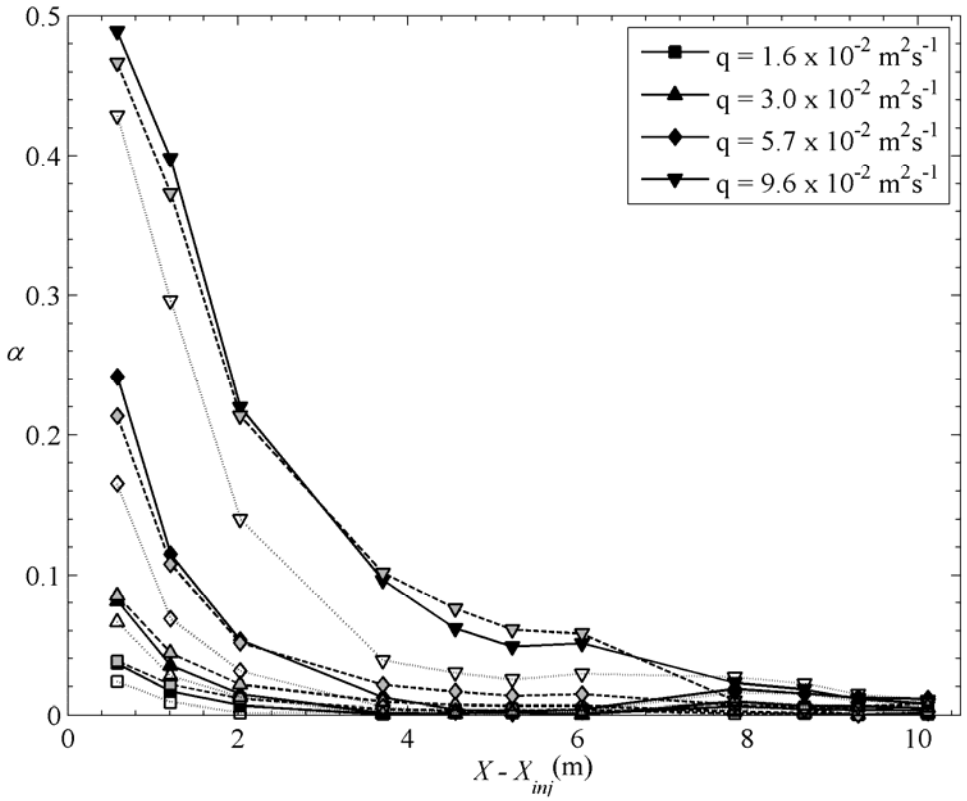

Figure 21. Near-wall void fraction determined from the large electrode spacing plotted versus downstream distance from the injector at 20.0 $m s^{-1}$. Solid symbols correspond to results with the porous plate injector (black and grey symbols correspond to injection into tunnel water and 15 wppm surfactant-laden water, respectively). Open symbols were injection with Slot A into a tunnel water background.

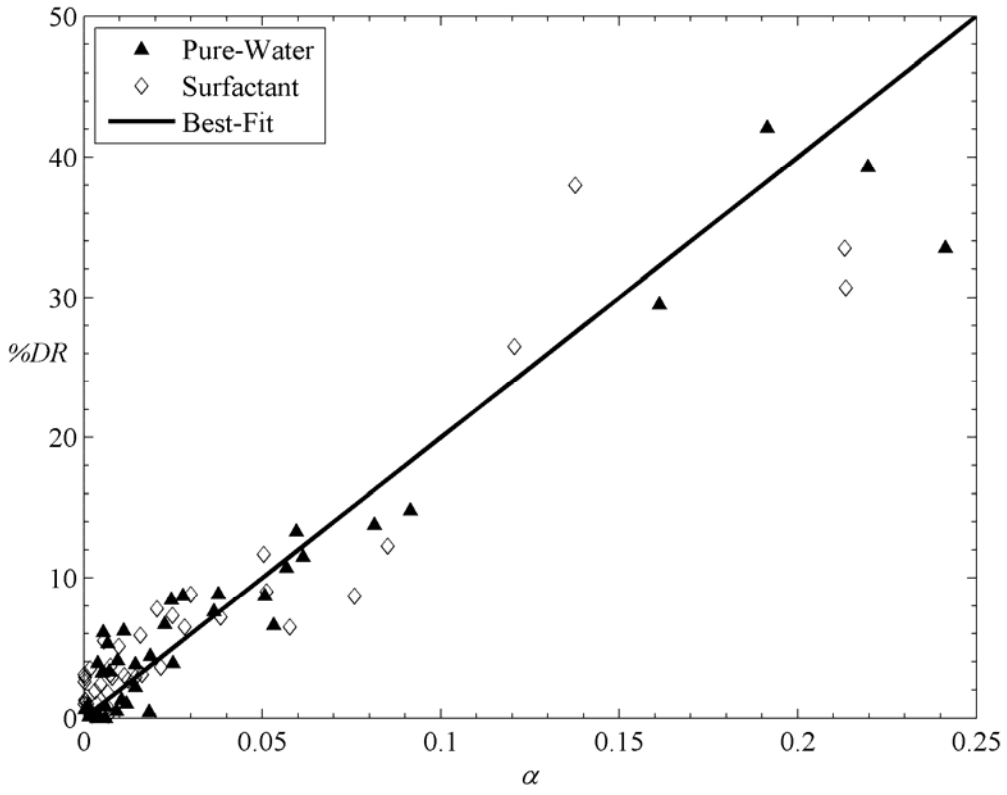

Figure 22. The percent drag reduction versus near-wall void fraction measured with surface electrical impedance probes using a porous plate injector with tunnel water or a 15 wppm surfactant-laden water background.

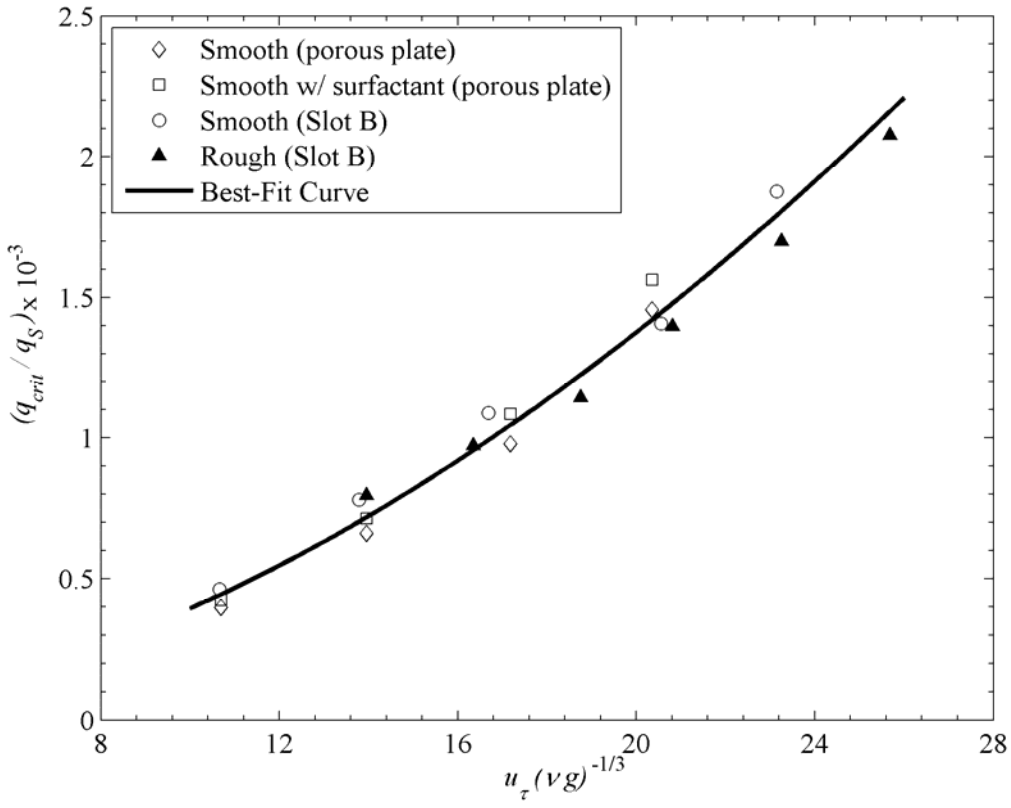

Figure 23. ALDR critical volumetric flux non-dimensionalized with the flux of fluid in the near-wall region scaled with the ratio of shear to buoyancy forces. Included are data from Elbing *et al*. (2008) with the porous plate injection into water or 15 wppm surfactant with a smooth surface, and slot injection into water with the surface smooth and fully rough.

REFERENCES

Bodgevich, V. G. & Evseev, A. R., 1976, "The distribution of skin friction in a turbulent boundary layer of water beyond the location of gas injection," *Investigations of Boundary Layer Control* (in Russian), Thermophysics Institute Publishing House, **62**.

Ceccio, S. L. & George, D. L., 1996, "A review of electrical impedance techniques for the measurement of multiphase flows," *Journal of Fluids Engineering*, **118**, 391-399.

Cho, J., Perlin, M. & Ceccio, S. L., 2005, "Measurement of near-wall stratified bubbly flows using electrical impedance," *Measurement Science and Technology*," **16**, 1021-1029.

Clark, H. & Deutsch, S., 1991, "Microbubble skin friction reduction on an axisymmetric body under the influence of applied axial pressure gradients," *Physics of Fluids* **A3**, 2948-2954.

Deutsch, S., Money, M., Fontaine, A. & Petrie, H., 2003, "Microbubble drag reduction in rough walled turbulent boundary layers," *Proceedings of the ASME-Fluids Engineering Division Summer Meeting* 2003, 1-9.

Elbing, B.R., Winkel, E.S., Lay, K.A., Ceccio, S.L., Dowling, D.R. & Perlin, M., 2008, "Bubble-induced skin-friction drag reduction and the abrupt transition to air-layer drag reduction," *Journal of Fluid Mechanics*, **612**, 201-236.

Etter R. J., Cutbirth, J. M., Ceccio, S. L., Dowling, D. R. & Perlin, M., 2005, "High Reynolds Number Experimentation in the U. S. Navy's William B. Morgan Large Cavitation Channel," *Measurement Science and Technology*, **16**(9), 1701-1709.

Fontaine, A. A. & Deutsch, S., 1992, "The influence of the type of gas on the reduction of skin friction drag by microbubble injection," *Experiments in Fluids* **13**, 128-136.

George D.L., Iyer, C.O. & Ceccio, S.L., 2000, "Measurement of the Bubbly Flow Beneath Partial Attached Cavities Using Electrical Impedance Probes," *Journal of Fluids Engineering*, **122**, 2000.

Hewitt, G.F., 1978, *Measurement of Two-Phase Flow Parameters*, Academic Press (London).

Kawakita, C. & Takano, S., 2000, "Microbubble skin friction reduction under the influence of pressure gradients and curved surfaces," *Journal of the Society of Naval Architects of Japan*, **188**, 11 – 21.

Kawamura, T., Moriguchi, Y., Kato, H., Kakugawa, A. & Kodama, Y., 2003, "Effect of bubble size on the microbubble drag reduction of a turbulent boundary layer," *Proceedings of the ASME Fluids Engineering Conference Summer Meeting* 2003, 1-8.

Kodama, Y., Kakugawa, A. & Takahashi, T., 1999, "Preliminary experiments on microbubbles for drag reduction using a long flat plate ship," *ONR Workshop on Gas Based Surface Ship Drag Reduction* (Newport, USA), 1-4.

Kodama, Y., Kakugawa, A., Takahashi, T. & Kawashima, H., 2000, "Experimental study on microbubbles and their applicability to ships for skin friction reduction," *Intl J. Heat Fluid Flow* **21**, 582–588.

Kodama, Y., Kakugawa, A., Takahashi, T., Nagaya, S. & Sugiyama, K., 2002, "Microbubbles: drag reduction mechanism and applicability to ships," *24th Symposium on Naval Hydrodynamics*, 1-19.

Kodama, Y., Hori, T., Kawashima, M. M. & Hinatsu, M., 2006, "A full scale microbubble experiment using a cement carrier," *European Drag Reduction and Flow Control Meeting*, Ischia, Italy, 1-2.

Lapham, G.S., Dowling, D.R. & Schultz, W.W., 1999, "In situ force-balance tensiometry," *Experiments in Fluids*,**27**, 157-166.

Lumley, J. L., 1973, "Drag reduction in turbulent flow by polymer additives," *J Polymer Science*, *Macromolecular Rev.*, **7**, 283–290.

Lumley, J. L., 1977, "Drag reduction in two phase and polymer flows," *Physics of Fluids* **20**, S64-S70.

Madavan, N. K., Deutsch, S. & Merkle, C. L., 1984a, "Reduction of turbulent skin friction by microbubbles," *Physics of Fluids* **27**, 356-363.

Madavan, N. K., Deutsch, S. & Merkle, C. L., 1984b, "Numerical investigation into the mechanisms of microbubble drag reduction," *ASME Journal of Fluids Engineering* **107**, 370-377.

Madavan, N. K., Deutsch, S. & Merkle, C. L., 1985, "Measurements of local skin friction in a microbubble modified turbulent boundary layer," *Journal of Fluid Mechanics* **156**, 237-256.

Maxwell, J., 1881, *A Treatise on Electricity and Magnetism*, Clarendon Press (Oxford, England).

McCormick, M. E. & Battacharyya, R., 1973, "Drag reduction of a submersible hull by electrolysis," *Naval Engineers Journal* **85**, 11-16.

Meng, J. C. S. & Uhlman, J. S., 1998, "Microbubble formation and splitting in a turbulent boundary layer for turbulence reduction," *Proceedings of the International Symposium on Seawater Drag Reduction*, 341-355.

Merkle, C. & Deutsch, S., 1990, "Drag reduction in liquid boundary layers by gas injection," Bushnell, D.M. and Hefner, J.N. (eds) *Viscous drag reduction in boundary layers, Progress in astronautics and aeronautics AIAA* **123**, 351-412.

Merkle, C. & Deutsch, S., 1992, "Microbubble drag reduction in liquid turbulent boundary layers," *Applied Mechanics Review* **45** (3), 103-127.

Nagamatsu, T. Kodama, T., Kakugawa, A., Takai, M., Murakami, K., Ishikawa., Kamiirisa, H., Ogiwara, S., Yoshida, Y., Suzuki, T., Toda, Y., Kato, H., Ikemoto, A., Yamatani, S., Imo, S. & Yamashita, K., 2002, "A full-scale experiment on microbubbles for skin friction reduction using SEIUN MARU Part 2: The full-scale experiment," *Journal of the Society of Naval Architects of Japan* **192**, 15-28.

Nagaya, S., Kakugawa, A., Kodama, Y. & Hishida, K., 2001, "PIV/LIF measurements on 2-D turbulent channel flow with microbubbles," *4th International Symposium on PIV*, Goettingen, Germany.

Pal, S., Deutsch, S. & Merkle, C. L., 1989, "A comparison of shear stress fluctuation statistics between microbubble modified and polymer modified turbulent flow," *Physics of Fluids* **A1**, 1360-1362.

Sabra, K.G., Winkel, E.S., Bourgoyne, D.A., Elbing, B.R., Ceccio, S.L., Perlin, M. & Dowling, D.R., 2007, "Using cross-correlations of turbulent flow-induced ambient vibrations to estimate the structural impulse response: Application to

structural health monitoring," *Journal of the Acoustical Society of America*, **121**(4), 1987-1995.

Sanders, W. C., Winkel, E. S., Dowling, D. R., Perlin, M. & Ceccio, S. L., 2006, "Bubble friction drag reduction in a high-Reynolds-number flat-plate turbulent boundary layer," *Journal of Fluid Mechanics*, **552**, 353-380.

Schultz-Grunow, F., 1941, "New frictional resistance law for smooth plates," *NACA* T M **17**, 1-24.

Shen, X., Perlin, M. & Ceccio, S. L., 2006, "Influence of bubble size on micro-bubble drag reduction," *Experiments in Fluids*, **41**, 415-424.

Takahashi, T., Kakugawa, A., Nagaya, S., Yanagihara, T. & Kodama, Y., 2001, "Mechanisms and scale effects of skin friction reduction by microbubbles," *Proceedings of the 2nd Symposium on the Smart Control of Turbulence*, University of Tokyo, 1-9.

Watanabe, O., Masuko, A. & Shirose, Y., 1998, "Measurements of drag reduction by microbubbles using very long ship models," *Journal of the Society of Naval Architects of Japan* **183**, 53-63.

White, F.M., 2006, *Viscous Fluid Flow*, 3rd Ed. (McGraw-Hill, New York), 430-438.

Winkel, E. S., Ceccio, S. L., Dowling, D. R. & Perlin, M., 2004, "Bubble size distributions produced by wall-injection of air into flowing freshwater, saltwater, and surfactant solutions," *Experiments in Fluids*, **37**, 802-810.

Winkel, E. S., 2007, "High Reynolds Number Flat Plate Turbulent Boundary Layer Measurements and Skin Friction Drag Reduction with Gas or Polymer Injection," *Doctoral thesis*, University of Michigan.

Winkel, E.S., Elbing, B.R., Ceccio, S.L., Perlin, M. & Dowling, D.R., 2008a "High-Reynolds-number turbulent-boundary-layer wall pressure fluctuations with skin-friction reduction by air injection," *Journal of the Acoustical Society of America*, **123**(5), 2522-2530.

Winkel, E.S., Oweis, G., Vanapalli, S.A., Dowling, D.R., Perlin, M., Solomon, M.J. & Ceccio, S.L., 2008b, "High Reynolds number turbulent boundary layer friction drag reduction from wall-injected polymer solutions," *Journal of Fluid Mechanics*, in press.

Wu, J. & Tulin, M.P., 1972, "Drag reduction by ejecting additive solutions into pure-water boundary layer," *Journal of Basic Engineering, Transactions of the ASME*, **94**, 749-756.

PART IV. EFFECT OF WALL ROUGHNESS ON POLYMER DRAG REDUCTION WITHIN A HIGH-REYNOLDS-NUMBER TURBULENT BOUNDARY LAYER

Chapter 9. Introduction

9.1 Abstract

This paper presents the findings from a large scale polymer drag reduction (PDR) study conducted at the US Navy's Large Cavitation Channel on a 12.9 m long flat plate model with the surface hydraulically smooth and fully rough. Testing was conducted at speeds to 20.1 $m s^{-1}$ and downstream distance based Reynolds numbers to 220 million. The current study extends the data set of Winkel *et al*. (2008b) with the same test model in the smooth surface configuration as well as extends the findings from Petrie *et al*. (2003) that studied the effect of surface roughness on PDR with a smaller model. The instrument suite included local skin-friction measurements at six stream-wise locations, peak polymer concentration at the wall, near-wall mean velocity profiles and sampling of the turbulent boundary layer (TBL).

Skin-friction measurements showed that the reduction in drag compared to the non-injection skin-friction supported the findings of Winkel *et al*. (2008b) that there is speed dependence in the results. Drag reduction results with the rough model showed a

slight improvement in drag reduction near the injector at low speeds (~6.7 $m s^{-1}$), but with increasing speed and downstream distance the level of drag reduction drastically drops compared to the smooth model results. At the top speed tested with the rough surface (20.0 $m s^{-1}$) no measureable level of drag reduction was observed at the first measurement location (0.56 m downstream of the injection location)! The significant drop in drag reduction with the surface roughness was shown to be partially influenced by increased diffusion, but the drop in drag reduction levels could not be fully accounted for by polymer diffusion based on intrinsic drag reduction estimates. By making estimates of the molecular weight *via* correlations between pressure drop apparatuses or a cone and plate rheometer results and molecular weight, sampling experiments on both the smooth and rough surfaces revealed that polymer degradation influences the performance of polymer solutions within the TBL. This approach accurately estimated the molecular weight of the non-injected solutions. For the highest speed on the rough model (20.0 $m s^{-1}$), 0.56 m downstream of the injector the molecular weight was less then one tenth the original molecular weight.

The estimated molecular weights (presented as intrinsic viscosity) were then scaled with a parameter dependent on the flow conditions (ξ) determined from the work of Vanapalli *et al*. (2006). This parameter successfully scaled the results from both the smooth- and rough-walled experiments. Three degradation regions in the flow were established from the results: (1) a flow condition below a critical ξ required for degradation, ξ_D, where the intrinsic viscosity (i.e. molecular weight) equals the original polymer solution; (2) a range of flow conditions ($\xi_D \leq \xi \leq \xi_\infty$) where the intrinsic viscosity

decreases linearly with ξ; and (3) flow conditions that produces values of ξ greater then ξ_∞, which results in the polymer solution having the same characteristics as the solvent (water in the current study).

Additionally, measurements of the near-wall mean velocity profiles with the smooth test model were combined with the drag reduction results to produce a relationship between the percentage of drag reduction (*%DR*) and the "effective slip" (S^+). Investigation of the literature showed that the relationship from the current study holds for results from other polymer or drag-reducing surfactants in channel, pipe or boundary layer flows. The combined results from current and previous studies are well approximated by $\%DR = 80\ [1 - \exp(-0.08\ S^+)]$, where $S^+ = U_p^+ - U_n^+$ and U^+ is the inner variable scaled speed of the (p) polymer and (n) Newtonian flows.

9.2 Background and Motivation

In nearly all transportation systems moving in a fluid, skin-friction drag is a major contributor to the total resistance and can constitute in excess of 60% of a ship's total resistance when the Froude number is on the order of 10^{-1}. Thus reduction of skin-friction in external flows is an ongoing research priority for fuel savings in marine transportation systems. As a result numerous research investigations spanning several decades have worked to reduce skin-friction by both active (e.g. gas or polymer injection) and passive (e.g. hydrophobic coatings) methods. The current study focuses on the active method of injecting dilute polymer solutions into a turbulent boundary layer (TBL). It has been known for over fifty years that the presence of high molecular weight polymers, even at

low concentrations (~10 weight-parts-per-million, wppm), in the near-wall region of a turbulent boundary layer flow can reduce the friction drag by as much as 70% compared to flow without polymer additives (see White & Mungal, 2008, for a recent review of polymer drag reduction).

Drag reduction with polymer additives have been used successfully in commercial applications that involve fluid flow in pipes or conduits (Sellin *et al*., 1982). These internal flow applications are better suited for polymer drag reduction (PDR) because once the solution is uniformly mixed no further dilution occurs, which results in sustained levels of high drag reduction in the absence of polymer degradation (use of lower molecular weight polymers are possible since they are less susceptible to degradation though the drag reduction efficiency is reduced). However, application of PDR to external flows does not have the advantages present in internal flows. The primary hindrance to PDR applications in external flows is the continual dilution of the injected solution (mixing and boundary layer growth), which requires use of large fluxes and/or high molecular weight polymer to maintain significant levels of drag reduction. The use of larger fluxes of polymer is not a desirable solution because the increased fluxes reduce the cost savings potential of PDR as well as requiring a larger amount of solution (or powder) carried by the ship (i.e. reduces the cargo or payload of the ship). As a result the use of relatively small fluxes of high molecular weight polymers has been pursued as a possible method of applying PDR to external flows. However, high molecular weight polymers are highly susceptible to degradation by chain scission (Patterson & Abernathy, 1970; Culter *et al*., 1975; Merrill & Horn, 1984), which effectively decreases the ability

of the polymer to reduce drag. To further complicate the problem, the majority of experiments have used hydraulically smooth surfaces, and both the dilution and degradation would presumably be accelerated with increased surface roughness.

Most experimental investigations of PDR with external TBL flows have focused on addressing the problems associated with continual dilution of the polymer solutions. These studies (Fruman & Tulin, 1976; Collin & Gorton, 1976; Gebel *et al*., 1978; Vdovin & Smolyakov, 1978 and 1981; Koskie & Tiederman, 1991; Brungart *et al*., 1991; Fontaine *et al*., 1992; Petrie & Fontaine, 1996; Petrie *et al*., 1996, 2003 and 2005; White *et al*., 2004; Winkel *et al*., 2008b) have been conducted over a wide range of scales, flow speeds, polymer solutions, injection conditions (concentrations and fluxes) and injection schemes. In general, these studies injected a polymer solution (typically a polyethylene oxide, PEO, solution) into a developed TBL through a slot or line source at the wall of the test model. Test parameters varied are typically the free-stream speed (U_∞), injection concentration (C_{inj}), injection volumetric flux per unit span (Q_{inj}) and the location downstream where drag reduction and/or polymer concentration are/is measured. There are three major drawbacks to most of these studies: (1) test models were typically on the order of one meter, which is two orders of magnitude smaller then a typical surface ship; (2) the influence of degradation on the results is typically ignored and most likely would not be observed due to the short test model length; and (3) the vast majority of studies only use hydraulically smooth surfaces (a ship surface would not by hydraulically smooth). Surface roughness increases turbulent intensity and shear rates (see Jiménez, 2004, for a recent review of turbulent flows over rough walls), which would most likely

result in increased diffusion and polymer degradation. There are a few studies in the literature that address some of these problems. Winkel *et al*. (2008b) studied PDR on the current test model, which is on the order of ten meters though only with the surface hydraulically smooth. Furthermore, while polymer degradation was never directly measured it was suggested that speed dependence in the drag reduction results was the product of polymer degradation and further supported with intrinsic drag reduction estimates. The one major exception to the studies of PDR on smooth surfaces is the work of Petrie *et al*. (2003). In that study a thorough investigation was reported of the drag reduction levels and corresponding concentration profiles with four surface conditions ranging from hydraulically smooth to fully rough. These experiments were conducted with a polymer ocean or slot-injected polymer into a developed boundary layer on the 0.76 m long test section tunnel wall. Their findings show that roughness can increase drag reduction levels in the region near the injector, but that the performance significantly diminishes with downstream distance and increased roughness. However, the influence of polymer degradation once again was not specifically investigated with this study and due to the small test section length the degradation effects, if any, would be less pronounced.

While degradation of polymer solutions within turbulent boundary layer flows have not been studied directly, polymer degradation has been widely studied since the first treatise of polymer chain scission by Frenkel (1944). Most early work on polymer degradation was performed with pipe flow apparatuses (Patterson & Abernathy, 1970; Culter *et al*., 1975; Sedov *et al*., 1979; Hunston & Zalkin, 1980; Merrill & Horn, 1984; Moussa & Tiu, 1994), but more recent work has been performed in rotational Taylor-

Couette flow devices (Kim *et al*., 2000; Nakken *et al*., 2001; Choi *et al*., 2002; Kalashnikov, 2002). From these studies it has been shown that polymer degradation is influenced by molecular weight, polymer concentration, solvent, turbulent intensity and flow geometry. The majority of studies to date have determined the dependence of polymer degradation on these parameters by assessing changes in either the friction factor or intrinsic viscosity. Only recently have there been studies where polymer degradation within turbulent flows have been quantified with measurements of the molar mass distributions *via* light scattering techniques (Vanapalli *et al*., 2005). Further review of the extensive polymer degradation literature is available in Moussa & Tiu (1994) and Vanapalli *et al*. (2005). The interested reader is referred to these studies for additional discussion. While much advancement in the understanding of polymer degradation has been achieved from these studies, to date the understanding has not been transferred to turbulent boundary layer flows. This is primarily due to the lack of direct measurements of the polymer rheology from samples taken from the TBL.

Thus within the literature there is a strong need for drag reduction, mixing and polymer degradation measurements from a high Reynolds number smooth- and rough-walled turbulent boundary layer modified with drag reducing polymer. The current study serves to bridge the gap between the small scale (on the order of one meter) rough surface study of Petrie *et al*. (2003) and a full scale surface ship (on the order of one hundred meters) as well as extend the data set from Winkel *et al*. (2008b) for measurement of PDR on a smooth test model at downstream distances on the order of ten meters. These results include direct measurement of the local skin-friction along the length of the model,

peak concentration at the wall and near-wall mean velocity profiles for the smooth model. Additionally, the first (to the author's knowledge) direct measurements of polymer degradation from a smooth- and rough-walled turbulent boundary layer are acquired.

Chapter 10. Experimentation

10.1 Test Facility

The experiments were conducted at the US Navy's William B. Morgan Large Cavitation Channel (LCC) in Memphis, TN. The LCC is the world's largest low-turbulence (free-stream turbulence < 0.5%) re-circulating water tunnel with a capacity of 5300 m^3 of water. The test section measures 13 m long with a 3.05 m square cross-section. Without a model in the test section flow speeds ranging from 0.5 to 18 $m\,s^{-1}$ can be achieved at absolute pressures ranging between 3.4 to 414 kPa. Additional LCC facility details can be found in Etter *et al*. (2005).

At the end of each day of testing the water was drained from the test section (i.e. the upper leg of the tunnel), but a complete tunnel drain and refill with fresh water was only performed approximately once per week of testing. At the start of the day air was scavenged from the tunnel for as long as an hour prior to data collection. If air remained in the free-stream following the air scavenge, deaeration was performed. A background chlorine concentration of 0.50 wppm was maintained throughout testing (exception during sampling experiments) to minimize the increase in background polymer and dye. During sampling experiments the entire tunnel was treated with sodium thiosulfate to remove background chlorine. Sampling tests were only performed once there were no

measureable levels of chlorine in the background water (ExStick CL200, Extech Instruments).

10.2 Test Model

The test model, herein termed HIPLATE (High-Reynolds-number, flat plate), was 12.9 m long, 3.05 m wide and 18 cm thick. This is the same test model used in the work of Sanders *et al.* (2006), Sabra *et al*. (2007), Elbing *et al*. (2008a), Winkel *et al*. (2008a) and Winkel *et al*. (2008b). The test model produced a 6% blockage in the test section which, coupled with boundary layer growth on the model and LCC walls, permitted free-stream speeds over 20 $m\,s^{-1}$. The leading edge was a 4:1 ellipse with a distributed roughness boundary layer trip starting 2.5 cm from the leading edge and extending 25 cm downstream. The roughness trip was made with 120 μm diameter sand grains (100 grit) loosely packed in an epoxy film. The model trailing edge was a 15° full angle truncated wedge. To minimize cavitation and stream-wise junction vortices at the model-sidewall intersections, 45° triangular-wedge edge-fairings were installed around the entire model. An inflatable seal was installed between the upper and lower surfaces to prevent bypass flow from the top and bottom of the model. Figure 24 shows a schematic of the HIPLATE with the instrument suite and injection location. The model was mounted slightly below the LCC test section centerline, spanned the entire test section width and had the working surface facing downward (schematically shown in figure 25). The coordinate system used throughout the paper has the X coordinate starting at the leading edge of the model and extending downstream in the flow direction, Y is zero at the model

surface and increases perpendicularly into the flow and Z extends in the span-wise direction and completes a right-handed coordinate system (see figure 24).

The test model was fitted with a single injector (schematic of injector cross section shown in figure 26) that spanned the center 2.65 m of the test model (87% of the model span) and was positioned 1.40 m downstream of the model leading edge. It was a slot-type injector inclined at a shallow 5.7° from the model surface and contracting at a full angle of 6.1°. The downstream edge was broken to give a convex downstream surface that produced a 15 mm opening on the test model surface in the stream-wise direction. This is the same injector used in Elbing *et al*. (2008) for Test 2. The polymer solution was delivered from a feed tank to a manifold that spanned 90% of the model width through 40 evenly spaced 12.8 mm diameter ports along the injector span. Within the manifold were three layers of baffles and porous brass screens to generate a pressure drop that would aid in even distribution of the polymer solution along the injector span. However, due to the viscoelastic properties of the polymer and the injector geometry this was insufficient to produce uniform injection of polymer into the TBL. This was remedied with the addition of porous material upstream of the injector surface opening in the contracting throat (see figure 26). This corrected the problem and, based on dye injection studies, produced span-wise uniform distribution of polymer into the boundary layer.

The model was tested with two surface conditions (hydraulically smooth and fully rough). The smooth model was made from polished 304 stainless steel having an average

roughness height, $k < 0.4$ μm, which makes k^+ less than unity at even the top speed tested. Here $k^+ = k / l_\nu$, l_ν ($= \nu / u_\tau$) is the viscous wall unit, ν is the kinematic viscosity of water, u_τ ($= \sqrt{\tau/\rho}$) is the friction velocity, τ is the wall shear stress and ρ is the fluid mass density. A surface is considered hydraulically smooth when $k^+ < 4$ (White, 2006), and therefore the current model was hydraulically smooth at all speeds tested. The only portion of the model in the smooth configuration that was not hydraulically smooth was the boundary layer trip at the leading edge, which was previously described.

The fully rough surface was produced with tightly packed glass bead grit having a diameter of 450 ± 250 μm in a film of epoxy paint (high build semi-gloss epoxy 97-130, Aquapon). The entire working surface, leading edge to start of the truncated wedge at the trailing edge, was covered with this roughness. The average roughness height was estimated to be approximately 450 μm ($90 < k^+ < 250$) over the first nine meters of the plate by measuring the surface profiles with a microscope. However, the last four meters of the model was not coated as uniformly resulting in approximately double the average roughness height. A second independent estimate of the average roughness height was made by assuming the surface was fully rough with sand-grain type roughness and using the baseline skin-friction coefficient curves (see figure 35). This assumption is supported by the lack of Reynolds number dependence in figure 35, and the surface is expected to be fully rough if $k^+ > 60$ (White, 2006). This method of estimation is presented in the baseline results section of the paper and table 4 provides the average roughness heights determined from the skin-friction measurements.

10.3 Instrumentation

10.3.1 Skin-friction balances

Local skin-friction measurements were made with floating-plate-type drag balances (schematically shown in figure 27) at six stream-wise locations (X = 1.96, 3.41, 5.94, 7.43, 9.23 and 10.68 m). The balances were originally designed by researchers at the Pennsylvania State University and slightly modified and fabricated in house. The floating plate is 15.2 cm in diameter, 0.79 cm thick and fabricated from 17-4PH stainless steel. The floating plate was fixed rigidly to a beryllium copper flexure that was instrumented with a full Wheatstone bridge of semiconductor strain gauges. The floating plate and housing were flush mounted using an eight point leveling system and had a 60 ± 20 μm annular gap. The strain gauges were excited using a Vishay signal-conditioning amplifier (Model 2310, Vishay). The sensor outputs were amplified and low-pass filtered at 10 Hz with the same Vishay unit. The output was sampled at 50 Hz via a data acquisition card (NI-DAQ, National Instruments) and LabView virtual instrument.

The balances were calibrated between zero and 9 or 15 N for the smooth and rough models, respectively. All calibrations were performed *in situ* by affixing a precision load cell (Model LCEB-5, Omega Engineering) on a linear traverse to the floating plate *via* a cable and suction cup or eyelet for the smooth or rough configuration, respectively. On the rough model floating plates an eyelet could be screwed into the center of the plate for the calibration (the hole was filled during testing). The precision load cell had been calibrated in the vertical position by hanging laboratory weights from it prior to use. The linear traverse was used to increase the tension on the cable and thus

on the floating plate. This setup has been shown to eliminate bias error caused by using pulleys and weights for the calibration (Elbing *et al*., 2008a). Typically five loads would be applied to each sensor for a single calibration and multiple calibrations were performed for each sensor to confirm the sensor stability, calibration repeatability and assess the overall uncertainties. Typical sensor uncertainty was approximately ± 5%.

The skin-friction sensors were used to directly measure the shear stress at the wall. Thus the percent drag reduction (*%DR*) could be determined from comparison between the skin-friction with and without the addition of the drag-reducing polymer solution. The definition of *%DR* is given by equation (10.1).

$$\%DR = \left(1 - \frac{\tau_w}{\tau_{wo}}\right) \times 100 \qquad (10.1)$$

Here τ_w and τ_{wo} are the wall shear stresses with and without injection of polymer, respectively. At each condition tested a minimum of 20 seconds at steady-state condition was used to determine the skin-friction. The steady-state condition was defined as a minimum of five seconds following the drop in skin-friction observed from the sensors; the time was extended, if necessary, until the sensor signal had become stable (small deviations from the mean). The extended length of time was required occasionally due to purging the injection lines at the start of a new batch of polymer. Each injection condition was repeated a minimum of three times and the baseline (non-injection) skin-friction was determined from a minimum of ten ramps from zero to the test free-stream speed.

10.3.2 Optical setup

The same optical setup (schematically shown in figure 28) was used to acquire near-wall concentration profiles with Planar Laser Induced Fluorescence (PLIF) and velocity profiles with Particle Image Velocimetry (PIV) measurements. This optical setup is the same used in Winkel *et al*. (2008b). PLIF and PIV measurements were made at three stream-wise locations (X-X_{inj} = 0.56, 4.54 and 9.28 m; where X_{inj} is the downstream distance from the leading edge of the model to the injection location). A plane in the flow was illuminated at each measurement location for both PLIF and PIV with a light sheet that was normal to the plate surface and aligned with the mean flow direction. A quartz window was installed in the model surface that allowed the light sheet to pass through the model surface and illuminate the image plane in the flow. The use of the quartz window also produced a mirrored image about the wall location in the collected images, which was used in the processing to precisely determine the wall location. The light sheet was formed from the beam of a pulsed New Wave Research Nd-YAG laser (station 1, Solo I; station 2, Solo 120XT; station 3, Gemini 200) operating at 532 nm wavelength with 15, 120 and 200 mJ at stations 1, 2 and 3, respectively. The beam (diameter of 3, 5 and 5.5 mm at station 1, 2 and 3, respectively) was expanded with a spherical lens, collimated with a second spherical lens and then the sheet was formed using a cylindrical lens. The sheet thickness was less than 100 μm at the test model surface for all three measurement stations. The sheet thickness was measured by passing the light sheet through the objective lens of a graded microscope and expanded across the tunnel test section onto a white screen, which made the laser sheet and grading clear. The illuminated plane was imaged with a high resolution CCD camera (Imager Pro, LaVision) by using a periscope

prism that protruded approximately 5 mm from the model surface and was positioned 5 cm in the span-wise direction from the light sheet and a 45° mirror. A converging (focal length = +75 mm) and a diverging (focal length = -300 mm) cylindrical lens was positioned between the prism and the CCD camera to allow stretching and focusing of the wall-normal direction. The high resolution camera (1200×1600 pixels) collected the stretched image of the illuminated plane. The camera was aligned such that the 1600 pixels were in the wall-normal direction, which along with the stretching increased the sensitivity for measuring the vertical velocity fluctuations and peak concentrations. Each camera was fitted with a 105 mm/f2.8 micro-Nikkor lens (Nikon) and two 2X teleconverters (TC-201, Nikon). The field of view (FOV) of the received image was nominally 5 mm (stream-wise) by 2.7 mm (wall-normal), which produced a nominal stretching ratio of 2.5:1. The spatial calibration was performed by imaging a precision test target that had 20 μm filled circles with 50 ± 0.02 μm center-to-center spacing. A LaVision PIV computer was used to control the laser, control the camera, adjust timing and record the images. The processing was then performed with DaVis software.

The near-wall mean flow velocity profiles were measured with PIV at the three optical measurement stations (X-X_{inj} = 0.56, 4.54 and 9.28 m). PIV measurements were made with both the smooth and rough surface conditions with and without polymer injection. However the increased viscous wall unit with the rough surface significantly limited the visible region of the boundary layer. During PIV testing the tunnel was flooded with tracer particles (titanium dioxide, J.T. Baker) having a nominal size of 1 μm and the image plane was illuminated with the laser sheet described above (now operating

in double-frame, double pulse mode). The only variation in the optical setup previously described was the addition of a blue optical bandpass filter with a peak transmission wavelength of approximately 532 nm between the stretching optics and the camera. This was implemented to minimize the amount of stray light (i.e. unwanted light or "noise") and only passed the 532 nm scattered light to the imager.

The PIV processing technique used is the traditional cross-correlation of two single-exposed images with multiple passes. Each pass reduced the interrogation window and had 50% overlap until the final interrogation window was 16×16 pixels, nominally 70 μm (stream-wise)×25 μm (wall-normal). The mean velocity profile in the wall normal direction was then determined from the mean of three profiles extracted from the mean scalar fields.

Polymer concentration profiles were measured in the near-wall region of the TBL with PLIF. Measurements were made at the three stream-wise located measurement stations. Each test was performed by mixing a known amount of fluorescent dye (Rhodamine 6G, Sigma Chemical) into the polymer solution to be injected. The polymer-dye solution was illuminated at the measurement location with the light sheet previously described. The light sheet would cause the dye laden polymer solution to fluoresce, which would then be imaged with the CCD camera. The optical filter used for the PIV measurements was replaced with a long-pass, orange optical filter that attenuated the 532 nm laser light and only passed the Stokes-shifted light (~590 nm) from the fluoresced dye to the camera.

The polymer concentration was determined by assuming the dye mixing is similar to the polymer mixing, and applying a calibration that related the intensity of the collected light by the imager to known dye concentrations. The calibration was performed with the use of a custom made calibration flow loop. The calibration flow loop consisted of a 5.1 cm (height) by 10.2 cm (width) by 25.4 cm (length) flow chamber, 0.12 m^3 reservoir, a 0.75 kW pump (A4C34FC21A, Performa) and tubing to connect the elements. The flow chamber had its surfaces blackened to prevent reflection of the laser light and would enclose the protruding prism and quartz window that provided optical access to the flow for the laser sheet (the upper side of the flow chamber was formed with the model working surface). Small quantities of the dye would be added to the flow loop and thoroughly mixed prior to acquiring 400 images with the camera. Each calibration used a minimum of ten dye concentrations and was repeated at least once.

10.3.3 TBL Sampling

To determine whether the injected polymer solutions were degraded from the turbulent flow a system was setup to draw samples from the TBL. The sampling experiments consisted of injecting dyed polymer solutions into the TBL and then drawing a sample from one of three downstream locations. The dye concentration was then determined with a spectrophotometer (1200, Cole-Parmer), which was used to determine the polymer concentration assuming the dye and polymer mixing are equivalent. A control (non-injected) sample was then prepared at the same concentration as the drawn sample. Both the test and control samples were analyzed in either a cone and plate

rheometer or one of two pressure drop apparatuses depending on the polymer concentration being tested.

Six sampling ports, schematically shown in figure 29, were positioned at three stream-wise locations (X = 1.96, 5.94 and 10.68 m). At each stream-wise location two ports were plumbed together within the test model and a single 2.54 cm inner diameter hose exited the model for sample collection. The sampling port was fabricated from an 11.4 cm diameter PVC disk and it was flush mounted on the test model working surface. A rectangular opening 5.6 cm (cross-stream) by 0.64 cm (stream-wise) was positioned at the center of the PVC disk and contacted the TBL. The corners of the port opening were rounded to minimize any sharp contractions that can cause polymer degradation. Each port had a 63.4 cm^3 cylindrical interior cavity that was fed from the rectangular opening and fed a 2.54 cm inner diameter hose. At each stream-wise position the 2.54 cm inner diameter hoses were connected with a wye pipe fitting that had the single exit line for sample collection.

The drawn samples were collected in a reservoir open to the atmosphere on the exterior of the tunnel. The flow rate was controlled by adjusting the tunnel static pressure and the height of the collection reservoir. A ball valve was fully opened once the skin-friction sensors showed that steady-state drag reduction had been achieved. A known volume of fluid was then purged from the lines and dumped into a waste bucket. Once the required purge volume was emptied, the test sample was collected. The collection was timed with a handheld stopwatch and weighed (SV-30, ACCULAB) to determine the

mass flow rate. Prior to testing, the sampling system was tested by gravity feeding samples through the port and no significant polymer degradation was observed at flow rates below 0.35 $kg\,s^{-1}$. This was used as the maximum allowable sampling rate during testing. The region of the boundary layer sampled was between 1.1 and 3.6 the flux of fluid in the near-wall region, Q_s, which corresponds to sampling from approximately $12 < Y^+ < 24$. Here the near-wall region corresponds to $0 < Y^+ < 11.6$, where Y^+ is the wall-normal distance scaled with inner variables. Since the influence that the polymer has on the flow occurs within the buffer region ($5 < Y^+ < 30$), the sampling rates fall within the range required to obtain the majority of the sample from this critical region of the flow.

While approximately 0.5 wppm chlorine was allowed to exist in the LCC background water during most testing, all chlorine was removed during sampling experiments. Chlorine was not removed during most testing to limit the build up of polymer and/or dye in the background water, but was removed for the sampling experiments since chlorine has been shown to degrade polymer solutions over time (Petrie *et al*., 2003). It was not a concern during non-sampling testing since the injected polymer solutions were only in contact with the background water for less than two seconds. However, during the sampling experiments the collected samples had been diluted with tunnel water and typically required approximately an hour of wait time between collection and characterization of the samples. The background chlorine was removed by adding sodium thiosulfate to the LCC background water until no measureable (ExStick CL200, Extech Instruments) level of chlorine remained. Petrie *et al*.

(2003) tested the effect that sodium thiosulfate residue and the products from its reaction with chlorine have on polymer drag reduction and found that its influence was negligible.

The accuracy of this approach is strongly influenced by the ability to precisely determine the polymer concentration of the drawn samples. Thus the polymer solution to be injected was carefully mixed with a known quantity of dye (Rhodamine 6G, Sigma Chemical) by slowly circulating the polymer-dye solution in a loop between the feed tank and the injection pump for over 20 minutes prior to testing to ensure a uniform dye concentration. Drag reduction results and estimates of the molecular weight from rheological analysis with and without performing this circulation are comparable. Thus it is assumed that this process was not responsible for any polymer degradation. The dye concentration of the drawn samples was determined with a spectrophotometer in absorption mode at 524 nm. Prior to injection a calibration curve was produced with dilutions of the injection stock solution with the mixed dyed. At least five concentrations were used to produce the spectrophotometer calibration curve, which spanned the entire operational range of the spectrophotometer (0 to ~14 wppm). Once the test sample was drawn it was measured in the spectrophotometer. Four separate measurements were obtained from each test sample and the average used to determine the dye concentration. Additionally, the sample was diluted in half and measured again to ensure that the results were self consistent. The spectrophotometer uncertainty was determined by taking known samples and testing at various concentrations and the results were typically within ±2% of the known concentration. Since according to Poreh & Hsu (1972) the molecular diffusivity of the polymer tested (POLYOX WSR301, Dow Chemical) is $O(10)^{-12}$ and the

turbulent diffusivity is $O(10)^{-8}$, it is assumed that the dye concentration of the drawn sample is directly proportional to the polymer concentration of the sample.

Once the polymer concentration of the test sample was determined, the control (non-injected) sample was prepared with the non-injected polymer solution and tunnel water. Prior to the injection approximately 18 kg of the dyed polymer solution to be injected was extracted from the injection feed tank for use in preparing control samples. The control sample was diluted to the test sample concentration with LCC tunnel water. Thus, any apparent change observed between the test and control samples would be from the polymer injection scheme, polymer sampling method and/or turbulent flow over the model. While the sampling port was tested separately for polymer degradation, the injection scheme was not tested due to time limitations. However, a sample collected from the smooth test model surface at the lowest test speed (6.7 $m s^{-1}$) from the furthest upstream sampling port (X-X_{inj} = 0.56 m) at the maximum injection rate revealed no significant degradation. These results are shown as viscosity versus shear rate in figure 30. The comparison between the test and control samples should be made at shear rates below the inertioelastic instability, which is marked by the rise in viscosity (~300 s^{-1}) following the steady decline in viscosity (shear thinning). The results for the test and control samples prior to the inertioelastic instability are nearly identical. This indicates that the sampling and injection schemes were not responsible for any significant degradation of the polymer solutions and any apparent change in the polymer performance at other test conditions was caused by the turbulent flow.

10.3.4 Rheological analysis

Rheological analysis was performed on the collected samples with either a pressure drop apparatus similar to that used in Virk (1975) or with a cone and plate rheometer. Additionally, rheological analysis of the stock polymer solution was performed to ensure that the polymer solution had not been degraded prior to use in the injection experiments.

The constant stress rheometer (AR-G2, TA Instruments) performed one of two types of tests on the collected samples depending on the sample polymer concentration. The rheometer required a minimum polymer concentration of 50 wppm to be used. The cone fixture measured 60 mm in diameter with 2.0° cone angle and 48 μm truncation. All tests were conducted at 25 °C and prior to data collection 45 seconds were allowed for the sample to reach a steady state condition. Once at steady state 45 seconds of data were collected. The first test was a characterization of the polymer shear viscosity over a broad range of applied shear stresses (0.1 – 10 Pa). This test measured the steady shear viscosity, shear-thinning and made an estimate of any elastic instability present. Any variation between a control and test sample would be indicative of degradation of the polymer sample, and thus this was the primary test performed. The second test was a fine characterization of the elastic instability, but this test could only be performed on samples with concentrations greater than 250 wppm. It was conducted over a much narrower range of stresses (2 to 8 Pa) than the broad characterization. Due to the reduced concentrations of the samples from the TBL this test was only performed on the stock solution batches.

One of two pressure drop apparatuses was used to characterize polymer samples that were at concentrations below the capability of the rheometer. A schematic of the generic pressure drop apparatus setup is shown in figure 31. The two setups had different diameters to increase the sensitivity depending on the polymer concentration of the sample being tested (i.e. smaller diameters increase the measurement sensitivity and reduce the dynamic range).

Both tubes were made from instrument grade stainless steel tubing with the inner diameter (ID) equal to 4.5 and 10.9 mm for the small and large tubes, respectively. Both setups consisted of three sections (entrance, test and end section), as illustrated in figure 31. The small tube entrance, test and end section lengths were 300 ID (1.35 m), 271 ID (1.22 m) and 30 ID (0.14 m), respectively. Similarly, the large tube had a 250 ID (2.73 m), 127 ID (1.38 m) and 30 ID (0.33 m) long entrance, test and end section lengths, respectively. Each test section was divided approximately in half with each half having a differential pressure transducer (216BPCLB, GP:50) connected between either the inlet or outlet and the midpoint.

The double pressure transducer setup for each tube was used to determine if degradation of the samples was occurring within the pressure drop setup. Figure 32 shows a typical comparison of the results obtained from both transducers with the large and small tubes. The results are plotted in the traditional Prandtl-von Kármán (PK) coordinates ($f^{-1/2}$ versus $Re_D f^{1/2}$). Here f is the Fanning friction factor defined in equation

(10.2), Re_D (= $U_{avg}D/v$) is the Reynolds number based on the tube diameter (D) and U_{avg} is the mean speed in the tube. The mean speed was obtained from the mass flow rate, which was determined by collecting the sample at the outlet in a reservoir on a scale (SV-30, Acculab) and recording the fill time with a handheld stop watch.

$$f = \frac{\tau}{\frac{1}{2}\rho U_{avg}^2} \qquad (10.2)$$

In the current study the wall shear stress was not directly measured, but f can be determined from the pressure drop along the measurement section of the pipe with the relationship given in equation (10.3).

$$f = \frac{D}{2\rho U_{avg}^2}\frac{\Delta p}{\Delta x} \qquad (10.3)$$

Here Δp is the measured pressure drop from the differential pressure transducer and Δx is the length of pipe over which the Δp was measured. These results reveal that minimal degradation occurred along the length of either tube over the range of flow rates tested. Included in figure 32 are the results obtained with pure water from both tubes, which are in good agreement with the friction-law for turbulent flow of a Newtonian fluid in a smooth, round pipe (commonly referred to as the PK law) that is given by equation (10.4). The maximum drag reduction (MDR) asymptote predicted by Virk *et al*. (1967) is also plotted in figure 32 and is given by equation (10.5).

$$\frac{1}{\sqrt{f}} = 4\log_{10}\left(\mathrm{Re}_D\sqrt{f}\right) - 0.4 \qquad (10.4)$$

$$\frac{1}{\sqrt{f}} = 19\log_{10}\left(\mathrm{Re}_D\sqrt{f}\right) - 32.4 \qquad (10.5)$$

Data from the pressure transducers were acquired with a data acquisition card (NI-DAQ, National Instruments) and recorded *via* a LabView virtual instrument. Each data point was typically determined from the average of 15 seconds of pressure difference data sampled at 50 Hz. The run time was increased for lower flow rates to increase accuracy of the mass flow rate measurement.

While the entrance length to achieve fully-developed pipe flow with Newtonian fluids is typically 60 to 80 ID, the substantial increase in the entrance length for the current setup was required because it is known that polymeric flows can increase the development length (Draad *et al*., 1998). The degree of extension is not well known and thus for the pressure drop tubes the entrance lengths were extended as far as space would permit. The matching of results from both pressure transducers, besides indicating that the setup was not causing degradation, also indicates that the entrance lengths were sufficient to produce fully-developed pipe flow at the measurement section. A flexible tube connected the entrance length to the pressure vessel that held the test sample prior to passing through the pipe. The vessel holding the test sample was pressurized with compressed nitrogen gas to approximately 120 kPa. This produced maximum average speeds of 3.0 and 1.8 $\mathrm{m\,s^{-1}}$ in the small and large tubes, respectively. The flow rate was

controlled with a gate valve positioned at the outlet of the end section prior to being dumped into a bucket through a second flexible tube.

10.3.5 LCC tunnel monitoring

The static pressure along the length of the model, the fluid velocity at a single point, the tunnel static pressure and the tunnel fluid temperature were monitored to aid in characterizing the boundary layer and for comparison with previous work. The static pressure along the length of the model was measured with a single differential pressure transducer (Model 230, Setra Systems). Eight stream-wise located pressure taps on the tunnel wall were used to measure the static pressure at X = 0.73, 1.96, 6.70, 7.93, 8.69, 9.92, 10.68 and 11.91 m. Each pressure tap had a 6.35 mm tube that fed into a single manifold that also had the pressure transducer attached. Ball valves were attached to each connection on the manifold, which allowed for manual switching between individual lines. The setup allowed differential pressure measurements to be made between any two pressure taps or between an individual pressure tap and atmosphere. At the start of each day of testing the lines were bled for at least 15 minutes and additional time would be allowed if air was observed in the lines.

A single point laser-Doppler-velocimetry (LDV) system described in Etter *et al*. (2005) was used to determine the velocity 6.2 cm upstream of the model leading edge and 23.6 cm below the model centerline. The close proximity of the measurement location to the leading edge of the model prevented a direct measurement of the free-stream velocity upstream of the model leading edge. A potential-flow analysis was performed around the

nose of the model to determine the upstream free-stream velocity and the free-stream velocity at the first static pressure tap (X = 0.73 m). The average of approximately 20,000 samples would be recorded with each test run to determine the average velocity at the measurement location. This measurement was used with the Bernoulli equation and static pressure measurements along the entire length of the model to determine the local free-stream velocity along the model length. Table 3 shows the free-stream speeds along the length of the smooth- and rough-walled models. The results from these measurements are in good agreement with results obtained from previous testing on the same model with free-stream speeds determined from direct LDV measurements along the length of the model.

The tunnel static pressure and temperature were also recorded simultaneously with the skin-friction measurements to monitor the LCC test section conditions. The tunnel static pressure measurement was used to correct for pressure sensitivity in the skin-friction sensors and the tunnel temperature was used to determine the temperature corrected water viscosity. Minimal temperature change was observed during testing with the exception of testing at the top speed (20 $m\,s^{-1}$).

10.4 Polymer Preparation and Metering

A single PEO polymer with a mean molecular weight, M_W, of 3.9 million (POLYOX WSR301, Dow Chemical) was tested. The structural unit for PEO polymer consists of carbon (C), hydrogen (H) and oxygen (O) molecules and is (-O-CH_2-CH_2-), which results in the polymer backbone consisting of (C-C) and (C-O) bonds. The carbon-

carbon and carbon-oxygen bond strengths and lengths are quite similar and thus the breaking (chain scission) of the backbones is approximately equally probable to be the breaking of a carbon-carbon or carbon-oxygen bond.

The polymer was supplied as a dry powder and mixed with water to produce the stock polymer solutions at a concentration of either 4000 or 6000 wppm. The polymer solution was prepared in a 4.6 m^3 mixing tank by slowly sprinkling the dry powder into a jet of water. The water jet was produced by passing filtered city water through a carbon filter (RT-2260-4, Aquapure Technologies) to remove the chlorine present. The mixing was performed only if no measureable level (Exstick CL200, Extech Instruments) of chlorine was observed in the supply line. The wetting of the dry polymer powder prior to contact with the free surface of the mixing tank was essential for the prevention of large polymer aggregates. The mixing tank was fitted with a 0.75 m diameter, 4-blade impeller that rotated at 30 RPM to promote mixing of the polymer solution. To prevent the formation of agglomerations additional mixing was performed with two small trolling motors that were positioned in the mixing tank near the free surface. The stock solution was stirred continuously until the solution appeared homogenous (one to three days). Then the stock solution was either transferred to a storage tank or to the injection system feed tank with a low shear-rate progressive cavity pump (1L8CDQAAA, Moyno). The stock solutions were monitored daily with the cone and plate rheometer. Figure 33 compares the results from a single batch of 4000 wppm stock solution between 16 and 104 hours after being mixed. Most batches were used within this range of time and

showed reduced scatter in the results. These characterizations confirmed the repeatability of the mixing process and the stability of the stock polymer solutions.

Once the stock polymer solution had been thoroughly mixed and sufficiently hydrated it was transferred from either the mixing or storage tank to the injection system feed tank. Fluorescent dye or tracer particles was/were added and thoroughly mixed in the feed tank dependent on whether concentration or velocity profiles were being acquired, respectively. If needed the stock polymer solutions were diluted to lower concentrations in the feed tank with the dechlorinated water line used to mix the stock solutions. The feed tank gravity fed a low shear-rate, stainless steel progressive cavity pump (2E012G1SSQAAA, Moyno) that was used to supply the prepared polymer solution to the injector manifold inlet (see figure 26). The feed tank was also used for monitoring the injection mass flow rate. This was achieved by anchoring a pressure transducer (PX437, Omega) at the bottom of the feed tank and calibrating the pressure with the volume of fluid in the tank. The output from the pressure transducer was recorded simultaneously with the skin-friction sensors at 50 Hz. The change in pressure signal with respect to time during injection testing was used to determine the injection mass flow rate. The desired flow rate for a given condition was set with a variable frequency drive controller (V74XP23P74, Yaskawa).

10.5 Test Matrix

Testing on the smooth model was conducted at free-stream speeds ranging from 6.7 to 20.1 $\mathrm{m\,s^{-1}}$ and measurements were made between X = 1.96 and 10.68 m. The

average temperature during testing with the smooth model was 26.1°C, which set the average kinematic viscosity of the water $\nu = 8.75\times10^{-7}$ m^2s^{-1} (processing of individual runs used the recorded tunnel water temperature). This produced downstream distance based Reynolds-numbers, Re_X $(=U_\infty X/\nu)$ of 1.5×10^7 to 2.5×10^8. The injection polymer concentration was either 4000 or 6000 wppm. The polymer injection rates were from 2 to 10 Q_s. Wu & Tulin (1972) determined $Q_s = 67.3\nu$ by assuming a linear velocity profile and integrating the stream-wise velocity.

Testing with the fully rough surface was conducted at free-stream speeds ranging from 3.2 to 20.0 $m\,s^{-1}$ and over the same range of downstream distances as the smooth model. The average water temperature during rough model testing was slightly lower at 25.3°C, which gave an average kinematic viscosity of the water, $\nu = 8.9\times10^{-7}$ m^2s^{-1}. Downstream distance based Reynolds-numbers from 7.0×10^6 to 2.4×10^8 were tested. Polymer injection concentrations were either 1000 or 4000 wppm with an injection rate between 2 and 10 Q_s.

For both the smooth and rough surfaces the skin-friction was measured at the six stream-wise located positions for all conditions. However, only a subset of conditions measured the near-wall polymer concentration profiles, near-wall mean velocity profiles and sampling of the boundary layer. The sampling tests were conducted at a single injection condition (4000 wppm solution injected at 10 Q_s) at speeds between 6.7 and 20.1 $m\,s^{-1}$ for both the smooth and rough surfaces. Collected samples from the smooth

surface were taken from X-X_{inj} = 0.56, 4.54 and 9.28 m, but the rough surface only was sampled from X-X_{inj} = 0.56 m.

Chapter 11. Results and Analysis

11.1 Baseline Results

11.1.1 Skin-friction

Figure 34 provides the baseline (non-injection) skin-friction coefficient results from two separate tests conducted on the HIPLATE model with the surface hydraulically smooth. Here $C_{fo}\,(=\tau_{wo}/0.5\rho U_{\infty}^{2})$ is the coefficient of friction without polymer injection. Also plotted with the smooth HIPLATE baseline results are the Schultz-Grunow (1941) friction curve given in equation (11.1) and the best-fit power-law curve provided by equation (11.2).

$$C_{fo} = 0.370\log^{-2.584}\left(\mathrm{Re}_{X}\right) \qquad (11.1)$$

$$C_{fo} = 0.0168\,\mathrm{Re}_{X}^{-0.123} \qquad (11.2)$$

The current results are in good agreement with the Schultz-Grunow (1941) friction curve. The slight deviation from the Schultz-Grunow (1941) friction curve is likely the product of a very mild pressure gradient present in the current experiment, and at lower Reynolds-numbers there could be residual effects from the boundary layer trip.

The baseline skin-friction results for the HIPLATE test model with the surface roughened are shown in figure 35. These results show that on the rough model at a fixed downstream location the friction coefficient is independent of Reynolds number. This indicates that the test model was fully rough since both White's and Schlichting's friction curves (provided in equations 11.3 and 11.4, respectively) for a fully rough flat plate (White, 2006) predicts that the coefficient of friction depends only on the average roughness height and downstream distance. By assuming that the roughness is a sand grain type roughness and that the model was fully rough, equations (11.3) and (11.4) can be used to estimate the average roughness of the model. Table 4 provides the average coefficient of friction for each measurement location and the average roughness height (k) determined from the average obtained from equations (11.3) and (11.4).

$$C_{fo} \approx \left[1.4 + 3.7 \log\left(\frac{X}{k}\right)\right]^{-2} \qquad (11.3)$$

$$C_{fo} \approx \left[2.87 + 1.58 \log\left(\frac{X}{k}\right)\right]^{-2.5} \qquad (11.4)$$

From table 4 it is apparent that the average roughness height was relatively uniform over the first nine meters of the test model and produced $k \sim 470 \pm 200$ μm. This estimate is in excellent agreement with direct measurement of the diameter of individual grit particles used to produce the roughness (average particle diameter = 450 ± 250 μm). However, further downstream the roughness level appears to be approximately double that of the upstream section of the model, which indicates that the downstream roughness was not applied as uniformly as the upstream section. This observation from the skin-friction

measurements is consistent with a visual examination of the surface-embedded particles upstream and downstream of approximately X = 9 m. Table 5 provides estimated friction velocities ($u_\tau = \sqrt{\tau_{wo}/\rho}$) and viscous wall units ($l_v = \nu/u_\tau$) for the rough model over the range of speeds tested with the roughened surface, which was determined from the mean coefficient of friction along the model length.

11.1.2 Mean velocity profiles

The near-wall mean velocity profiles were measured at the three downstream optical measurement stations (X-X_{inj} = 0.56, 4.54 and 9.28 m) at free-stream speeds of 6.7 and 20.1 m s^{-1} for the smooth surface condition. Measurements were also made with the rough surface configuration but the FOV prevented viewing the log-region, which is of interest for drag reduction results. Thus only the smooth model results are included in the discussion. Figure 36 shows the results from all the measurements made on the smooth model and the results in the log region collapse on a curve having the form of equation (11.5) with κ = 0.40 and B = 5.0.

$$U^+ = \frac{1}{\kappa} Ln\left(Y^+\right) + B \qquad (11.5)$$

Here U^+ is the mean velocity (U) scaled with the friction velocity. The smooth model results are primarily in the log region, but measurements at 6.7 m s^{-1} were able to capture the buffer region almost to the viscous sublayer. Equation (11.5) with κ = 0.40 and B =

5.0 is used subsequently when comparing the drag reduced results to the Newtonian (i.e. zero drag reduction) results.

11.2 Drag Reduction

It is useful to introduce a common scaling parameter (K) at the start of the drag reduction discussion since it has been used by numerous researchers (Vdovin & Smol'yakov, 1978 and 1981; Fontaine *et al*., 1992; Petrie *et al*., 2003; White & Mungal, 2008; Winkel *et al*., 2008b) over the years to assess the performance of polymer solutions in TBL flows. The K-parameter (defined by equation 11.6) was first proposed by Vdovin & Smol'yakov (1978) and is the flux of polymer injected into the boundary layer scaled with downstream distance from the point of injection and the flow speed (i.e. approximately a ratio of injection polymer flux to fluid flux). It has been used to scale results of both percent drag reduction and peak concentration at the wall.

$$K = \frac{Q_{inj} C_{inj}}{U_{\infty}\left(X - X_{inj}\right)} 10^{-6} \qquad (11.6)$$

Here Q_{inj} is the volumetric flux of polymer per unit span injected and C_{inj} is the injection concentration in wppm. It is important to note that K is not a universal scaling, but only a useful tool in assessing global trends in the results. Thus the current drag reduction results from the smooth surface condition are plotted in figure 37 versus K along with previous results from the same test model (Winkel *et al*., 2008b). The smooth model results of Winkel *et al*. (2008b) are used frequently in the current paper since only a small

subset of conditions were repeated on the smooth surface to validate comparison between the data sets. While the data set is quite limited, similar trends are observed with the current study and Winkel *et al*. (2008b). A peak in drag reduction occurs at approximately $K \sim 10^{-7}$ and the results appear to have speed dependence (i.e. decreasing drag reduction with increasing speed). The speed dependence was unexpected since previous studies in the literature have not observed such an apparent effect; it is addressed subsequently. Included in figure 37 are the best-fit curves to the results for each speed between the peak drag reduction point and the point where the drag reduction drops to approximately ten (this region corresponds approximately to the intermediate diffusion zone that is discussed subsequently).

Measurements of the near-wall mean velocity profiles showed the well known trend of an upward shift in the log region proportional to the drag reduction. Figure 38 shows the results from three injection conditions and the upward shift in the log layer is apparent. Included in the plot is the viscous sublayer ($U^+ = Y^+$), the Newtonian log region (equation 11.5 with $\kappa = 0.40$ and $B = 5.0$) and the ultimate profile that was first proposed by Virk *et al*. (1970). The equation for the ultimate profile is given by equation (11.7). The ultimate profile limits the extent that the log region can shift upward and the current results are in excellent agreement with this limit.

$$U^+ = 11.7 Ln\left(Y^+\right) - 17.0 \qquad (11.7)$$

The upward shift in the log region has been termed the effective slip (S^+) and is defined as the difference in scaled velocity with and without polymer (= $U_p^+ - U_n^+$). Here U_p^+ and U_n^+ are the inner variable scaled stream-wise velocity with the polymer solution (i.e. with the reduced drag) and without the polymer (i.e. the Newtonian results with κ = 0.40 and B = 5.0) at a fixed Y^+, respectively. Shown in figure 39 is the percent drag reduction as a function of the effective slip. The current results are in good agreement with previous work with various polymer solutions or surfactants in channel, pipe or boundary layer flows (White *et al*., 2004; Fontaine *et al*., 1992; Wei & Willmarth, 1992; Warholic *et al*., 1999a; Warholic *et al*., 1999b; Petrie *et al*., 2005; Koskie & Tiederman, 1991; pipe flow data compiled by Virk, 1975). A best-fit curve to the current and compiled sources was made with the assumption that at zero *%DR* the effective slip is also zero and as the effective slip approaches infinity the percent drag reduction must remain finite and less then 100. With these assumptions the best-fit curve provided by equation (11.8) was obtained and is included in figure 39.

$$\%DR = 80\left[1 - \exp\left(-0.08S^+\right)\right] \qquad (11.8)$$

The rough model drag reduction results are now compared with the smooth model results (figure 37) as well as findings from previous PDR work on rough surfaces (Petrie *et al*., 2003). Figure 40 once again uses the K parameter to "scale" the drag reduction results. Included in the plot are the rough surface data, smooth model speed dependent best-fit curves to the intermediate-zone and results reported in Petrie *et al*. (2003) with a 60-grit sandpaper surface. The Petrie *et al*. (2003) 60-grit sandpaper roughness was

selected because, like HIPLATE, that roughness was sufficient at the speeds tested for their test model surface to be considered fully rough. These results support the findings from Petrie *et al*. (2003) that near the point of injection (right side of the plot) the presence of roughness can improve drag reduction (likely caused by a reduced initial-zone, which corresponds to a region prior to peak in drag reduction). However, it is also apparent that the improvement does not persist downstream (to the left on the plot). Both Petrie *et al*. (2003) and the current study fail to observe any measureable drag reduction over a decade earlier than with the smooth model. Furthermore, at the top speed tested (solid triangles, 20 $\mathrm{m\,s^{-1}}$) no measureable drag reduction was observed at the first measurement location (X-X_{inj} = 0.56 m). It should be noted that while negative drag reduction was observed with the rough model these findings are within the uncertainty of the measurement (±5%). Some of the reduced performance of the polymer solutions is the result of increased diffusion from the near-wall region (where the drag reduction mechanism is active, Dubief *et al*., 2004), and the following will assess if diffusion alone could be responsible for the significantly diminished PDR performance.

11.3 Polymer Diffusion

To assess the role of diffusion on the current results, the maximum concentration (C_M) in the near-wall region is plotted versus K. Figure 41 shows the results from the rough HIPLATE model and findings from Winkel *et al*. (2008b) with the smooth model. The concentration results from the current study were acquired only in the final-zone (left side of the plot) and were in excellent agreement with the findings of Winkel *et al*. (2008b). Also shown in the plot are the best-fit curves for the initial ($K^{0.2}$), intermediate

($K^{2.7}$) and final ($K^{6/7}$) diffusion zones as determined from several studies (Fruman & Tulin, 1976; Vdovin & Smol'yakov, 1978; Vdovin & Smol'yakov, 1981; Fontaine *et al.*, 1992; Winkel *et al*., 2008b) compiled in Winkel *et al*. (2008b). The initial-zone is characterized by a thin sheet of high concentrated polymer near the surface and is typically limited to tens of centimeters downstream of the point of injection. The engineering of PDR with injection schemes is limited to this region of diffusion. Preliminary findings from a recent study (Elbing *et al*., 2008b) indicate that the maximum extension of this region is only on the order of one meter, and results from Petrie *et al*. (2003) indicate that the length is inversely proportional to the surface average roughness height. The intermediate diffusion zone is the region over which the thin highly concentrated layer of polymer is initially broken into filaments and eventually diffused through the boundary layer thickness. The length of this region should be on the order of ten boundary layer thicknesses. The final-zone is the region where the polymer has been diffused throughout the boundary layer and any further dilution is the product of fluid entrainment from boundary layer growth. Only the scaling of the final-zone is well known since the concentration profile in that region is well established and the dilution scales with the boundary layer growth (i.e. $K^{6/7}$ is determined from boundary layer growth with a $1/7^{th}$ power-law velocity profile). The relationships for the intermediate- and initial-zones are much more sensitive to flow conditions (i.e. the intermediate is sensitive to the boundary layer thickness and turbulence intensity and the initial-zone is sensitive to the injection condition and surface roughness). Thus the proper scaling remains unclear. However, the results compiled in Winkel *et al*. (2008b) follow the general trend of the curves shown in figure 41 with a significant amount of scatter.

The rough model results shown in figure 41 appear to be entirely in the final-zone with a slope close to that observed on the smooth model in the final region. These results indicate that the roughness significantly shortens (or possibly eliminates) the development length and the expected increased velocity fluctuations enhance the transition to the final-zone. Unfortunately with the limited data set it is difficult to definitively state much about the diffusion process since all the results are within the final-zone. It is important to note that no results are included from the first measurement station (X-X_{inj} = 0.56 m). This is due to the dye concentrations selected causing the results from the PLIF to be saturated at the first measurement station. This is unfortunate since the concentration at this location would have offered significantly more insight into the diffusion process with roughness as well as provide a better understanding of the reduced PDR performance near the injector.

11.4 Intrinsic Drag Reduction

The above results indicate that diffusion most likely plays a significant role in reducing the downstream persistence of PDR by shortening the initial and transition diffusion zones. However, to determine if diffusion is the primary contributor a comparison between smooth and rough model results of *%DR* versus near-wall peak concentration is required. This comparison can be done with the use of an empirical drag reduction curve (given by equation 11.9) first proposed by Virk *et al*. (1967) that provides a relationship between the polymer concentration and the percent drag reduction for a given polymer solution. For a given polymer type and molecular weight there are

two properties, intrinsic drag reduction ([*%DR*]) and intrinsic concentration ([*C*]), that determine the drag reduction performance of the solution. The concept of intrinsic drag reduction and intrinsic concentration has been used successfully in several research efforts (Little & Patterson, 1974; Choi & Jhon, 1996; Winkel *et al*., 2008b) to describe the behavior of a given solution. Thus it is used in the current study to estimate if the expected *%DR* for the measured maximum concentration was achieved. If the expected *%DR* from the intrinsic drag reduction matches the measured *%DR* then the reduced performance with the surface roughness would primarily be from diffusion of the polymer solution away from the near-wall region.. First, an accurate estimate of the intrinsic drag reduction and intrinsic concentration for the polymer solution tested (WSR301 with a water solvent) is needed to make use of equation (11.9). Fortunately, Winkel *et al*. (2008b) used the same solution and provided a speed dependent range for both properties: $17 \leq [\%DR] \leq 32$ wppm^{-1} and $2 \leq [C] \leq 3$ wppm. The product of the intrinsic drag reduction and intrinsic concentration gives the maximum drag reduction the polymer can achieve.

$$\frac{\%DR}{C_M} = \frac{[C][\%DR]}{[C] + C_M} \qquad (11.9)$$

Figure 42 shows the curves obtained for WSR301 in Winkel *et al*. (2008b) for the three speeds. The current results show that for most of the cases the expected drag reduction was not achieved and that the results fell farther below the expected curves with increasing speed and increasing distance from the injection location. This indicates that the molecular weight of the polymer solution must be changing between different

speeds and downstream distances since the intrinsic drag reduction and intrinsic concentration should remain constant for a given polymer solution at a single mean molecular weight. This observation indicates that polymer degradation by scission of the polymer chains is taking place (i.e. the molecular weight of the polymer solution is being reduced by the turbulent flow). The speed dependence observed in Winkel *et al*. (2008b) was also suspected to be caused by polymer degradation by chain-scission. However, no direct measurement of the polymer rheology was available to conclusively determine if chain scission was responsible.

11.5 Polymer Degradation

The sampling experiments conducted in the current study were attempts at making a quantitative measurement of the polymer solution rheology within a TBL. Sampling was performed on both the smooth and rough surface conditions with a single injection condition (C_{inj} = 4000 wppm, Q_{inj} = 10 Q_s). Results from the smooth model at U_∞ = 6.7 m s^{-1} were already shown (see figure 30), and no measureable amount of degradation was observed. However, the remainder of the smooth model results and all the rough model results showed varying degrees of degradation (i.e. deviations from the control sample). Results from the pressure drop apparatus for the three conditions tested (X-X_{inj} = 0.56 m at 6.8, 13.6 and 20.0 m s^{-1}) on the rough model are shown in figure 43. For the rough model the samples were drawn from the model surface as previously described and then diluted to approximately 10 wppm so that they could all be tested in the same pressure drop apparatus (only the small pressure drop apparatus was available at that point in testing). The drag reducing potential of a polymer sample is determined by

the onset shear stress (point where the curve intersects the Newtonian turbulent pipe flow curve) and the slope of the curve after it diverges from the Newtonian turbulent pipe flow curve. The smaller the onset shear stress (i.e. the smaller $Re_D f^{1/2}$ at the point where the polymer results diverge from the Newtonian curve) and the steeper the slope following the onset of drag reduction, the more efficient the polymer solution is at reducing drag (i.e. the higher the molecular weight is for a given polymer type). If the test and control sample had not been physically altered they would be identical when tested in the pressure drop apparatus. However, inspection of figure 43 reveals that significant deviation from the control sample is observed at all three speeds tested. This gives strong evidence that the physical structure of the polymer chains had been altered by the turbulent flow. Since *%DR* is most sensitive to molecular weight, it is highly likely that this reduction in performance is the result of a decrease in the molecular weight of the test samples (i.e. chain scission of the polymer).

It is possible to relate the sampling results to parameters directly proportional to the length of the polymer chain. For samples tested in the pressure drop apparatuses this is done by first determining the intersection of the polymeric results with the Newtonian curve. This determines the drag reduction onset condition (i.e. the minimum shear stress required for drag reduction). The intersection of the two curves give f^* and Re_D^*, which are the onset of drag reduction Fanning friction factor and the onset of drag reduction pipe diameter based Reynolds number. From the definition of the Fanning friction factor and the definition of shear stress a relationship between the onset shear rate (γ^*) and the onset Fanning friction factor is produced and given by equation (11.10).

$$\gamma^* = \frac{1}{2}\frac{U_{avg}^2}{\nu} f^* \qquad (11.10)$$

Vanapalli *et al*. (2005) produced a relationship from data compiled in Virk (1975) for PEO polymer solutions between the minimum shear rate for drag reduction, γ^*, and the solution molecular weight. This relationship is provided in equation (11.11).

$$\gamma^* = \left(3.35 \times 10^9\right) M_W^{-1} \qquad (11.11)$$

While the above relationship has been able to relate the pressure drop apparatus results to the molecular weight, one additional step is performed to present the findings in a form more common in the literature. The use of intrinsic viscosity ($[\eta]$) as a measure of the polymer rheology has been used widely (Virk *et al*., 1967; Little & Patterson, 1974; Virk, 1975; Wei & Willmarth, 1992; Choi & Jhon, 1996; Kalashnikov, 1998), and thus the current results are presented in this form. The intrinsic viscosity is related to the molecular weight by using the Mark-Houwink relationship that is provided in Bailey & Callard (1959) and shown in equation (11.12).

$$[\eta] = 0.01248 M_W^{0.78} \qquad (11.12)$$

Furthermore the use of intrinsic viscosity as a measure of molecular weight is convenient for assessing the sampling results from the cone and plate rheometer. The intrinsic viscosity by definition is a ratio of the viscosity at zero shear and infinite shear and is given by equation (11.13). Here C is the sample concentration and ν_o and ν_∞ are the polymer kinematic viscosity at zero shear and infinite shear, respectively. The viscosity of the solvent (i.e. water) was used as the viscosity at infinite shear and the zero shear viscosity was estimated from the rheometer results.

$$[\eta] \equiv \frac{1}{C}\left(\frac{\nu_o - \nu_\infty}{\nu_\infty}\right) \qquad (11.13)$$

Results from the control samples measured with either the pressure drop apparatus or the rheometer gave the non-degraded WSR301 an intrinsic viscosity, $[\eta] = 1730 \pm 200$, which is within the range of previous studies using PEO solutions at similar molecular weights (Shin, 1965, $[\eta] = 1650$; Castro, 1966, $[\eta] = 1500$; Virk *et al*., 1967, $[\eta] = 2010$; McNally, 1968, $[\eta] = 1590$; Kalashnikov & Tsiklauri, 1996, $[\eta] = 2500$). Table 6 compiles the results for both the smooth and rough sampling experiments and shows that degradation was occurring on both the smooth- and rough-walled model.

Vanapalli *et al*. (2006) proposed a universal scaling for polymer chain scission in turbulence, which is used here to assess the importance of flow parameters from the current sampling experiment. In that work Vanapalli *et al*. argued that the maximum force on a polymer chain (F_{max}) within a turbulent flow should follow the relationship provided in equation (11.14).

$$F_{\max} = A^{3/2} \frac{\pi \rho \nu^2 \,\mathrm{Re}^{3/2} L^2}{4 d^2 \ln(L/a)} \qquad (11.14)$$

Here A is a geometrical proportionality constant, a is the diameter of the polymer chain, d is a length scale associated with bulk fluid flow and L is the contour length of the polymer chain. Thus the longer the polymer chain (i.e. the higher the molecular weight) the greater the force applied to the chain and the more likely the chain will scission. In the current study the natural log of the ratio of contour length to polymer chain diameter varies only slightly and thus it is ignored. The contour length is directly proportional to the molecular weight (based on the definition of contour length) and therefore $L^{0.78} \propto [\eta]$. Here it is conjectured that the maximum force on the chain will be proportional to the wall shear stress since for the current study the solution is being sampled from the buffer region. In the work of Vanapalli *et al*. (2006) the pipe diameter was used for the bulk fluid flow scale, but such a length scale is not so readily available for the current work. The first thought would be to use the boundary layer thickness, but near the injection location this would significantly over estimate the flow influence of the polymer solution. Thus a measure of the diffusion length (d_λ) is required. Near the injector the length scale would be significantly less then the boundary layer thickness, but far downstream it

should coincide with the boundary layer thickness. Thus d_λ was scaled with the form given by equation (11.15). The -1/5th power on the Reynolds number was selected based on baseline LDV measurements of the boundary layer provided in Sanders *et al*. (2006). Also of note is that based on static pressure measurements along the length of the model the boundary layer thickness of the rough model should be approximately 1.5 times that of the smooth model. Thus in the following scaling the rough model diffusion length was increased by a factor of 1.5.

$$d_\lambda = \varepsilon\left(X - X_{inj}\right)\mathrm{Re}_X^{-1/5} \qquad (11.15)$$

Here ε is a proportionality constant for comparison between the smooth and rough boundary layers. For the smooth-walled condition ε is unity and for the rough-walled condition ε is 1.5 (based on the rough-walled boundary layer thickness being approximately 1.5 times larger than the smooth-walled TBL). With the above mentioned relationships equation (11.14) can be rearranged to produce equation (11.16). Furthermore the intrinsic viscosity should be linearly related to ξ.

$$[\eta] \propto \xi = \left[u_\tau \frac{d_\lambda}{\nu} \mathrm{Re}_X^{-3/4} \right]^{0.78} \qquad (11.16)$$

The sampling results scaled with the above relationship are shown in figure 44. This scaling successfully collapses results from both the smooth- and rough-walled models. Thus the selection of the diffusion length scale was properly selected. The

collapse of the data appears to be linear as predicted. Thus in turbulent boundary layer flow if the flow condition is such that ξ is below some critical value, ξ_D (approximately 0.035 in the current analysis), then the polymer solution remains non-degraded (i.e. the intrinsic viscosity remains constant at a value equal to the stock solution). Once the flow conditions are such that ξ_D is exceeded the polymer chains begin to break (i.e. the polymer degrades and the intrinsic viscosity decreases). The decrease in intrinsic viscosity is linearly related to ξ and will continue to decrease until $[\eta] = 0$, at this point a second critical ξ value is reached, ξ_∞. For flow conditions greater or equal to ξ_∞ the polymer solution is degraded such that the solution behavior is equivalent to the solvent (i.e. from the definition of the intrinsic viscosity at zero the viscosity at zero and infinite shear are identical and equal to the solvent viscosity).

Chapter 12. Summary and Conclusions

Several conclusions can be drawn from the current PDR study conducted on a 12.9 m long flat plate test model with the surface hydraulically smooth and fully rough at downstream-distance based Reynolds numbers to 2×10^8. The baseline (non-injection) results for both the skin-friction and near-wall mean velocity profiles are in good agreement with past work. The smooth model friction curve is approximated well by the Schultz-Grunow (1941) friction curve. The rough model friction curve is independent of Reynolds number at a fixed downstream location, which indicates that the model has a fully rough surface condition. Only measurements of the near-wall mean velocity profiles from the smooth surface model are included due to the FOV for the measurements. The FOV for the smooth model was able to accurately measure velocities in the buffer and log regions of the boundary layer. The log region was well approximated by $U^+ = 2.5\ln(Y^+) + 5.0$.

Drag reduction results for the smooth model determined from direct measurement with the skin-friction balances agree well with the findings of Winkel *et al*. (2008b), which was used as the primary data set for smooth surface results. The smooth results from Winkel *et al*. (2008b) and the current study are speed dependent with drag reduction decreasing as speed is increased, which in Winkel *et al*. (2008b) was believed to be from

polymer degradation by chain scission. Mean velocity profiles with the drag reduced flow showed an upward shift, termed effective slip (S^+), from the Newtonian (non-injection) results in the log region. This effective slip increased with increased drag reduction. The percent drag reduction as a function of the effective slip was compared with previous studies that used either polymer or surfactants to reduce the drag in channel, pipe or boundary layer flows. The combined results showed excellent agreement and was well approximated by $\%DR = 80\ [1 - \exp(-0.08\ S^+)]$.

The drag reduction with the fully rough surface condition showed a slight improvement in drag reduction levels near the injector. The improved performance near the injector is probably due to the shortening of the initial-zone where the drag reduction levels were suppressed on the smooth model, but this region of the flow was not investigated. Regardless, the improvement is limited to within the first meter downstream of the injector at lower speeds. With increased speed or downstream distance the performance drastically decreases in comparison to the smooth results. These findings are in agreement with the work of Petrie *et al*. (2003) on a fully rough surface test model. At the highest speed tested on the HIPLATE (20.0 ms^{-1}) no measureable drag reduction was observed even at the first measurement location (X-X_{inj} = 0.56 m).

The diffusion of polymer solutions within the turbulent boundary layer was studied with measurements of the peak polymer concentration at the wall for both the smooth and rough surface conditions. This was done to determine whether the reduced performance in the drag reduction results was only the product of increased diffusion

from the wall. The smooth model results were only from a select few conditions, but agreed with the findings of Winkel *et al*. (2008b). The rough model results showed good agreement with the smooth model results in the final diffusion zone. However, all the results from the rough model appear to be in the final diffusion zone, which indicates that the initial-zone had been shortened (or possibly eliminated) and the intermediate-zone was also shortened (due to increased turbulent intensity). These findings support the possibility that the reduced performance is at least partially caused by increased diffusion away from the wall relative to the smooth surface condition. However, use of the concept of intrinsic drag reduction (Virk *et al*., 1967) for the rough model results indicate that for the measured concentration the expected drag reduction levels were still not achieved in most cases. This indicates that the molecular weight of the polymer solution had changed (i.e. the polymer was degraded by scission of the polymer chain), which was further supported by the observation that the decrease in expected performance was greater with increased speed and downstream distance.

A direct measurement of polymer degradation was made by collecting samples from the TBL at various downstream locations for both the smooth and rough surface conditions. The sampling method was shown to not be responsible for the degrading of the polymer solutions with a collection at low speed (6.7 $m s^{-1}$) from the first measurement location (X-X_{inj} = 0.56 m), which showed no apparent decrease in molecular weight from the non-injected solution. All other measurements from both the smooth and rough surface conditions showed varying degrees of degradation of the polymer solutions. Combining the work of Vanapalli *et al*. (2005), Virk (1975) and the Mark-Houwink

relationship provided by Bailey & Callard (1959) the pressure drop apparatus results were related to intrinsic viscosity (i.e. a common measure related to the molecular weight of a solution). Additionally, the rheometer results provided an estimate of the zero shear viscosity of the solution, which was used to estimate the intrinsic viscosity. The control samples showed reasonable agreement with previous work using PEO solutions at similar molecular weight ($[\eta] = 1730$). The results from the test samples conclusively show that degradation of the polymer solutions by chain scission has a significant impact on the drag reduction results. In the extreme case, the intrinsic viscosity of the sample collected 0.56 m downstream of the injection location with the rough-walled surface at 20.0 $\mathrm{m\,s^{-1}}$ was only 0.15 of the non-degraded intrinsic viscosity (i.e. the molecular weight was ~0.1 of the non-degraded WSR301 molecular weight).

Finally, a new parameter, ξ, was formed by reworking the scaling introduced by Vanapalli *et al*. (2006) for chain scission of homogeneous polymer solutions in internal turbulent flows. The new parameter is dependent on the flow conditions and distance from the injection location. This parameter was used successfully to scale results from both the smooth- and rough- walled results. The intrinsic viscosity as predicted by Vanapalli *et al*. (2006) is approximately linear with respect to ξ. Furthermore, three degradation regions in the flow can be established from the results: (1) Flow conditions below a critical ξ required for degradation, ξ_D, where the intrinsic viscosity (i.e. molecular weight) equals the original polymer solution; (2) a range of flow conditions ($\xi_D \leq \xi \leq \xi_\infty$) where the intrinsic viscosity decreases linearly with ξ; and (3) flow conditions that

produce values of ξ greater then ξ_∞, which result in the polymer solution having the same characteristics as the solvent (i.e. the intrinsic viscosity equals zero).

TABLES AND FIGURES

X (m)	1.96	3.41	5.94	7.43	9.23	10.68
Smooth Model U_∞ ($m\,s^{-1}$)						
6.68	6.62	6.62	6.65	6.68	6.73	6.77
8.79	8.71	8.72	8.76	8.79	8.85	8.90
10.8	10.7	10.7	10.7	10.8	10.9	10.9
15.3	15.1	15.2	15.2	15.3	15.4	15.4
13.5	13.3	13.4	13.4	13.5	13.5	13.6
20.1	19.9	19.9	20.0	20.1	20.2	20.3
Rough Model U_∞ ($m\,s^{-1}$)						
6.75	6.66	6.67	6.72	6.76	6.82	6.88
7.92	7.81	7.83	7.88	7.93	7.99	8.06
9.08	8.96	8.98	9.04	9.09	9.16	9.23
10.1	9.94	9.97	10.0	10.1	10.2	10.3
11.3	11.1	11.1	11.2	11.3	11.4	11.5
12.4	12.3	12.3	12.4	12.5	12.6	12.7
13.6	13.4	13.5	13.6	13.6	13.7	13.8
15.8	15.6	15.7	15.8	15.9	16.0	16.1
20.0	19.7	19.8	19.9	20.0	20.2	20.3

Table 3. Free-stream speed along the length of smooth- and rough-walled models determined from static pressure measurements. The average speeds along the length of the model are in bold.

X (m)	1.96	3.41	5.94	7.43	9.23	10.68
$C_{fo} \times 10^3$	4.5	3.9	3.8	3.7	4.0	3.7
k (μm)	400	350	550	580	1100	830

Table 4. Average roughness height on the rough model determined from the average C_{fo} at each downstream distance.

U_∞ (m s^{-1})	6.8	7.9	9.1	10.1	11.3	12.4
u_τ (m s^{-1})	0.30	0.35	0.40	0.45	0.50	0.55
l_v (μm)	3.3	2.8	2.5	2.2	2.0	1.8

Table 5. Friction velocities and viscous wall units determined from skin-friction measurements near the injection location.

Model	U_∞ (m s^{-1})	X-X_{inj} (m)	$\%DR$	u_τ (m s^{-1})	M_W ($\times 10^6$)	[η]
Smooth	6.6	0.56	57	0.15	4.1	1780
Smooth	6.7	4.54	63	0.13	1.6	840
Smooth	6.8	9.28	56	0.13	1.3	740
Smooth	13.3	0.56	54	0.29	3.3	1520
Smooth	13.4	4.54	50	0.29	0.9	570
Smooth	13.6	9.28	40	0.30	0.7	420
Rough	6.7	0.56	65	0.19	2.4	1190
Rough	13.4	0.56	22	0.56	1.3	720
Rough	19.7	0.56	-1	0.93	0.4	260

Table 6. Test sample intrinsic viscosities from the smooth- and rough-walled models and the corresponding flow conditions. A single injection condition was used for these tests (C_{inj} = 4000 wppm, Q_{inj} = 10 Q_s). All samples except the smooth model result at 6.6 m s^{-1} from X-X_{inj} = 0.56 m were degraded relative to the control (non-injected) samples, which had a mean [η] = 1730.

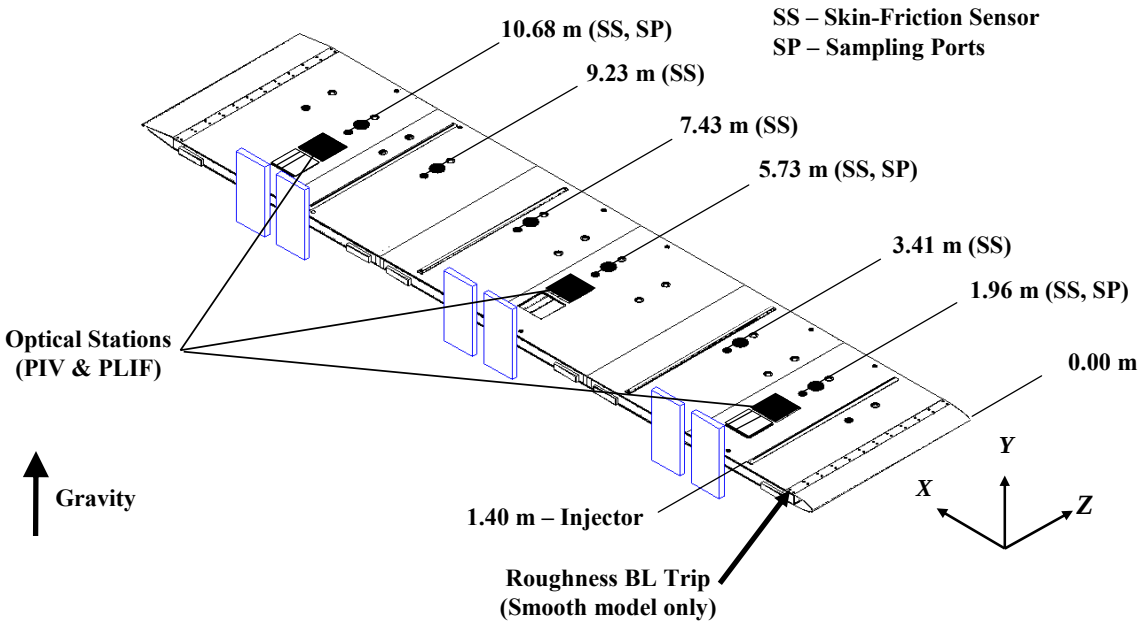

Figure 24. HIPLATE test model schematic showing the instrument suite and injection location. The model had three primary measurement locations (X = 1.96, 5.73 and 10.68 m) where skin-friction, near-wall velocity, near-wall polymer concentration and sampling of the boundary layer were possible.

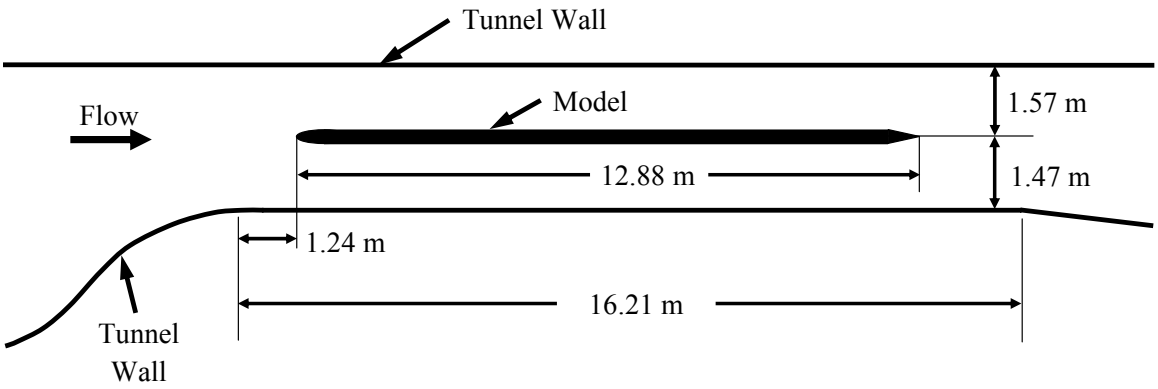

Figure 25. Schematic of the HIPLATE mounted in the LCC test section with gravity and the working surface downward.

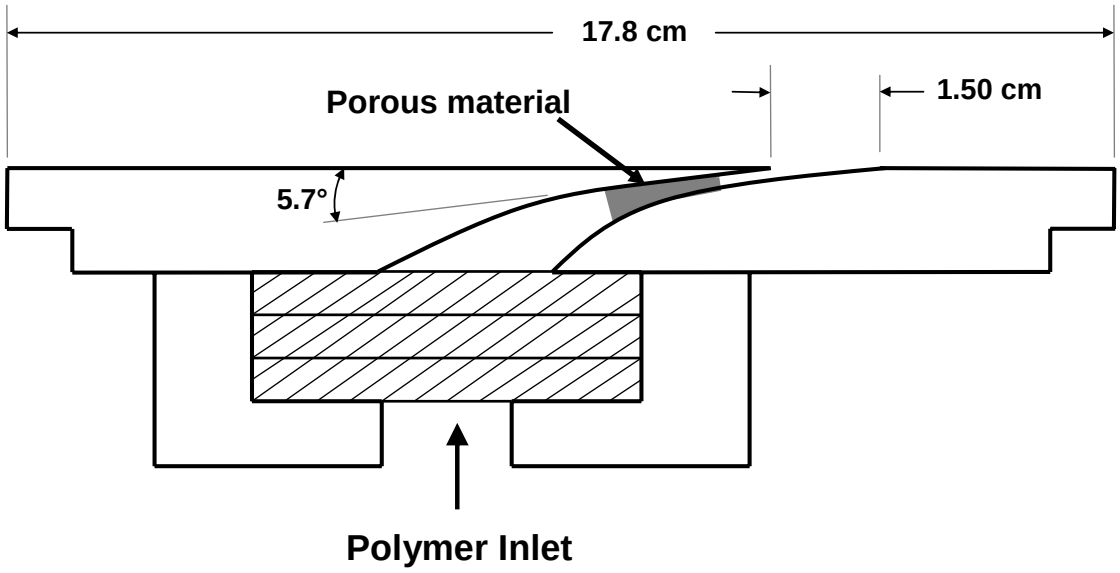

Figure 26. Cross-sectional schematic of the slot injector. The polymer solution was delivered to the manifold through 40 evenly spaced ports along the injector span. Three layers of baffles and screens in addition to the porous material in the injector throat created a pressure drop that evenly distributed the polymer along the injector span.

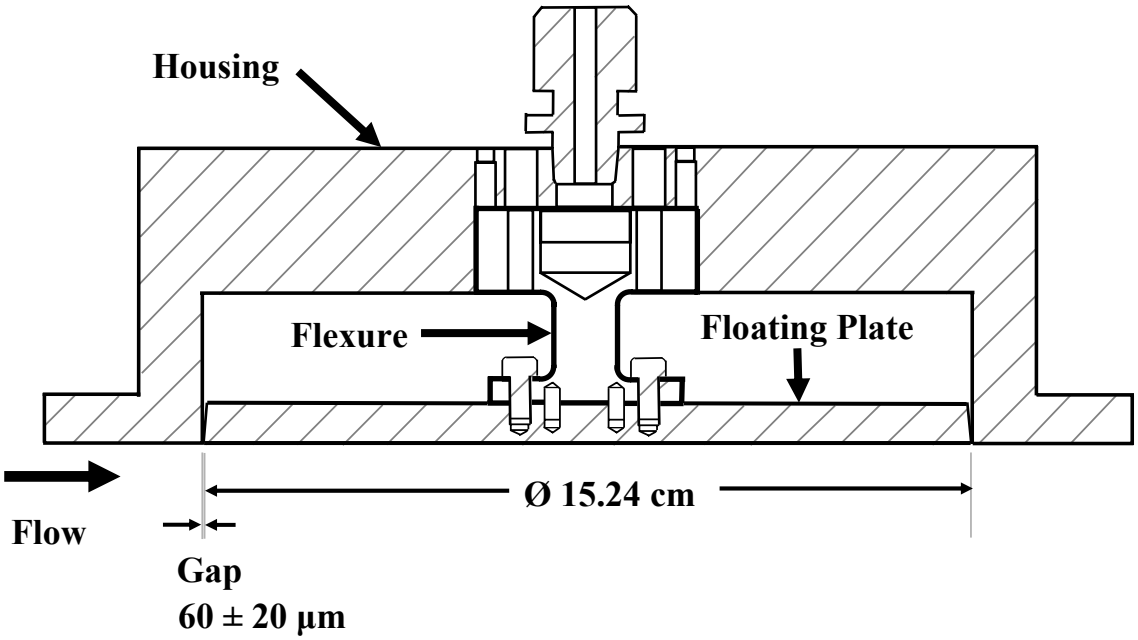

Figure 27. Cross sectional schematic of a skin-friction balance with floating plate, flexure and housing.

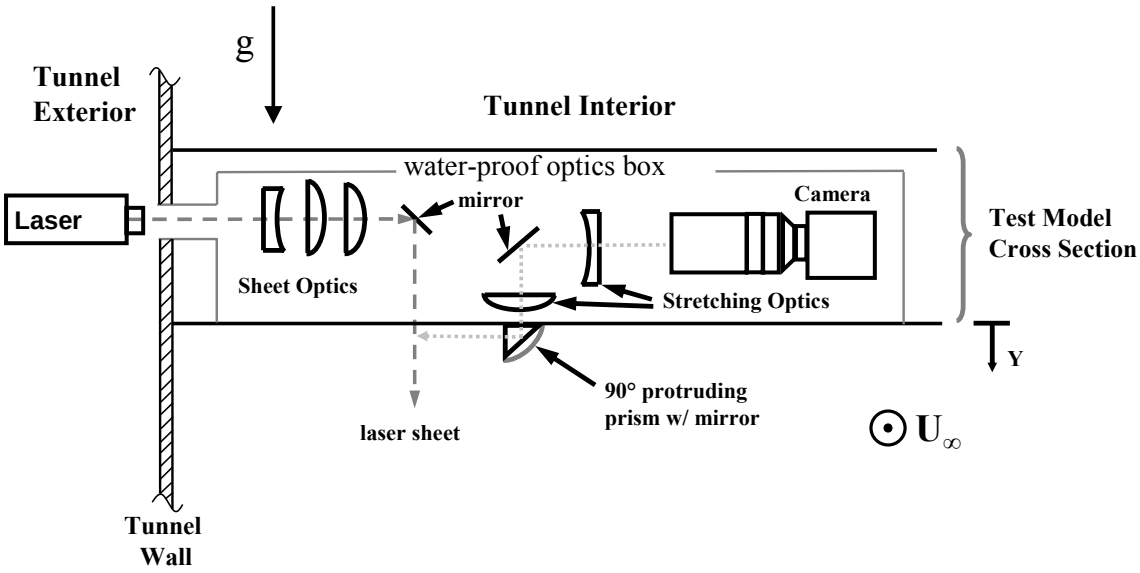

Figure 28. Optical setup used to measure near-wall concentration and velocity profiles.

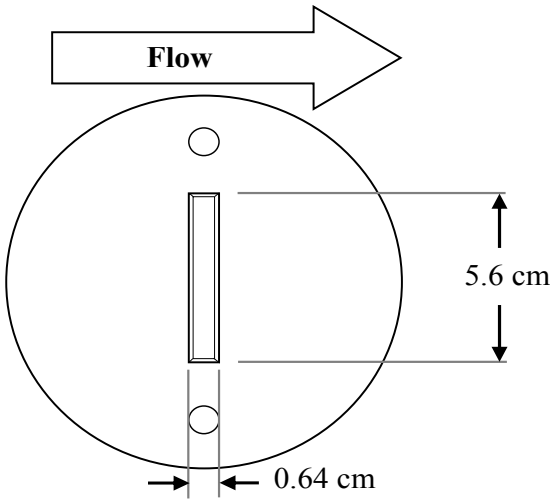

Figure 29. Schematic of one of the sampling ports that were flush mounted on the model surface and used to draw samples from the boundary layer.

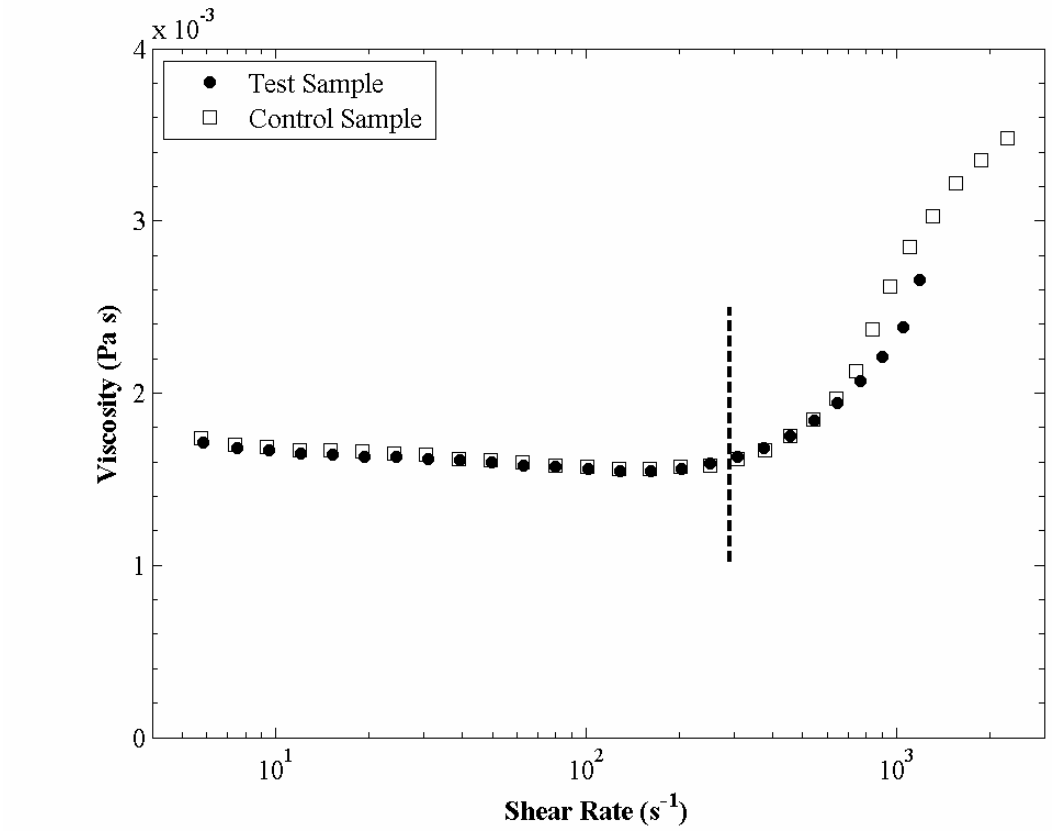

Figure 30. The test sample was drawn from X-X_{inj} = 0.56 m on the smooth model at a free-stream speed of 6.7 m s^{-1}. The polymer solution had a concentration of 4000 wppm and was injected at 10 Q_s. The test and control samples had a polymer concentration of ~350 wppm. The dashed line corresponds to the approximate location of the inertioelastic instability.

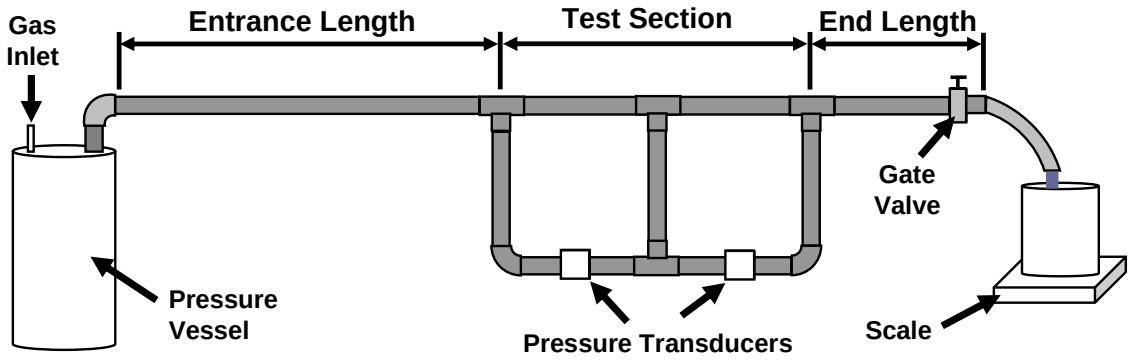

Figure 31. Generic setup for the pressure drop apparatuses used to characterize polymer samples at concentrations insufficient for testing with the cone and plate rheometer.

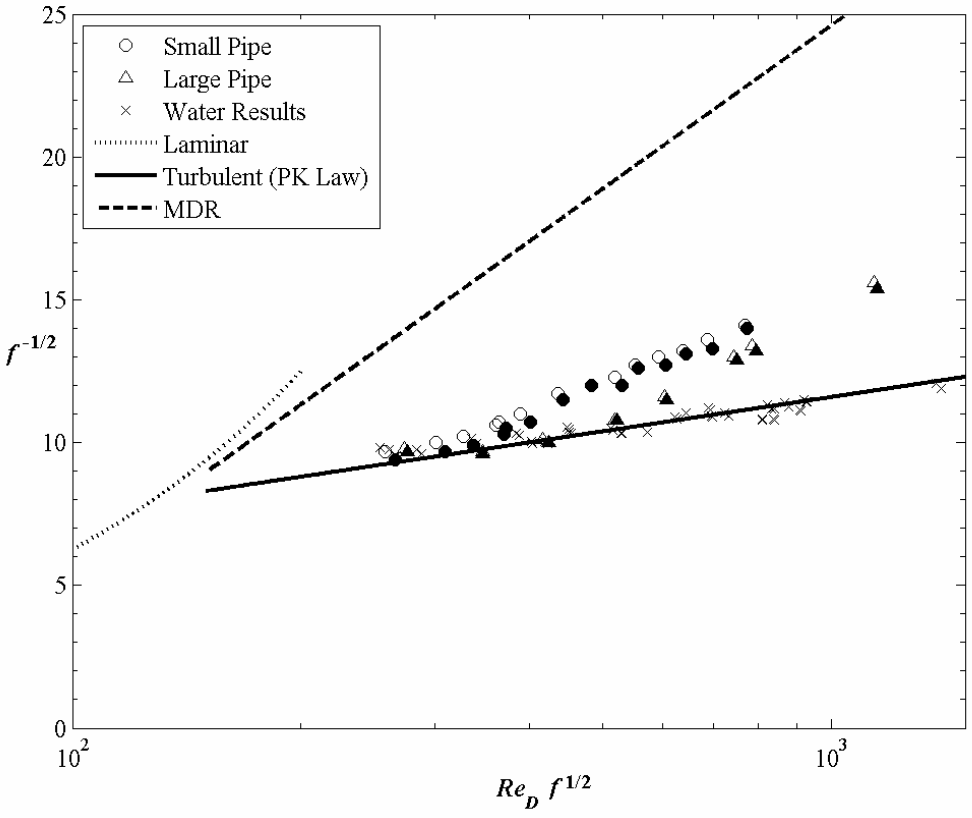

Figure 32. Friction curves from the small and large pressure drop tubes showing minimal deviation from the upstream (outlined symbols) and downstream (solid symbols) pressure transducers. Also included are the results from both tubes using water, which is in good agreement with PK law for Newtonian turbulent pipe flow.

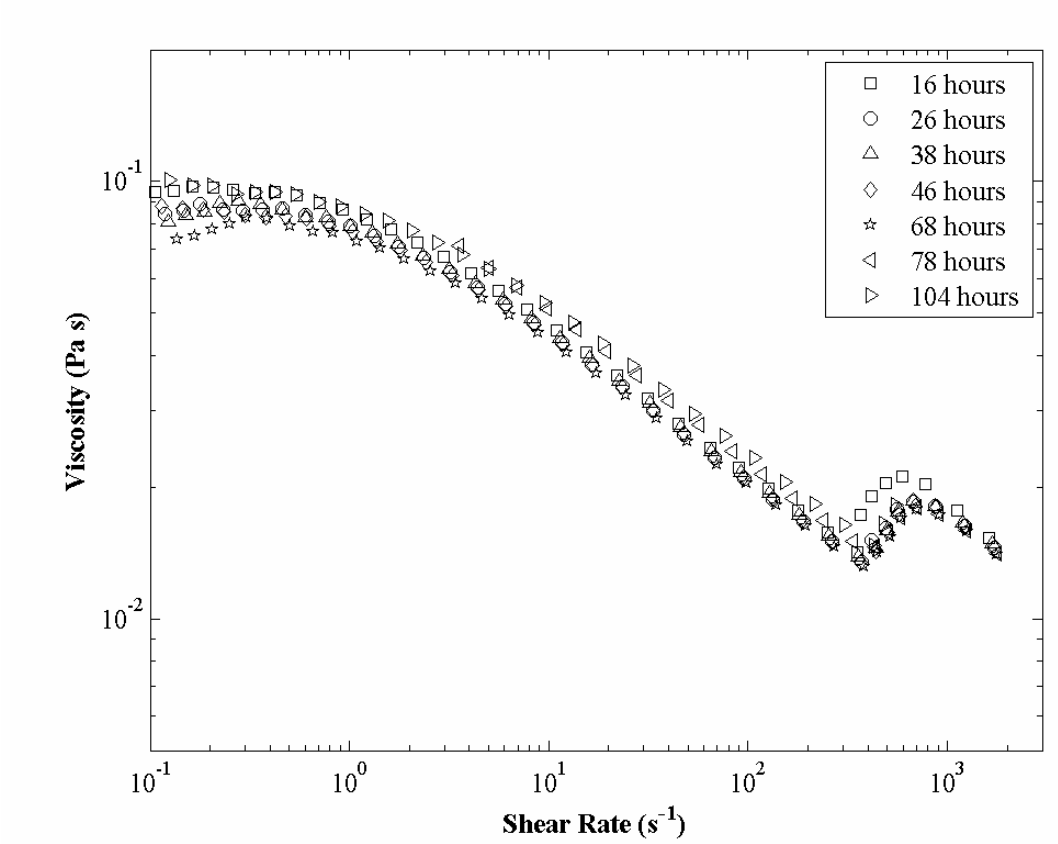

Figure 33. Rheological characterization of a single batch of 4000 wppm stock polymer solution ranging from 16 to 104 hours after being mixed. The inertioelastic instability occurs at a lower shear rate with the 16 hour stock solution, which indicates greater than 16 hours is required for hydration. Batches were allowed to hydrate for a minimum of 24 hours prior to testing.

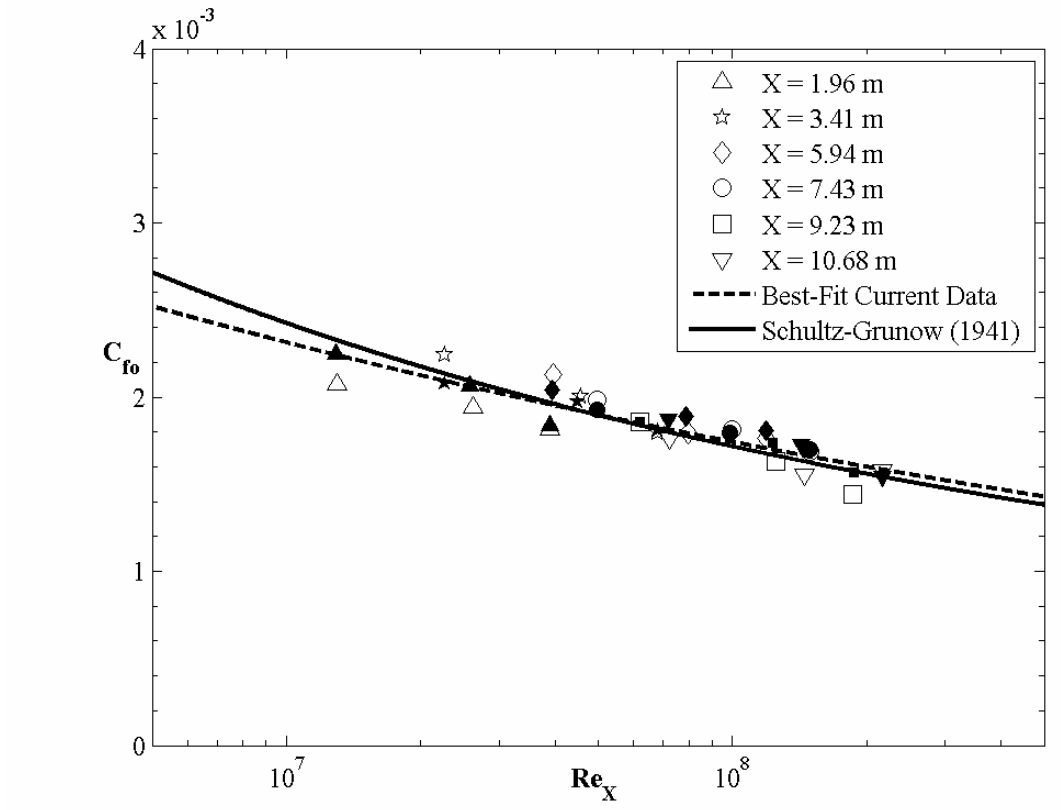

Figure 34. Baseline (non-injection) skin-friction results from the HIPLATE test model with the surface hydraulically smooth. Also included for comparison are the Schultz-Grunow (1941) friction curve for turbulent flow over a zero-pressure-gradient flat plate and the best fit curve (equation 11.2) to the current data.

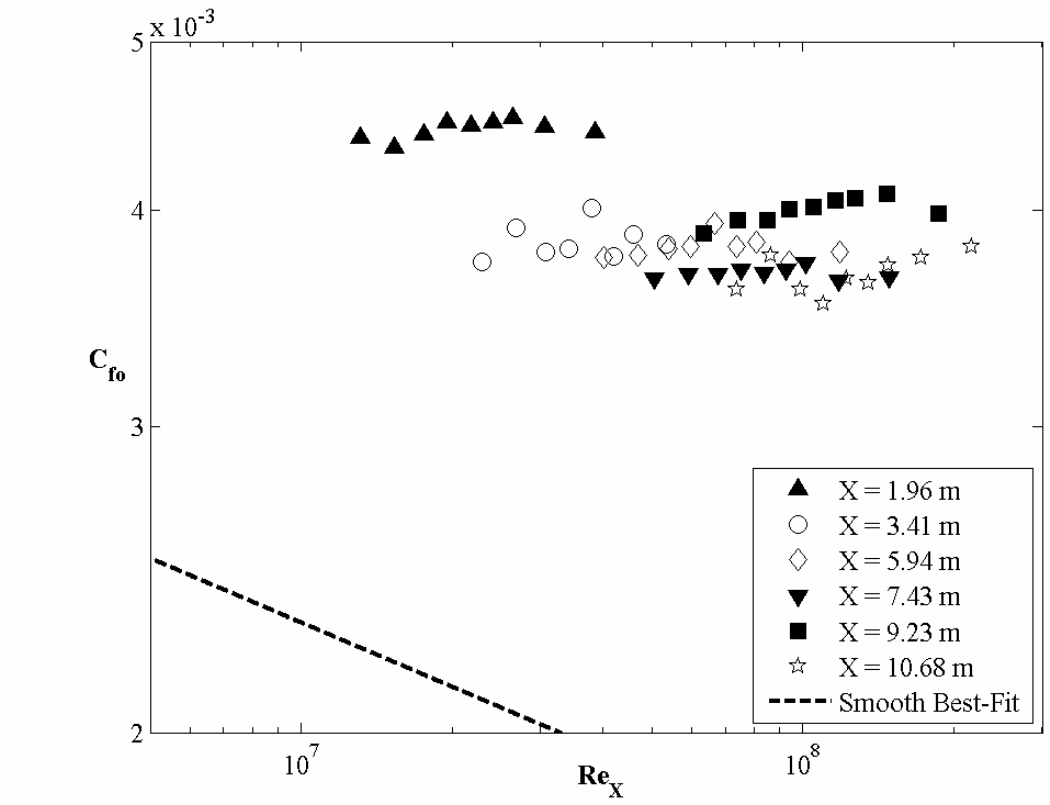

Figure 35. Baseline (non-injection) skin-friction results from the test model with a roughened surface from each downstream location at speeds from 6.7 to 20.3 $m s^{-1}$. The Reynolds independence at each downstream location indicates that the model was fully rough. Also included for comparison is the best-fit curve from the smooth model.

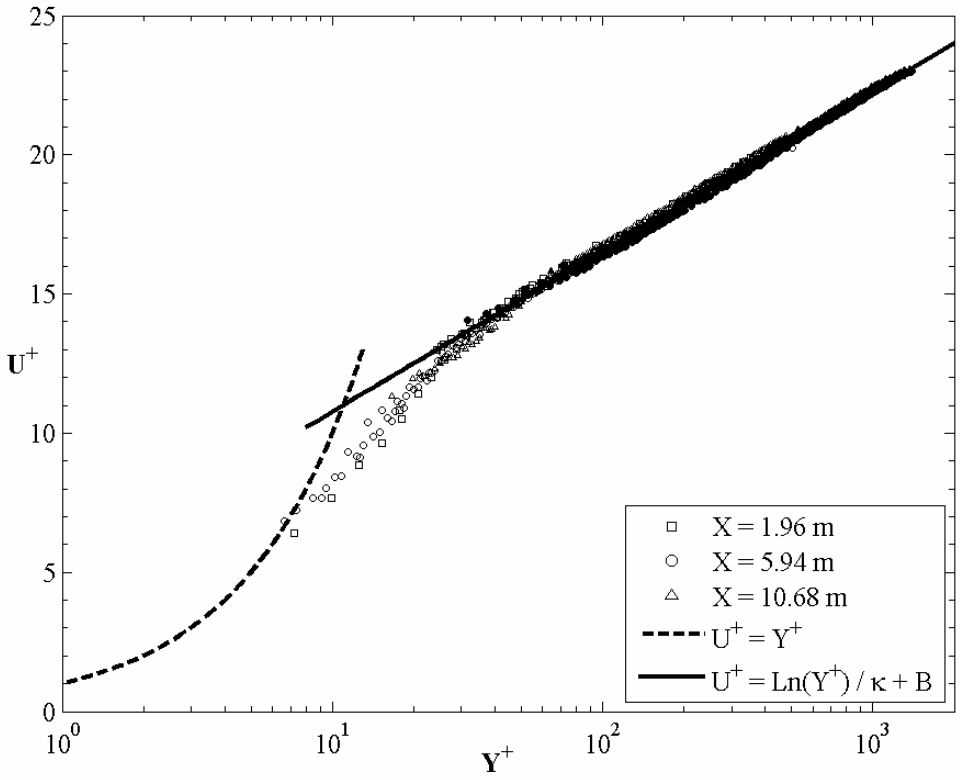

Figure 36. Baseline (non-injection) mean near-wall velocity profiles with the smooth surface at (open symbols) 6.7 and (solid symbols) 20.1 $m\,s^{-1}$. Included in the graph for comparison are the viscous sublayer profile ($U^+ = Y^+$) and the log-law (equation 11.5) with $\kappa = 0.40$ and $B = 5.0$.

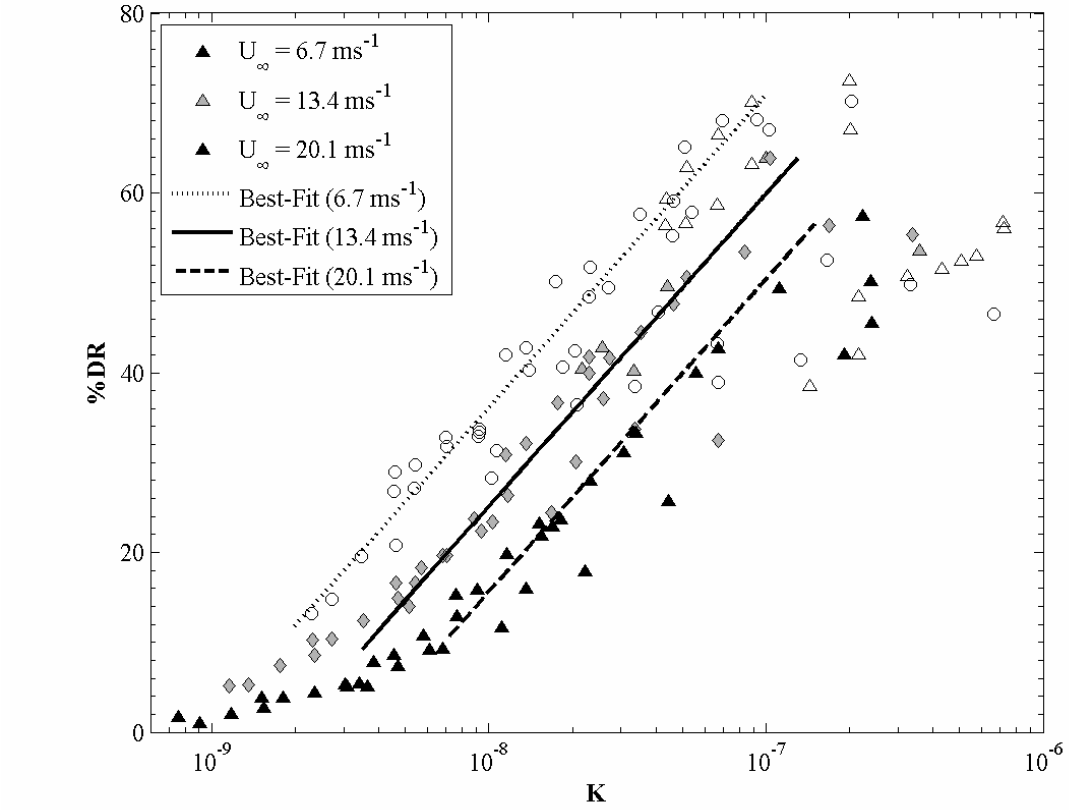

Figure 37. Percent drag reduction data from the smooth surface scaled versus *K*. Data on the same test model from (o) Winkel *et al*. (2008b) and the (△) current study are included. The best-fit curves are fitted to results in the intermediate-zone at each speed tested.

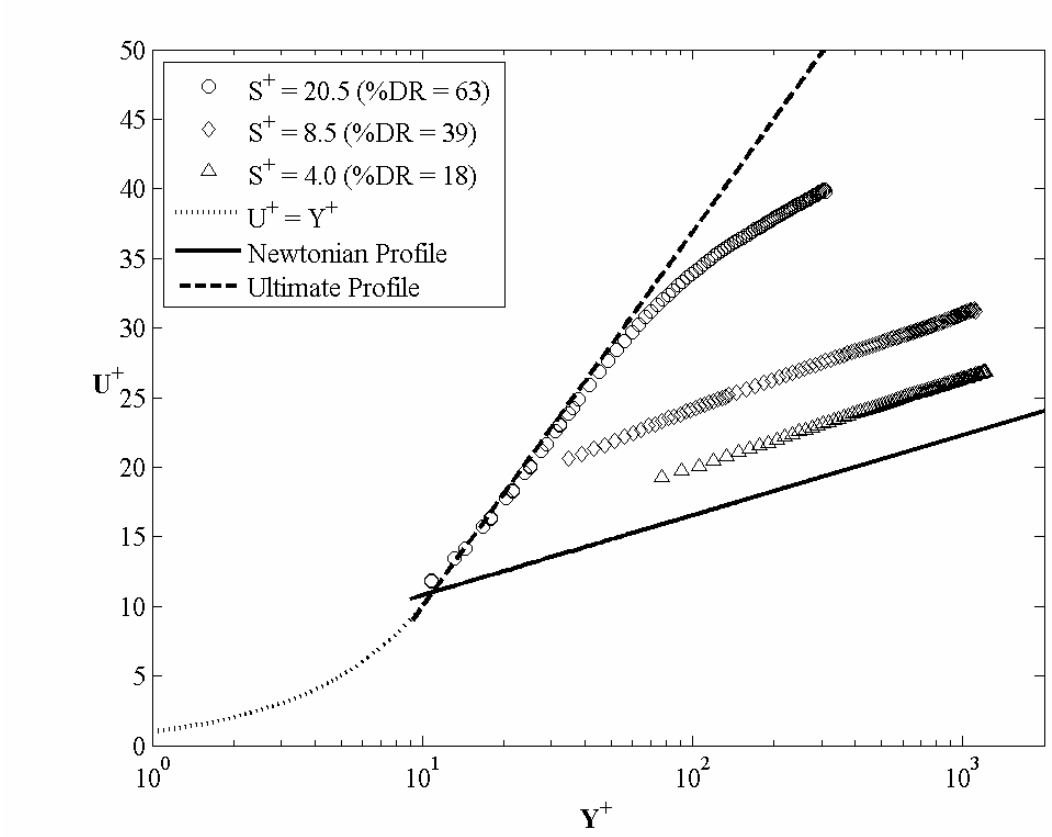

Figure 38. Mean near-wall velocity profiles with addition of drag reducing polymers on the hydraulically smooth surface with injection of 4000 wppm solution at three test conditions: (o) U_∞ = 6.7 m s^{-1}, X-X_{inj} = 4.54 m, Q_{inj} = 10 Q_s; (◊) U_∞ = 20.1 m s^{-1}, X-X_{inj} = 4.54 m, Q_{inj} = 10 Q_s; (△) U_∞ = 20.1 m s^{-1}, X-X_{inj} = 0.56 m, Q_{inj} = 2 Q_s. Increasing drag reduction results in an upward shift of the log region, termed the effective slip.

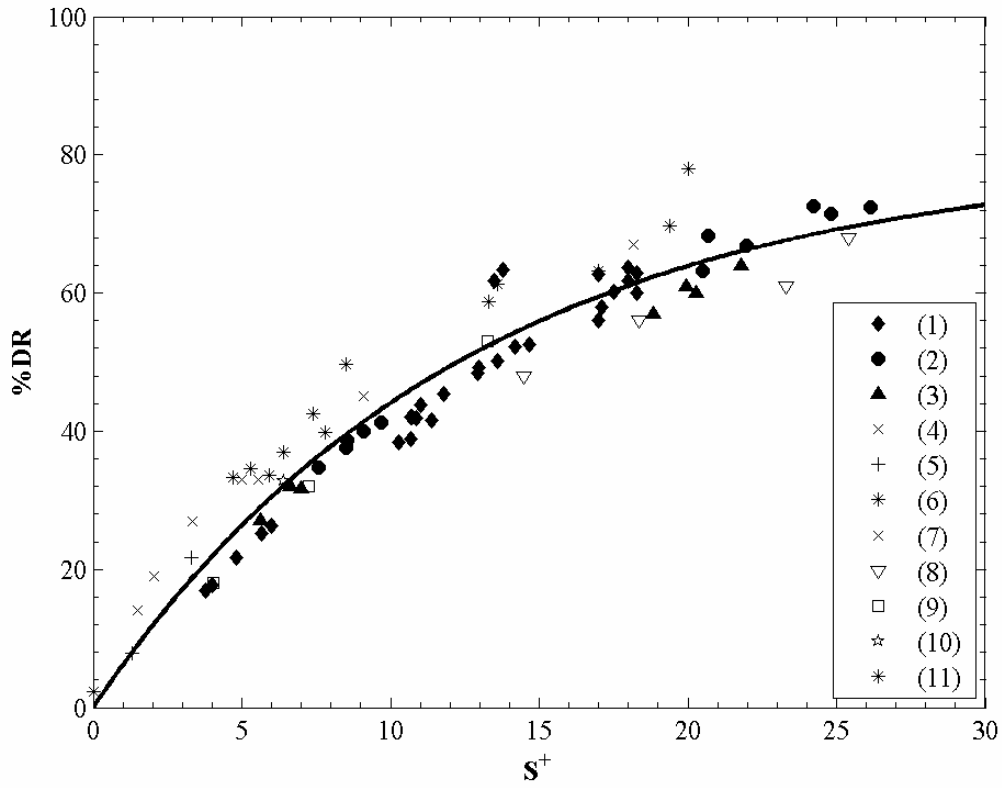

Figure 39. The percent drag reduction as a function of the effective slip, S^+, from the current results: (1) X-X_{inj} = 0.56 m, (2) X-X_{inj} = 4.54 m, (3) X-X_{inj} = 9.28 m. Other symbols are drag reduction results with polymers or surfactants in boundary, channel or pipe flows from: (4) White *et al*., 2004; (5) Fontaine *et al*., 1992; (6) Wei & Willmarth, 1992; (7) Warholic *et al*., 1999a; (8) Warholic *et al*., 1999b; (9) Petrie *et al*., 2005; (10) Koskie & Tiederman, 1991; (11) pipe flow data compiled by Virk, 1975. The solid line corresponds to the best-fit curve provided by equation (11.8).

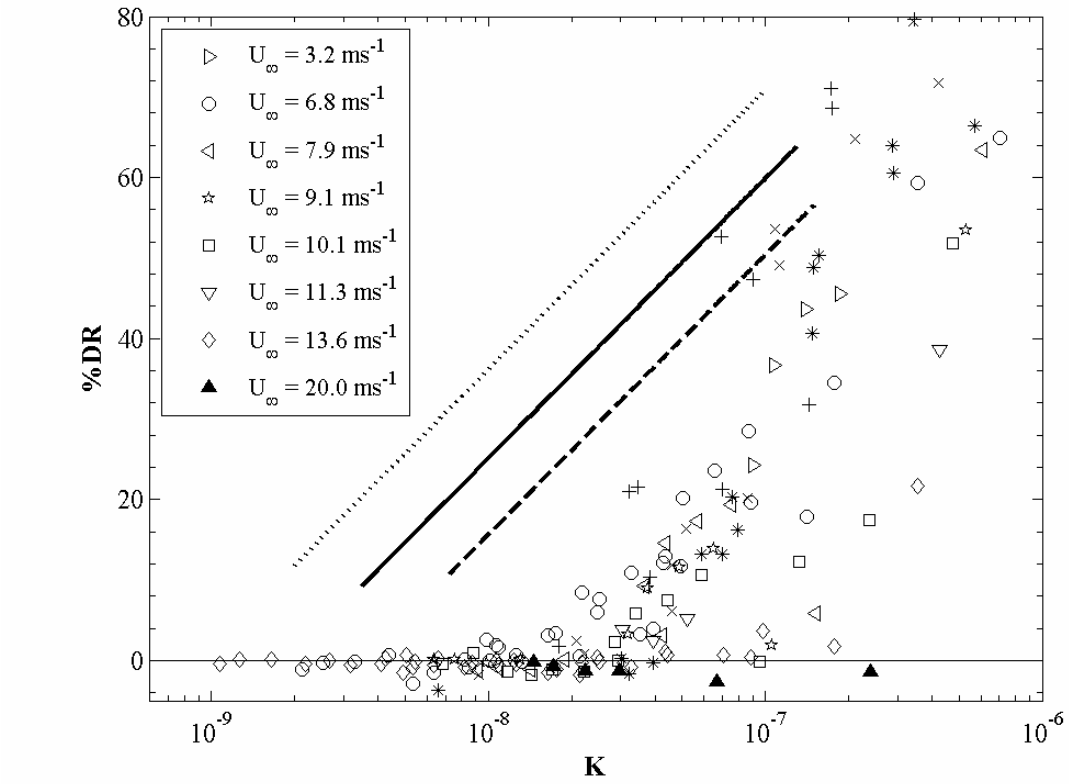

Figure 40. Percent drag reduction data from the fully rough surface condition scaled with the *K*-parameter. The best-fit curves to the intermediate-zone with the smooth model (see figure 37) are included for comparison. Also included in the plot are results from Petrie *et al*. (2003) on their fully rough surface at (+) 4.6, (×) 7.6 and (∗) 10.7 m s^{-1}.

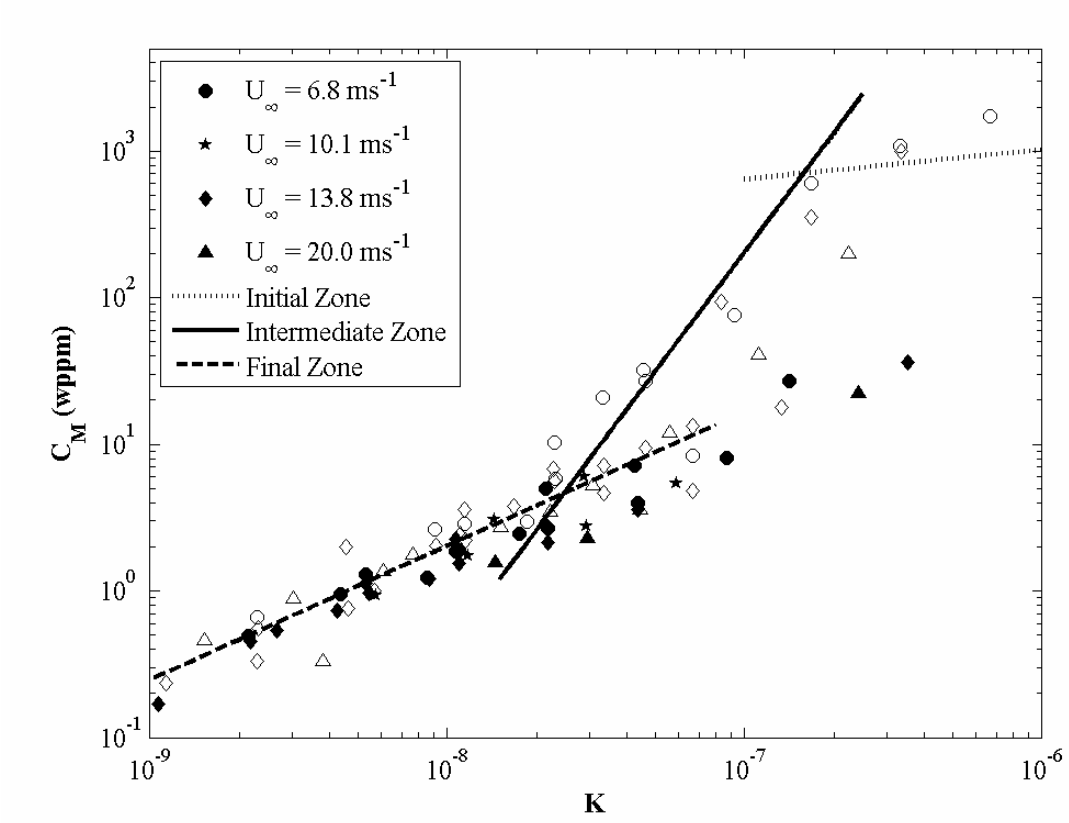

Figure 41. The maximum concentration at the wall from the rough model (solid symbols) scaled versus the *K*-parameter. Data (open symbols) from the smooth model reported in Winkel *et al*. (2008b) are included for comparison. Also plotted are the best-fit curves to the initial-, intermediate- and final-zones determined from several research efforts compiled in Winkel *et al*. (2008b).

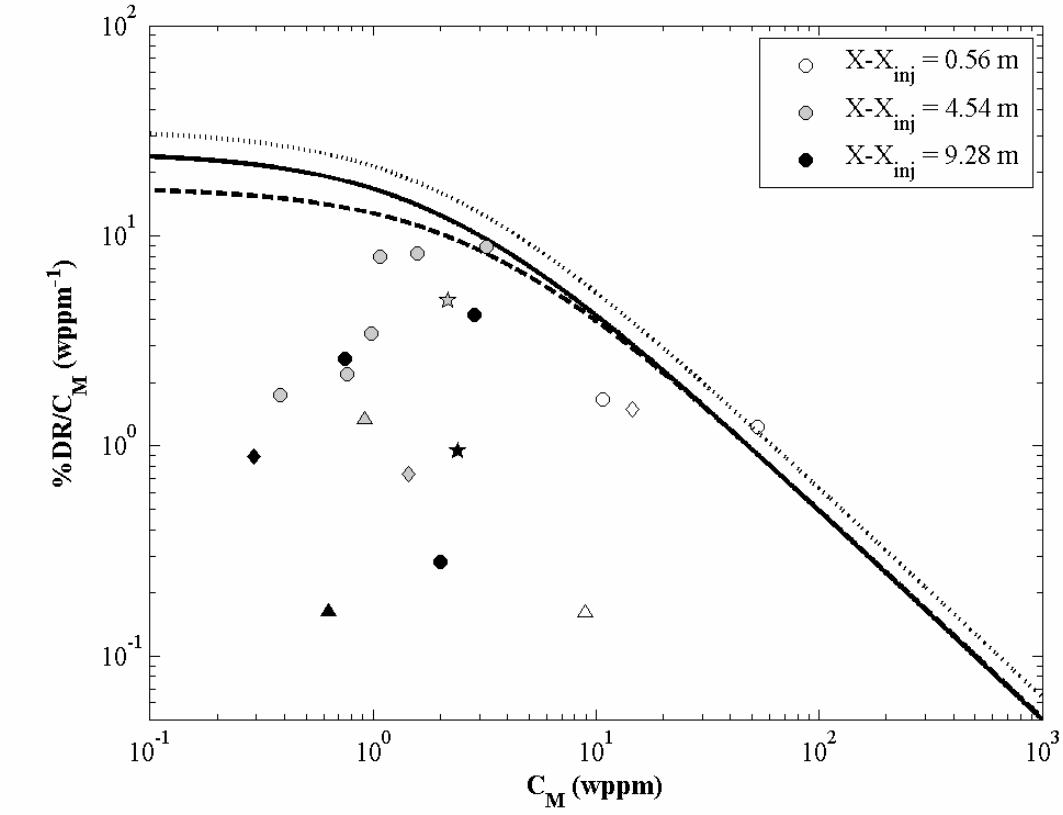

Figure 42. Intrinsic drag reduction results from the rough model based on percent drag reduction and maximum concentration data. Results were obtained at (o) 6.8, (☆) 10.1, (◊) 13.6 and (△) 20.0 m s^{-1}. The curves correspond to results obtained from Winkel *et al*. (2008b) on the same test model with the same polymer at (short dashed line) 6.7, (solid line) 13.3 and (long dashed line) 20.1 m s^{-1}.

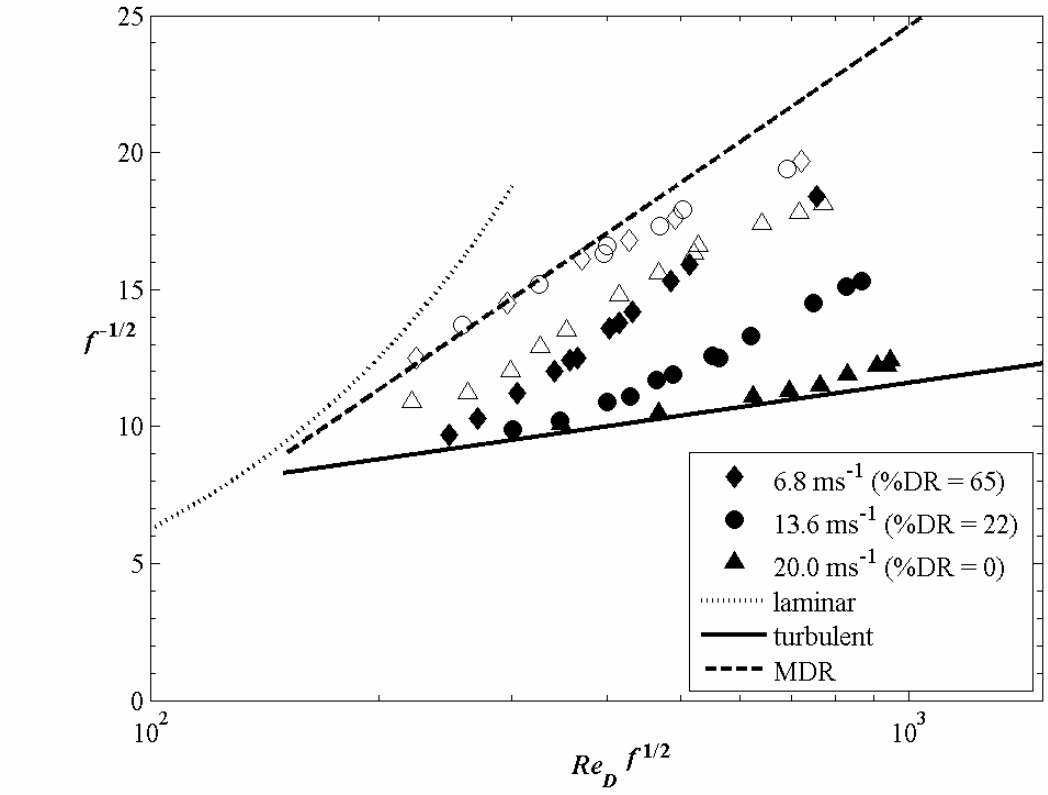

Figure 43. Results from the pressure drop apparatus with samples drawn from the (solid symbols) rough walled TBL and the corresponding (open symbols) control samples. Increasing the free-stream speed results in a higher onset shear stress (i.e. degrades the polymer solution).

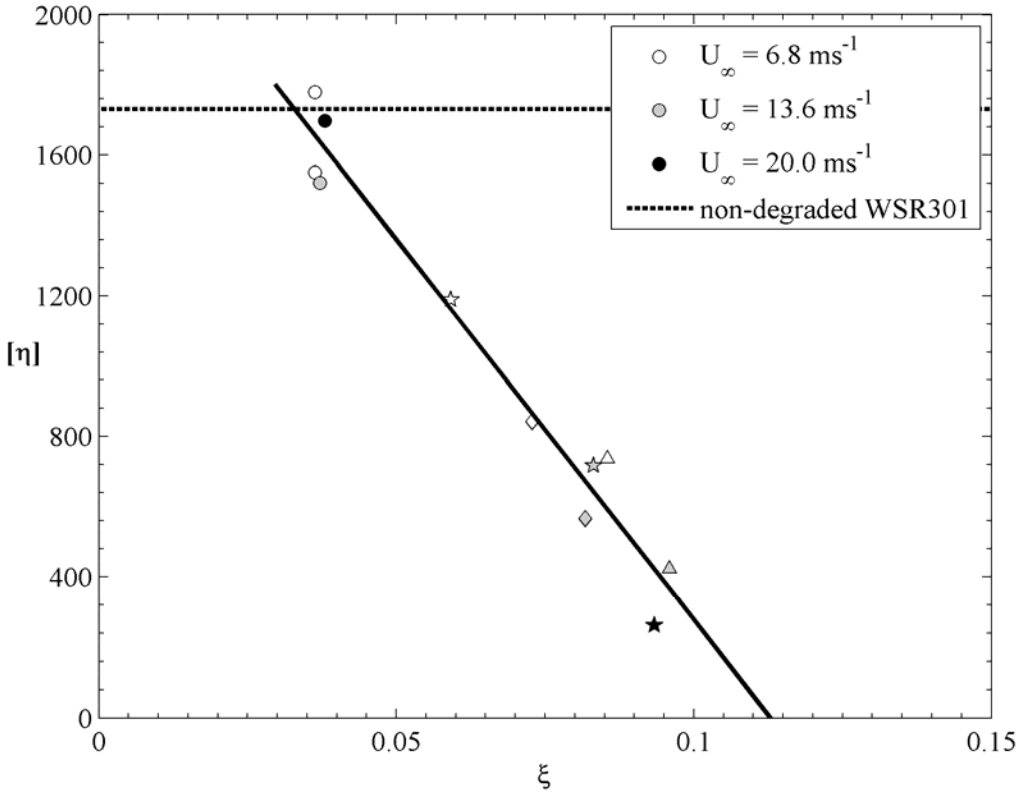

Figure 44. Intrinsic viscosity results scaled using a reworked relationship provided by Vanapalli *et al*. (2006) for scission of polymer chains in homogeneous, internal turbulent flows (ξ defined in equation 11.16). Results from the smooth model at X-X_{inj} = (o) 0.56, (◊) 4.54 and (△) 9.28 m, and the rough model results at X-X_{inj} = (☆) 0.56 m. The solid line is the linear least-squares fit to the data and the dashed line corresponds to the intrinsic viscosity of a non-degraded sample of WSR301 ([η] = 1730).

REFERENCES

Bailey, F. E. & Callard, R. W., 1959, "Some Properties of Poly(ethylene oxide) in Aqueous Solutions", *Journal of Applied Polymer Science*, **1**(1), 56-62.

Brungart, T.A., Harbison, W.L., Petrie, H.L. & Merkle, C.L., 1991, "A fluorescence technique for measurement of slot injected fluid concentration profiles in a turbulent boundary layer," *Experiments in Fluids*, **11**, 9-16.

Castro, W.E., 1966, "The effect of certain additives on transition in pipe flow," *PhD thesis, West Virginia University*, Morgantown, W.Va.

Choi, H.J. & Jhon, M.S., 1996, "Polymer-induced turbulent drag reduction," *Ind. Eng. Chem. Res.*, **35**, 2993-2998.

Choi, H.J., Lim, S.T., Lai, P.Y. & Chan, C.K., 2002, "Turbulent drag reduction and degradation of DNA," *Physical Review Letters*, **89**(8), 088302.

Collins, D.J. & Gorton, C.W., 1976, "An experimental study of diffusion from a line source in a turbulent boundary layer," *AIChE Journal*, **22**(3), 610-612.

Culter, J.D., Zakin, J.L. & Patterson, G.K., 1975, "Mechanical degradation of dilute solutions of high polymers in capillary tube flow," *Journal of Applied Polymer Science*, **19**, 3235-3240.

Draad, A.A., Kuiken, G.D.C. & Nieuwstadt, F.T.M., 1998, "Laminar-turbulent transition in pipe flow for Newtonian and non-Newtonian fluids," *Journal of Fluid Mechanics*, **377**, 267-312.

Dubief, Y., White, C. M., Terrapon, V. E., Shaqfeh, E. S. G., Moin, P. & Lele, S. K., 2004, "On the Coherent Drag-Reducing and Turbulence-Enhancing Behaviour of Polymers in Wall Flows," *Journal of Fluid Mechanics*, **514**, 271-280.

Elbing, B.R., Winkel, E.S., Lay, K.A., Ceccio, S.L., Dowling, D.R. & Perlin, M., 2008a, "Bubble-induced skin-friction drag reduction and the abrupt transition to air-layer drag reduction," *Journal of Fluid Mechanics*, **612**, 201-236.

Elbing, B.R., Dowling, D.R., Solomon, M.J., Perlin, M. & Ceccio, S.L., 2008b, "Polymer degradation within a high-Reynolds-number, flat-plate turbulent boundary layer that is fully rough," *Proceedings of the 27th Symposium on Naval Hydrodynamics*, Seoul, Korea.

Etter, R.J., Cutbirth, J.M., Ceccio, S.L., Dowling, D.R. & Perlin, M., 2005, "High Reynolds number experimentation in the U.S. Navy's William B. Morgan Large Cavitation Channel," *Measurement Science and Technology*, **16**(9), 1701-1709.

Fontaine, A.A., Petrie, H.L. & Brungart, T.A., 1992, "Velocity profile statistics in a turbulent boundary layer with slot-injected polymer," *Journal of Fluid Mechanics*, **238**, 435-466.

Frenkel, J., 1944, "Orientation and rupture of linear macromolecules in dilute solutions under the influence of viscous flow," *Acta Physicochimica URSS*, **19**(1), 51-76.

Fruman, D.H. & Tulin, M.P., 1976, "Diffusion of a tangential drag-reducing polymer injection on a flat plate at high Reynolds number," *Journal of Ship Research*, **20**(3), 171-180.

Gebel, C., Reitzer, H. & Bues, M., 1978, "Diffusion of macromolecular solutions in the boundary layer," *Rheol. Acta*, **17**, 172-175.

Hunston, D.L. & Zakin, J.L., 1980, "Flow-assisted degradation in dilute polystyrene solutions," *Polymer Engineering and Science*, **20**(7), 517-523.

Jiménez, J., 2004, "Turbulent flows over rough walls," *Annual Review of Fluid Mechanics*, **36**, 173-196.

Kalashnikov, V.N. & Tsiklauri, M.G., 1996, "Supermolecular structures and flow birefringence in polymer solutions," *Colloid Polymer Science*, **274**, 1119-1128.

Kalashnikov, V.N., 1998, "Dynamical similarity and dimensionless relations for turbulent drag reduction by polymer additives," *Journal of Non-Newtonian Fluid Mechanics*, **75**, 209-230.

Kalashnikov, V.N., 2002, "Degradation accompanying turbulent drag reduction by polymer additives," *Journal of Non-Newtonian Fluid Mechanics*, **103**, 105-121.

Kim, C.A., Kim, J.T., Lee, K., Choi, H.J. & Jhon, M.S. (2000) "Mechanical degradation of dilute polymer solutions under turbulent flow," *Polymer*, **41**(21), 7611-7615.

Koskie, J.E. & Tiederman, W.G., 1991, "Polymer drag reduction of a zero-pressure-gradient boundary layer," *Physics of Fluids*, **3**(10), 2471-2473.

Little, R.C. & Patterson, R.L., 1974, "Turbulent friction reduction by aqueous poly(ethylene oxide) polymer solutions as a function of salt concentration," *Journal of Applied Polymer Science*, **18**, 1529-1539.

McNally, W.A., 1968, "Heat and momentum transport in dilute polyethylene oxide solutions," *PhD thesis, University of Rhode Island*

Merrill, E.W. & Horn, A.F., 1984, "Scission of macromolecules in dilute solution: Extensional and turbulent flows," *Polymer Communications*, **25**(5), 144-146.

Moussa T. & Tiu C., 1994, "Factors affecting polymer degradation in turbulent pipe flow," *Chemical Engineering Science*, **49**(10), 1681-1692.

Nakken, T., Tande, M. & Elgsaeter, A., 2001, "Measurements of polymer induced drag reduction and polymer scission in Taylor flow using standard double-gap sample holders with axial symmetry," *Journal of Non-Newtonian Fluid Mechanics*, **97**(1), 1-12.

Patterson, R.W. & Abernathy, F.H., 1970, "Turbulent flow drag reduction and degradation with dilute polymer solutions," *Journal of Fluid Mechanics*, **43**(4), 689-710.

Petrie, H.L. & Fontaine, A.A., 1996, "Comparison of turbulent boundary layer modifications with slot-injected and homogeneous drag-reducing polymer solutions," *Proceedings of the ASME Fluids Engineering Division*, **237**, 205-210.

Petrie, H.L., Brungart, T.A. & Fontaine, A.A., 1996, "Drag reduction on a flat plate at high Reynolds number with slot-injected polymer solutions," *Proceedings of the ASME Fluids Engineering Division*, **237**, 3-9.

Petrie, H.L., Deutsch, S., Brungart, T.A. & Fontaine, A.A., 2003, "Polymer drag reduction with surface roughness in flat-plate turbulent boundary layer flow," *Experiments in Fluids*, **35**, 8-23.

Petrie, H., Fontaine, A., Moeny, M & Deutsch, S., 2005, "Experimental study of slot-injected polymer drag reduction," *Proceedings of the 2nd International Symposium on Seawater Drag Reduction*, Busan, Korea, 605-620.

Poreh, M. & Hsu, K.S., 1972, "Diffusion of drag reducing polymers in a turbulent boundary layer," *Journal of Hydronautics*, **6**(1), 27-33.

Sabra, K.G., Winkel, E.S., Bourgoyne, D.A., Elbing, B.R., Ceccio, S.L., Perlin, M. & Dowling, D.R., 2007, "Using cross-correlations of turbulent flow-induced

ambient vibrations to estimate the structural impulse response: Application to structural health monitoring," *Journal of the Acoustical Society of America*, **121**(4), 1987-1995.

Sanders, W.C., Winkel, E.S., Dowling, D.R., Perlin, M. & Ceccio, S.L., 2006, "Bubble friction drag reduction in a high-Reynolds-number flat-plate turbulent boundary layer," *Journal of Fluid Mechanics*, **552**, 353-380.

Schultz-Grunow, F., 1941, "New frictional resistance law for smooth plates," *NACA* T M **17**, 1-24.

Sedov, L.I., Ioselevich, V.A., Pilipenko, V.N. & Vasetskaya, N.G., 1979, "Turbulent diffusion and degradation of polymer molecules in a pipe and boundary layer," *Journal of Fluid Mechanics*, **94**(3), 561-576.

Sellin, R.H.J., Hoyt, J.W., Pollert, J. & Scrivener, O., 1982, "The effect of drag-reducing additives on fluid flows and their industrial applications: Part 2. Basic applications and future proposals," *Journal of Hydraulic Research*, **20**(3), 235-292.

Shin, H., 1965, "Reduction of drag in turbulence by dilute polymer solutions," *ScD thesis, Massachusetts Institute of Technology*, Cambridge.

Vanapalli, S.A., Islam, M.T. & Solomon, M.J., 2005, "Scission-induced bounds on maximum polymer drag reduction in turbulent flow," *Physics of Fluids*, **17**(9), 095108.

Vanapalli, S.A., Ceccio, S.L. & Solomon, M.J., 2006, "Universal scaling for polymer chain scission in turbulence," *Proceedings of the National Academy of Sciences of the United States of America*, **103**(45), 16660-16665.

Vdovin, A.V. & Smol'yakov, A.V., 1978, "Diffusion of polymer solutions in a turbulent boundary layer," *Journal of Applied Mechanics and Technical Physics*, **19**(2), 66-73.

Vdovin, A.V. & Smol'yakov, A.V., 1981, "Turbulent diffusion of polymers in a boundary layer," *Journal of Applied Mechanics and Technical Physics*, **22**(4), 98-104.

Virk, P.S., Merrill, E.W., Mickley, H.S., Smith, K.A. & Mollo-Christensen, E.L., 1967, "The Toms phenomenon: turbulent pipe flow of dilute polymer solutions," *Journal of Fluid Mechanics*, **20**, 22-30.

Virk, P.S., Mickley, H.S. & Smith, K.A., 1970, "The ultimate asymptote and mean flow structure in Toms' Phenomenon," *Journal of Applied Mechanics*, **37**(2), 488-493.

Virk, P.S., 1975, "Drag Reduction Fundamentals," *Journal of the American Institute of Chemical Engineers*, **21**(4), 625-656.

Warholic, M.D., Massah, H. & Hanratty, T.J., 1999a, "Influence of drag-reducing polymers on turbulence: effects of Reynolds number, concentration and mixing," *Experiments in Fluids*, **27**, 461-472.

Warholic, M.D., Schmidt, G.M. & Hanratty, T.J., 1999b, "The influence of a drag-reducing surfactant on a turbulent velocity field," *Journal of Fluid Mechanics*, **388**, 1-20.

Wei, T. & Willmarth, W.W., 1992, "Modifying turbulent structure with drag-reducing polymer additives in turbulent channel flows," *Journal of Fluid Mechanics*, **245**, 619-641.

White, F.M. (2006) *Viscous Fluid Flow*, 3rd Ed. (McGraw-Hill, New York), 430-438.

White, C.M., Somandepalli, V.S.R. & Mungal, M.G., 2004, "The turbulence structure of drag-reduced boundary layer flow," *Experiments in Fluids*, **36**, 62-69.

White, C.M. & Mungal, M.G., 2008, "Mechanics and prediction of turbulent drag reduction with polymer additives," *Annual Review of Fluid Mechanics*, **40**, 235-256.

Winkel, E.S., Elbing, B.R., Ceccio, S.L., Perlin, M. & Dowling, D.R., 2008a, "High-Reynolds-number turbulent-boundary-layer wall pressure fluctuations with skin-friction reduction by air injection," *Journal of the Acoustical Society of America*, **123**(5), 2522-2530.

Winkel, E.S., Oweis, G., Vanapalli, S.A., Dowling, D.R., Perlin, M., Solomon, M.J. & Ceccio, S.L., 2008b, "High Reynolds number turbulent boundary layer friction drag reduction from wall-injected polymer solutions," *Journal of Fluid Mechanics*, in press.

Wu, J. & Tulin, M.P., 1972, "Drag reduction by ejecting additive solutions into pure-water boundary layer," *Journal of Basic Engineering, Transactions of the ASME*, **94**, 749-756.

PART V. DIFFUSION OF DRAG-REDUCING POLYMER SOLUTIONS WITHIN A ROUGH WALL TURBULENT BOUNDARY LAYER

Chapter 13. Introduction

13.1 Abstract

Diffusion of drag-reducing polymer solutions within a turbulent boundary layer with and without surface roughness was investigated with slot injection on a 0.94 m long flat-plate test model. Tests were conducted at free-stream flow speeds to 10 $m s^{-1}$ and downstream distance based Reynolds numbers to 10 million. Three surface conditions were investigated (hydraulically smooth, transitionally rough and fully rough) with polymer solution injection into water and the smooth surface additionally had polymer solution injected into a polymer ocean at maximum drag reduction (MDR). Mean velocity profiles were acquired with PIV without injection and during injection the only measurement was the polymer concentration profiles made with PLIF. Measured mean and instantaneous concentration profiles were consistent with previous work, and periodic lifting from the wall of high concentration filaments in the initial and start of the intermediate-zone was observed. Analysis of the individual diffusion zones (initial, intermediate, and final) revealed the scaling parameters for each region. The maximum concentration in the final-zone scales with K if the downstream distance is fixed and $K^{6/7}$

if the flux of injected polymer is fixed, which illustrates that K does not provide a universal scaling. The initial-zone, studied with the smooth surface condition in the MDR polymer ocean, revealed that the diffusion process is governed by the Reynolds number based on distance from the injector (Re_{xo}), non-dimensional volumetric injection flux (Q_{inj}/Q_s) and the injection concentration (C_{inj}). Further analysis of the initial-zone diffusion process indicates that the maximum initial-zone length is ~1 m when supplying sufficient quantities of polymer solution to achieve significant drag reduction levels. The rough surfaces were used to study the intermediate-zone where it was found that the maximum concentration scaled with $K^{3/2}(1+k^{+})^{-0.2}$ over the range of parameters tested.

13.2 Background and Motivation

Since Toms (1948) first presented results indicating that skin-friction drag in turbulent flows could be reduced with the addition of small quantities of a polymer solution, numerous research investigations have been performed and applications for polymer drag reduction (PDR) have been developed. Most successful applications to date for PDR are with internal flows, and Sellin *et al.* (1982) provides a good summary of various PDR applications. However, researchers have struggled to successfully apply PDR to external flow applications due to the continual dilution (mixing and boundary layer growth) of the injected polymer solution. One important application on which these external flow research efforts have focused is the implementation of PDR on surface ships. The desire to reduce the skin-friction drag on the surface of ships is great because it can account for more than 60% of the total drag for Froude numbers of order 0.1 (or less). Laboratory scale experiments have achieved skin-friction drag reduction levels as

high as 75%; thus, PDR has been considered a possible method for fuel cost savings and improved performance (i.e. higher top speed, increased payload and/or longer range).

While PDR has been able to achieve high levels of drag reduction (drag herein refers to skin-friction drag), these levels tend to be limited to the region immediately downstream of the injector and to low speeds where skin-friction is not very high. This limited performance has been attributed primarily to the dilution of the polymer solution within the turbulent boundary layer (TBL). The dilution causes the near-wall polymer concentration to continuously decrease from mixing and boundary layer growth, and it is the polymer concentration near the wall that is believed to be responsible for the reduction in drag (see White & Mungal, 2008 for a recent review of PDR). Currently the largest laboratory PDR tests were recently conducted on a large flat-plate (12.9 m long, termed HIPLATE) at high speeds (~20 $m s^{-1}$) and large downstream distance based Reynolds numbers (to 220 million). The first studies from the HIPLATE with PDR (Winkel *et al*., 2008) were conducted with the surface hydraulically smooth and their results indicate that at higher speeds the reduced performance cannot be fully explained by increased diffusion. Polymer degradation (chain-scission) was suspected to be an additional contributor to the limited PDR performance. To further complicate the problem, most investigations to date have been performed on smooth surfaces, and it is known that roughness increases turbulent intensity and shear rates (see Jiménez, 2004, for a recent review of turbulent flows over rough walls). The increased turbulent intensity presumably increases the polymer diffusion rate and the higher shear rates would increase the probability of polymer degradation by chain scission. Therefore, if degradation

occurred on a smooth model it would only be increased due to the higher shear rates present in a rough-walled turbulent boundary layer. Two recent studies have investigated PDR with rough surfaces. The first was Petrie *et al.* (2003) where a rather thorough investigation of four surface conditions (a hydraulically smooth, two transitionally rough and a fully rough) were studied with skin-friction and concentration profile measurements with either slot-injection or with a polymer ocean. Their findings show that roughness can increase drag reduction levels in the region near the injector, but that the performance significantly diminishes with downstream distance and increased roughness. The increased performance near the injection location was assumed to be caused by the shortening of the initial diffusion zone where reduced drag reduction levels are observed on smooth models. Elbing *et al.* (2008) presents preliminary results from the HIPLATE with the surface fully rough that are consistent with the fully rough results of Petrie *et al.* (2003). Additionally, strong evidence was presented that indicates that polymer degradation is potentially a major contributor to the reduced performance with rough surfaces. However, it is difficult from either Petrie *et al*. (2003) or Elbing *et al.* (2008) to separate the two mechanisms (i.e. diffusion and degradation).

Thus the current study focuses on quantifying the diffusion process with a small scale model (~1 m) and three surface conditions corresponding to hydraulically smooth, transitionally rough and fully rough. The investigation varies the surface condition, flow speed, injection condition and background polymer concentration to determine how surface roughness affects the diffusion process of drag-reducing polymer solutions within a TBL.

Chapter 14. Experimentation

14.1 Test Facility

Testing was conducted in the University of Michigan 9-inch re-circulating water tunnel. The tunnel has a circular contraction with a 6.4:1 ratio following a series of metal screens to promote flow uniformity entering the test section. The test section inlet has a 22.9 cm diameter that is faired into a 1.07 m (length), 0.21 m (width) and 0.21 m (height) test section where the test model was mounted. Sidewall acrylic windows (93.9 cm × 10.0 cm viewing area) allowed optical access to the test section. The maximum test section velocity without the model is 18 $m\,s^{-1}$ and the static pressure can be varied from near vacuum to 200 kPa. The tunnel volume was measured *in situ* by adding known but minute quantities of salt and monitoring the conductivity of the tunnel water with a conductivity meter (1481-00, Cole-Parmer). The tunnel volume was determined to be 3.2 m^3. The tunnel water was filtered to approximately 1 μm, deaerated to reduce the level of dissolved gases and treated with sodium thiosulfate. The sodium thiosulfate removed all measureable levels of background chlorine and was closely monitored throughout testing (ExStick CL200, Extech Instruments). Petrie *et al.* (2003) showed that the use of sodium thiosulfate for the removal of chlorine had no significant effect on PDR performance.

14.2 Test Model

The test model, schematically shown in figure 45, was fabricated from grey PVC and measured 0.94 m long, 0.21 m wide and 6.4 cm thick, which produced a 30% blockage in the test section. The model was rigidly mounted slightly above the test section centerline, spanned the entire width of the test section and had the working surface downward. The model's leading edge was a 4:1 ellipse to prevent flow separation prior to injection. The boundary layer was "tripped" 11.7 cm downstream of the model leading edge with a 9.5 mm stream-wise thick strip of loosely packed glass bead grit having an average roughness height ~10 μm.

A tapered slot injector, schematically shown in figure 46, was mounted within the model producing the slot opening at the model surface 22.9 cm downstream of the model leading edge. The slot was inclined 25° from the test surface and contracted at a full angle of 5.5°, which produced a 1.0 mm gap on the model surface. Polymer solution was fed from both sides of the tunnel into a manifold that spanned the width of the model interior. The polymer solution then passed through a second manifold that was packed with a porous material (silicon carbide, Scotchbrite), which produced a pressure drop near the injector throat that promoted uniform injection. The injector uniformity was monitored regularly *via* dye injection studies. While the current injector design was not tested for polymer degradation, it used an injector design similar to that used in Winkel *et al*. (2008) with the addition of the porous material used in Elbing *et al*. (2008), and both the injector design and porous material did not cause degradation of the polymer solutions.

The model was tested with three surface conditions (hydraulically smooth, transitionally rough and fully rough). The smooth surface had an average roughness height, k, of approximately 1.7 μm, which was sufficient for the model to be considered hydraulically smooth at all speeds tested (see table 9). The model surface was roughened by affixing (2Ton Clear Epoxy, Devcon) wet/dry 240- or 60-grit sandpaper to the entire model surface. For the speeds tested the 240- and 60-grit sandpaper corresponds to transitionally and fully rough surface conditions (see table 10), respectively. Besides spanning smooth to fully rough surface conditions, the grit sizes were also selected to fall within the range tested in Petrie *et al.* (2003). Herein the 240- and 60-grit sandpaper is referenced as the transitionally and fully rough surface, respectively.

14.3 Instrumentation

14.3.1 Optical setup

The same optical setup, schematically shown in figure 47, was used to acquire Planar Laser Induced Fluorescence (PLIF) and Particle Image Velocimetry (PIV) measurements. The PIV measurements were acquired at two locations (x-x_{inj} = 0.0 and 61.6 cm) while the PLIF measurement was made at a single downstream location (x-x_{inj} = 61.6 cm). Here x is defined as the stream-wise distance downstream from the test model leading edge and x_{inj} is the stream-wise distance from the model leading edge to the injection location (see figure 45). For each measurement, a plane was illuminated by a light sheet that was normal to the plate surface and aligned with the mean flow direction. The light sheet was formed with the beam of a pulsed Nd-YAG laser (Solo I, New Wave

Research) operating at the 532 nm wavelength. The light sheet thickness at the model surface was approximately 150 μm, as determined by passing the laser sheet through a graded microscope. The sheet was formed by initially expanding the laser beam with a spherical lens, then collimating it with a second spherical lens and finally forming the sheet with a cylindrical lens. The illuminated plane was imaged with a high resolution camera (Imager Pro, LaVision), which had a nominal field of view of 10 mm (stream-wise) by 13 mm (wall-normal). The camera was rotated slightly below the model plane to produce a well defined wall location in the acquired images. A LaVision PIV computer was used to control the laser and camera, adjust timing and record the images. Then the processing was performed with DaVis software.

PLIF was used to acquire polymer concentration profiles in the TBL at x-x_{inj} = 61.6 cm and was the primary measurement acquired. Each test was conducted by uniformly mixing a known quantity of fluorescent dye (Rhodamine 6G, Sigma Chemical) into the polymer solution to be injected. The polymer-dye solution was illuminated with the light sheet described previously. The plane of fluoresced dye laden polymer solution was recorded with the high resolution camera. During PLIF measurements a long-pass, orange optical filter was placed in front of the camera lens to attenuate the 532 nm light from the laser and only pass the Stokes-shifted light (~590 nm) from the fluoresced dye to the imager.

The dye concentration was determined by applying a calibration relating the collected light intensity to known dye concentrations. A calibration was performed *in situ*

at the conclusion of each day of testing. Minimal day to day variation was observed in the calibrations. Each calibration used known quantities of thoroughly mixed dye in the tunnel and 500 images. A minimum of five concentrations were acquired each day. From the calibration the light intensity versus dye concentration was linear only at levels below approximately 0.2 weight-parts-per-million (wppm) though Rhodamine 6G dye is typically linear to ~ 5 wppm. This discrepancy was due to the attenuation of the laser sheet created from the calibration technique, which required the laser sheet to pass through approximately 8.7 cm of dyed water prior to reaching the image plane (only necessary for the calibration). This was corrected by applying a technique similar to that used by Walker & Tiederman (1989). The correction produced similar results to those obtained by using a linear fit to the low concentration measurements (< 0.2 wppm). Thus for simplicity the linear calibration from low concentration measurements was used in the final analysis of the data. Also, to limit error produced by using only low level concentration data for the calibration, the injected dye concentration was typically below 3 wppm.

The mean flow velocity at the point of injection, x_{inj}, and at the downstream measurement location (x-x_{inj} = 61.6 cm) was acquired with PIV. Measurements were made at the injection location only for the smooth surface condition with a water background. At the measurement location mean velocity profiles were acquired for each model surface condition (smooth, transitionally rough and fully rough), and with and without a polymer ocean for the smooth surface. The only change in the optical PIV setup from the PLIF setup is that the optical filter was removed. During testing the entire tunnel

volume was flooded with tracer particles (titanium dioxide, J.T. Baker) having a nominal size of 1 μm. Once again the laser sheet, previously described, was used to illuminate the image plane (now operating in double-frame, double pulse mode). The PIV technique used to process the images was the traditional cross-correlation of two single-exposed images with multiple passes. Each pass reduced the interrogation window and had 50% overlap until the final interrogation window was 0.155×0.155 mm (16 by 16 pixels). For each configuration measurements were made for the range of 3.3 through 12.3 $\mathrm{m\,s^{-1}}$ free-stream speed.

14.3.2 Pressure drop apparatus

A pressure drop tube, similar to that used by Virk (1975), was used to characterize and monitor the polymer solutions. The pressure drop setup is shown schematically in figure 48. The pressure drop apparatus had a 1.0 cm inner diameter (ID) and was divided into three sections: a 181 ID (1.81 m) long entrance length, a 152 ID (1.52 m) long test section and a 63 ID (0.63 m) long end section. The test section had a differential pressure transducer (PX2300-2PI, Omega) connected across the inlet and outlet, which was used to determine the Fanning friction factor within the pipe test section. The definition of the Fanning friction factor is given by equation (14.1), and since the wall shear stress was not directly measured the Fanning friction factor was determined with the relationship provided by equation (14.2).

$$f \equiv \frac{\tau}{\frac{1}{2}\rho U_{avg}^2} \qquad (14.1)$$

$$f = \frac{D}{2\rho U_{avg}^2}\frac{\Delta p}{\Delta x} \qquad (14.2)$$

Here f is the Fanning friction factor, τ is the wall shear stress, U_{avg} is the average velocity in the pipe, ρ is the mass density of water, D is the pipe inner diameter, Δp is the pressure difference across the test section and Δx is the test section length. A flexible tube connected the entrance length to a pressure vessel, which held the sample to be tested. Compressed nitrogen gas pressurized the vessel to approximately 120 kPa, which produced a maximum average velocity in the tube of 2.2 $\mathrm{m\,s^{-1}}$. The flow rate was measured by collecting the sample for a known time duration in a container at the apparatus outlet. The sample was weighed on a scale (SV-30, Acculab), the fill time having been recorded with a handheld stop watch. These measurements were used to determine the Reynolds number based on the pipe diameter, $Re_D = U_{avg} D/\nu$ (where ν is the kinematic viscosity of water), as well as the Fanning friction factor (14.1). Data from the pressure transducer were recorded with a LabView virtual instrument through a NI-DAQ card.

At the start of each day of testing, a sample was diluted to 10 wppm from the stock solution and tested in the pressure drop apparatus. These results indicated that the stock solution was relatively stable to 211 hours after mixing, which was the maximum duration between mixing and testing of a sample. The pressure drop tube was used also to monitor the performance of the tunnel when a polymer ocean was formed. Once an ocean was prepared at a desired concentration (sufficient to achieve MDR) a sample would be drawn from the tunnel and characterized with the pressure drop tube. Periodically during

testing samples would be drawn to verify that the ocean was still at levels sufficient for MDR. Testing was halted once the polymer ocean had degraded to levels insufficient for MDR.

The results from the pressure drop apparatus can be used to estimate the molecular weight, M_w, of the sample tested. First the intersection of the polymeric results and the well established Newtonian friction relationship for turbulent pipe flow needs to be determined. This defines the drag reduction onset condition. The intersection of the two curves gives f^* and $Re_D{}^*$, which are the onset of drag reduction Fanning friction factor and the onset of drag reduction pipe diameter based Reynolds number. From the definition of the Fanning friction factor and the definition of shear stress a relationship between the onset shear rate (γ^*) and the onset Fanning friction factor is produced and given by equation (14.3).

$$\gamma^* = \frac{1}{2}\frac{U_{avg}^2}{\nu} f^* \qquad (14.3)$$

Vanapalli *et al*. (2005) produced a relationship from data compiled in Virk (1975) for PEO polymer solutions (i.e. polymer type used in the current study) between the minimum shear rate for drag reduction (γ^*) and the solution molecular weight. This relationship is provided by equation (14.4).

$$\gamma^* = \left(3.35 \times 10^9\right) M_W^{-1} \qquad (14.4)$$

While there was significant scatter in the friction relationship results, the above approach produced repeatable results that are in excellent agreement with previous estimates of the molecular weight of the polymer used in the current study. The measurement of the molecular weight was ±8%.

14.3.3 Injection metering

The injection flow rate was measured by positioning the pressure vessel with the injection solution on a scale (SV-30, Acculab) and recording the change in weight (converted to mass) with respect to time with a handheld stop watch. The pressure vessel was pressurized with nitrogen gas between 60 and 140 kPa, which produced mass flow rates to 0.21 $kg\,s^{-1}$. Repeated runs were performed at the same condition to determine the accuracy of the flow rate measurement, and results indicate that the flow rate uncertainty was better than ±5%.

14.4 Polymer Mixing and Delivery

14.4.1 Polymer preparation

All testing was performed with polyethylene oxide water-soluble-resin (WSR) that had a mean molecular weight of 4.0 million (POLYOX WSR301, Dow Chemical) determined from the pressure drop apparatus measurements. The polymer started as a dry powder that was then mixed with water to produce the solutions used during testing. The polymer solutions were prepared by first filling a 0.12 m^3 reservoir with filtered tap water, which typically had a chlorine concentration of approximately 2 wppm. This water would

be treated with sodium thiosulfate to remove background chlorine, which has been shown to cause increased degradation of polymer solutions (Petrie *et al*., 2003). The chlorine level was monitored with a portable chlorine meter (ExStick CL200, Extech Instruments), and mixing would begin once there was no measureable level of chlorine. The reservoir was slowly emptied into separate containers while lightly sprinkling the dry powder into the stream of water. Once the desired quantity of polymer was wetted the containers were emptied back into the large reservoir and allowed to hydrate for a minimum of 45 hours. The batch was stirred periodically to promote uniformity of the polymer mixture. Each batch was characterized daily with the pressure drop apparatus to ensure that the polymer solution had not been degraded prior to testing. Figure 49 shows the estimated M_w versus duration of time following mixing from all the characterizations for seven separate batches. These results show minimal change in the molecular weight was observed over the first 211 hours (within the uncertainty of the measurement). The single characterization measured beyond 211 hours appears to have been significantly degraded. The maximum duration between mixing and the time tested was 211 hours and the majority of tested occurred within 100 hours of mixing. The stock solution, once hydrated, was diluted to a desired test concentration for injection. The dilution water was treated with sodium thiosulfate to remove the background chlorine. A small amount of Rhodamine 6G (typically < 3 wppm) was added to the injection sample to facilitate the PLIF measurements.

A polymer ocean was produced by adding sodium thiosulfate to the tunnel (the addition of sodium thiosulfate was performed daily regardless of whether a polymer

ocean was being prepared) until no measureable level of chlorine existed in the background water. Stock polymer solution was injected slowly into the tunnel through the model injector with the tunnel water nearly stationary. Periodically the water would be circulated slowly (< 1 $m\,s^{-1}$) to disperse the polymer throughout the tunnel volume. Once the required quantity of stock polymer solution was added to the tunnel, the tunnel would be circulated at low speed (~ 5 $m\,s^{-1}$) for approximately five minutes to produce a uniform polymer concentration. Once mixed a sample was drawn from the tunnel and characterized in the pressure drop apparatus. Additional samples were drawn periodically during testing with the polymer ocean, and testing was ended once significant deviation was observed from the stock characterizations.

14.4.1 Polymer injection method

The dye-laden polymer solution used for injection tests was fed to the polymer inlet manifold (see figure 46) by two 2.5 cm diameter flexible hoses that connected on each side of the tunnel test section. Each line was connected to a separate dip tube that drew the test solution from the bottom of the pressure vessel. The vessel was pressurized with nitrogen gas between 60 and 140 kPa (gage), which produced mass flow rates to 0.21 $kg\,s^{-1}$. The pressure difference between the vessel and the tunnel static pressure determined the injection rate. Typically the tunnel static pressure was fixed and the pressure in the vessel was adjusted with a regulator to obtain a desired injection rate.

14.5 Test Matrix

Testing was performed with three surface conditions: (1) hydraulically smooth, (2) transitionally rough and (3) fully rough. For the smooth surface, tests were performed with a water background and a homogeneous polymer solution background at concentrations sufficient for MDR (herein referred to as a MDR polymer ocean). The roughened surfaces were tested only with the water background. Speeds tested with polymer injection ranged from 5.5 to 10.6 $\mathrm{m\,s^{-1}}$. The polymer volumetric injection fluxes ranged from 1 to 15 Q_s, where Q_s is the flux of water in the near-wall region. The near-wall region is defined as $0 < y^+ < 11.6$, where y^+ is the wall normal distance (y) scaled with the viscous wall unit, $l_v = \nu/u_\tau$. Here u_τ ($=\sqrt{\tau/\rho}$) is the friction velocity. Wu & Tulin (1972) determined $Q_s = 67.3\nu$ by assuming a linear velocity profile and integrating the stream-wise velocity. Five nominal injection concentrations were tested (30, 100, 300, 1000 and 4000 wppm) and measurements made at a single downstream location, $x\text{-}x_{inj}$ = 61.6 cm. Concentration profiles are measured in the current study without a measure of the skin-friction. While skin-friction measurements would be advantageous, it was unnecessary since the focus of the current study is on the effect of surface roughness on polymer diffusion. Furthermore, the use of the skin-friction balances typically used to measure drag reduction was impossible with the test model selected for this study due to the model and sensor sizes.

Chapter 15. Results and Analysis

The results section is divided into two subsections: §15.1 Mean Velocity Profiles and §15.2 Polymer Diffusion. The first section includes mean velocity profiles and boundary layer parameters determined from measurements at the injection and measurement locations. The diffusion section provides experimental results from the concentration profiles obtained on the smooth- and rough-walled test model. These results are used to analyze the diffusion zones typical of a TBL modified with the addition of drag-reducing polymer additives.

15.1 Mean Velocity Profiles

At the start of testing the smooth surface boundary layer was characterized at the point of injection. Mean velocity profiles were acquired at speeds from 3.2 to 9.8 $\mathrm{m\,s^{-1}}$ and are shown in figure 50 normalized with the free-stream speed, U_∞, and the boundary layer thickness, δ. Here the boundary thickness was determined by directly measuring the free-stream speed and fitting the results to the form given in equation (15.1). From the figure it is apparent that speeds at and above 4.9 $\mathrm{m\,s^{-1}}$ are independent of Reynolds number, $Re_x = U_\infty x / \nu$. Thus the injection experiments were conducted only at speeds at or above 4.9 $\mathrm{m\,s^{-1}}$. The profiles above 4.9 $\mathrm{m\,s^{-1}}$ show good collapse to the power law curve given by equation (15.1) with $\alpha = 0.173$, where U is the velocity a distance y from the

wall. Table 7 provides a summary of the boundary layer parameters determined from the measured mean velocity profiles. Here δ^* is the displacement thickness defined in equation (15.2), θ is the momemtum thickness and Re_θ ($=U_\infty\theta/\nu$) is the momentum thickness based Reynolds number. The ratio of the distance downstream of the boundary layer trip to the trip height for the injection and measurement location are 1.1×10^4 and 7.2×10^4, respectively. Also of interest is the ratio of the boundary layer thickness to trip height, which are nominally 300 and 1000 for the injection and measurement locations on the smooth model, respectively.

$$\frac{U}{U_\infty}=\left(\frac{y}{\delta}\right)^\alpha \qquad (15.1)$$

$$\delta^* \equiv \int_0^\delta \left(1-\frac{U}{U_\infty}\right)dy=\frac{\alpha\delta}{\alpha+1} \qquad (15.2)$$

Additional boundary layer measurements were acquired at the downstream measurement location ($x=$ 84.5 cm) for each test configuration (*i.e.* smooth surface with and without a polymer ocean, 240-grit surface and 60-grit surface). These measurements were compiled and curves of the form provided in equations (15.1) and (15.3) were fitted to these data. Use of equation (15.3) is only appropriate for the smooth surface with a water background, but provides an estimate for other test configurations. This is due to only the smooth surface with a water background acquiring measurements from two downstream locations. Estimates for other test configurations appear reasonable since the predicted boundary layer thickness at the injection location for the rough surfaces are

comparable to the measurements on the smooth surface. Table 8 provides the constants, α, β and γ, in equations (15.1) and (15.3) for each test configuration.

$$\frac{\delta}{x} = \gamma \, \mathrm{Re}_x^{\beta} \qquad (15.3)$$

Skin-friction was not measured directly in the current study, however for assessing the roughness and analyzing the results it is useful to have an estimate of the turbulent scales (friction velocity and viscous wall unit). Equations (15.1) and (15.3) can be used with the smooth surface results to estimate the coefficient of friction ($C_f = 2\tau/\rho U_\infty^2$), although there would be a large degree of uncertainty due to the limited measurement locations along the model. Thus the coefficient of friction without polymer was determined from the average of: (1) the current experimental results; (2) White's (2006) momentum-integral analysis for a zero-pressure gradient, smooth flat plate; and (3) the Schultz-Grunow (1941) friction curve. Over the range of speeds the variation in friction velocities determined from the three independent methods varied by less then 5%. Table 9 shows the average coefficient of friction and the turbulent scales obtained from the above approach for the smooth model.

For the rough surfaces, the analysis found in White (2006) for turbulent flow over a rough-walled surface was used only to determine the turbulent scales. The experimental results were not used due to the lack of multiple measurement locations. White's analysis requires knowledge of the Reynolds number and the average roughness height to determine the skin-friction coefficient. The Reynolds number is known from the boundary layer measurements, but the average roughness height is more difficult to

define. An attempt to directly measure the average roughness height with a portable roughness meter was made, but even the transitionally rough surface exceeded the limit of its capability. Thus the average diameter of the roughness elements for each grit size was used as the average roughness height. These values are 53.5 and 268 μm for the transitionally and fully rough surfaces, respectively. The implicit relationship provided by White (2006) is provided in equation (15.4).

$$\mathrm{Re}_x \approx 1.73\left(1+0.3k^+\right)e^Z\left[Z^2-4Z+6-\frac{0.3k^+}{1+0.3k^+}(Z-1)\right] \qquad (15.4)$$

Here k^+ is the average roughness height, k, scaled with l_v and $Z=\kappa(2/C_f)^{1/2}$ (where κ is the Kármán constant chosen as 0.41 for the current analysis). An iterative process was used to determine the coefficient of friction for each Reynolds number tested with the transitionally rough surface. However, equation (15.4) was used only for three speeds tested with the fully rough surface to verify that over the range of speeds tested the surface could be considered fully rough. Thus a few select conditions were determined from equation (15.4) and compared with White's and Schlichting's (White, 2006) friction correlations for a fully rough surface, given in equations (15.5) and (15.6), respectively. These results were nearly identical and thus for simplicity the coefficient of friction was determined from the average of equations (15.5) and (15.6) for the fully rough surface.

$$C_f \approx \left[1.4+3.7\log_{10}\left(\frac{x}{k}\right)\right]^{-2} \qquad (15.5)$$

$$C_f \approx \left[2.87 + 1.58 \log_{10}\left(\frac{x}{k}\right) \right]^{-2.5} \qquad (15.6)$$

The results from the above analysis for the rough surfaces are provided in table 10 at the injection (x = 22.9 cm) and measurement (x = 84.5 cm) locations for three nominal speeds that spanned the range tested. According to White (2006) a hydraulically smooth wall corresponds to $k^+ < 4$, a transitionally rough wall has $4 < k^+ < 60$ and a fully rough wall as $k^+ > 60$. Thus over the range of speeds tested the 240-grit sandpaper was appropriately termed transitionally rough and the 60-grit sandpaper was appropriately termed fully rough. Of note is that the average roughness height for the smooth surface was measured to be 1.7 μm, which even at the highest speed tested $k^+ < 1$. Thus over the range of speeds tested the model without sandpaper applied to the surface was hydraulically smooth.

15.2 Polymer Diffusion

15.2.1 Mean concentration profiles

Mean polymer concentration, C, profiles normalized with the injection concentration, C_{inj}, for various injection conditions (acquired at a free-stream speed of 5.5 $\mathrm{m\,s^{-1}}$) are shown in figure 51. The profiles do not extend to the model surface due to a bright region near the model surface in the images created by reflected laser light from the model surface. Based on a comparison of calibrations, the results are repeatable and valid beyond y = 100 μm, which was selected as the minimum wall normal distance. The results show that at higher polymer injection conditions the peak in concentration appears

away from the wall surface (i.e. the minimum wall-normal distance measured). This has been observed by other researchers (Walker & Tiederman, 1989; Brungart *et al.*, 1991; Fontaine *et al.*, 1992; Winkel *et al.*, 2008) and is typical of PLIF measurements. Brungart *et al.* (1991) attributed this to a bias error caused by a slight index of refraction gradient created from the sheet of high concentrated polymer solution. The bias error decreases with decreasing polymer concentration until the polymer solution is considered dilute. This assumption is consistent with the observed profiles from the current study. That is the peak away from the wall was observed only with measurements of high concentration polymer. However, it is possible that this observation is not entirely the product of a bias error associated with a change in the index of refraction. The current study observed similar results to those reported by Fontaine *et al.* (1992) and Petrie *et al.* (2005) in the initial diffusion zone, characterized by a thin sheet of high concentration polymer, where the sheet periodically lifts off the wall in highly concentrated filaments. An example of this "lifting" phenomenon is provided in figure 52. Several instantaneous images are included from a single test condition (C_{inj} = 1000 wppm; Q_{inj} = 6.3 Q_s; U_∞ = 5.5 m s^{-1}) in figure 52. The test condition selected corresponds to the end of the intermediate-zone rather than the start of the intermediate-zone. This was done intentionally to illustrate not only a polymer sheet at the (right) wall and (left) "lifted", but also to provide a comparison of when (middle) polymer filaments are no longer present and the polymer solution is diffusing throughout the boundary layer. The only difference between the sheet shown in figure 52 and the sheet observed in the initial-zone is that the contrast is greater (there is less grey in the image and nearly almost all white/polymer or black/water). Thus lifting of the sheet, especially in the initial-zone, causes the near-wall

region to exhibit near-complete depletion of polymer. This would cause a significant drop in the mean concentration at the wall. This observation could also be responsible for the reduced drag reduction levels in the initial diffusion zone observed by numerous researchers (Petrie *et al.*, 1996; Petrie *et al.*, 2003; Petrie *et al.*, 2005; Elbing *et al.*, 2008; Winkel *et al.*, 2008). For the remainder of the discussion the maximum measured polymer concentration is used as the wall concentration, but the actual values are expected to be to 10% higher.

A diffusion length scale, λ, is introduced to further investigate the mean polymer concentration profiles. The definition of λ varies in the literature, but for the current study it is defined as the distance from the wall to where the polymer concentration drops to half the maximum concentration, $C/C_M(y/\lambda = 1) \equiv 0.5$. Here C_M is the maximum measured polymer concentration near the wall. Concentration profiles in the intermediate and final-zones typically have a self-similar profile that can be described by the empirical relationship derived by Morkovin (1965) and given in equation (15.7).

$$\frac{C}{C_M} = \exp\left[-0.693\left(\frac{y}{\lambda}\right)^a\right] \qquad (15.7)$$

Most experimental studies have found that for polymeric flows a = 1.5 in the intermediate-zone and a = 2.15 in the final-zone. Fontaine *et al*. (1992) noted that they measured some profiles that did not assume the form of equation (15.7). This alternative profile shape, see figure 53, has increased polymer concentration in the vicinity of the

wall. This alternative profile shape has been observed by other researchers (Wetzel & Ripken, 1970; Sommer & Petrie, 1991), but to date the majority of studies have not reported such profiles. Fontaine *et al.* (1992) suspects that the lack of reported profiles of this alternative form is due to a bias error that favors lower concentration measurements typical of the sampling technique used in most previous studies. Profiles from the current study take both the Morkovin (1965) and Fontaine *et al.* (1992) form, as shown in figure 53. The curves selected from the current study represent the extreme cases and the profile that best approximates the Morkovin (1965) form in the intermediate region. The high concentration result obviously is shifted upward in the near-wall region as a result of the peak occurring away from the wall, but still has the Morkovin (1965) form.

15.2.2 K-scaling

At this point in the discussion it is useful to introduce the scaling parameter K, defined in equation (15.8). This scaling parameter was first proposed by Vdovin & Smol'yakov (1978) and is the flux of polymer injected into the boundary layer non-dimensionalized with the downstream distance from the point of injection and the flow speed.

$$K = \frac{Q_{inj} C_{inj}}{U_{\infty}\left(x - x_{inj}\right)} 10^{-6} \qquad (15.8)$$

Here Q_{inj} is the volumetric flux of polymer solution per unit span injected and C_{inj} is the injection concentration in wppm. While the effectiveness of K-scaling is somewhat

limited (i.e. it is not a universal scaling), it has been successfully used to assess the overall performance of various polymer solutions. In the current study *K*-scaling is used to define and assess the performance of the polymer solutions within the various diffusion zones. With polymeric flows there are typically three observed diffusion zones: (1) initial or development, (2) intermediate or transition (some studies divide this region into two separate zones, intermediate and transition) and (3) final. The initial-zone is the region immediately downstream of the injector and is typically limited to distances on the order of tens of centimeters. The initial-zone is characterized by a thin layer of high concentration polymer at the wall surface and a near-zero polymer concentration throughout the remainder of the boundary layer. It is in this region (and at the start of the intermediate-zone) where the periodic "lifting" of the highly concentrated polymer filaments from the wall has been observed by Fontaine *et al*. (1992) and in the current study. The intermediate-zone is characterized by the rapid diffusion from the wall of the thin layer of high concentrated polymer solution observed in the initial-zone. The concentration profiles are typically of the form given in equation (15.7) with a wide range of values for *a* reported. However, most common for the intermediate region with dilute polymer solutions are values of *a* between 1.5 and 1.7. The final-zone is the most well understood diffusion region of the flow. In the final-zone the diffusion layer coincides with the boundary layer growth since the polymer has diffused through the entire boundary layer and any further dilution is from fluid entrainment due to boundary layer growth. Concentration profiles are well represented by equation (15.7) with $a = 2.15$.

Figure 54 shows the maximum measured polymer concentration versus K from the current investigation on the hydraulically smooth surface. Included in the plot are the three best-fit curves for the three diffusion zones from several research efforts (Fruman & Tulin, 1976; Vdovin & Smol'yakov, 1978; Vdovin & Smol'yakov, 1981; Fontaine *et al.*, 1992; Winkel *et al.*, 2008) compiled in Winkel *et al.* (2008). The current results are within the scatter of the results. However, measurements of λ/δ indicate that the current results should fall within the intermediate and final-zones only. Figure 54 does support this with the dashed lines that correspond to the best fit curves for data in the intermediate and final-zones. The slope in the final-zone is similar to that presented in Winkel *et al.* (2008), which is the slope based on fluid entrainment in a boundary layer assuming a $1/7^{th}$ power-law velocity profile. However, the slope for the intermediate-zone is decreased significantly. The slope in the intermediate-zone is conjectured to be a function of initial-zone development length, surface roughness, boundary layer thickness and turbulent fluctuations. The transition to the intermediate-zone is dependent on the development length, which the development length is dependent on injection conditions, turbulent fluctuations and surface roughness. The slope in the intermediate-zone is conjectured to increase with increased surface roughness, decreased boundary layer thickness and increased turbulent intensity. However, with the limited data set from the current study it is difficult to determine the appropriate scaling of these parameters, but further discussion and analysis of the intermediate diffusion process follows (§15.2.5) with analysis of the roughened surfaces.

15.2.3 Final diffusion zone

The final-zone is discussed first since it is the region that is best understood to date. As previously stated, the final-zone corresponds to the dilution of the polymer solution by fluid entrainment from boundary layer growth. With knowledge of the boundary layer growth and the concentration profiles it is possible to determine the expected *K*-scaling in the final-zone. To determine this scaling we start with the definition for the average concentration at a given downstream location, given by equation (15.9).

$$\overline{C} \equiv \frac{\dot{m}_p}{\dot{m}_s} 10^6 \qquad (15.9)$$

$\overline{C}$ is the mean concentration through the boundary layer at some downstream location, $\dot{m}_p$ is the mass flux of polymer injected per unit span and $\dot{m}_s$ is the mass flux of solution per unit span. The polymer mass flux is defined from the injection condition in equation (15.10) and the solution mass flux is determined from the fluid flux through the boundary layer at the point of interest, defined in equation (15.11).

$$\dot{m}_p = Q_{inj} C_{inj} \rho 10^{-6} \qquad (15.10)$$

$$\dot{m}_s = U_\infty \left(\delta - \delta^* \right) \rho \qquad (15.11)$$

When these relationships are substituted into equation (15.9) the mass density cancels and can be written as:.

$$\overline{C} = \frac{Q_{inj} C_{inj}}{U_\infty \left(\delta - \delta^*\right)} \qquad (15.12)$$

The mean concentration in the boundary layer can be related to the maximum (wall) concentration in the final-zone by noting that the concentration profile in the final-zone is well established as having the form of equation (15.7) with $a = 2.15$ and $\lambda = 0.64\,\delta$. When this concentration profile is integrated numerically it is found that $\overline{C} \cong 0.64\ C_M$. In addition δ^*, defined in equation (15.2), can be related to the flow parameters using equation (15.1). Now the relationships given in equations (15.3) and (15.2) with the results from the numerical integration of the concentration profile are inserted into equation (15.12) and produce a relationship between the maximum concentration and injection and flow conditions.

$$C_M = \frac{(\alpha + 1)\nu^\beta Q_{inj} C_{inj}}{0.64\,\gamma (U_\infty x)^{\beta+1}} \qquad (15.13)$$

For the current study the measurement location was fixed and the speed was varied only by a factor of two, thus we find that the maximum polymer concentration is approximately proportional to K (i.e. $Q_{inj} C_{inj}$) in the current study. However, in the final-zone the dilution is the product of fluid entrainment and thus the K dependence should depend on the downstream distance. Thus for a fixed quantity of injected polymer and assuming that in the final-zone $x/x_{inj} >> 1$, the relationship in equation (15.14) is obtained.

$$C_M = \frac{(\alpha+1)}{0.64\gamma}\left(\frac{\nu}{Q_{inj}C_{inj}}\right)^{\beta} 10^{6(\beta+1)} K^{\beta+1} \qquad (15.14)$$

Following the momentum-integral analysis of White (2006) for a flat-plate boundary layer with the traditional 1/7th power-law velocity profile β equals -1/7. Thus C_M would scale with $K^{6/7}$ in the final-zone, which is the scaling used by Winkel *et al.* (2008) for the final-zone. Therefore, the maximum concentration in the final-zone should scale with $K^{6/7}$ when a fixed quantity of polymer is used and the measurement location is varied and scale with K if a fixed measurement location is used and the flux of polymer varied. However, as seen in figure 54, either scaling collapses the data quite well.

15.2.4 Initial diffusion zone

Numerous studies have provided brief discussions on the initial-zone (Poreh & Cermak, 1964; Poreh & Hsu, 1972; Gebel, *et al*., 1978), but very few detailed investigations have been conducted on the initial-zone since it comprises a relatively short region within the flow. One exception is the work of Collins & Gorton (1976), which acquired concentrations profiles within 10 cm downstream of injection. Unfortunately these results are limited in use due to the injection scheme employed (discrete injection along the model span instead of a uniform slot or line source) and the concentration profiles were acquired with a Pitot probe at high concentrations (this measurement method has large uncertainties and a bias error towards lower concentrations when the polymer solutions are not dilute). Even though the initial-zone comprises only a short region within the flow it is critical to properly understand because

any improvements to PDR by clever injection schemes will only influence this region of the flow. If the initial-zone could be extended the cost benefit of PDR would significantly improve since the high concentration polymer would remain in the near-wall region longer, which would thus extend the downstream distance of high levels of drag reduction and delay intermediate-zone diffusion that rapidly transfers polymer from the surface. In the current study the measurement location was fixed and this significantly hinders the potential for quantifying the evolution of the polymer solution in the initial-zone. Furthermore, the measurement location was positioned so far downstream that even with the highest injection fluxes only the end of the initial-zone was observed, if at all. This limitation inspired a subset of experiments aimed at determining how far the initial-zone could be extended with "ideal" injection. Numerous efforts to optimize the injection method for PDR have been conducted, including Walker *et al*. (1986), with minimal success. Thus our current studied focused on attempting to extend the initial-zone downstream to our measurement location by suppressing the turbulent fluctuations in the flow with polymers. This was accomplished with a MDR polymer ocean having a background polymer concentration of at least 30 wppm and injecting polymer solutions into this modified TBL. Diffusion from the near-wall region still occurs at MDR, but the rate of diffusion will be minimized and thus the maximum development length possible should be achieved. Figure 55 shows the maximum concentration versus K from the MDR polymer ocean experiments. These results indicate that the initial-zone was extended by comparison of the solid lines given in Winkel *et al*. (2008) to the dashed lines that are the solid curves but with K multiplied by 0.15 and that roughly follow the current results. This can be thought of as extending the development length by a factor of

6.7. While this increase in the initial-zone length is beneficial, the overall improvement in the drag reduction performance would be minimal. This lack of improvement is because the initial-zone typically is on the order of tens of centimeters, which means that even if the length were increased by a factor of ten, the initial-zone is still only on the order of a meter. To help quantify this statement a relationship provided by Gebel *et al*. (1978), given in equation (15.15), will be used. This is a relationship between the maximum polymer concentration, the downstream distance and an initial-zone length, L_o. Here L_o is the distance from the injection slot at which the wall concentration drops to e^{-1} of its original value (i.e. the *e*-folding distance).

$$\frac{C_M}{C_{inj}} = \exp\left[\frac{-\left(x - x_{inj}\right)}{L_o}\right] \qquad (15.15)$$

If it is assumed that the evolution of the peak concentration takes the form of equation (15.15) then L_o for this ideal mixing condition can be estimated from the current measurements. For the values in the initial-zone with injection into the polymer ocean, the average L_o is approximately 0.9 m. If the goal is to implement PDR technology on a ship that is on the order of 100 meters, an increase of a meter in the initial-zone is a negligible improvement. Also of note is that figure 55 should only be used in the analysis of the initial-zone where concentrations are sufficient for MDR. This is due to the fact that in any real world application the dilution in the near-wall region will be with pure-water and not polymer solution, thus the near-wall concentration will be reduced continually to amounts insufficient for MDR in the intermediate- and final-zones.

These findings show that under ideal conditions the initial-zone can be extended, but further analysis of the MDR polymer ocean findings can produce further insight. The MDR asymptote from Virk *et al*. (1967) was used to estimate the percent drag reduction ($\%DR = 100\times[\tau_{wo}- \tau_w]/ \tau_{wo}$, where τ_w and τ_{wo} are the skin-friction with and without polymer injection, respectively) on the current model in the MDR polymer ocean by following the analysis of Larson (2003). Over the range of Reynolds numbers tested the *%DR* was predicted to be approximately 70. This was used with the water background skin-friction estimates for the smooth model (given in Table 9) to determine the local skin-friction and inner variables (friction velocity and viscous wall unit) for the MDR polymer ocean. Figure 56 shows the scaled mean velocity profiles at the measurement location (x = 84.5 cm) along with the ultimate mean velocity asymptote predicted by Virk *et al*. (1970), which is given by equation (15.16).

$$u^+ = 11.7\ \ln\left(y^+\right) - 17.0 \qquad (15.16)$$

The measured mean velocity profile shown in figure 56 is in excellent agreement with the ultimate mean velocity asymptote and thus the composite of the ultimate mean velocity asymptote and the viscous sublayer profile ($u^+ = y^+$) will be used subsequently as the assumed velocity profile for the MDR polymer ocean. Of note is that the ultimate asymptote was developed for homogeneous solutions, which is not the situation in the current study and thus the use of this profile is only approximate with injection. Similar to the work of Wu & Tulin (1972) the above profile can be integrated to determine the volumetric flux within a given region of the boundary layer. Equation (15.17) shows the

relationship used to determine the flux of fluid per unit span in the region extending from the wall to some thickness t, Q_t, where the velocity profile is defined as $u^+ = y^+$ for $y^+ < 10.4$ and equal to equation (15.16) for $y^+ \geq 10.4$.

$$Q_t = \nu \int_0^{t/l_\nu} u^+ dy^+ = \Phi \nu \qquad (15.17)$$

The above results give confidence in the estimated inner variables, upon which the initial-zone results are expected to be dependent. Thus the concentration profiles from the MDR polymer ocean were scaled using inner variables. This scaling failed to collapse all the profiles from injection into the MDR polymer ocean. However, for the profiles within the initial diffusion zone (where the definition of L_o in equation 15.15 was used as the definition of the initial-zone) the inner variable scaling produces a reasonable collapse, as shown in figure 57.

These profiles were used to define an integral diffusion length scale, L^*, which is defined in equations (15.18) and (15.19). While L^* is similar to λ, the integral approach is a more robust measurement in the initial-zone where steep concentration gradients are present.

$$\Psi = \int_0^{\infty} C(y) dy \qquad (15.18)$$

$$0.5\Psi = \int_0^{L^*} C(y) dy \qquad (15.19)$$

L^* is scaled now with the free-stream speed and the injection flux to account for the initial thickness of the layer at the point of injection, L^*U_∞/Q_{inj} and plotted versus the K-parameter previously used. These results only collapsed data at a given concentration. Thus a more appropriate scaling was required. L^*U_∞/Q_{inj} was shown to be dependent on the Reynolds number based on the distance from the injector ($Re_{xo} = U_\infty x_o/\nu$, where $x_o = x–x_{inj}$), the scaled volumetric flux being injected (Q_{inj}/Q_s) and C_{inj}. By investigation it was shown that the relationship takes the form given in equation (15.20).

$$\frac{L^*U_\infty}{Q_{inj}} = A_1 \mathrm{Re}_{xo}^{c_1}\left(\frac{Q_{inj}}{Q_s}\right)^{c_2} C_{inj}^{c_3} \qquad (15.20)$$

Here c_i (i = 1, 2, 3) are constants to be determined and throughout the analysis below A_i are also constants (where again i = 1, 2, 3). In the initial-zone the development downstream of the injector can be thought of as the development of a second boundary layer submerged within the free-stream TBL. Thus it is assumed that L^* grows in the initial-zone similar to the boundary layer thickness in a TBL. In the current study the TBL is a polymer ocean at MDR and thus the traditional boundary layer growth relationship is not appropriate for the analysis. Instead, Giles (1968) determined the relationship between the overall drag coefficient and the Reynolds number based on the model length for a polymer ocean at MDR. That relationship can be used to determine the boundary layer thickness dependence on the downstream distance based Reynolds number, given in equation (15.21), using momentum-integral analysis.

$$\frac{\delta_p}{x_o} = A_2 \, \mathrm{Re}_{xo}^{-0.3} \qquad (15.21)$$

Here δ_p is the boundary thickness of the "polymer boundary layer" at the model surface in the initial diffusion zone. Thus it is assumed that L^* is proportional to δ_p, which allows equation (15.20) to be rewritten in the form provided by equation (15.22). This form makes it apparent that $c_1 = 0.7$.

$$L^* = 67.3 A_1 x_o \, \mathrm{Re}_{xo}^{c_1 - 1} \left(\frac{Q_{inj}}{Q_s} \right)^{c_2 + 1} C_{inj}^{c_3} \qquad (15.22)$$

Furthermore integrating equation (15.17) over a range of wall unit distances from $2 \le Q_{inj} / Q_s \le 14$ produced the relationship between the injected thickness, t, and Q_{inj}/Q_s, which is given by equation (15.23).

$$\frac{t}{l_\nu} = 10.5 \left(\frac{Q_{inj}}{Q_s} \right)^{0.6} \qquad (15.23)$$

It is assumed that l_ν scales with the free-stream speed and that the influence of the volumetric flux is primarily a shifting forward of the virtual origin of this "polymer boundary layer". Thus t should be proportional to δ_p from equation (15.21) when x_o is on the order of L^*. Thus inserting the relationship from equation (15.23) into equation (15.21) and rearranging produces equation (15.24). Rearranging equation (15.22) and noting that near the injector $L^* \sim x_o$, it is found that $c_2 \approx -0.74$.

$$\mathrm{Re}_{xo} = A_3 \left(\frac{Q_{inj}}{Q_s} \right)^{0.86} \qquad (15.24)$$

Finally c_3 was determined by fitting the data with a best-fit power-law curve and determining that $c_3 \approx 0.142$. Figure 58 shows the results using the above scaling arguments for data collected in the initial-zone with injection of polymer into the MDR polymer ocean. Also included in the graph is the best-fit curve to the results, which is provided in equation (15.25).

$$\frac{L^* U_\infty}{Q_{inj}} = \left(4.16 \times 10^{-4}\right) \mathrm{Re}_{xo}^{0.7} \left(\frac{Q_{inj}}{Q_s} \right)^{-0.74} C_{inj}^{0.142} \qquad (15.25)$$

These results have the expected finding that the diffusion length increases with increased volumetric injection flux, increased downstream distance and decreased speed. The one less-intuitive finding is that the diffusion length increases with increased polymer concentration. This prevents the possibility of keeping the polymer solution near the wall by injecting small quantities of high concentrated polymer solution. This observation is most likely the product of the increased viscoelastic properties of the polymer solution as concentration increases. Injecting highly concentrated solutions apparently results in extreme filamentation at the injection location that promotes three-dimensionality and thus increases diffusion of the polymer from the wall.

Since the current research effort focuses on implementing PDR on surface ships several of the parameters in the above scaling have narrow ranges. The free-stream speed for such an application is between 5 and 20 ms^{-1} and thus using U_∞ = 10 ms^{-1} is an excellent approximation. The volumetric flux being injected is also bounded by the flux of fluid from the wall through the buffer layer, $y^+ \leq 30$, because the drag reduction phenomenon is known to occur in this region of the flow (Dubief *et al*., 2004). Numerical integration of equation (15.17) for $y^+ \leq 30$ shows that the flux in this region is approximately 6 Q_s. Thus the maximum volumetric flux being injected should be on the order of 10 Q_s. These bounded values can be used to produce a relationship between injection concentration and initial-zone length when combined with equation (15.25), the initial-zone length definition provided by equation (15.15) and noting that $L^* U_\infty / Q_{inj}$ has a maximum value of ~15 in the initial-zone. This relationship is given by equation (15.26) with $L^* U_\infty / Q_{inj} = 15$, $Q_{inj} = 10\ Q_s$ and $x\text{-}x_{inj} = L_o$. In the following analysis U_∞ = 10 ms^{-1} and $\nu = 10^{-6}$ $\mathrm{m}^2\mathrm{s}^{-1}$.

$$L_o = 3.69 \times 10^7 \frac{\nu}{U_\infty} C_{inj}^{-0.203} \qquad (15.26)$$

This demonstrates that the initial-zone length can be increased significantly by injecting very low concentrations of polymer solution. However, the concentration must also be sufficient to deliver appropriate quantities of polymer to the flow to produce significant levels of drag reduction. Thus it is important to compare both the initial-zone length and the *%DR* as a function of injected polymer concentration (with $U_\infty \sim 10$ ms^{-1} and $Q_{inj} \sim 10\ Q_s$). The *%DR* as a function of concentration is given by an empirical drag

reduction curve first proposed by Virk *et al*., (1967) and given by equation (15.27). It provides a relationship between polymer properties, polymer concentration and *%DR*. This can be used to determine the *%DR* as a function of injected polymer concentration. The polymer properties, denoted as *[%DR]* and *[C]*, are the intrinsic drag reduction and intrinsic viscosity, respectively. Winkel *et al*. (2008) used the same polymer (WSR301) tested in the current study and provided a range for both properties: $17 \leq [\%DR] \leq 32$ wppm^{-1} and $2 \leq [C] \leq 3$ wppm. The product of the intrinsic drag reduction and intrinsic concentration gives the maximum drag reduction the polymer can achieve, $\%DR_M = [\%DR][C]$, which has already been estimated to be 70. Now with equation (15.15) and $x - x_{inj} = L_o$ the maximum polymer concentration, C_M, as a function of injected polymer concentration is known, which when inserted into equation (15.27) produces the *%DR* as a function of injected polymer concentration at the end of the initial-zone ($[C]$ = 2.5 wppm and $[\%DR]$ = 28 wppm^{-1} was used in the analysis, which sets the $\%DR_M$ = 70). This relationship along with the initial-zone length and the product of the *%DR* and initial-zone length are plotted versus injected polymer concentration in figure 59.

$$\frac{\%DR}{\%DR_M} = \frac{C_M}{[C] + C_M} \qquad (15.27)$$

Figure 59 illustrates that to produce initial-zone lengths longer than ~1 m the *%DR* must significantly decrease (real-world applications will exhibit a more dramatic drop since the dilution will be with pure-water and not polymer solution). Additionally, even with *%DR* decreasing to ~10 the initial-zone length is still below 4 m. This shows that to achieve *%DR* levels approaching $\%DR_M$ multiple injection locations would be

required with spacing on the order of 1 m. These results indicate that even with an ideal injection scheme its influence on the overall performance of PDR is limited to the first meter downstream of the injector. Furthermore, the product of the *%DR* and initial-zone length produces an optimum injection condition of approximately 30 wppm injection, which produces an initial-zone length of ~1.6 m. This approach significantly over estimates the initial-zone length in real-world applications and it is still limited to be on the order of one meter.

15.2.5 Intermediate diffusion zone

The intermediate-zone is the region where the thin layer of high concentration polymer present in the initial-zone is diffused rapidly through the boundary layer. This region extends downstream until the final-zone is reached. It is difficult to study the intermediate-zone since it is sensitive to the initial-zone development length, boundary layer thickness, turbulent intensity and surface roughness as well as the injection conditions. The current study is limited significantly in assessing the intermediate diffusion zone behavior as testing was conducted over a limited range of flow speeds at a single measurement location. Furthermore the length of the intermediate-zone should be on the order of 10δ (smooth model intermediate-zone ~ 10 cm) which, with the thin boundary layer and a single measurement location, facilitate a narrow range of flow conditions for measurements in the intermediate-zone. To properly analyze this diffusion zone multiple measurements locations are required within the initial, intermediate and final diffusion zones preferably with a thick boundary layer. However, some qualitative

observations from the current study are possible and the intermediate-zone dependence on surface roughness can be investigated.

The concentration profiles for the rough surfaces were similar in shape to those previously discussed for the smooth model with injection into the water background. Figures 60 and 61 show the maximum polymer concentration versus K for the transitionally rough and fully rough surfaces, respectively. The roughness appears to shorten the initial-zone length, which results in the data collected on the rough surfaces being either in the intermediate or final diffusion zone. These results illustrate that the K parameter scales individual experimental data reasonably, and thus the reason it has been a useful tool in assessing the performance of various polymer solutions. However, the K parameter fails to collapse data from the three surface conditions even over the same range of injection and flow conditions. It is suspected that the maximum concentration should also depend on k^+ since the roughness length will impact the transition to the intermediate-zone and the friction velocity is a measure of the turbulent intensity. The other major parameter expected to influence the intermediate-zone is the boundary layer thickness, however the boundary layer thickness had minimal variation in the current study. By investigation, the current results in the intermediate-zone were collapsed reasonably well with the relationship given by equation (15.28). The use of $(1+k^+)$ was selected so that as k goes to zero the scaling remains finite. This scaling is shown in figure 62 with the intermediate-zone defined as $C_M/C_{inj} < e^{-1}$ (Gebel *et al*., 1978) and $\lambda/\delta < 0.64$ (Poreh & Cermak, 1964).

$$C_M = \left(5.14 \times 10^{12}\right) K^{1.5} \left(1 + k^+\right)^{-0.2} \qquad (15.28)$$

While the above relationship shows an excellent collapse of the data over the range of injection, flow and surface conditions, a much more thorough investigation is required to assess the intermediate-zones dependence on other parameters and how universal the scaling factors are. However, these results stress the need to not only scale the results with the injection and flow conditions (K) but also the scaled roughness height (k^+).

Chapter 16. Summary and Conclusions

While limited in scope the current study provides corroborative evidence of previous research efforts and several conclusions are drawn about the diffusion process of polymer solutions injected within a turbulent boundary layer with smooth or rough surfaces. The measured concentration profiles from both the smooth and rough surfaces had a form similar to that predicted by Morkovin (1965) or that observed by Fontaine *et al.* (1992) (with higher concentration extending from the wall). The peak polymer concentration was observed away from the wall when high polymer concentrations were present, which previously had been attributed solely to a bias error from the PLIF measurement technique. However, it was observed also in current and previous studies that the high concentration layer of polymer periodically lifts from the wall under these same conditions, and thus could be partially responsible for the observed peak occurring away from the wall.

The maximum measured polymer concentrations were scaled using K and the three typical diffusion zones (initial, intermediate and final) were observed. Comparison between the current study with a hydraulically smooth surface and previous work compiled in Winkel *et al.* (2008) showed agreement within the scatter of previous studies. However, the slope in the intermediate-zone for the current study was reduced

significantly compared to the best-fit curve of Winkel *et al*. (2008). This variation in slope is not surprising since the intermediate diffusion zone slope is conjectured to be the most sensitive to test conditions (boundary layer thickness, free-stream speed, downstream distance and injection conditions).

Analysis of the final diffusion zone illustrates that K is not a universal scaling but is still a useful parameter for analysis of PDR results. In the current study where the polymer flux was varied and the downstream location was fixed C_M scaled with K; however, if the flux of injected polymer is fixed and the downstream distance varied, C_M should scale with $K^{6/7}$ (assuming a $1/7^{\text{th}}$ power-law velocity profile).

The initial-zone diffusion was investigated using a polymer ocean at concentrations sufficient for MDR, which thus extended the initial-zone to its maximum length for the conditions tested. Concentration profiles in the initial-zone collapse when scaled using inner variables and were used to determine an integral diffusion length scale, L^*. The scaled integral diffusion length (L^*U_∞/Q_{inj}) had to be less than 15 to be within the initial-zone and scaled with Re_{xo}, (Q_{inj}/Q_s) and C_{inj} in the initial-zone. These findings indicate that the initial-zone length, even under ideal injection conditions, can only be extended to approximately 1 m and still supply sufficient quantities of polymer to produce significant drag reduction. Furthermore, in real-world applications this length will be reduced regardless of the injection scheme.

Analysis of the intermediate diffusion zone was limited to the dependence on a narrow range of injection and flow conditions, but investigated three separate surface conditions (smooth, transitionally and fully rough). Results from the three surface conditions reveal that C_M scales with the product of $K^{3/2}$ and $(1+k^+)^{-0.2}$ in the current study. Due to the minimal range of flow and injection conditions the universality of this scaling could not be investigated; regardless, it shows that the surface roughness plays a significant role in the intermediate diffusion process.

TABLES AND FIGURES

$U_\infty\ (ms^{-1})$	$\delta\ (mm)$	$\delta^*\ (mm)$	$\theta\ (mm)$	Re_x	Re_θ
3.2	1.9			7.4×10^5	
4.9	2.9	0.43	0.32	1.1×10^6	1.6×10^3
5.3	2.9	0.43	0.32	1.2×10^6	1.7×10^3
6.6	2.9	0.42	0.31	1.5×10^6	2.1×10^3
8.2	2.8	0.42	0.31	1.9×10^6	2.5×10^3
9.8	2.8	0.41	0.31	2.3×10^6	3.0×10^3

Table 7. Summary of boundary layer parameters at the point of injection (x_{inj} = 22.9 cm) determined from the PIV measurements on the smooth model configuration.

Surface	Background	α	γ	β
Smooth	Water	0.173	3.64×10^{-2}	-0.0749
Smooth	Polymer Ocean	NA[1]	4.48×10^{-2}	-0.1354
240-grit	Water	0.179	1.16×10^{-4}	0.3253
60-grit	Water	0.272	8.48×10^{-6}	0.5144

Table 8. Summary of constants used to characterize the boundary layer at the measurement location (x = 84.5 cm) determined from the PIV measurements.

[1] The smooth surface polymer ocean velocity is not well approximated by the form given in equation (15.1).

$x\ (cm)$	$U_\infty\ (ms^{-1})$	$Re_x\ (\times 10^{-6})$	$C_f\ (\times 10^3)$	$u_\tau\ (ms^{-1})$	$l_v\ (\mu m)$
22.9	3.2	0.7	3.5	0.13	7.4
22.9	4.9	1.1	3.3	0.20	5.0
22.9	5.3	1.2	3.2	0.21	4.7
22.9	6.6	1.5	3.1	0.26	3.8
22.9	8.2	1.9	3.1	0.32	3.1
22.9	9.8	2.3	3.0	0.38	2.6
84.5	3.3	2.8	2.9	0.13	7.9
84.5	5.0	4.2	2.7	0.18	5.4
84.5	5.4	4.6	2.7	0.20	5.0
84.5	6.7	5.7	2.6	0.24	4.1
84.5	8.4	7.1	2.6	0.30	3.3
84.5	10.2	8.6	2.5	0.36	2.8
84.5	12.0	10.2	2.4	0.42	2.4

Table 9. Summary of friction coefficients and turbulent scale estimates for the smooth model configuration with a tap-water background.

Surface	x (cm)	U_∞ (ms^{-1})	Re_x ($\times 10^{-6}$)	u_τ (ms^{-1})	l_v (μm)	k^+
240-grit	22.9	5.4	1.2	0.27	3.7	14
240-grit	22.9	8.5	1.9	0.42	2.4	22
240-grit	22.9	10.3	2.4	0.51	2.0	27
240-grit	84.5	5.4	4.5	0.24	4.2	13
240-grit	84.5	8.5	7.2	0.37	2.7	20
240-grit	84.5	10.3	8.7	0.45	2.2	24
60-grit	22.9	5.6	1.3	0.32	3.1	86
60-grit	22.9	7.7	1.8	0.44	2.3	120
60-grit	22.9	10.7	2.5	0.62	1.6	165
60-grit	84.5	5.6	4.7	0.28	3.6	74
60-grit	84.5	7.7	6.5	0.38	2.6	100
60-grit	84.5	10.7	9.1	0.53	1.9	140

Table 10. Turbulent scales for the roughened surfaces determined by using the average diameter of the roughness elements for k and applying White's (2006) analysis of turbulent flow past a rough plate.

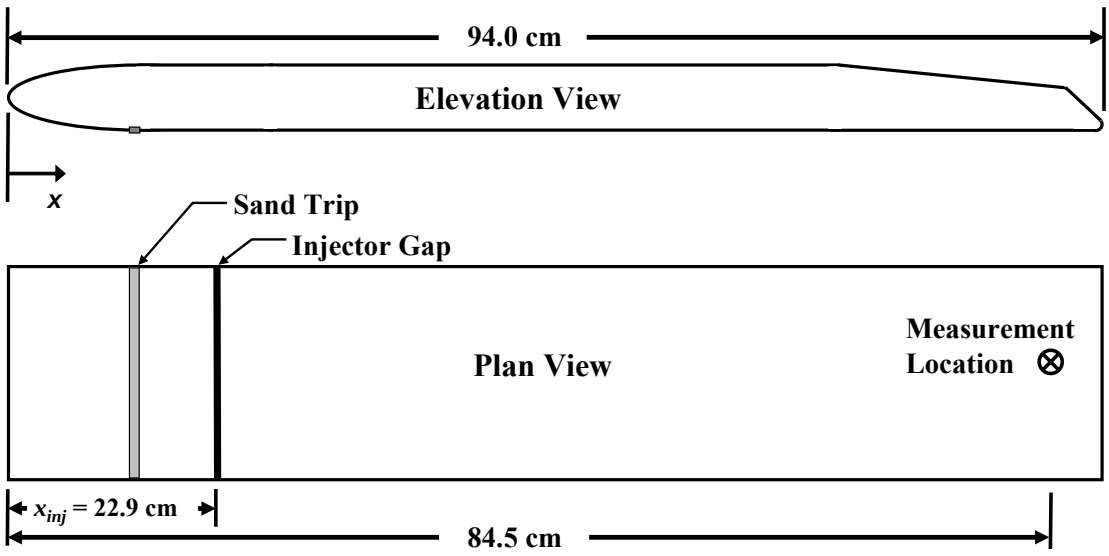

Figure 45. Schematic of the test model with the injection and measurement locations shown. The working surface is downward in the side elevation view at the top of figure.

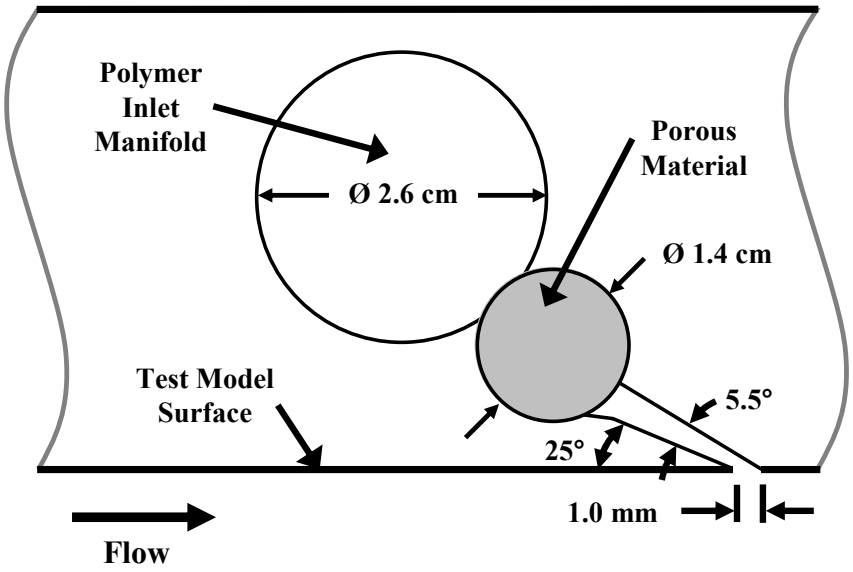

Figure 46. Schematic elevation view of the flush-mounted slot used to inject the polymer solution into the TBL. The 1.0 mm gap is flush with the model working surface and contacts the boundary layer flow.

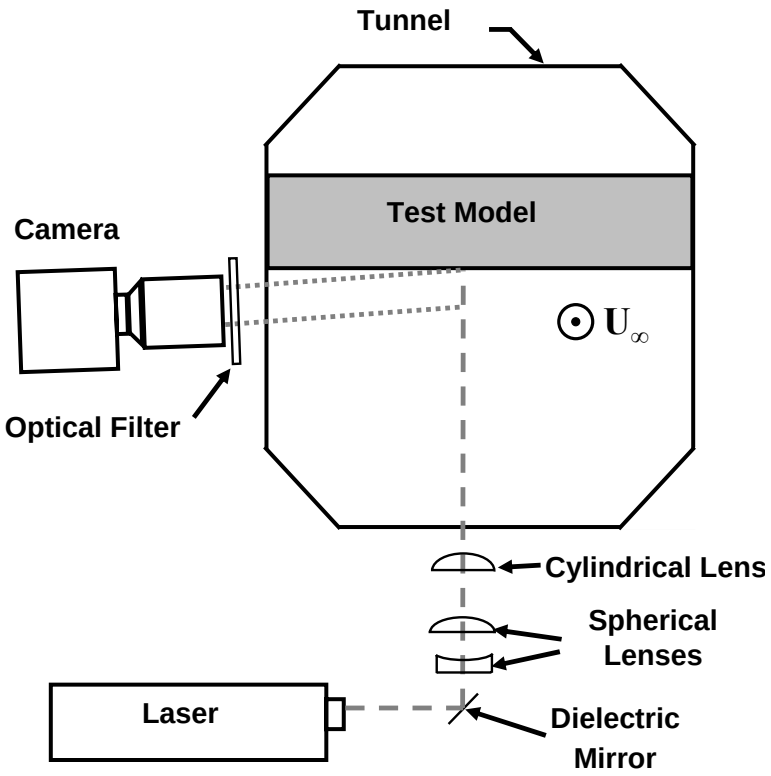

Figure 47. Optical setup used to measure both the mean velocity profiles and the mean concentration profiles with PIV and PLIF, respectively.

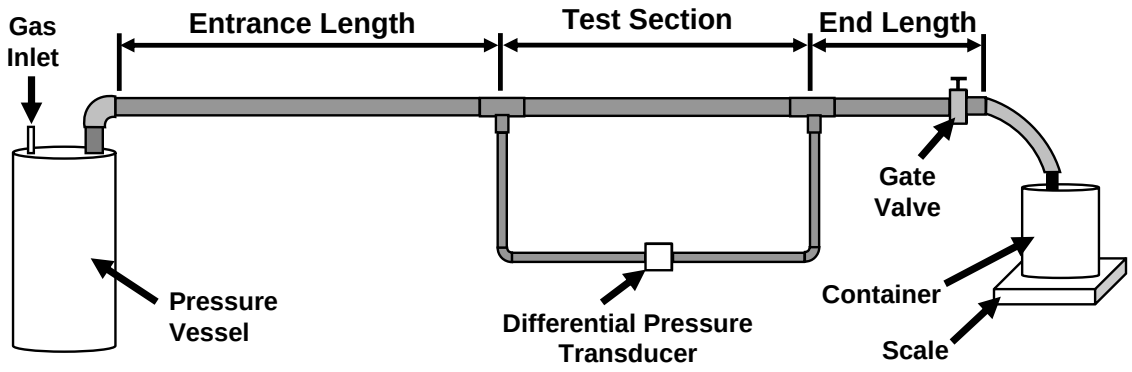

Figure 48. Schematic of the pressure drop apparatus used to characterize and monitor the polymer solutions throughout testing.

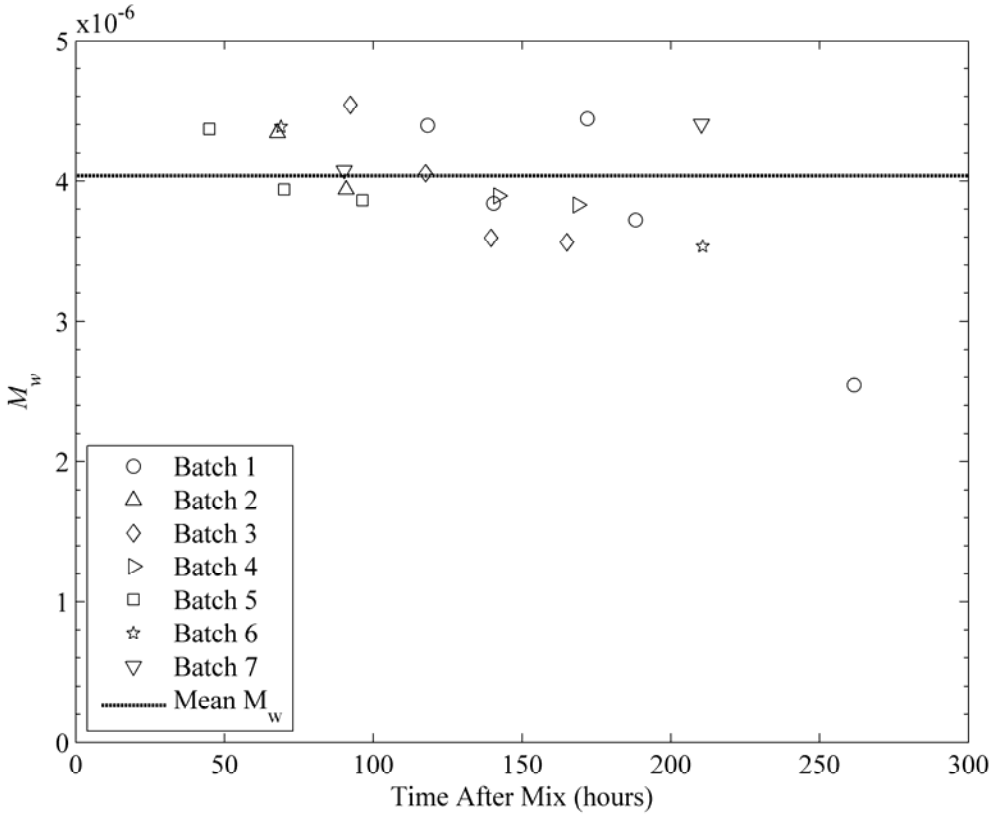

Figure 49. Polymer solution batch characterizations performed with the pressure drop apparatus. Results are presented as the mean molecular weight plotted versus the time following the mixing of the batch. Mild degradation appears to begin approximately 100 hours after mixing, but significant polymer degradation was not observed until ~250 hours following mixing. Majority of testing was conducted within 100 hours following the batch mixing and all injection testing was conducted within 211 hours of mixing.

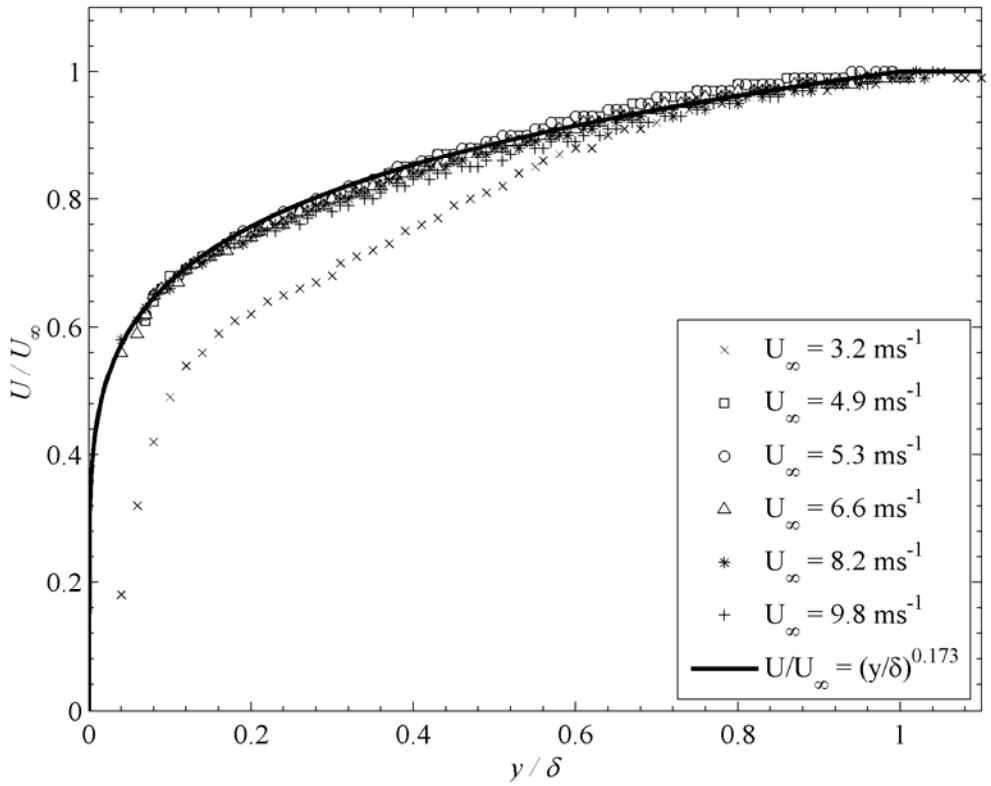

Figure 50. Mean velocity profiles at the injection location normalized with outer variables. For speeds at or above 4.9 m s^{-1} the profiles exhibit good collapse. The best-fit curve of the data greater than or equal to 4.9 m s^{-1} is included for comparison.

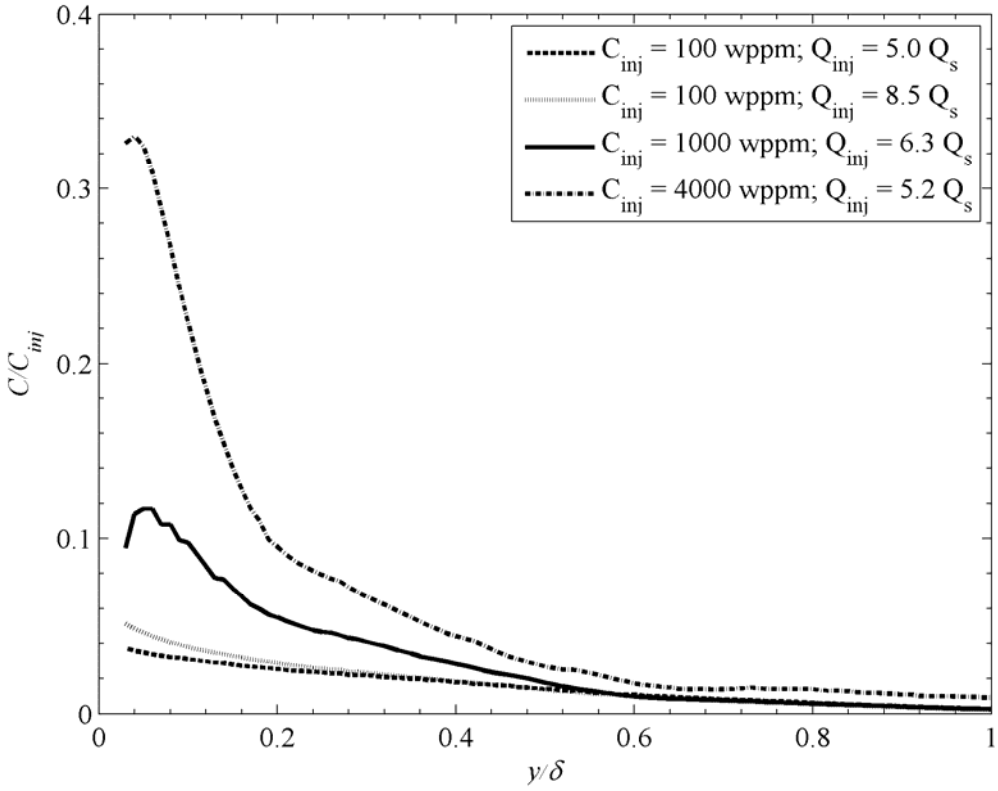

Figure 51. Mean polymer concentration profiles for various injection conditions at a free-stream speed of 5.5 m s^{-1}. All results were acquired at x = 84.5 cm. Q_{inj} is the volumetric flux of polymer injected per unit span.

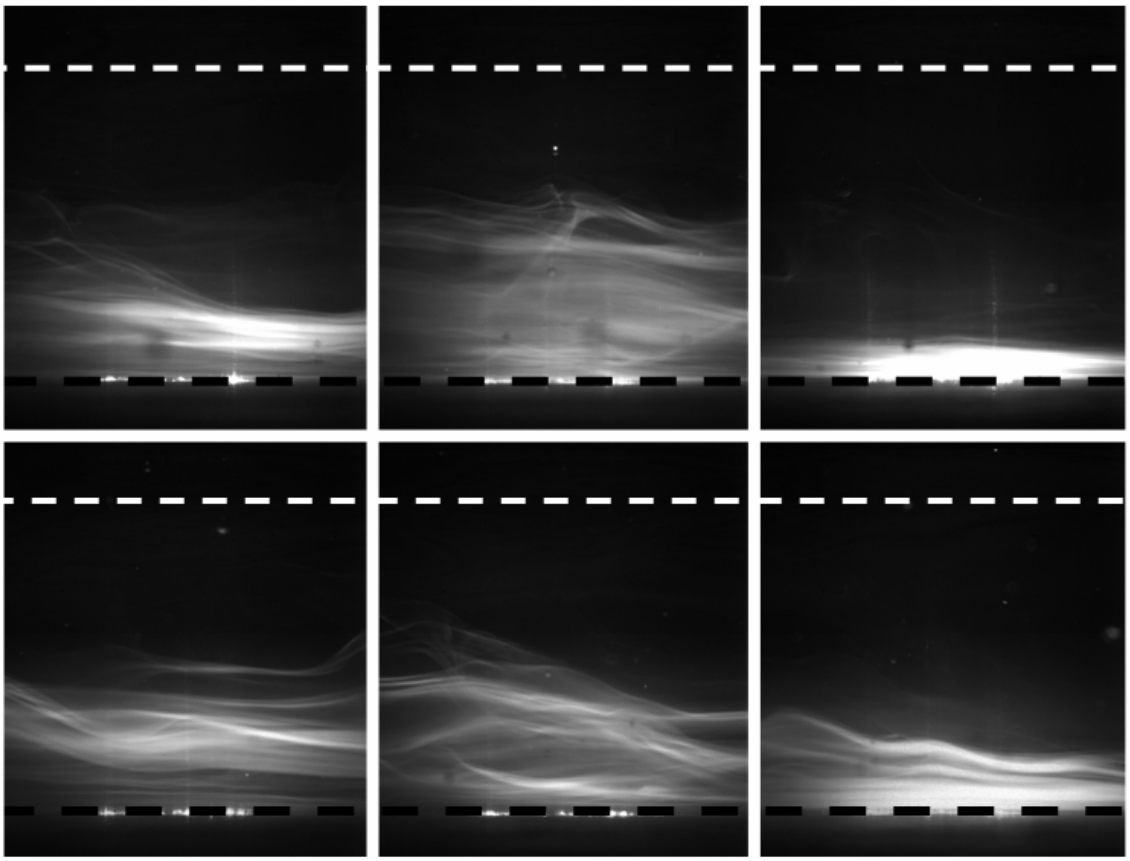

Figure 52. Instantaneous PLIF images from a single test condition (C_{inj} = 1000 wppm; Q_{inj} = 6.3 Q_s; U_∞ = 5.5 m s^{-1}) illustrating some of the typical flow patterns observed at the end of the initial-zone and start of the intermediate-zone. The bright regions are polymer solution with the maximum concentration on the order of the injection concentration (1000 wppm). Black and white dashed lines correspond to the wall and boundary layer thickness locations, respectively. The condition presented is at the start of the intermediate-zone rather than the end of the initial-zone. This condition was selected to compare between (left) a "lifted" polymer sheet, (right) a polymer sheet near the wall and (middle) the polymer diffusing through the boundary layer.

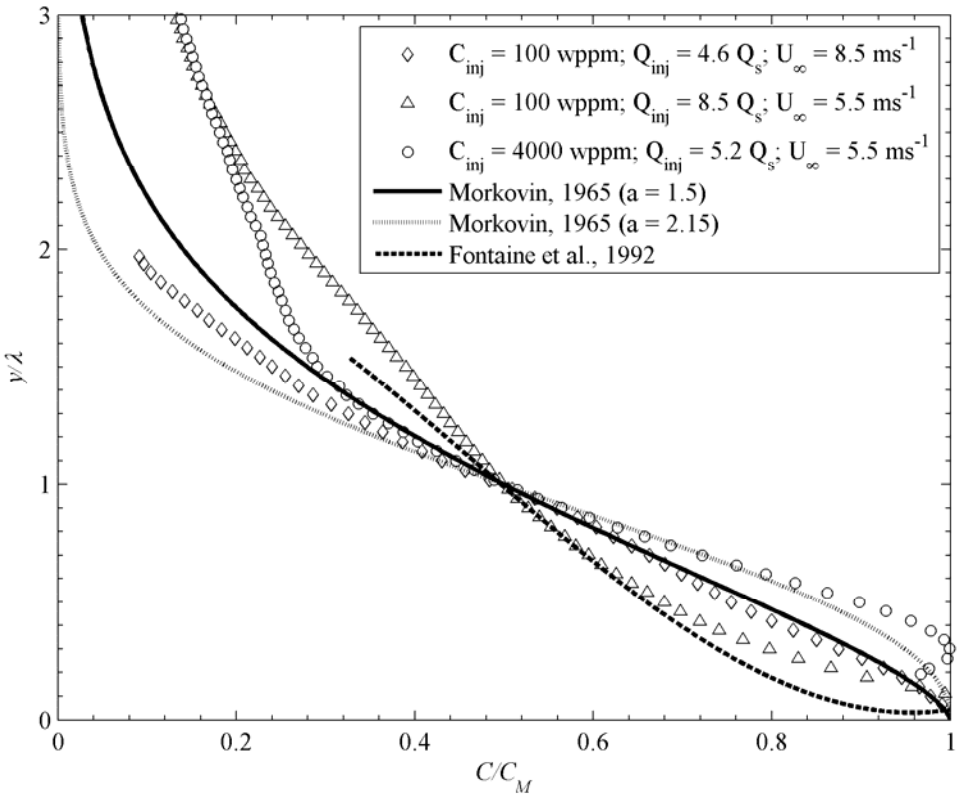

Figure 53. Mean polymer concentration profiles scaled with the diffusion length, λ. Results correspond to the intermediate and final-zones of diffusion and can be approximated by curves of the form purposed by Morkovin (1965) and given in equation (15.7) or observed by Fontaine *et al.* (1992).

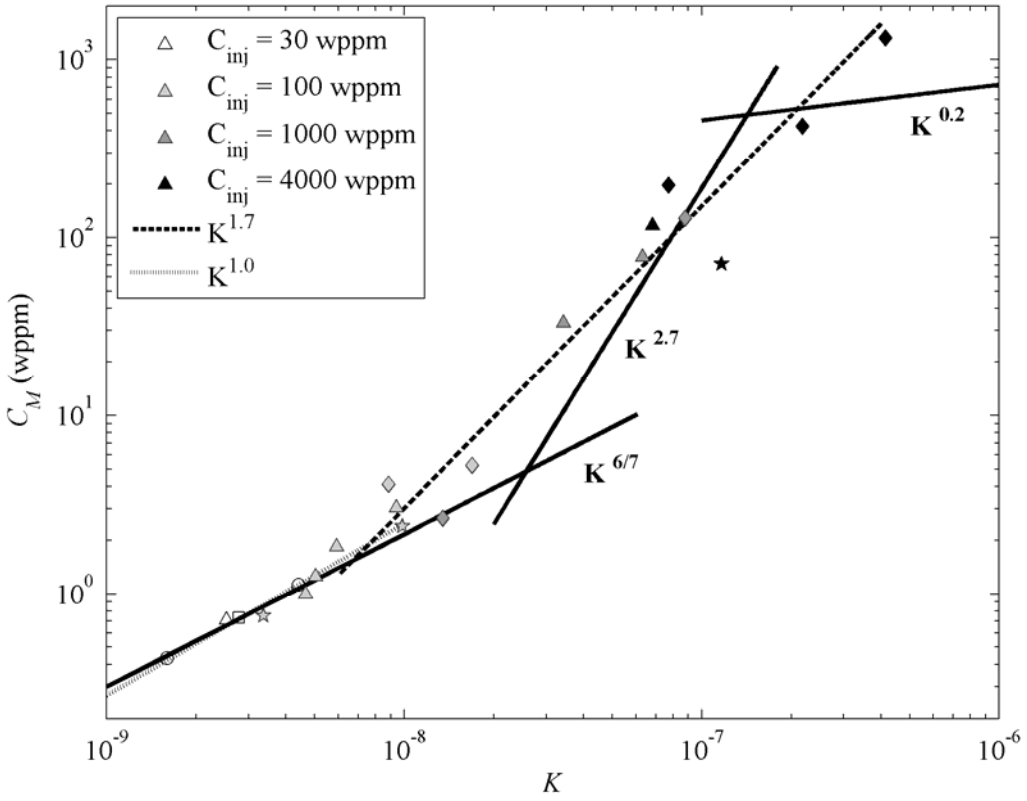

Figure 54. Maximum local concentration, C_M, measured with PLIF versus K for the hydraulically smooth surface. Data were collected with injection fluxes between 0.7 and 10 Q_s at free-stream speeds of 5.5 (◊), 7.4 (o), 8.5 (△), 9.1 (□) and 10.2 (☆) m s^{-1}. Dashed lines are best fit curves of the current data in the intermediate ($K^{1.7}$) and final ($K^{1.0}$) zones. The solid lines correspond to best-fit curves presented in Winkel *et al.* (2008).

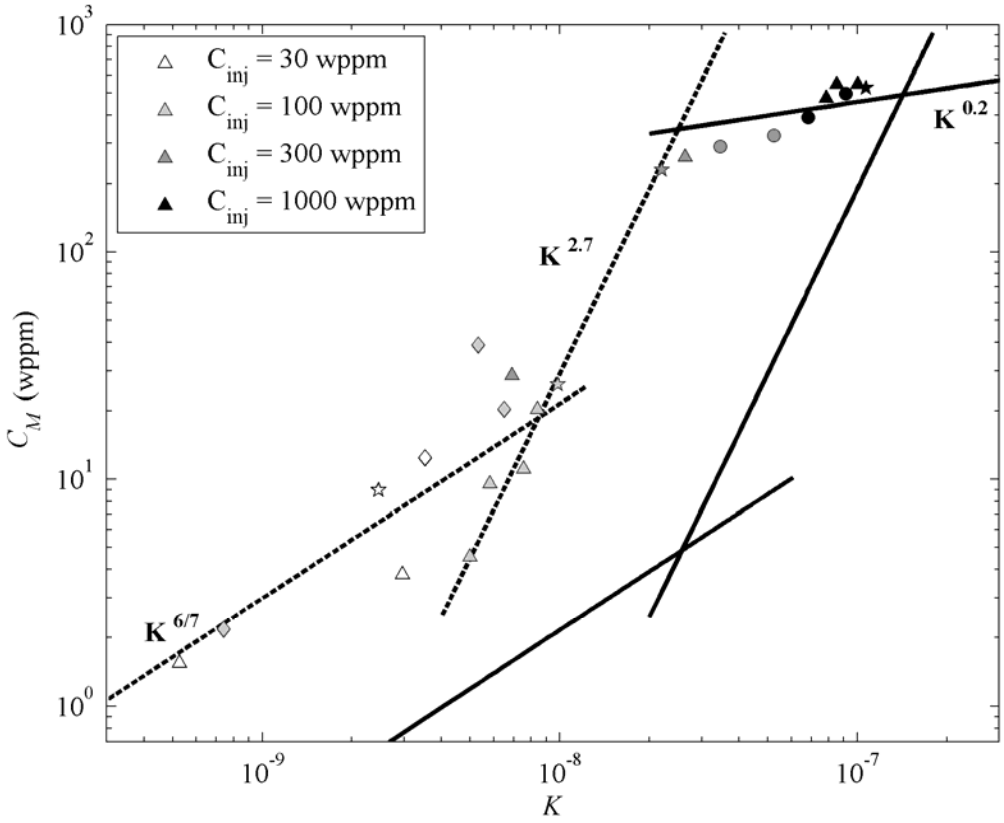

Figure 55. Maximum polymer concentration, C_M, versus K for the hydraulically smooth surface in a polymer ocean of at least 30 wppm. Data were collected with injection fluxes between 0.4 and 12 Q_s at free-stream speeds of 5.5 (◊), 7.4 (o), 8.5 (△) and 10.2 (☆) m s^{-1}. The solid lines are the best fit curves from Winkel *et al.* (2008) and the dashed lines are the solid lines with K multiplied by 0.15.

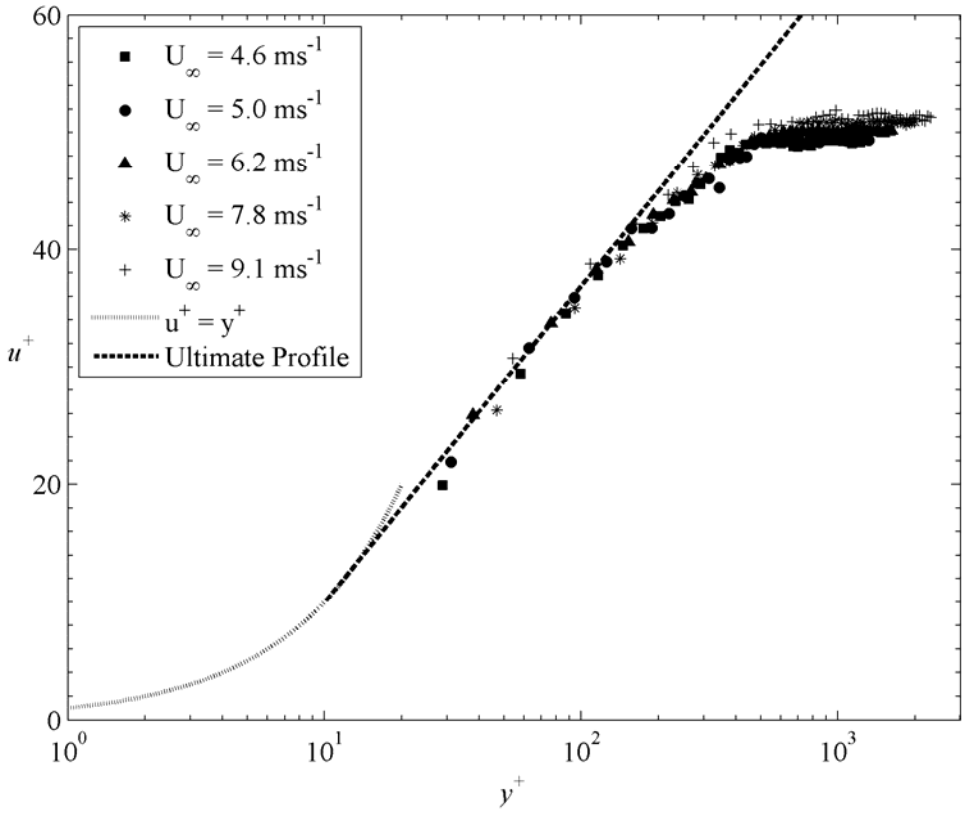

Figure 56. Mean velocity profiles at the downstream measurement location non-dimensionalized with inner variables. The inner variables were determined from the smooth model results with a water background and an estimate of *%DR* = 70, following the analysis of Larson (2003). The results are in good agreement with the ultimate mean velocity asymptote of Virk *et al*. (1970).

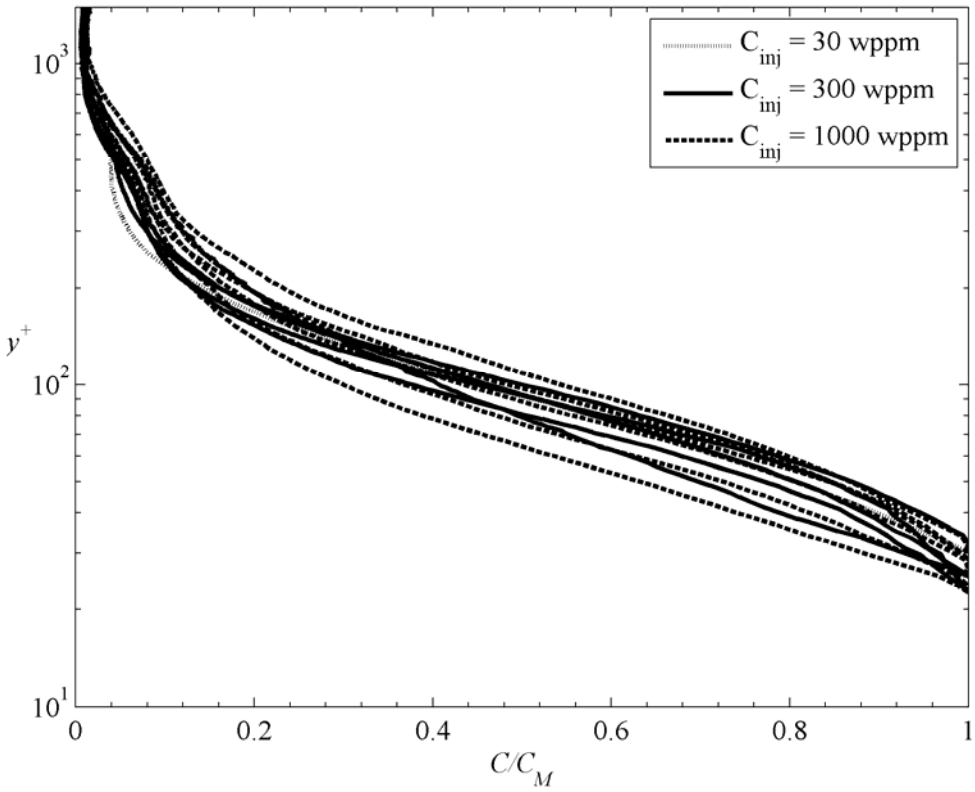

Figure 57. Mean concentration profiles scaled with inner variables for conditions in the initial diffusion zone from tests with the MDR polymer ocean.

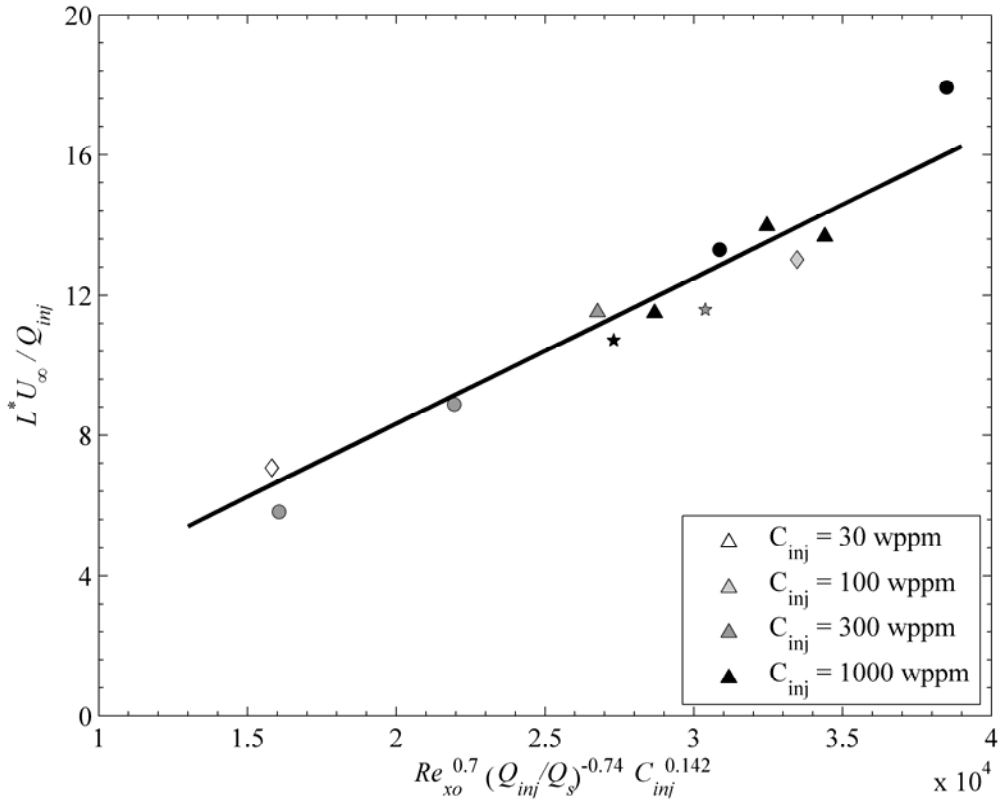

Figure 58. Results from the integral diffusion length scaling with data from the initial diffusion zone when injecting polymer solutions into a MDR polymer ocean.

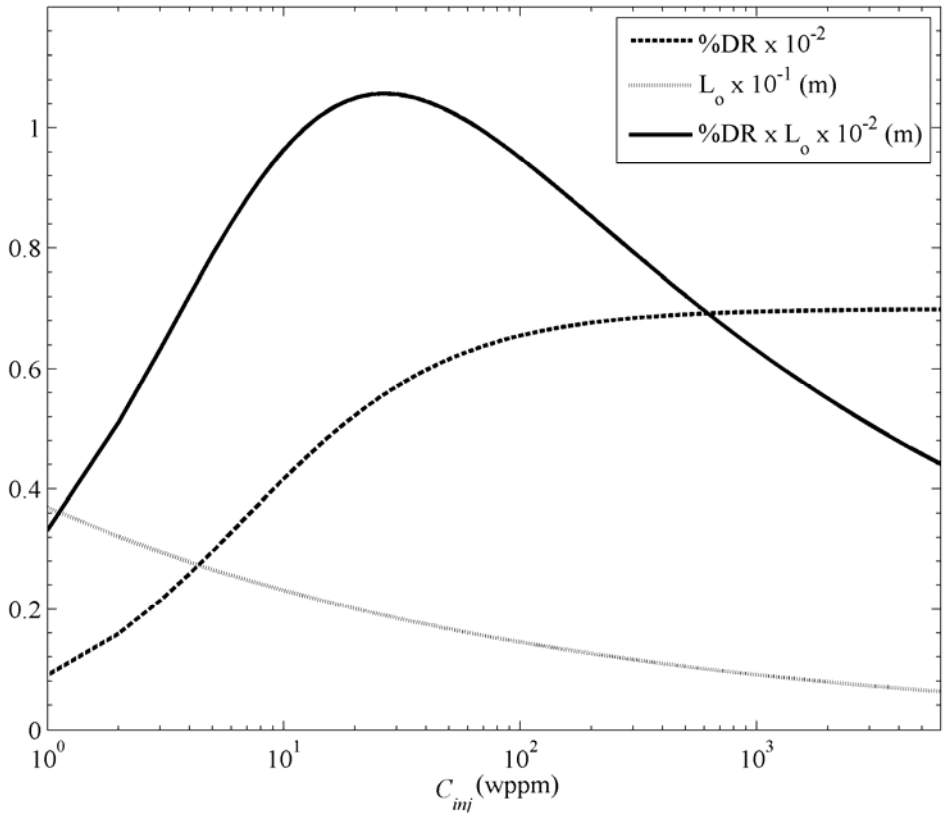

Figure 59. The optimum initial-zone length and the *%DR* at L_o versus the injection concentration determined from polymer injection into the MDR polymer ocean. Also included is the product of the initial-zone length and the corresponding *%DR*, which illustrates the optimized initial-zone length is on the order of one meter.

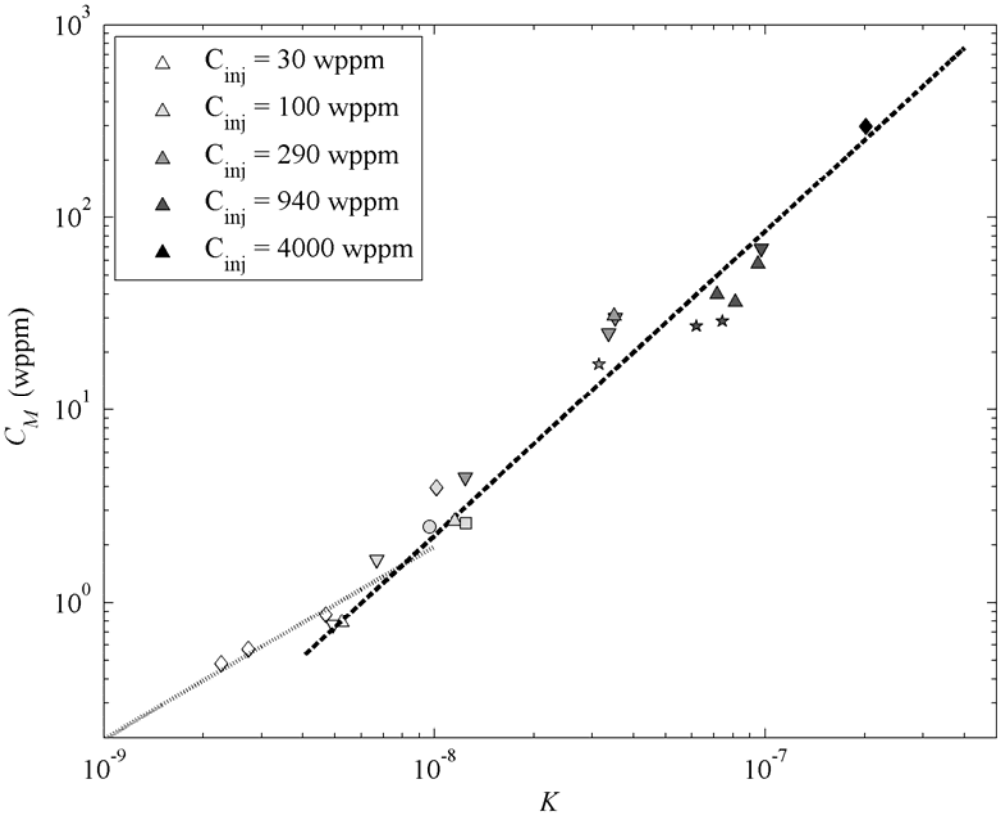

Figure 60. Maximum local polymer concentration, C_M, versus K with the transitionally rough surface. Data were collected with injection fluxes between 2.5 and 14 Q_s at free-stream speeds of 5.6 (◊), 6.9 (▽), 7.6 (o), 8.6 (△), 9.3 (□) and 10.2 (☆) m s^{-1}. The long-dash and short-dash lines are the best fit curves to the data in the intermediate and final-zones, respectively.

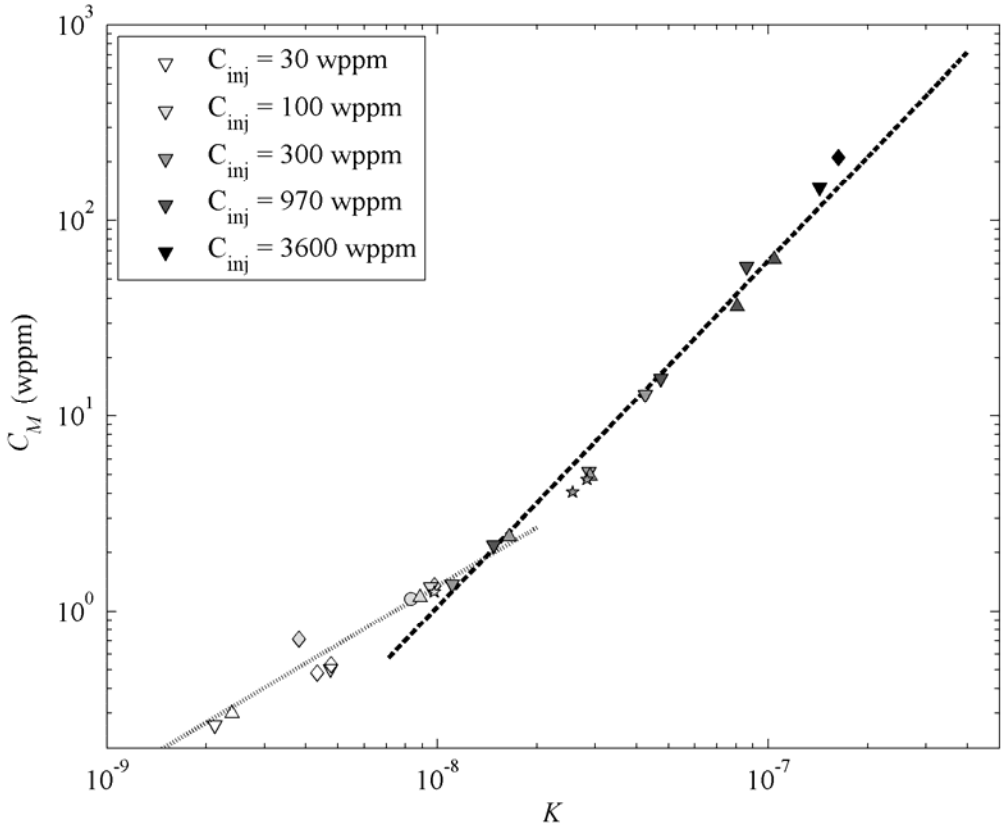

Figure 61. Maximum local polymer concentration, C_M, versus K with the fully rough surface. Data were collected with injection fluxes between 1.0 and 10 Q_s at free-stream speeds of 5.7 (◊), 7.1 (▽), 7.8 (o), 8.8 (△) and 10.6 (☆) m s^{-1}. The long-dash and short-dash lines are the best fit curves to the data in the intermediate and final-zones, respectively.

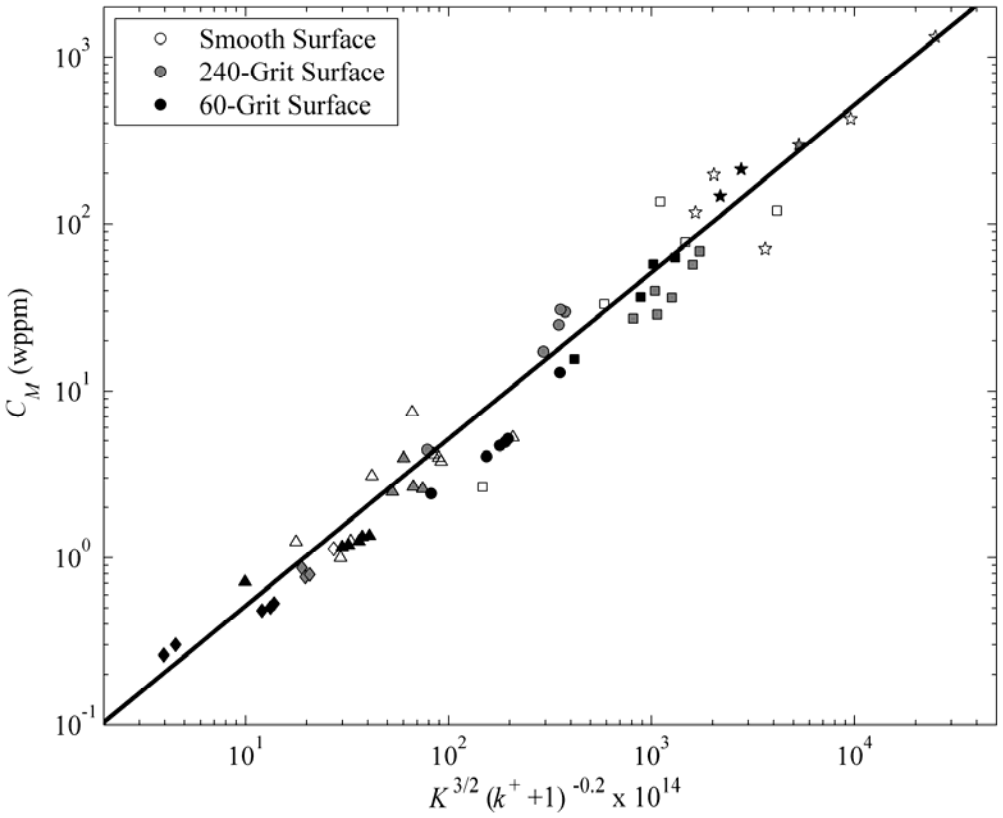

Figure 62. Scaling of peak concentration results within the intermediate-zone of diffusion for the smooth, transitionally rough (240-grit) and fully rough (60-grit) surface conditions. Injection concentrations of 30 (◊), 100 (△), 1000 (o) and 4000 (☆) wppm were tested.

REFERENCES

Brungart, T.A., Harbison, W.L., Petrie, H.L. & Merkle, C.L., 1991, "A fluorescence technique for measurement of slot injected fluid concentration profiles in a turbulent boundary layer," *Experiments in Fluids*, **11**, 9-16.

Collins, D.J. & Gorton, C.W., 1976, "An experimental study of diffusion from a line source in a turbulent boundary layer," *AIChE Journal*, **22**(3), 610-612.

Dubief, Y., White, C.M., Terrapon, V.E., Shaqfeh, E.S.G., Moin, P. & Lele, S.K., 2004, "On the coherent drag-reducing and turbulence-enhancing behaviour of polymers in wall flows," *Journal Fluid Mechanics*, **514**, 271-280.

Elbing, B.R., Dowling, D.R., Solomon, M.J., Perlin, M. & Ceccio, S.L., 2008, "Polymer degradation within a high-Reynolds-number, flat-plate turbulent boundary layer that is fully rough," *Proceedings of the 27th Symposium on Naval Hydrodynamics*, Seoul, Korea.

Fontaine, A.A., Petrie, H.L. & Brungart, T.A., 1992, "Velocity profile statistics in a turbulent boundary layer with slot-injected polymer," *Journal of Fluid Mechanics*, **238**, 435-466.

Fruman, D.H. & Tulin, M.P., 1976, "Diffusion of a tangential drag-reducing polymer injection on a flat plate at high Reynolds number," *Journal of Ship Research*, **20**(3), 171-180.

Gebel, C., Reitzer, H. & Bues, M., 1978, "Diffusion of macromolecular solutions in the boundary layer," *Rheol. Acta*, **17**, 172-175.

Giles, W.B., 1968, "Similarity laws of friction-reduced-flows," *Journal of Hydronautics*, **2**(1), 34-40.

Jiménez, J., 2004, "Turbulent flows over rough walls," *Annual Review of Fluid Mechanics*, **36**, 173-196.

Larson, R.G., 2003, "Analysis of polymer turbulent drag reduction in flow past a flat plate," *Journal of Non-Newtonian fluid Mechanics*, **111**, 229-250.

Morkovin, M.V., 1965, "On eddy diffusivity, quasi-similarity and diffusion experiments in turbulent boundary layers," *International Journal of Heat and Mass Transfer*, **8**, 129-145.

Petrie, H.L., Brungart, T.A. & Fontaine, A.A., 1996, "Drag reduction on a flat plate at high Reynolds number with slot-injected polymer solutions," *Proceedings of the ASME Fluids Engineering Division*, **237**, 3-9.

Petrie, H.L., Deutsch, S., Brungart, T.A. & Fontaine, A.A., 2003, "Polymer drag reduction with surface roughness in flat-plate turbulent boundary layer flow," *Experiments in Fluids*, **35**, 8-23.

Petrie, H., Fontaine, A., Moeny, M & Deutsch, S., 2005, "Experimental study of slot-injected polymer drag reduction," *Proceedings of the 2nd International Symposium on Seawater Drag Reduction*, Busan, Korea, 605-620.

Poreh, M. & Cermak, J.E., 1964, "Study of diffusion from a line source in a turbulent boundary layer," *International Journal of Heat and Mass Transfer*, **7**, 1083-1095.

Poreh, M. & Hsu, K.S., 1972, "Diffusion of drag reducing polymers in a turbulent boundary layer," *Journal of Hydronautics*, **6**(1), 27-33.

Schultz-Grunow, F., 1941, "New frictional resistance law for smooth plates," *NACA* T M **17**, 1-24.

Sellin, R.H.J., Hoyt, J.W., Pollert, J. & Scrivener, O., 1982, "The effect of drag-reducing additives on fluid flows and their industrial applications: Part 2. Basic applications and future proposals," *Journal of Hydraulic Research*, **20**(3), 235-292.

Sommer, S.T. & Petrie, H.L., 1991, "Concentration statistics of active and passive additives downstream of a line source in a LEBU modified turbulent boundary layer," In: *Laser Anemometry: Advances and applications; Proceedings of the 4th International Conference*, **2**, Cleveland, Ohio, 473-481.

Toms, B.A., 1948, "Some observations on the flow of linear polymer solutions through straight tubes at large Reynolds numbers," *Proceedings of the First International Congress on Rheology*, **2**, 135-141.

Vdovin, A.V. & Smol'yakov, A.V., 1978, "Diffusion of polymer solutions in a turbulent boundary layer," *Journal of Applied Mechanics and Technical Physics*, **19**(2), 66-73.

Vdovin, A.V. & Smol'yakov, A.V., 1981, "Turbulent diffusion of polymers in a boundary layer," *Journal of Applied Mechanics and Technical Physics*, **22**(4), 98-104.

Virk, P.S., Merrill, E.W., Mickley, H.S., Smith, K.A. & Mollo-Christensen, E.L., 1967, "The Toms phenomenon: turbulent pipe flow of dilute polymers solutions," *Journal of Fluid Mechanics*, **20**, 22-30.

Virk, P.S., Mickley, H.S. & Smith, K.A., 1970, "The ultimate asymptote and mean flow structure in Toms' Phenomenon," *Journal of Applied Mechanics*, **37**(2), 488-493.

Virk, P.S., 1975, "Drag Reduction Fundmentals," *AIChE Journal*, **21**(4), 625-656.

Walker, D.T., Tiederman, W.G. & Luchik, T.S., 1986, "Optimization of the injection process for drag-reducing additives," *Experiments in Fluids*, **4**, 114-120.

Walker, D.T. & Tiederman, W.G., 1989, "The concentration field in a turbulent channel flow with polymer injection at the wall," *Experiments in Fluids*, **8**, 86-94.

Wetzel, J.M. & Ripken, J.F., 1970, "Shear and diffusion in a large boundary layer injected with polymer solution," *Project Report*, 114. St. Anthony Falls Hydraulic Laboratory, University of Minnesota.

White, C.M. & Mungal, M.G., 2008, "Mechanics and prediction of turbulent drag reduction with polymer additives," *Annual Review of Fluid Mechanics*, **40**, 235-256.

White, F.M., 2006, *Viscous Fluid Flow*, 3rd Ed., McGraw Hill, Inc., 430-438.

Winkel, E.S., Oweis, G., Vanapalli, S.A., Dowling, D.R., Perlin, M., Solomon, M.J. & Ceccio, S.L., 2008, "High Reynolds number turbulent boundary layer friction drag reduction from wall-injected polymer solutions," *Journal of Fluid Mechanics*, in press.

Wu, J. & Tulin, M.P., 1972, "Drag reduction by ejecting additive solutions into pure-water boundary layer," *Journal of Basic Engineering, Transactions of the ASME*, **94**, 749-756.

PART VI. CONCLUSION (GLOBAL)

With the growing need for renewable energy sources and more efficient use of current supplies, the current study aims to develop methods to reduce fuel consumption. Specifically, the reduction of fuel consumption for marine transportation, which according to the UNFCCC Subsidiary Body for Scientific and Technological Advice 2008 report on greenhouse gas emissions from ships consumed 1.9 billion barrels of fuel in 2007 excluding military use. The current work addressed several issues concerning the implementation of two drag reduction methods, polymer drag reduction (Part II, IV and V) and air injection drag reduction (Part III), for surface ships. Successful implementation of such technology would have the potential of saving over a billion barrels of fuel each year as well as lowering greenhouse gas emissions and improving air quality.

Drag reduction with the injection of air shows the most promise for implementation on a surface ship since high levels of drag reduction (approaching 100% drag reduction) with no apparent decrease with downstream distance once an air-layer formed. Air injection drag reduction (Part III) was studied on a 12.9 m long flat plate model with the surface either hydraulically smooth or fully rough. Additionally the background water surface tension and the injector design were varied during experimentation. While bubble drag reduction (BDR) was studied, the primary focus of

the work was on the proper scaling of the critical air flux required to achieve air-layer drag reduction (ALDR). ALDR results in drag reduction between 80% and 100% over the entire model length (12.9 m) and stable air-layers were achieved at downstream distance based Reynolds numbers of 160 million at a maximum speed of 15.3 ms^{-1}. The proposed scaling that assumed the critical volumetric flux is a function of the ratio between shear and buoyancy forces ($u_\tau/[\nu g]^{1/3}$) showed good collapse of results independent of surface condition, background water surface tension and injector design.

Conversely, results for polymer drag reduction (PDR) experiments indicate that with polymers available today PDR does not seem ideal for reduced fuel consumption on a surface ship (increased performance such has top speed is possible). PDR is limited both by the diffusion of the solution through the boundary layer and the breaking of the polymer chains (i.e. polymer degradation) within the flow. Both problems, diffusion and degradation, are enhanced with increase surface roughness and surface ships are typically not hydraulically smooth. In Part IV PDR was studied on a 12.9 m long flat plate test model with the surface either hydraulically smooth or fully rough. The primary finding from this experiment was that the polymer chains break under certain flow conditions resulting in decreased drag reduction efficiency of the polymer solutions. Furthermore, the scaling of Vanapalli *et al*. (2006) that was validated in Part II was reworked to develop a new scaling parameter for injected solutions within boundary layer flows.. While Part IV observed that increased roughness caused an increase in diffusion, the limited results prevent an in depth analysis of the diffusion process. For this reason a separate study (Part V) was conducted on a ~1 m long test model that focused solely on

the diffusion of polymer solutions with a TBL with three separate surface roughness conditions. These results found a correlation between the near-wall polymer concentration and the surface roughness, injection and flow condition. Showing that increased surface roughness shortens the initial zone length (region immediately downstream of the point of injection that has high concentration levels near the model surface), which limits the ability to improve performance with proper engineering of the injection scheme. A separate experiment was conducted to produce an idealized injection condition (smooth surface with injection into maximum drag reduced flow, which suppresses the turbulent fluctuations that cause the solution to be rapidly diffused through the boundary layer), which showed that the maximum initial zone length is on the order of one meter long.

In conclusion the work presented has shown the ability to achieve skin-friction drag reduction approaching 100% at downstream distances in excess of 10 meters by forming a thin layer of air at the model surface (i.e. ALDR). These results indicate that ALDR is a viable candidate for implementation on a surface ship. However, further investigation is required to determine (1) how sensitive is the air layer to flow disturbances, (2) can the required air flux for ALDR be reduced with proper engineering at the injection location and (3) can stable air layers persist ~100 meters downstream of the injection location. Polymer drag reduction using the most efficient, readily available polymer (polyethylene oxide) shows limited downstream persistence of high levels of drag reduction and drastically worse performance if surface roughness is increased. The limited downstream persistence is the product of polymer diffusion and degradation by

chain scission (i.e. breaking of the polymer chains). These findings suggest that future work on PDR should be concentrated on the development of more efficient drag reducing polymers that are less susceptible to chain scission.